BIOMEDICAL APPLICATIONS OF HYBRID POLYMER-BASED MATERIALS

Presented by Hamidreza Enshaei

UNIVERSITAT POLITÈCNICA
DE CATALUNYA
BARCELONATECH

IMEM

Biomedical applications of hybrid polymer-based materials

Presented by Hamidreza Enshaei

Supervisors: Prof. Carlos Alemán and Dr. Núria Saperas

Thesis submitted to obtain the degree of Doctor of Philosophy in Chemical Engineering at the Universitat Politècnica de Catalunya

Barcelona, 2022

Departament d'Enginyeria Química

Grup d'Innovació en Materials i Enginyeria Molecular

Acknowledgments

I would like to express my deepest appreciation to my supervisor Prof. Carlos Alemán for giving me the golden opportunity of being a part of his research team. Without his valuable guidance and constant feedback, the planning and development of this research work would not have been successful.

I cannot begin to express my thanks to my supervisor Dr. Núria Saperas, who has been a great help in concluding this thesis, which would be impossible without her endless kindness, support, valuable critiques, and profound belief in my abilities.

I would also like to extend my gratitude to Dr. Luis Javier del Valle, Dr. Lourdes Franco and Prof. Elaine Armelin for their willingness to share their time and immense knowledge on any occasion. I gratefully thank Dr. Anna Puiggalí and Dr. Brenda Molina for their support, guidance and patience that cannot be underestimated.

I would also like to express my gratitude to all my past and present colleagues and friends from IMEM and PSEP research groups. People who were my second family far from home for the last five years. I would like to thank Sonia, Neudys, Vitor, Ludka, Filip, Matteo, Maricarmen, Samuele, Helena, Adrian, Karima, Jordi, Marc, Didac, Hamidreza, Reza, Amir, Sofia, Irene, Guillem, Mar, Angelica, Georgina and Maricruz for all the happy memories that they made for me and letting me record them with my selfies. Moreover, thanks for all the help and guidance they always gave me as excellent friends in the good and less good moments. And a special thanks to Ina and Max for always having my back and supporting me unconditionally (best team ever, forever).

I am grateful to my family, especially my dear mother and brother, for the constant support and love they always gave me to keep me motivated and confident. My accomplishments and successes are because they believed in me.

Abstract

Polymers have been widely used in biomedical applications for drug delivery purposes in the last decades. However, ordinary long-term drug delivery systems are sometimes associated with undesired side effects if the concentration of the released drug is higher than needed. Therefore, scientists look for new techniques to enhance the efficiency and safety of the release by controlling the release time, rate and accuracy in targeting specific tissues or cells to spare the rest of the body from side effects. In this thesis, several polymeric platforms (microfibers, hydrogels, nanoparticles, nanomembranes) and their combinations have been used to modulate and control the release of different kinds of drugs.

Five different platforms have been obtained. They are described in the results section of the thesis (chapter 3):

1) In section 3.1, an electrically triggered release system is presented. Specifically, the release of the antibiotic chloramphenicol (CAM) from conducting polymer nanoparticles made of poly(3,4-ethylenedioxythiophene (PEDOT) has been studied and characterized. In addition, the designed platform allows for in situ monitoring of bacterial growth inhibition through the electrochemical detection of β-nicotinamide adenine dinucleotide (NADH).

2) A pharmacological chaperone (pyrimethamine, PYR) has been also encapsulated in PEDOT nanoparticles (section 3.2). Release experiments carried out with and without electrical stimuli demonstrate that release can be increased up to ~50% when sustained CV stimulation is applied for 30 min.

3) Section 3.3 describes a controlled release device consisting of a polypeptide hydrogel (Poly(γ-glutamic acid, PGGA) loaded with a small hydrophobic drug (curcumin, CUR) which was previously encapsulated in PEDOT nanoparticles. This platform allows to tune CUR release when applying an electrical stimulus.

4) In the next section (3.4), the pharmacological chaperone ambroxol hydrochloride (AH) is loaded in polymeric electrospun microfibers of poly(ε-caprolactone (PCL). In order to regulate the release, electrospun microfibers have been coated with additional PCL layers using dip-coating or spin-coating. AH functionality was verified with a thermal denaturation assay utilizing GCase, demonstrating that the electrospinning procedure did not affect the functionality of the drug.

5) Finally, section 3.5 reports drug release from a complex platform consisting of two spin-coated layers of PGGA hydrogel, loaded with PEDOT microparticles and separated by an electrospun layer of PCL microfibers. Poly(hydroxymethyl-3,4-ethylenedioxythiophene) (PHMeDOT) was polymerized through the whole three-layered system while forming a dense network of electrical conduction paths. The platform has been loaded with levofloxacin (LVX) before performing the release experiment. Although the release of LVX is fast, this device allows for real-time electrochemical monitoring of the remaining antibiotic inside the platform.

Taken together, the studies presented in this thesis provide an overview of new hybrid polymeric platforms that allow to optimize and control drug release while, in some cases, achieving additional functionalities.

List of abbreviations

Abbreviation	Meaning
AFM	Atomic force microscopy
AH	Ambroxol hydrochloride
APS	Ammonium persulfate
ATR	Attenuated total reflection
CA	Chronoamperometry
CA	Contact angle
CAM	Chloramphenicol
CDI	1-[3-(dimethylamino)propyl]-3-ethylcarbodiimide methiodide
CPs	Conducting polymers
CRTL	Control
CUR	Curcumin
CV	Cyclic voltammetry
Cys	Cystamine dihydrochloride
DBSA	Dodecyl benzenesulfonic acid
DDS	Drug delivery system
DLS	Dynamic light scattering
DMEM	Dulbecco's modified eagle's medium
EDC	1-[3-(dimethylamino)propyl]-3-ethylcarbodiimide methiodide
EDOT	3,4-ethylenedioxythiophene
EIS	Electrochemical impedance spectroscopy

ER	Endoplasmic reticulum
EtOH	Ethanol
FA	Formic acid
FBS	Fetal bovine serum
FDA	Food and Drug Administration
FTIR	Fourier transform infrared
Glu	Glutamic acid
IC	Inhibitory concentration
ICP	Intrinsically conducting polymer
ITO	Indium tin oxide
LB	Langmuir–blodgett
LB	Lysogeny broth (cell medium)
LBL	Layer-by-layer
LC	Loading capacity
LEA	Loss of electroactivity
LSDs	Lysosomal storage disorders
LVX	Levofloxacin
MEC	Minimum effective concentration
MFs	Electrospun microfibers
MSC	Maximum safe concentration
MTT assay	Cell cytotoxicity test using 3-(4,5-dimethylthiazol-2-yl)-2,5-diphenyltetrazolium
MU	4-methylumbelliferone

MWCO	Molecular weight cut-off
NADH	β-nicotinamide adenine dinucleotide
NADPH	β-nicotinamide adenine dinucleotide phosphate
NAX	Nalidixic acid
NMs	Nanomembranes
NPs	Nanoparticles
OCP	Open circuit
PAni	Polyaniline
PBS	Phosphate buffered saline
PC	Pharmacological chaperone
PCL	Poly(ε-caprolactone)
PCs	Pharmacological chaperones
PDI	Polydispersity
PEDOT	Poly(3,4-ethylenedioxythiophene)
PET	Poly(ethylene terephthalate)
PGA	Poly(glycolic acid)
PGGA	Poly(γ-glutamic acid)
PHMeDOT	Poly(hydroxymethyl-3,4-ethylenedioxythiophene)
PIP	Piperine
PLA	Poly(lactic acid)
PLACL	Poly(L lactic acid)-co-poly(ε-caprolactone)
PLGA	Poly(lactic-coglycolic acid)
PPy	Polypyrrole

PS	Polystyrene
PTh	Polythiophene
PU	Polyurethane
PYR	Pyrimethamine
SAM	Self-assembled monolayer
SC	Specific capacitance
SD	Standard deviation
SEM	Scanning electron microscopy
sINP	Semi-interpenetrated
SPCE	Screen-printed carbon electrode
SR	Swelling ratio
ST	Electrical stimulation
TFE	2,2,2-trifluoroethanol
TGA	Thermal gravimetric analysis
Tween-20	Polyoxyethylenesorbitan monolaurate
XPS	X-ray photoelectron spectroscopy
β-hex	β-hexosaminidase

Table of contents

X

1

Chapter

Introduction

Introduction

1.1 Polymers in biomedical applications

Biomaterials are essentially materials mainly utilized and adapted to interact with biological systems.[1] They can stay in the biological environment (living system) for prolonged periods[2] and for that, they should have non-toxicity, biocompatibility, good performance, minor side effects, and in some cases, acceptable mechanical properties.[3] They have numerous biomedical applications such as cardiac valves, artificial hearts, vascular grafts, breast prosthesis, dental materials,[4] contact and intraocular lenses,[5] fixtures of extracorporeal oxygenators, dialysis and plasmapheresis systems, coating materials for medical products, implants, surgical materials, tissue adhesives, etc.[6] A vast range of biomaterials, from the most rigid metal, like titanium, and ceramics to soft polymeric ones, like hydrogels, have been investigated to satisfy the demands of the biomedical society.[7]

Biopolymers have advantages compared to other types of biomaterials such as (a) simple producing, (b) ease of secondary processability, (c) affordable cost, and (d) being designable in preferred mechanical and physical characteristics.[3]

Biopolymers are polymers that have a biological nature[8] and based on their origin can be categorized in two classes [9] (**Figure 1.1.1**): natural polymers, which already have been used in medical applications for thousands of years, and chemically synthesized polymers, which are synthesized from natural resources, such as proteins, amino acids, sugars, fats, etc.[10] Some synthetic polymers, such as acrylics, polyamides, polyesters, polyethylene, polysiloxanes, and polyurethane, as well as natural polymers like chitosan, carrageenan, and alginate are utilized in biomedical applications such as tissue regeneration, drug delivery systems, orthopaedic devices, gene delivery, etc.[9,11] In general, synthetic

19

polymers offer more significant advantages than natural ones because they can be tailored to give a broader range of properties.[12]
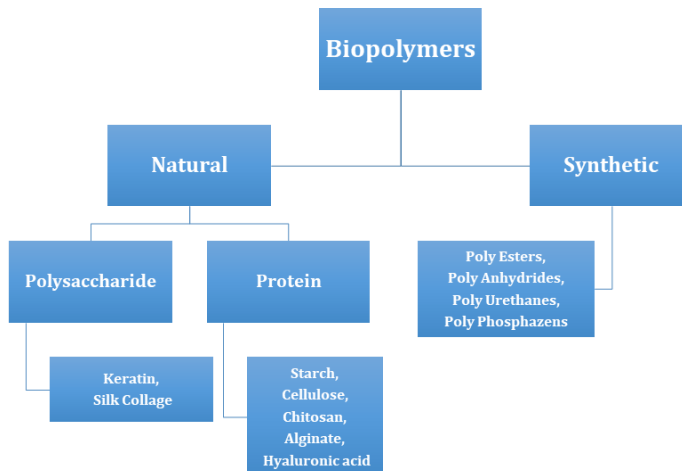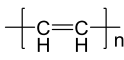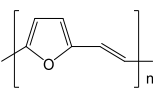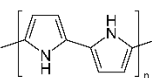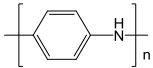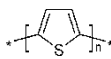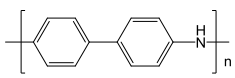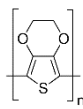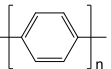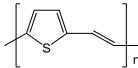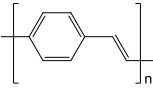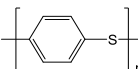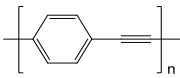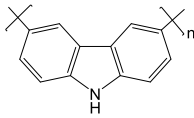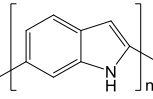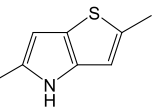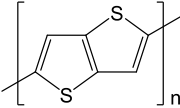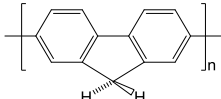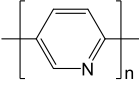
Figure 1.1.1. Classification of biopolymers. Adapted with permission from ref.[9] Copyright 2021 Elsevier Inc.

1.1.1 Conducting polymers (CPs)

Before CPs were developed, polymers were assumed to be electrical insulators.[13] About 30 years after CPs invention, researchers still pay considerable attention to them due to the numerous applications of these polymers in the scientific field.[14] They have been studied extensively because of their more straightforward synthesis process, high mechanical and electrical resilience, low working temperature, and low cost.[15] The most well-known CPs, which have been investigated extensively about their synthesis, characterization and applications, are polyaniline (PAni), poly(3,4-ethylenedioxythiophene) (PEDOT), polythiophene (PTh), polypyrrole (PPy) and their derivatives.[16–18] **Table 1.1.1** shows a list of representative CPs and their structures.

Table 1.1.1. Typical CP Structures. Adapted with permission from ref. [19] Copyright 2009 Taylor & Francis Group, LLC.

Name	structure	Name	structure
Polyacetylene (PAc)		Poly(thienylene-vinylene) (PTV)	
Polypyrrole (PPy)		Polyaniline (PAni)	
Polythiophene (PTh)		Poly(diphenylamine)	
Poly(ethylenedioxythiophene) (PEDOT)		Poly(para-phenylene) (PPP)	
Poly(thienylene-vinylene) (PTV)		Poly(phenylene-vinylene) (PPV)	
Poly(phenylenesulfide) (PPS)		Poly(phenylene ethynylene) (PPE)	
Polycarbazole		Poly(indole)	
Poly(thieno[3,2-b]pyrrole)		Poly(thieno[3,2-b]thiophene)	
Poly(fluorene)		Polypyridine	

In the 1990s, the opportunity to use CPs in biomedical applications, like tissue engineering, was envisaged. This was due to their role in adjust cellular activities, such as cell adhesion, proliferation, migration and differentiation.[20–23] The sensitivity of cells or tissues to electrical stimuli in muscles, cardiac cells, nerves, etc. originated more studies on CPs.[24–27]

CPs, because of their electrical characteristics, high theoretical capacitance, proper wave sorption,[28] excellent redox activity, and outstanding electrochemical demeanor, have expansive applications in diverse areas, such as supercapacitors, nanocoatings, catalysis, corrosion inhibitors, biomedical application and sensors (**Figure 1.1.2**).[13,29–31]

They can be found in different shapes, like particles, hydrogels and films,[31] providing different electrical, optical, and mechanical characteristics.[32]
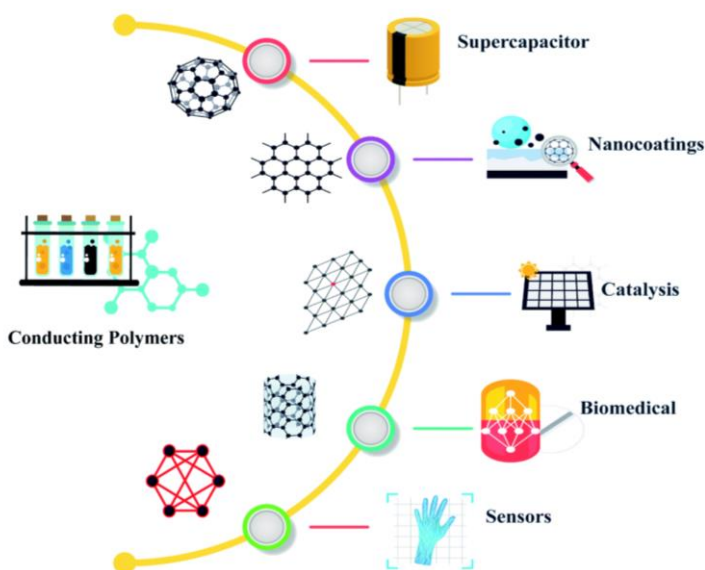
Figure 1.1.2. CPs applications. Reprinted with permission from ref.[13] Copyright 2021 American Chemical Society.

Poly(3,4-ethylenedioxythiophene) (PEDOT) (**Figure 1.1.3**), due to its high conductivity, stability, optimal opacity and easy fabrication, has been chosen as a conducting polymer in this project. It has various applications in antistatic coating, organic display devices, energy storage and transformation, and sensors.[33,34]
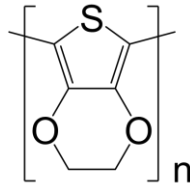
Figure 1.1.3. PEDOT chemical structure.

1.1.1.1 Biomedical applications

In recent years, the most significant research advances in CPs applications have been in medical applications. The individual functions of controlled surface energy, controlled release and stimulation are used for numerous internal (implant) or external applications to the human body.[19] CPs have countless applications in medical science, such as biomedical implants, tissue engineering, biosensors, drug delivery, etc.[14]

a) CPs in tissue engineering

Biodegradable scaffolds are crucial in tissue engineering.[35] Since electrical stimulation positively impacts the behavior and function of electroactive tissues, more promising tissue regeneration demands electrical conductivity within biodegradable scaffolds. Furthermore, scaffolds need chemical, electrical and mechanical properties for cell growth and adhesion. All these objectives can be achieved by using conducting materials.[36–38]

b) CPs in biosensors

Nowadays there's a need for the sensors and electronics that can create adaptable interfaces with some biological environment while not losing biocompatibility and stability. Incorporating biocompatible material with CPs offers a comprehensive platform with exceptional properties and beneficial

functionality for bioelectronics and biosensors. These temporary implant sensors have been broadly operated to gather vital physiological changes such as oxygen content, potential, temperature, strain, blood pressure, pH and fluorescence.[39–41]

c) Actuators

An actuator is a device that can convert an external stimulus, like electrical and thermal stimuli, to a physical motion. Therefore, this device can be used as an artificial muscle.[42]

CPs are the most exciting material to use as actuators due to their low operating voltage and extensive stress range. Among all CPs, polypyrrole (PPy) has received a lot of attention due to its electrochemical activity in a wide range of pH and simple preparation.[43,44]

d) CPs in drug delivery

Many drug delivery system devices have been generated during the last few decades to improve the drug-targeting specificity and reduce systemic drug toxicity. One of the delivery systems' main flaws is preserving accurate control on switching the release "on" or "off". CPs have been utilized due to their reversible electrochemical response to overcome this drawback.[45] The strength of the interactions between the drug and CP carrier can be regulated by controlling the oxidation and reduction state. This capacity results in a benefit to the controlled release of many drugs, which can be delivered by reducing the strength of such interactions by applying oxidation or reduction voltages (depending on the chemical structure of the drug). Furthermore, CPs can control drug movement with electric charge flow for targeting a tissue. In other words, by applying more stimuli, more drug is released while without external impulses, fewer drug is

released.[46,47] Simple loading and low effect on drug activity are additional CPs's advantages.[48]

1.1.2 Controlled drug delivery systems

A drug delivery system (DDS) is a kind of device that transports the drug to the body and enhances its efficacy and safety by controlling the rate, time, and location of the drug release in the body.[49]

The customary drug therapy demands periodic drug doses at a short interval.[50] Designing a sustained or controlled release drug delivery system aims to decrease the dosing frequency, reduce the dose, control blood plasma drug levels, better patient compliance, and provide consistent drug delivery.[51–54] A controlled release system, by preserving the drug concentration in the body in the optimum remedial range and under the toxicity point, increases the drug's general efficacy. On the other hand, aimless delivery can cause major and sometimes lethal side effects.[55] Blood plasma drug concentrations also should be in the medicinal range to stay effectual and endured. This range is between the minimum effective concentration (MEC) and the maximum safe concentration (MSC) (**Figure 1.1.4**).[56]

25
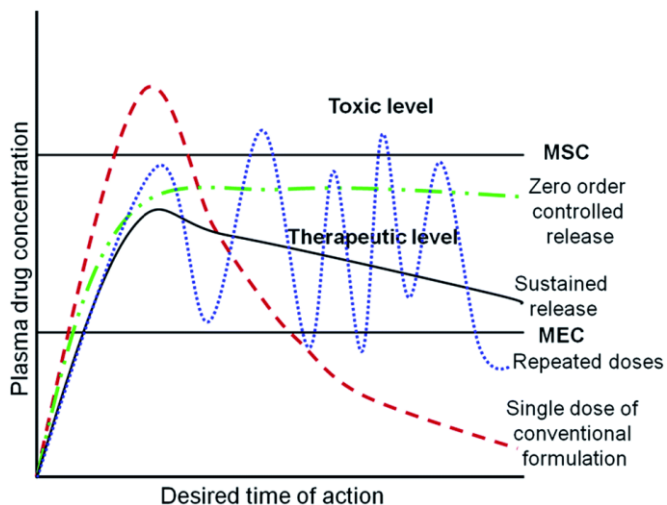
Figure 1.1.4. A schematic diagram for conventional and controlled drug delivery. Reproduced with permission from ref.[57] Copyright 2015 Royal Society of Chemistry.

1.1.2.1 Triggered drug delivery

Increasing demands for accurate and customized treatment led to emergence of stimuli-responsive drug delivery systems.[58–60] An external impulse, such as ultrasound,[61,62] magnetic field,[63,64] pH,[65,66] light,[67,68] temperature[69,70] or electrical field,[71,72] makes the stimuli-responsive system to release its biological cargo to reach the intended concentration for medical treatment. This releasing method can be used in hormone therapy,[73] pain control, accurate chemotherapy drug delivery,[74] and anti-inflammatory or antibiotic drugs delivery from implants.[75]

Electrical stimuli are especially attractive as: (i) they allow to generate accurate and precise signals easily, remotely and repeatedly without large and complex instruments being required, and (ii) it is possible to miniaturise the electrical devices and develop them into a wireless implant.[76] The materials that are capable of being investigated for electrically responsive drug delivery are graphene, carbon nanotubes, nanoparticles and CPs.[77,78]

1.1.2.2 Drug release mechanisms

Generally, in polymeric systems, drug delivery is the process through which a drug molecule moves from a polymeric matrix to its surface and then is released into the environment.[79]

The main mechanisms of controlled release (**Figure 1.1.5**) are: [80]

a) drug release through water-filled pores.

b) release through the polymer matrix.

c) osmotic pumping.

d) erosion.

27
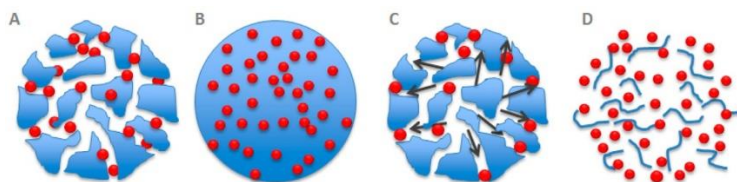
Figure 1.1.5. Drug release mechanisms from polymeric NPs: (A) diffusion through water-filled pores, (B) diffusion through the polymer matrix, (C) osmotic pumping, and (D) erosion. Reprinted with permission from ref.[56] Copyright 2016 American Chemical Society.

a) Drug Diffusion through Water-Filled Pores

Diffusion in the degradable polymeric matrix through pores network causes a controlled drug release rate. Water molecules, which are instantaneously absorbed by polymeric NPs, fill all the pores, enlarging them. This size-changing process facilitates, in some cases, the drug release.[81]

b) Drug Diffusion through the Polymer Matrix

In this case, drugs just diffuse out of the matrix. In nondegradable drug delivery reservoirs, diffusion is the major force causing the drug release. This uniform release rate is related to the permeability and thickness of the polymeric matrix (e.g. fibres and films).[82]

28

c) Osmotic Pumping

Convection force is the other way to transport the drug through the pores. Osmotic pressure leads the water to penetrate a non-swelling system and force the drugs out of the pores. This force is known as osmotic pumping.[83]

d) Erosion

In biodegradable scaffolds, *surface erosion* occurs when degradation starts at the matrix surface and continues to the inner matrix network, while the matrix size shrinks gradually.[84] In surface erosion, degradation is always much higher than water influx into the polymeric scaffold.[85] On the other hand, when water infiltrates the bulk of the polymer scaffold and a consistent degradation starts in all the matrix homogeneously, *bulk erosion* occurs.[86] In bulk erosion, degradation is lower than water penetration into the polymeric scaffold.[87]

Apart from the mechanisms, there are several routes to deliver the drug to the body, such as:

1. Oral Drug Delivery (tablets or capsules).

2. Parenteral Drug Delivery (subcutaneous, intramuscular, intravenous, and intra-arterial injections).[49]

3. Transdermal Drug Delivery (gels, patches, nanoparticles, electro transports, needle-free injections).[88,89]

4. Transmucosal Drug Delivery (buccal, nasal, rectal, etc.)

5. Nasal Drug Delivery (nasal drops and sprays).[90]

6. Gastric Drug Delivery (ingestible self-orienting millimeter-scale applicator (SOMA)).[91,92]

7. Colorectal Drug Delivery.

8. Pulmonary Drug Delivery (inhalers and dry powders).

9. Cardiovascular Drug Delivery (implant by surgery or catherization).[93]

10. Drug Delivery to the Central Nervous System (nanoparticles, gels, injections, etc.,).[80]

Table 1.1.2 shows major drug delivery routes advantages and disadvantages.

29

Table 1.1.2. Comparison of major routes of drug delivery for systemic absorption. Adapted with permission from ref.[49] Copyright 2020 Springer Nature.

Issue	Oral	Intravenous	Intramuscular/ subcutaneous	Transnasal	Transdermal	Pulmonary
Delivery to blood circulation	Indirect through GI tract	Direct	Indirect absorption from tissues	Indirect	Indirect	Indirect
Onset of action	Slow	Rapid	Moderate to rapid	Rapid	Moderate to rapid	Rapid
Bioavailability	Low to high	High	High	Moderate	Low	Moderate to high
Dose control	Moderate	Good	Moderate	Moderate to good	Poor	Moderate to good
Administration	Self	Health professional	Self or health professional	Self	Self	Self
Patient convenience	High	Low	Low	High	Moderate	High
Adverse effects	Gastrointestinal upset	Acute reactions	Acute reactions	Insignificant	Skin irritation	Insignificant
Use for proteins and peptides	No	Yes	Yes	Yes	No	Yes

1.2 Different forms of drug carriers and techniques to obtain them

Biopolymer scaffolds[94] can be developed in various shapes such as nanoparticles, films,[95] nanofibers, and hydrogels[96] to use as biomedical devices. The following is a brief description of the scaffolds used in this project.

1.2.1 Polymeric electrospun nanofibers

Nowadays, nanotechnology has become remarkably entrenched in human life. The benefits, such as high surface area, flexibility in surface functionality, and highly porous membranes, lead to development in diverse branches such as biomedical, cosmetics, supercapacitors and nanosensors, protective clothing, environmental protection and filtration.

Nanofibers, nanoparticles, nanotubes, and nanowires are most favourite scaffolds in nanotechnology. However, nanofibers have received lots of attention from academics and industries due to their high surface area, aspect ratio and flexibility, among other characteristics.[97,98]

There are numerous manufacturing systems available (**Table 1.2.1**) to obtain biomaterials with optimal physicochemical properties for tissue engineering, such as self-assembly,[99] template synthesis,[100] phase-separation,[101] melt-blowing,[102] and electrospinning.[103]

Among them, electrospinning has extensively been used for manufacturing scaffolds for tissue engineering,[104–106] drug delivery systems,[107,108] wound dressings,[109,110] artificial organs,[111] and vascular grafts.[112] It is a multipurpose, beneficial and simple process for producing micro or nanoscale fibers by applying a high voltage to a polymer solution or melt.[113]

Different synthetic polymers such as poly(ε-caprolactone) (PCL), poly(lactic acid) (PLA), poly(glycolic acid) (PGA), poly(lactic-coglycolic acid) (PLGA), polystyrene (PS), polyurethane (PU), poly(ethylene terephthalate) (PET), and poly(L lactic acid)-co-poly(ε-caprolactone) (PLACL), or natural polymers like collagen, gelatin, and chitosan have been widely studied as electrospun nanofibers.[114]

31

Table 1.2.1. Comparison of various methods applied in scaffold fabrication in terms of benefits and difficulties associated with their usage.[115-117] Adapted with permission from ref.[118] Copyright 2021 Elsevier.

Scaffold Fabrication Method	Advantages	disadvantages
Electrospinning	Uniform, aligned fiber, strong interconnectivity of porosity, 80–95% porosity, 100–1100 nm fiber diameter, <80% cell viability, ECM like structure, superior mechanical properties, large surface area, and facile and simple fabrication.	Needs high voltage apparatus, solvents used may be toxic, and difficulties in packaging, shipping, and handling.
Self-assembly	80–90% porosity, 70–90% cell viability, 5–300 nm.	Using peptides, complex process, not scalable, poor control over fiber dimension.
Phase Separation	Simple fabrication, 60–95% porosity.	Use of potentially toxic solvents, poor control over architecture, and restricted range of pore sizes.
Gas Foaming	Solvent-free, no loss of bioactive molecules in the scaffold matrix.	Needs high pressure, poor interconnectivity of porosity, the existence of skimming film layers on the scaffold surface.
Solvent Casting	Simple fabrication, high mechanical stability.	Lacks reproducibility, uncontrolled structure.
Freeze Drying	30–80% porosity, 50–450 nm, cell viability <90%, it needs neither high temperature nor a separate leaching step.	Need freeze-dryer, limited to small pore size, irregular porosity, the long processing time.
3D Printing	Fabrication desired structure (flexibility in production).	Needs 3D printer, uses toxic organic solvents, lacks the mechanical strength.

There are three categories of parameters that affect the diameter and the morphology of electrospun nanofibers: intrinsic properties of the solution, processing, and ambient factors.[119,120]

The intrinsic properties of the solution, such as concentration, viscosity, molecular weight, electrical conductivity, surface tension of the solvent, elasticity and polarity, have a notable influence on the morphology and the final diameter of the electrospun nanofibers.[118]

Processing factors such as voltage, the distance between the needle tip and the collector, and the polymer solution's feeding rate are essential items in the electrospinning process.[119,120]

The environmental parameters such as humidity and temperature while producing an electrospun sheet are also important, especially for obtaining uniform fibrous mats.[121]

The electrospinning setup (**Figure 1.2.1**) includes a high voltage power supply, syringe pump, a solution loaded syringe with a blunt-tip needle, and a collector.[122]
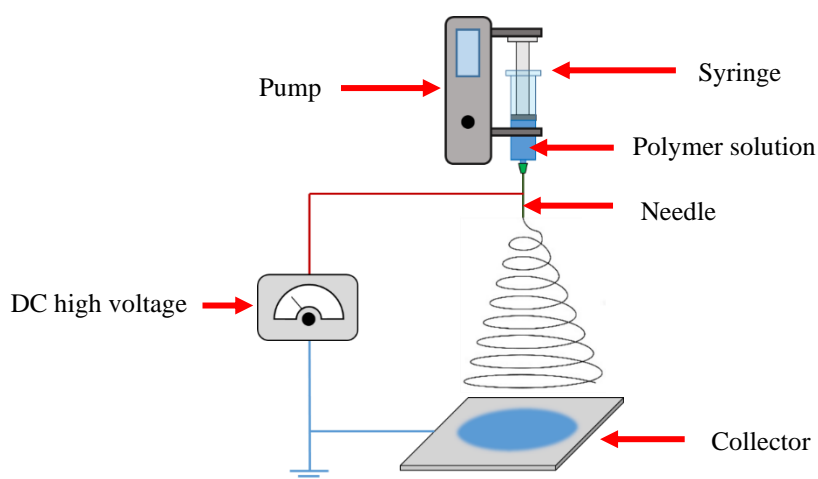
Figure 1.2.1. A schematic representation of the electrospinning setup.

In this Thesis, we used polycaprolactone (PCL) (**Figure 1.2.2**) to construct electrospun fibers. PCL is a semicrystalline biodegradable polymer that belongs to the family of polyesters.[123] It is one of the most essential biodegradable polymers in medicine.[12] Compared with other polyester family members such as poly(glycolic acid) (PGA), poly(lactide) (PLA), and poly(lactide-co-glycolide) (PLGA), PCL has been less frequently used as a material for fabricating biomaterial scaffolds.[123] Due to the slow degradation, high permeability to many drugs and non-toxicity, PCL was initially investigated as a long-term

drug/vaccine delivery vehicle.[124] Some PCL applications are sutures, scaffolds in tissue engineering and biocompatible medical devices. [12]
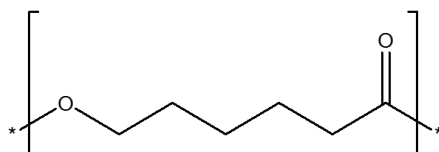
Figure 1.2.2. PCL chemical structure.

1.2.2 Polymeric nanomembranes

A nanomembrane is an autonomous structure with a thickness of 10 to a few hundreds of nm.[125,126] Some researchers have seen nanomembranes as molecular filters[127] or sensors for humidity in optical microcavity,[128] but many have noticed their immense ability in biomedical applications.[129]

Scientists have paid a lot of attention to nanomembranes due to their unique properties such as low weight, high flexibility, robustness, adhesion strength, and, in some cases, transparency.[130–132] Therefore, they are able to be utilized in diverse bioengineering fields[133–136] such as designing sensors,[137,138] antimicrobial surfaces,[139,140] nanobiological reactors,[141] biomotors,[142] biointerfaces for cellular matrices,[143] and specially drug release devices[144,145] and tissue engineering.[146,147]

They are sufficiently strong and can remain without extra backing structure. Membrane mechanical properties depend on porosity, manufacturing process and material. Permeability and bioactivity grow as porosity grow, while mechanical properties reduce exponentially.[148]

Generally, nanomembranes can be generated on solid support, fluid-fluid, or air-fluid interfaces. Also, there are different techniques to produce nanomembranes, like layer-by-layer (LbL) assembly,[149–151] langmuir–blodgett

(LB) transfer,[152] electrophoretic deposition[153] cross-linking of self-assembled monolayer (SAM) techniques, and spin-coating.[153–155]

Spin-coating was used in this Thesis to prepare PCL membranes. Spin-coating (**Figure 1.2.3**) is a valuable process that can be used to prepare single- or multi-layered uniform thin membranes with thicknesses below 10 nm. The steps needed to obtain these nanomembranes are: solution deposition, steady substrate rotation, and drying and detachment. Therefore, by an optimum spinning speed, time, and solution concentration customized ultra-thin films can be obtained.[156,157]

Removing the nanomembranes from the substrate is usually done by destroying the sacrificial layer, which is generated on the initial substrate. By destroying this layer, the produced membrane detaches from the surface.[157,158]
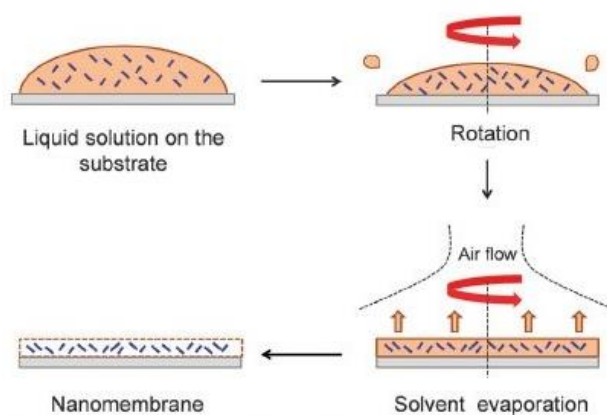
Figure 1.2.3. Schematic illustration of the spin-coating processes. Reproduced with permission from ref.[126] Copyright 2015 Royal Society of Chemistry.

1.2.3 Nanoparticles (NPs)

The current development in biomolecular therapeutics has elevated the demand to design new intelligent approaches for drug delivery, ensuring the optimum bioavailability of the encapsulated therapeutical substance, hence, the remedial potency.[159]

NPs, due to their nanometre size, can penetrate via cell membranes, extend circulation time and improve the stability and solubility of encapsulated cargos helping to increase safety and efficient delivery and overcome drug resistance.[160–166]

1.2.3.1 NPs types

a) Polymeric NPs

Either natural or synthetic materials, monomers or preformed polymers can be utilized to synthesize polymeric NPs, which lead to a broad diversity of probable configurations and properties (**Figure 1.2.4**). They can be designed to have accurate control of many NP characteristics and, due to their biocompatibility and straightforward formulation, they are reliable delivery carriers.[167]

They can transport the drug via different techniques such as encapsulation in the NP core, through entangling in the polymeric matrices, chemically connecting to the polymer, or by attachment to the NP surface. Therefore, NPs are able to deliver different cargos with different hydrophobicity or even molecular weights such as small molecules, vaccines and proteins, aimed at specific cells or tissues.

Nanocapsules (nanoscale shell made from polymer) and nanospheres (solid spherical polymeric matrices) are the most common forms of polymeric NPs. Besides, NPs are classified further into forms such as polymersomes, dendrimers, and micelles.[168]

b) Inorganic NPs

For different drug delivery systems and especially in the imaging industry, inorganic materials like iron, gold, and silica are utilized to synthesize

nanostructured materials. (**Figure 1.2.4**) These NPs can be designed accurately to have different sizes, structures, and geometries.[169]

c) Lipid-based NPs

Lipid-based NPs, as a delivery system, grants many benefits, such as biocompatibility, simple formulation, high bioavailability, self-assembly, oversized cargo-carrying capability, and a series of physicochemical properties that can control their biological characteristics (**Figure 1.2.4**). [170,171]
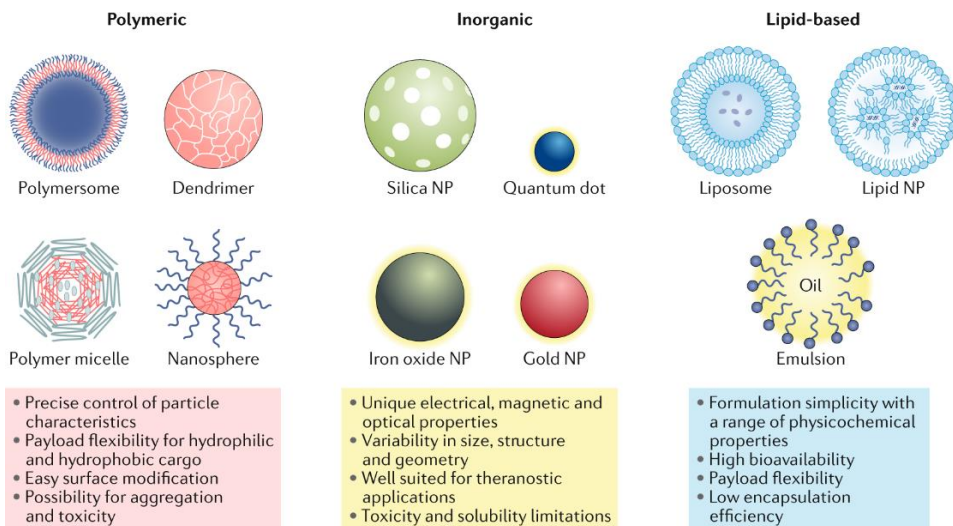
Figure 1.2.4. Classes of NPs and their advantages. Reprinted by permission from ref. [167] Copyright 2020 Springer Nature.

1.2.4 Hydrogels

Hydrogels are hydrophilic polymers with a three-dimensional network that can absorb and store water and aqueous solutions. These materials can initially be dry and dehydrated but absorb several times their weight in an aqueous solution.

These polymers absorb water without dissolving in it, swell, and then resist water flow. They are cross-linked polymers, with highly porous structure that causes them to absorb a large amount of water and aqueous solutions.[172] The ability of hydrogels to swell depends on the pH, temperature, ionic strength of the environment, the type of solvent, and the polymer structure. This property distinguishes hydrogels from other polymers. Physical cross-links can be formed by an entanglement of chains, crystal formation in the polymer structure, or weak interactions such as hydrogen bonding or van der Waals, which can absorb water and swell.[173]

Hydrogels can be classified from different points of view. They may be neutral or charged, depending on the polymer structure. Also, the structural morphology of the hydrogels may be amorphous or semicrystalline. In addition, their lattice structure may consist of non-covalent interactions (physical hydrogels), such as hydrogen bonds, electrostatics or π-π interactions, or in the form of supermolecules (chemical hydrogels) when polymer chains are covalently crosslinked. In terms of size, porosity with micrometre or nanometre dimensions can be created in the structure of hydrogels.

In a broad sense, hydrogels can be divided into two categories:

1) Traditional hydrogels obtained from hydrophilic polymers with relatively low cross-linking and considerable volume change when in the aqueous medium. These hydrogels are mainly non-electrically charged and do not show much swelling response to changes in the properties of the environment.

2) Stimulus-sensitive hydrogels, which can be even hydrophobic, show volume changes due to environmental changes, such as temperature, electric charge, etc., and are often charged.

During the last four decades, hydrogels have been extensively studied as controlled release carriers of drugs due to their excellent tissue compatibility, easy production, and solvent permeability.[174]

1.2.4.1 Smart hydrogels and their application

Today, intelligent polymer hydrogels have many applications in various fields. One of their most critical applications is in the development of intelligent drug delivery systems. Using the technology of intelligent polymer hydrogels in the preparation of drug release systems makes it possible to achieve the fundamental goals of drug release systems, which are the release of drugs at a specific rate and predetermined intervals. Based on the type of stimuli applied to smart polymer hydrogels, they are divided into different categories such as hydrogels that respond to temperature, pH, pressure, electric field, light, the presence of ions and unique molecules, etc. [175–177]

In this thesis, poly(γ-glutamic acid) (PGGA), in the presence of conducting PEDOT NPs, was used to obtain smart hydrogels (**Figure 1.2.5**). PGGA is a biocompatible, biodegradable, and anionic polypeptide and has an identical biomimetic secondary structure to natural proteins. Besides, it has been proved that PGGA can enhance cell adhesion and boost cell growth.[178–180]
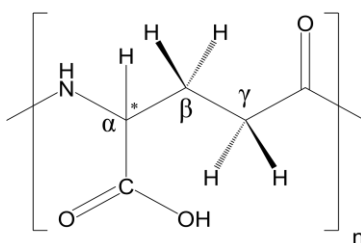
Figure 1.2.5. PGGA chemical structure.

1.3 References

1. Tathe, A., Ghodke, M. & Pratima Nikaje, A. A brief review: biomaterials and their application. *Int J Pharm Pharm Sci* **2**, 19–23 (2010).

2. Heness, G. & Ben-Nissan, B. Innovative bioceramics. *Materials Forum* **27**, 104–114 (2004).

3. Raghavendra, G. M., Varaprasad, K. & Jayaramudu, T. Biomaterials. in *Nanotechnology Applications for Tissue Engineering* 21–44 (Elsevier, 2015). doi:10.1016/B978-0-323-32889-0.00002-9.

4. Isa, Z. M. & Hobkirk., J. A. Dental Implants: Biomaterial, Biomechanical And Biological Considerations. *Annals of Dentistry* **7**, 27–35 (2000).

5. Anselme, K. Osteoblast adhesion on biomaterials. *Biomaterials* **21**, 667–681 (2000).

6. Mehdizadeh, M. & Yang, J. Design Strategies and Applications of Tissue Bioadhesives. *Macromolecular Bioscience* **13**, 271–288 (2013).

7. Ulery, B. D., Nair, L. S. & Laurencin, C. T. Biomedical applications of biodegradable polymers. *Journal of Polymer Science Part B: Polymer Physics* **49**, 832–864 (2011).

8. Johnson, R. M., Mwaikambo, L. Y. & Tucker, N. *Biopolymers*. (2003).

9. Varma, K. & Gopi, S. Biopolymers and their role in medicinal and pharmaceutical applications. in *Biopolymers and their Industrial Applications* 175–191 (Elsevier, 2021). doi:10.1016/B978-0-12-819240-5.00007-9.

10. Hernández, N., Williams, R. C. & Cochran, E. W. The battle for the "green" polymer. Different approaches for biopolymer synthesis: bioadvantaged vs. bioreplacement. *Org. Biomol. Chem.* **12**, 2834–2849 (2014).

11. Anderson, J. M. Biological responses to materials. *Annual Review of Materials Science* **31**, 81–110 (2001).

12. Lu, Y. & Chen, S. C. Micro and nano-fabrication of biodegradable polymers for drug delivery. *Advanced Drug Delivery Reviews* **56**, 1621–1633 (2004).

13. K, N. & Rout, C. S. Conducting polymers: a comprehensive review on recent advances in synthesis, properties and applications. *RSC Advances* **11**, 5659–5697 (2021).

14. Sharma, S., Sudhakara, P., Omran, A. A. B., Singh, J. & Ilyas, R. A. Recent Trends and Developments in Conducting Polymer Nanocomposites for Multifunctional Applications. *Polymers* **13**, 2898 (2021).

15. Hatchett, D. W. & Josowicz, M. Composites of Intrinsically Conducting Polymers as Sensing Nanomaterials. *Chemical Reviews* **108**, 746–769 (2008).

16. Liu, Z., Zhang, L., Poyraz, S. & Zhang, X. Conducting Polymer - Metal Nanocomposites Synthesis and Their Sensory Applications. *Current Organic Chemistry* **17**, 2256–2267 (2013).

17. Naseri, M., Fotouhi, L. & Ehsani, A. Recent Progress in the Development of Conducting Polymer-Based Nanocomposites for Electrochemical Biosensors Applications: A Mini-Review. *The Chemical Record* **18**, 599–618 (2018).

18. Elbasri, M., Majid, S., Lafdi, K. & el Rhazi, M. Highly improved electrocatalytic oxidation of methanol on poly (1, 5-diaminonaphthalene)/nickel nanoparticles film modified carbon nanofiber. *J. Mater. Environ. Sci,* **8**, 2860–2869 (2017).

19. Wallace, G. G., Teasdale, P. R., Spinks, G. M. & Kane-Maguire, L. A. P. *Conductive Electroactive Polymers. Conductive Electroactive Polymers* (CRC Press, 2002). doi:10.1201/9781420031898.

20. Boni, R., Ali, A., Shavandi, A. & Clarkson, A. N. Current and novel polymeric biomaterials for neural tissue engineering. *Journal of Biomedical Science 2018 25:1* **25**, 1–21 (2018).

21. Guimard, N. K., Gomez, N. & Schmidt, C. E. Conducting polymers in biomedical engineering. *Progress in Polymer Science* **32**, 876–921 (2007).

22. Stenger-Smith, J. D. Intrinsically electrically conducting polymers. Synthesis, characterization, and their applications. *Progress in Polymer Science* **23**, 57–79 (1998).

23. Wong, J. Y., Langer, R. & Ingber, D. E. Electrically conducting polymers can noninvasively control the shape and growth of mammalian cells. *Proceedings of the National Academy of Sciences* **91**, 3201–3204 (1994).

24. Alegret, N., Dominguez-Alfaro, A. & Mecerreyes, D. 3D Scaffolds Based on Conductive Polymers for Biomedical Applications. *Biomacromolecules* **20**, 73–89 (2019).

25. Ferrigno, B. *et al.* Bioactive polymeric materials and electrical stimulation strategies for musculoskeletal tissue repair and regeneration. *Bioactive Materials* **5**, 468–485 (2020).

26. Petty, A. J., Keate, R. L., Jiang, B., Ameer, G. A. & Rivnay, J. Conducting Polymers for Tissue Regeneration in Vivo †. *Chemistry of Materials* **32**, 4095–4115 (2020).

27. Tomczykowa, M. & Plonska-Brzezinska, M. Conducting Polymers, Hydrogels and Their Composites: Preparation, Properties and Bioapplications. *Polymers* **11**, 350 (2019).

28. Huo, J., Wang, L. & Yu, H. Polymeric nanocomposites for electromagnetic wave absorption. *Journal of Materials Science* **44**, 3917–3927 (2009).

41

29. Shankar, K., Mor, G. K., Paulose, M., Varghese, O. K. & Grimes, C. A. Effect of device geometry on the performance of TiO2 nanotube array-organic semiconductor double heterojunction solar cells. *Journal of Non-Crystalline Solids* **354**, 2767–2771 (2008).

30. Abidian, M. R. & Martin, D. C. Experimental and theoretical characterization of implantable neural microelectrodes modified with conducting polymer nanotubes. *Biomaterials* **29**, 1273–1283 (2008).

31. Zeng, T.-W. *et al.* Hybrid poly (3-hexylthiophene)/titanium dioxide nanorods material for solar cell applications. *Solar Energy Materials and Solar Cells* **93**, 952–957 (2009).

32. Bansal, V., Sharma, P., Sharma, N. & Pal, O. Applications of chitosan and chitosan derivatives in drug delivery. *Advances in Biological Research* **5**, 28–37 (2011).

33. Shen, Z. Exploitation of rare earth catalysts in polymer syntheses. *Frontiers of Chemistry in China* **1**, 247–259 (2006).

34. Qiu, Y., Duan, L. & Wang, L. Z. PEDOT anode of flexible organic light emitting devices. *Sci China Ser E-Tech Sci* **47**, 1152–1155 (2002).

35. Almouemen, N., Kelly, H. M. & O'Leary, C. Tissue Engineering: Understanding the Role of Biomaterials and Biophysical Forces on Cell Functionality Through Computational and Structural Biotechnology Analytical Methods. *Computational and Structural Biotechnology Journal* **17**, 591–598 (2019).

36. Broda, C. R., Lee, J. Y., Sirivisoot, S., Schmidt, C. E. & Harrison, B. S. A chemically polymerized electrically conducting composite of polypyrrole nanoparticles and polyurethane for tissue engineering. *Journal of Biomedical Materials Research - Part A* **98 A**, 509–516 (2011).

37. Mostafavi, E. *et al.* Electroconductive nanobiomaterials for tissue engineering and regenerative medicine. *liebertpub.com* **2**, 120–149 (2020).

38. Ning, C., Zhou, Z., Tan, G., Zhu, Y. & Mao, C. Electroactive polymers for tissue regeneration: Developments and perspectives. *Progress in Polymer Science* **81**, 144–162 (2018).

39. Chen, X. & Ahn, J.-H. Biodegradable and bioabsorbable sensors based on two-dimensional materials. *Journal of Materials Chemistry B* **8**, 1082–1092 (2020).

40. Hwang, S.-W. *et al.* Biodegradable elastomers and silicon nanomembranes/nanoribbons for stretchable, transient electronics, and biosensors. *ACS Publications* **15**, 2801–2808 (2015).

41. Rodrigues, D. *et al.* Skin-Integrated Wearable Systems and Implantable Biosensors: A Comprehensive Review. *Biosensors* **10**, 79 (2020).

42. Panda, S. & Acharya, B. Electronic Applications of Conducting Polymer Nanocomposites. in 211–220 (2019). doi:10.1007/978-981-13-7091-5_20.

42

43. Takashima, W., Pandey, S. S. & Kaneto, K. Cyclic voltammetric and electrochemomechanical characteristics of freestanding polypyrrole films in diluted media. *Thin Solid Films* **438–439**, 339–345 (2003).

44. Madden, J. D. W. *et al.* Artificial Muscle Technology: Physical Principles and Naval Prospects. *IEEE Journal of Oceanic Engineering* **29**, 706–728 (2004).

45. Kim, S., Kim, J.-H., Jeon, O., Kwon, I. C. & Park, K. Engineered polymers for advanced drug delivery. *European Journal of Pharmaceutics and Biopharmaceutics* **71**, 420–430 (2009).

46. Oh, J. K., Drumright, R., Siegwart, D. J. & Matyjaszewski, K. The development of microgels/nanogels for drug delivery applications. *Progress in Polymer Science* **33**, 448–477 (2008).

47. Qu, J. *et al.* Biocompatible conductive hydrogels based on dextran and aniline trimer as electro-responsive drug delivery system for localized drug release. *International Journal of Biological Macromolecules* **140**, 255–264 (2019).

48. Zhu, Y., Li, J., Wan, M. & Jiang, L. Superhydrophobic 3D microstructures assembled from 1D nanofibers of polyaniline. *Macromolecular Rapid Communications* **29**, 239–243 (2008).

49. Kewal K., J. *Drug Delivery Systems*. vol. 2059 (Springer New York, 2020).

50. Verma, R. Formulation aspects in the development of osmotically controlled oral drug delivery systems. *Journal of Controlled Release* **79**, 7–27 (2002).

51. Aulton, M. *Pharmaceutics : the science of dosage form design*. vol. 2001 (Churchill Livingstone, 2002).

52. Brahmankar DM & Jaiswal SB. *Biopharmaceutics and Pharmacokinetics: Pharmacokinetics.* (Vallabh Prakashan, 2009).

53. Lee, V. *Controlled drug delivery: fundamentals and applications*. (1987).

54. Kakar, S., Singh, R. & Semwal, A. Drug release characteristics of dosage forms: a review. *Journal of Coastal Life Medicine* **2**, 332–336 (2014).

55. Brannon-Peppas, L., Birnbaum, D. T. & Kosmala, J. D. Simultaneous Analysis of Particle Size Distribution, Particle Shape, and Drug Delivery from Biodegradable Microparticles. *Polymer preprints-america* **38**, 600–601 (1997).

56. Kamaly, N., Yameen, B., Wu, J. & Farokhzad, O. C. Degradable Controlled-Release Polymers and Polymeric Nanoparticles: Mechanisms of Controlling Drug Release. *Chemical Reviews* **116**, 2602–2663 (2016).

43

57. Das, D. & Pal, S. Modified biopolymer-dextrin based crosslinked hydrogels: application in controlled drug delivery. *RSC Advances* **5**, 25014–25050 (2015).

58. Said, S. S., Campbell, S. & Hoare, T. Externally Addressable Smart Drug Delivery Vehicles: Current Technologies and Future Directions. *Chemistry of Materials* **31**, 4971–4989 (2019).

59. Weaver, C. L., LaRosa, J. M., Luo, X. & Cui, X. T. Electrically Controlled Drug Delivery from Graphene Oxide Nanocomposite Films. *ACS Nano* **8**, 1834–1843 (2014).

60. Wang, Y. C. & Foster, A. Experimental and numerical study of temperature developments in PIR core sandwich panels with joint. *Fire Safety Journal* **90**, 1–14 (2017).

61. Brotchie, A. Drug delivery: Ultrasound soothes the pain. *Nature Reviews Materials* **2**, 17058 (2017).

62. Paris, J. L., Cabañas, M. V., Manzano, M. & Vallet-Regí, M. Polymer-Grafted Mesoporous Silica Nanoparticles as Ultrasound-Responsive Drug Carriers. *ACS Nano* **9**, 11023–11033 (2015).

63. Fuller, E. G. *et al.* Externally Triggered Heat and Drug Release from Magnetically Controlled Nanocarriers. *ACS Applied Polymer Materials* **1**, 211–220 (2019).

64. Tietze, R. *et al.* Magnetic nanoparticle-based drug delivery for cancer therapy. *Biochemical and Biophysical Research Communications* **468**, 463–470 (2015).

65. Hrubý, M., Koňák, Č. & Ulbrich, K. Polymeric micellar pH-sensitive drug delivery system for doxorubicin. *Journal of Controlled Release* **103**, 137–148 (2005).

66. Balamurali, V. *et al.* pH Sensitive Drug Delivery Systems: A Review. *American Journal of Drug Discovery and Development* **1**, 24–48 (2010).

67. Alvarez-Lorenzo, C., Bromberg, L. & Concheiro, A. Light-sensitive Intelligent Drug Delivery Systems. *Photochemistry and Photobiology* **85**, 848–860 (2009).

68. Lajunen, T. *et al.* Light induced cytosolic drug delivery from liposomes with gold nanoparticles. *Journal of Controlled Release* **203**, 85–98 (2015).

69. Sershen, S. R., Westcott, S. L., Halas, N. J. & West, J. L. Temperature-sensitive polymer-nanoshell composites for photothermally modulated drug delivery. *Journal of Biomedical Materials Research* **51**, 293–298 (2000).

70. Needham, D. & Dewhirst, M. W. The development and testing of a new temperature-sensitive drug delivery system for the treatment of solid tumors. *Advanced Drug Delivery Reviews* **53**, 285–305 (2001).

71. Neumann, S. E., Chamberlayne, C. F. & Zare, R. N. Electrically controlled drug release using pH-sensitive polymer films. *Nanoscale* **10**, 10087–10093 (2018).

72. Schmidt, D. J., Moskowitz, J. S. & Hammond, P. T. Electrically Triggered Release of a Small Molecule Drug from a Polyelectrolyte Multilayer Coating. *Chemistry of Materials* **22**, 6416–6425 (2010).

73. Jeon, G., Yang, S. Y., Byun, J. & Kim, J. K. Electrically Actuatable Smart Nanoporous Membrane for Pulsatile Drug Release. *Nano Letters* **11**, 1284–1288 (2011).

74. Guduru, R. *et al.* Magneto-electric Nanoparticles to Enable Field-controlled High-Specificity Drug Delivery to Eradicate Ovarian Cancer Cells. *Scientific Reports* **3**, 2953 (2013).

75. Green, R. & Abidian, M. R. Conducting Polymers for Neural Prosthetic and Neural Interface Applications. *Advanced Materials* **27**, 7620–7637 (2015).

76. Samanta, D., Hosseini-Nassab, N. & Zare, R. N. Electroresponsive nanoparticles for drug delivery on demand. *Nanoscale* **8**, 9310–9317 (2016).

77. Zhao, Y., Tavares, A. C. & Gauthier, M. A. Nano-engineered electro-responsive drug delivery systems. *Journal of Materials Chemistry B* **4**, 3019–3030 (2016).

78. Servant, A., Methven, L., Williams, R. P. & Kostarelos, K. Electroresponsive Polymer-Carbon Nanotube Hydrogel Hybrids for Pulsatile Drug Delivery In Vivo. *Advanced Healthcare Materials* **2**, 806–811 (2013).

79. Langer, R. New Methods of Drug Delivery. *Science* **249**, 1527–1533 (1990).

80. Jain, K. K. *Applications of Biotechnology in Neurology*. (Humana Press, 2013). doi:10.1007/978-1-62703-272-8.

81. Webber, W. L., Lago, F., Thanos, C. & Mathiowitz, E. Characterization of soluble, salt-loaded, degradable PLGA films and their release of tetracycline. *Journal of Biomedical Materials Research* **41**, 18–29 (1998).

82. Fu, Y. & Kao, W. J. Drug release kinetics and transport mechanisms of non-degradable and degradable polymeric delivery systems. *Expert Opinion on Drug Delivery* **7**, 429–444 (2010).

83. Keraliya, R. A. *et al.* Osmotic Drug Delivery System as a Part of Modified Release Dosage Form. *ISRN Pharmaceutics* **2012**, 1–9 (2012).

84. Uhrich, K. E., Cannizzaro, S. M., Langer, R. S. & Shakesheff, K. M. Polymeric Systems for Controlled Drug Release. *Chemical Reviews* **99**, 3181–3198 (1999).

85. Caballero-George, C., Marin, E. & Briceño, M. Critical evaluation of biodegradable polymers used in nanodrugs. *International Journal of Nanomedicine* 3071 (2013) doi:10.2147/IJN.S47186.

86. Park, H., Park, K. & Shalaby, W. *Biodegradable hydrogels for drug delivery*. (CRC Press, 1993).

45

87.   Lalatsa, A., Schätzlein, A. G., Mazza, M., Le, T. B. H. & Uchegbu, I. F. Amphiphilic poly(l-amino acids) — New materials for drug delivery. *Journal of Controlled Release* **161**, 523–536 (2012).

88.   Donnelly, R. F., Garland, M. J. & Alkilani, A. Z. Microneedle-Iontophoresis Combinations for Enhanced Transdermal Drug Delivery. in *Springer* 121–132 (2014). doi:10.1007/978-1-4939-0363-4_7.

89.   Jain, K. K. Role of Nanobiotechnology in Drug Delivery. in *Methods in Molecular Biology* vol. 2059 55–73 (Humana Press Inc., 2020).

90.   Singh, R. M., Kumar, A. & Pathak, K. Mucoadhesive in situ nasal gelling drug delivery systems for modulated drug delivery. *Expert Opinion on Drug Delivery* **10**, 115–130 (2013).

91.   Abramson, A. *et al.* An ingestible self-orienting system for oral delivery of macromolecules. *Science* **363**, 611–615 (2019).

92.   Brayden, D. J. & Baird, A. W. Stomaching Drug Delivery. *New England Journal of Medicine* **380**, 1671–1673 (2019).

93.   Jain, K. K. *Applications of Biotechnology in Cardiovascular Therapeutics*. (Humana Press, 2011). doi:10.1007/978-1-61779-240-3.

94.   Velema, J. & Kaplan, D. Biopolymer-based biomaterials as scaffolds for tissue engineering. *Advances in Biochemical Engineering/Biotechnology* **102**, 187–238 (2006).

95.   Rhim, J. W. & Ng, P. K. W. Natural biopolymer-based nanocomposite films for packaging applications. *Critical Reviews in Food Science and Nutrition* **47**, 411–433 (2007).

96.   Liu, L. S., Kost, J., Yan, F. & Spiro, R. C. Hydrogels from Biopolymer Hybrid for Biomedical, Food, and Functional Food Applications. *Polymers* **4**, 997–1011 (2012).

97.   Gray, S. II. A letter concerning the electricity of water, from Mr. Stephen Gray to Cromwell Mortimer, M. D. Secr. R. S. *Philosophical Transactions of the Royal Society of London* **37**, 227–260 (1731).

98.   Afshari, M. Introduction. in *Electrospun Nanofibers* vol. 186 1–8 (Elsevier, 2017).

99.   Yao, T. *et al.* Self-assembly of electrospun nanofibers into gradient honeycomb structures. *Materials & Design* **168**, 107614 (2019).

100.   Rasouli, R., Barhoum, A., Bechelany, M. & Dufresne, A. Nanofibers for Biomedical and Healthcare Applications. *Macromolecular Bioscience* **19**, 1800256 (2019).

101.   Kang, J., Hwang, J.-Y., Huh, M. & Yun, S. il. Porous Poly(3-hydroxybutyrate) Scaffolds Prepared by Non-Solvent-Induced Phase Separation for Tissue Engineering. *Macromolecular Research* **28**, 835–843 (2020).

46

102. Jin, K. *et al.* Bimodal Nanofiber and Microfiber Nonwovens by Melt-Blowing Immiscible Ternary Polymer Blends. *Industrial & Engineering Chemistry Research* **59**, 5238–5246 (2020).

103. Heidari, M., Bahrami, S. H., Ranjbar-Mohammadi, M. & Milan, P. B. Smart electrospun nanofibers containing PCL/gelatin/graphene oxide for application in nerve tissue engineering. *Materials Science and Engineering: C* **103**, 109768 (2019).

104. Dhandayuthapani, B., Yoshida, Y., Maekawa, T. & Kumar, D. S. Polymeric Scaffolds in Tissue Engineering Application: A Review. *International Journal of Polymer Science* **2011**, 1–19 (2011).

105. JOSE, M., THOMAS, V., JOHNSON, K., DEAN, D. & NYAIRO, E. Aligned PLGA/HA nanofibrous nanocomposite scaffolds for bone tissue engineering. *Acta Biomaterialia* **5**, 305–315 (2009).

106. Cooper, J. A., Lu, H. H., Ko, F. K., Freeman, J. W. & Laurencin, C. T. Fiber-based tissue-engineered scaffold for ligament replacement: design considerations and in vitro evaluation. *Biomaterials* **26**, 1523–1532 (2005).

107. Chou, S.-F., Carson, D. & Woodrow, K. A. Current strategies for sustaining drug release from electrospun nanofibers. *Journal of Controlled Release* **220**, 584–591 (2015).

108. Goonoo, N., Bhaw-Luximon, A. & Jhurry, D. Drug Loading and Release from Electrospun Biodegradable Nanofibers. *Journal of Biomedical Nanotechnology* **10**, 2173–2199 (2014).

109. Boateng, J. & Catanzano, O. Advanced Therapeutic Dressings for Effective Wound Healing—A Review. *Journal of Pharmaceutical Sciences* **104**, 3653–3680 (2015).

110. Rieger, K. A., Birch, N. P. & Schiffman, J. D. Designing electrospun nanofiber mats to promote wound healing – a review. *Journal of Materials Chemistry B* **1**, 4531 (2013).

111. Szentivanyi, A. L., Zernetsch, H., Menzel, H. & Glasmacher, B. A review of developments in electrospinning technology: New opportunities for the design of artificial tissue structures. *International Journal of Artificial Organs* **34**, 986–997 (2011).

112. Theron, J. P. *et al.* Modification, crosslinking and reactive electrospinning of a thermoplastic medical polyurethane for vascular graft applications. *Acta Biomaterialia* **6**, 2434–2447 (2010).

113. Bhardwaj, N. & Kundu, S. C. Electrospinning: A fascinating fiber fabrication technique. *Biotechnology Advances* **28**, 325–347 (2010).

114. Ramakrishna, S., Fujihara, K., Teo, W.-E., Lim, T.-C. & Ma, Z. *An Introduction to Electrospinning and Nanofibers*. (WORLD SCIENTIFIC, 2005). doi:10.1142/5894.

115. Lu, T., Li, Y. & Chen, T. Techniques for fabrication and construction of three-dimensional scaffolds for tissue engineering. *International Journal of Nanomedicine* 337 (2013) doi:10.2147/IJN.S38635.

48

116. Gervaso, F., Sannino, A. & Peretti, G. M. The biomaterialist's task: Scaffold biomaterials and fabrication technologies. *Joints* **1**, 130–137 (2013).

117. Garg, T., Singh, O., Arora, S. & Murthy, R. S. R. Scaffold: A Novel Carrier for Cell and Drug Delivery. *Critical Reviews in Therapeutic Drug Carrier Systems* **29**, 1–63 (2012).

118. Rahmati, M. *et al.* Electrospinning for tissue engineering applications. *Progress in Materials Science* **117**, 100721 (2021).

119. Sun, B. *et al.* Advances in three-dimensional nanofibrous macrostructures via electrospinning. *Progress in Polymer Science* **39**, 862–890 (2014).

120. Reneker, D. H. & Chun, I. Nanometre diameter fibres of polymer, produced by electrospinning. *Nanotechnology* **7**, 216 (1996).

121. Casper, C. L., Stephens, J. S., Tassi, N. G., Chase, D. B. & Rabolt, J. F. Controlling surface morphology of electrospun polystyrene fibers: effect of humidity and molecular weight in the electrospinning process. *ACS Publications* **37**, 573–578 (2004).

122. Balusamy, B., Celebioglu, A., Senthamizhan, A. & Uyar, T. Progress in the design and development of "fast-dissolving" electrospun nanofibers based drug delivery systems - A systematic review. *Journal of Controlled Release* **326**, 482–509 (2020).

123. Aghdam, R. M. *et al.* Investigating the effect of PGA on physical and mechanical properties of electrospun PCL/PGA blend nanofibers. *Journal of Applied Polymer Science* **124**, 123–131 (2012).

124. Nair, L. S. & Laurencin, C. T. Biodegradable polymers as biomaterials. *Progress in Polymer Science* **32**, 762–798 (2007).

125. Ciganė, U., Palevičius, A. & Janušas, G. Review of nanomembranes: materials, fabrications and applications in tissue engineering (bone and skin) and drug delivery systems. *Journal of Materials Science* **56**, 13479–13498 (2021).

126. Pérez-Madrigal, M. M., Armelin, E., Puiggalí, J. & Alemán, C. Insulating and semiconducting polymeric free-standing nanomembranes with biomedical applications. *Journal of Materials Chemistry B* **3**, 5904–5932 (2015).

127. Kamoun, E. A., Kenawy, E.-R. S., Tamer, T. M., El-Meligy, M. A. & Mohy Eldin, M. S. Poly (vinyl alcohol)-alginate physically crosslinked hydrogel membranes for wound dressing applications: Characterization and bio-evaluation. *Arabian Journal of Chemistry* **8**, 38–47 (2015).

128. Kim, J. O. *et al.* Development of polyvinyl alcohol–sodium alginate gel-matrix-based wound dressing system containing nitrofurazone. *International Journal of Pharmaceutics* **359**, 79–86 (2008).

129. P. M., Visakh., Yu, Long. & Nazarenko, Olga. *Nanostructured Polymer Membranes, Processing and Characterization.* vol. 1 (John Wiley & Sons, Incorporated, 2016).

130. D. Sattler, K. *Handbook of Nanophysics*. (CRC Press, 2010). doi:10.1201/9781420075533.

131. Jiang, C., Rybak, B. M., Markutsya, S., Kladitis, P. E. & Tsukruk, V. v. Self-recovery of stressed nanomembranes. *Applied Physics Letters* **86**, 121912 (2005).

132. Markutsya, S., Jiang, C., Pikus, Y. & Tsukruk, V. v. Freely Suspended Layer-by-Layer Nanomembranes: Testing Micromechanical Properties. *Advanced Functional Materials* **15**, 771–780 (2005).

133. Jakšić, Z. & Jakšić, O. Biomimetic Nanomembranes: An Overview. *Biomimetics* **5**, 24 (2020).

134. Jia, P. *et al.* Large-area freestanding gold nanomembranes with nanoholes. *Materials Horizons* **6**, 1005–1012 (2019).

135. Wang, X., Chen, Y., Schmidt, O. G. & Yan, C. Engineered nanomembranes for smart energy storage devices. *Chemical Society Reviews* **45**, 1308–1330 (2016).

136. Zanghelini, F. *et al.* Biosensing breast cancer cells based on a three-dimensional TIO 2 nanomembrane transducer. *Biosensors and Bioelectronics* **92**, 313–320 (2017).

137. Jiang, C., Markutsya, S., Pikus, Y. & Tsukruk, V. v. Freely suspended nanocomposite membranes as highly sensitive sensors. *Nature Materials* **3**, 721–728 (2004).

138. Kittle, J. D. *et al.* Ultrathin Chitin Films for Nanocomposites and Biosensors. *Biomacromolecules* **13**, 714–718 (2012).

139. Tai, Z., Ma, H., Liu, B., Yan, X. & Xue, Q. Facile synthesis of Ag/GNS-g-PAA nanohybrids for antimicrobial applications. *Colloids and Surfaces B: Biointerfaces* **89**, 147–151 (2012).

140. Wong, S. Y. *et al.* Bactericidal and virucidal ultrathin films assembled layer by layer from polycationic N-alkylated polyethylenimines and polyanions. *Biomaterials* **31**, 4079–4087 (2010).

141. Bellino, M. G., Tropper, I., Duran, H., Regazzoni, A. E. & Soler-Illia, G. J. A. A. Polymerase-Functionalized Hierarchical Mesoporous Titania Thin Films: Towards a Nanoreactor Platform for DNA Amplification. *Small* **6**, 1221–1225 (2010).

142. Jaber, J. A., Chase, P. B. & Schlenoff, J. B. Actomyosin-Driven Motility on Patterned Polyelectrolyte Mono- and Multilayers. *Nano Letters* **3**, 1505–1509 (2003).

143. Hajicharalambous, C. S. *et al.* Nano- and sub-micron porous polyelectrolyte multilayer assemblies: Biomimetic surfaces for human corneal epithelial cells. *Biomaterials* **30**, 4029–4036 (2009).

144. Berg, M. C., Zhai, L., Cohen, R. E. & Rubner, M. F. Controlled Drug Release from Porous Polyelectrolyte Multilayers. *Biomacromolecules* **7**, 357–364 (2006).

49

145. Wood, K. C., Boedicker, J. Q., Lynn, D. M. & Hammond, P. T. Tunable Drug Release from Hydrolytically Degradable Layer-by-Layer Thin Films. *Langmuir* **21**, 1603–1609 (2005).

146. Pérez-Madrigal, M. M., Armelin, E., del Valle, L. J., Estrany, F. & Alemán, C. Bioactive and electroactive response of flexible polythiophene:polyester nanomembranes for tissue engineering. *Polymer Chemistry* **3**, 979 (2012).

147. Armelin, E. *et al.* Biodegradable free-standing nanomembranes of conducting polymer:polyester blends as bioactive platforms for tissue engineering. *J. Mater. Chem.* **22**, 585–594 (2012).

148. Christy, P. N. *et al.* Biopolymeric nanocomposite scaffolds for bone tissue engineering applications – A review. *Journal of Drug Delivery Science and Technology* **55**, 101452 (2020).

149. Decher, G., Hong, J. D. & Schmitt, J. Buildup of ultrathin multilayer films by a self-assembly process: III. Consecutively alternating adsorption of anionic and cationic polyelectrolytes on charged surfaces. *Thin Solid Films* **210–211**, 831–835 (1992).

150. Decher, G. Fuzzy Nanoassemblies: Toward Layered Polymeric Multicomposites. *Science* **277**, 1232–1237 (1997).

151. Decher, G., Lvov, Y. & Schmitt, J. Proof of multilayer structural organization in self-assembled polycation-polyanion molecular films. *Thin Solid Films* **244**, 772–777 (1994).

152. Corkery, R. W. Langmuir−Blodgett (L−B) Multilayer Films. *Langmuir* **13**, 3591–3594 (1997).

153. Gurrappa, I. & Binder, L. Electrodeposition of nanostructured coatings and their characterization—A review. *Science and Technology of Advanced Materials* **9**, 043001 (2008).

154. Hall, D. B., Underhill, P. & Torkelson, J. M. Spin coating of thin and ultrathin polymer films. *Polymer Engineering & Science* **38**, 2039–2045 (1998).

155. Stroock, A. D., Kane, R. S., Weck, M., Metallo, S. J. & Whitesides, G. M. Synthesis of Free-Standing Quasi-Two-Dimensional Polymers. *Langmuir* **19**, 2466–2472 (2003).

156. Martino, S., D'Angelo, F., Armentano, I., Kenny, J. M. & Orlacchio, A. Stem cell-biomaterial interactions for regenerative medicine. *Biotechnology Advances* **30**, 338–351 (2012).

157. Llorens, E. *et al.* Nanomembranes and Nanofibers from Biodegradable Conducting Polymers. *Polymers* **5**, 1115–1157 (2013).

158. Cheng, W., Campolongo, M. J., Tan, S. J. & Luo, D. Freestanding ultrathin nano-membranes via self-assembly. *Nano Today* **4**, 482–493 (2009).

159. Ghitman, J., Biru, E. I., Stan, R. & Iovu, H. Review of hybrid PLGA nanoparticles: Future of smart drug delivery and theranostics medicine. *Materials & Design* **193**, 108805 (2020).

160.   Liu, X. *et al.* Glucose and H $_2$ O $_2$ Dual-Responsive Polymeric Micelles for the Self-Regulated Release of Insulin. *ACS Applied Bio Materials* **3**, 1598–1606 (2020).

161.   Jose *et al.* Transferrin-Conjugated Docetaxel–PLGA Nanoparticles for Tumor Targeting: Influence on MCF-7 Cell Cycle. *Polymers* **11**, 1905 (2019).

162.   Strand, M. S. *et al.* Precision delivery of RAS-inhibiting siRNA to KRAS driven cancer via peptide-based nanoparticles. *Oncotarget* **10**, 4761–4775 (2019).

163.   Knight, F. C. *et al.* Mucosal Immunization with a pH-Responsive Nanoparticle Vaccine Induces Protective CD8 [+] Lung-Resident Memory T Cells. *ACS Nano* **13**, 10939–10960 (2019).

164.   Caldorera-Moore, M., Vela Ramirez, J. E. & Peppas, N. A. Transport and delivery of interferon-α through epithelial tight junctions via pH-responsive poly(methacrylic acid-grafted-ethylene glycol) nanoparticles. *Journal of Drug Targeting* **27**, 582–589 (2019).

165.   Zhang, L. *et al.* Microfluidic-assisted polymer-protein assembly to fabricate homogeneous functionalnanoparticles. *Materials Science and Engineering: C* **111**, 110768 (2020).

166.   Peer, D. *et al.* Nanocarriers as an Emerging Platform for Cancer Therapy. in *Nano-Enabled Medical Applications* 61–91 (Jenny Stanford Publishing, 2020). doi:10.1201/9780429399039-2.

167.   Mitchell, M. J. *et al.* Engineering precision nanoparticles for drug delivery. *Nature Reviews Drug Discovery* **20**, 101–124 (2021).

168.   Rideau, E., Dimova, R., Schwille, P., Wurm, F. R. & Landfester, K. Liposomes and polymersomes: a comparative review towards cell mimicking. *Chemical Society Reviews* **47**, 8572–8610 (2018).

169.   Yang, W., Liang, H., Ma, S., Wang, D. & Huang, J. Gold nanoparticle based photothermal therapy: Development and application for effective cancer treatment. *Sustainable Materials and Technologies* **22**, e00109 (2019).

170.   Fonseca-Santos, B., Gremião, M. P. D. & Chorilli, M. Nanotechnology-based drug delivery systems for the treatment of Alzheimer's disease. *International Journal of Nanomedicine* **10**, 4981 (2015).

171.   Sercombe, L. *et al.* Advances and challenges of liposome assisted drug delivery. *Frontiers in Pharmacology* **6**, 286 (2015).

172.   F. L. BUCHHOLZ & A. T. GRAHAM. *Modern Superabsorbent Polymer Technology*. *Chemie Ingenieur Technik* vol. 70 (Wiley, 1998).

173.   Kabiri, K. & Zohuriaan-Mehr, M. J. Superabsorbent hydrogel composites. *Polymers for Advanced Technologies* **14**, 438–444 (2003).

174. Serra, L., Doménech, J. & Peppas, N. A. Drug transport mechanisms and release kinetics from molecularly designed poly(acrylic acid-g-ethylene glycol) hydrogels. *Biomaterials* **27**, 5440–5451 (2006).

175. Eeckman, F., Moës, A. J. & Amighi, K. Surfactant induced drug delivery based on the use of thermosensitive polymers. *Journal of Controlled Release* **88**, 105–116 (2003).

176. Eeckman, F., Moës, A. J. & Amighi, K. Synthesis and characterization of thermosensitive copolymers for oral controlled drug delivery. *European Polymer Journal* **40**, 873–881 (2004).

177. Geever, L. M. *et al.* The synthesis, characterisation, phase behaviour and swelling of temperature sensitive physically crosslinked poly(1-vinyl-2-pyrrolidinone)/poly(N-isopropylacrylamide) hydrogels. *European Polymer Journal* **42**, 69–80 (2006).

178. Gentilini, C. *et al.* Functionalized Poly(γ-Glutamic Acid) Fibrous Scaffolds for Tissue Engineering. *Advanced Healthcare Materials* **1**, 308–315 (2012).

179. Zhang, D., Feng, X., Zhou, Z., Zhang, Y. & Xu, H. Economical production of poly(γ-glutamic acid) using untreated cane molasses and monosodium glutamate waste liquor by Bacillus subtilis NX-2. *Bioresource Technology* **114**, 583–588 (2012).

180. Clarke, D. E., Pashuck, E. T., Bertazzo, S., Weaver, J. V. M. & Stevens, M. M. Self-Healing, Self-Assembled β-Sheet Peptide–Poly(γ-glutamic acid) Hybrid Hydrogels. *Journal of the American Chemical Society* **139**, 7250–7255 (2017).

Chapter 2

Objectives

Objectives

The objectives of this thesis have been raised in the form of five projects related to the development of biomedical platforms for the release of drugs using polymeric materials. These projects reflect an evolution in complexity at the level of the materials employed, going from individual materials with a unique format to the assembly of various materials and formats. In addition, different degrees of complexity at the level of functionality have been attained. Thus, some of the platforms incorporate new functions (apart from the release of drugs) to obtain multifunctional biomedical platforms. More specifically, the five objectives of this Thesis are:

1. Develop, characterize and evaluate a nanotheranostic platform based on conductive polymer nanoparticles (CP NPs) to load and slowly release chloramphenicol (CAM) antibiotic, while simultaneously detecting the bacterial growth and inhibition in real time.

2. Evaluate the encapsulation of pyrimethamine (PYR), a representative pharmacological chaperone (PC), in electro-responsive CP NPs for its controlled release by applying electrical stimuli.

3. Prepare a polymeric platform for the on-demand electrostimulated release of curcumin (CUR) using a polypeptide-based hydrogel containing CUR-loaded CP NPs, showing the advantages of such system in terms of voltage-induced release with respect to CUR-loaded polypeptide hydrogel and CUR-loaded CP NPs.

4. Design thermoplastic-based layered systems for sustained release of small drugs. Specifically, design sandwiched systems consisting of electrospun microfibers (MFs) coated with films to encapsulate and release another

PC: ambroxol. MFs will be used toencapsulate the drug, whereas films will act as protectors, regulating the drug release.

5. Engineer, prepare, characterize and prove a dual functional polymeric platform for levofloxacin (LVX)-release under simultaneous real time monitoring by electrochemical detection. LVX is one of the outstanding representatives of the third generation of quinolone antibiotics.

Chapter 3

Results and Discussion

Results and Discussion

3.1 Nanotheranostic Interface Based on Antibiotic-Loaded Conducting Polymer Nanoparticles for Real Time Monitoring of Bacterial Growth Inhibition

Conducting polymers have been increasingly used as biologically interfacing electrodes for biomedical applications due to their excellent and fast electrochemical response, reversible doping-dedoping characteristics, high stability, easy process ability and biocompatibility. These advantageous properties can be used for the rapid detection and eradication of infections associated to bacterial growth since these are a tremendous burden for individual patients as well as the global healthcare system. Herein, we present a smart nanotheranostic electroresponsive platform, which consists of chloramphenicol (CAM)-loaded in poly(3,4-ethylendioxythiophene) nanoparticles (PEDOT/CAM NPs) for concurrent release of the antibiotic and real-time monitoring of bacterial growth. PEDOT/CAM NPs, with an antibiotic loading content of 11.9±1.3% w/w, have been proved to inhibit the growth of *Escherichia coli* (*E. coli*) and *Streptococcus sanguinis* (*S. sanguinis*) due to the antibiotic release by cyclic voltammetry. Furthermore, in situ monitoring of bacterial activity has been achieved through the electrochemical detection of β-nicotinamide adenine dinucleotide (NADH), a redox active species produced by the microbial metabolism that diffuse to the extracellular medium. According to these results, the proposed nanotheranostic platform has great potential for real-time monitoring of the response of bacteria to the released antibiotic, contributing to the evolution of the personalized medicine.

59

3.1.1 Introduction

Even though microbial pathogens have always accompanied humanity, they still cause a significant morbidity and mortality, affecting over 250 million people worldwide per year.[1–3] The main sources of infection include water and food contamination, as well as body fluids. In addition, contamination can be easily spread in clinical facilities developing nosocomial infections, where immune-compromised patients are in contact with microbial pathogens residing on hospital. Most alarmingly, common drugs are becoming less effective against well-known infections and new pathogens are continually being found.[4,5] While much effort and funds have been devoted to the design and development of new antibacterial vaccines and drugs, more attention is needed to limit and control infectious outbreaks. It is necessary to promote the implementation of early detection systems that can warn in qualitative and quantitative manners. Hence, there is an urgent need for an early and rapid diagnostic tool that can detect pathogenic microorganisms and, at the same time, assess their responsiveness to antimicrobial drugs. Electrochemical biosensors for early pathogen detection[6] are a promising alternative to conventional methodologies, which are mainly based on cell culturing, molecular methods and mass spectrometry.[7] Electrochemical methods offer many advantages, the main ones being rapid detection, high sensitivity, low-cost, simplicity, and lack of time-consuming pre-treatments. Other interesting advantages include that most electrochemical-based sensors are label-free devices and can be developed as miniaturized, flexible, disposable, wearable and/or implantable formats.[8–10] Therefore, electrochemical strategies have been recognized as effective tools for the successful detection of whole bacteria, cellular derived signalling molecules, bacterial metabolites and by-products, and enzymes.

Pathogen identification via direct detection of cellular biogenic metabolites is a straightforward electrochemical sensing approach that does not require the use

Nanotheranostic Interface Based on Antibiotic-Loaded Conducting Polymer Nanoparticles for Real-Time Monitoring of Bacterial Growth Inhibition

61

of highly specialized materials and/or instruments. Within this context, voltammetric techniques have been previously used to sense bacterial metabolites and by-products, such as pyoverdine, pyocyanin and 2-heptyl-3-hydroxy-4-quinolone and 2-heptyl-4-hydroxyquinoline. Nevertheless, these products are just produced by some type of bacteria. For example, Buzid et al.[11] detected pyocyanin, 2-heptyl-3-hydroxy-4-quinolone and 2-heptyl-4-hydroxyquinoline from *Pseudonomas aeruginosa* (*P. aeruginosa*) cultures using differential pulse voltammetry and employing a thin electrode of boron-doped diamond improved with cationic surfactant hexadecyltrimethylammonium bromide. Sismaet et al.[12] used square-wave voltammetry to measure the concentration of pyocyanin of *P. aeruginosa* isolates from different clinical patients. Results indicated that all isolates were measurable and pyocyanin concentration was correlated with patient symptoms and comorbidity. Sedki et al.[13] utilized reduced graphene oxide-hyperbranched chitosan nanocomposites to monitor *E. coli* and *P. aeruginosa* growth by following the oxidation of bacteria metabolites (i.e. undefined electrochemically active secreted biomolecules). However, other authors have been focused on the electrochemical detection of well-defined redox active species released by bacteria to the extracellular environment, such as low molecular weight thiols,[14] β-nicotinamide adenine dinucleotide (NADH),[15] β-nicotinamide adenine dinucleotide phosphate (NADPH) and flavins.[16,17] On the other hand, antibiotic-loaded biomaterials are under continuous development for infection control. Indeed, antibiotics are routinely delivered in orthopaedic applications such as prosthetic hips.[18–20] Nevertheless, many times there is no control over the quantity of released drug and, frequently, the amount of antibiotic loaded on the implant is at excessive concentration (i.e. much higher than the minimum inhibitory concentration). Despite this limitation, some antibiotics, such as ciprofloxacin hydrochloride,[21] gentamicin,[22] ampicillin,[22] and vancomycin,[23] have been loaded on polymeric platforms for subsequent controlled release in

response to external stimulation (e.g. electrical[21] and changes in pH[22,23]) rather than diffusion or biodegradation of the polymeric matrix. Moreover, the integration of the two functionalities, controlled antibiotic release to kill bacteria using minimal antibiotic concentrations and real-time pathogen monitoring, in a single polymeric device have not been tried yet.

In this work, we present a system capable of slowly release a previously loaded antibiotic and, at the same time, recording the bacterial growth and inhibition. This approach allows us to envisage a future where the infection treatment and testing efficacy of the antibiotic treatment can be performed simultaneously. For this purpose, poly(3,4-ethylenedioxythiophene) (PEDOT) nanoparticles (NPs) loaded with chloramphenicol (CAM) have been synthesized and, subsequently, fixed to a screen-printed carbon electrode (SPCE) using a chitosan layer. CAM is a wide-spectrum antibiotic that inhibits protein synthesis blocking the ribosome functions,[24,25] while PEDOT is a conducting polymer with superior capacitive performance, high conductivity, stability in aqueous media and biocompatibility.[26–30] Moreover, PEDOT NPs were successfully used to detect extracellular NADH coming from the respiration reactions of bacteria that diffuses across cell membrane without the interference from the eukaryotic NADH pool, allowing to distinguish prokaryotic from eukaryotic cells.[15] Overall, this work presents an efficient approach for a rapid, real-time and accurate monitoring of the susceptibility of bacteria to the effect of CAM antibiotic. The proposed system is expected to lead to a more personalized medicine using simple materials and equipment that identify more efficient and specific treatments in a short period of time.

3.1.2   Methods

3.1.2.1   *Synthesis of poly(3,4-ethylenedioxythiophene) nanoparticles (PEDOT NPs)*

A 30 mL Corex tube was filled with 15.8 mL of milli-Q water. After this, 96 µL of dodecyl benzenesulfonic acid (DBSA) were added and the solution was stirred at 40 °C for 1 h with a magnetic stirrer set at 750 rpm and protected from light with aluminium foil. 72 µL of 3,4-ethylenedioxythiophene (EDOT) monomer and 2 mL of ethanol were then added slowly, and the mixture was allowed to stir for 1 h at 750 rpm and 40 °C. Finally, 0.73 mg of ammonium persulfate (APS) dissolved in 2 mL of milli-Q water were added to the mixture drop by drop while stirring. The reaction was maintained in agitation at 40 ºC overnight. In this process, the color of the reaction mixture changed from light grey to dark blue. No sedimentation was observed after the reaction occurred, indicating a good colloidal stability. The side products and unreacted chemicals were removed by a sequence of 3 centrifugations at 11000 rpm for 40 min at 4 ºC. After each centrifugation, the resulting supernatants were decanted and the pellet was dispersed in 15 mL of deionized water by using a vortex and a sonication bath (15 min at room temperature). The last pellet was left under vacuum in the same tube for two days, then weighted and dispersed in the corresponding media at the desired concentration.

3.1.2.2   *Synthesis of chloramphenicol-loaded PEDOT NPs (PEDOT/CAM NPs)*

96 µL of DBSA were added to a 30 mL tube filled with 15.8 ml of milli-Q water and the solution was stirred for 1 h at 750 rpm and 40 °C. After this, 72 µL of EDOT and 2 ml of drug solution (8 mg/ml CAM in ethanol) were added drop by drop while stirring and the resulting solution was stirred at 750 rpm and 40 °C

63

during 1 h. Finally, 0.73 mg of APS were dissolved in 2 mL of milli-Q water and were added to the mixture. The reaction was protected from light (aluminum foil) and maintained in agitation at 40 ℃ overnight. The color of the reaction mixture changed from light grey to dark blue. No sedimentation was observed after the reaction occurred, indicating good colloidal stability. The side products, extra drug and unreacted chemicals were removed by a sequence of 3 centrifugations at 11000 rpm for 40 min at 4 ℃. The resulting supernatants were decanted and the pellet was re-dispersed in deionized water by using a vortex and an ultrasonic bath (15 min at room temperature). The last pellet was left under vacuum for two days, then weighted and re-dispersed in the corresponding media at the desired concentration.

3.1.2.3   Determination of the drug loading ratio

The drug content was determined by taking 10 μL of PEDOT/CAM NPs suspension (10 mg/ml NPs in milli-Q water) into 990 μL of drug solvent (ethanol). The suspension was sonicated and vortexed for 10 min, leading to a complete drug release in the alcoholic medium. Then, the NPs dispersion was centrifuged with a micro-centrifuge for 15 min at 2500 rpm. Finally, the supernatant was evaluated using a UV-Vis spectrometer. The calibration curve was prepared with the drug dissolved in ethanol and read at 280 nm (**Figure 3.1.1**). The same procedure was applied to determine the drug released during the dialysis or after the electrical stimuli assays.
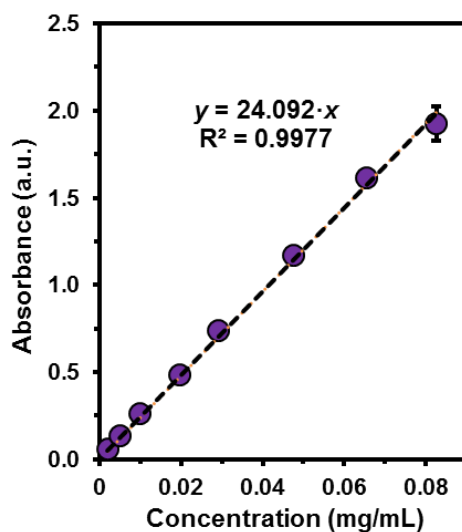
Figure 3.1.1. Calibration curve for CAM in ethanol.

3.1.2.4 *Dynamic light scattering (DLS)*

DLS studies were performed using NanoBrook Omni Zeta Potential Analyzer from Brookheaven Instruments. Measurement consisted of 3 runs of 120 s each, which were averaged to obtain the effective diameter (D_{eff}). Samples were analyzed at 25 ºC using a scattering angle of 90º. In order to know the (ζ)-potential, particles were re-suspended in 1 mM KCl solution and 30 consecutive measurements were taken of each sample.

3.1.2.5 *Fourier transform infrared (FTIR) spectroscopy*

FTIR transmittance spectra were recorded on a FTIR Jasco 4100 spectrophotometer. Samples were deposited on an attenuated total reflection accessory (Top-plate) with a diamond crystal (Specac model MKII Golden Gate Heated Single Reflection Diamond ATR). For each sample, 64 scans were performed between 4000 and 600 cm^{-1} with a resolution of 4 cm^{-1}.

3.1.2.6   RAMAN spectroscopy

Samples were characterized by micro-Raman spectroscopy using a commercial Renishaw inVia Qontor confocal Raman microscope. The Raman setup consisted of a laser (at 785 nm with a nominal 300 mW output power) directed through a microscope (specially adapted Leica DM2700 M microscope) to the sample, after which the scattered light is collected and directed to a spectrometer with a 1200 lines·mm^{-1} grating. The exposure time was 10 s, the laser power was adjusted to 0.001-0.05% of its nominal output power depending on the sample, and each spectrum was collected with 30 accumulations.

3.1.2.7   X-ray photoelectron spectroscopy (XPS)

XPS analyses were performed in a SPECS system equipped with a high-intensity twin-anode X-ray source XR50 of Mg/Al (1253 eV/1487 eV) operating at 150 W, placed perpendicular to the analyzer axis, and using a Phoibos 150 MCD-9 XP detector. The X-ray spot size was 650 µm. The pass energy was set to 25 and 0.1 eV for the survey and the narrow scans, respectively. Charge compensation was achieved with a combination of electron and argon ion flood guns. The energy and emission current of the electrons were 4 eV and 0.35 mA, respectively. For the argon gun, the energy and the emission current were 0 eV and 0.1 mA, respectively. The spectra were recorded with pass energy of 25 eV in 0.1 eV steps at a pressure below 6×10^{-9} mbar. These standard conditions of charge compensation resulted in a negative but perfectly uniform static charge. The C 1s peak was used as an internal reference with a binding energy of 284.8 eV. The surface composition was determined using the manufacturer's sensitivity factors.

3.1.2.8   Scanning electron microscopy (SEM)

SEM micrographs were obtained using a Focused Ion Beam Zeiss Neon 40 scanning electron microscope operating at 5 kV. Samples were mounted on a double-side adhesive carbon disc and sputter-coated with a thin layer of carbon to prevent sample charging problems.

3.1.2.9   Atomic force microscopy (AFM)

AFM was conducted to obtain topographic images of the NPs surface using silicon TAP 150-G probe (Budget Sensors, Bulgaria) with a frequency of 150 kHz and a force constant of 5 N/m. Images were obtained with a Molecular Imaging PicoSPM microscope using a NanoScope IV controller under ambient conditions in tapping mode. AFM measurements were performed on various parts of the samples, which produced reproducible images similar to those displayed in this work.

3.1.2.10 Cytotoxicity evaluation

The cytotoxicity of free CAM, PEDOT, and PEDOT/CAM NPs was evaluated by the MTT assay using the MG-63 cell line. Free CAM was dissolved in ethanol (the final concentration of ethanol in the cell media was smaller than 10 %). All the other substances were prepared in milli-Q water. Cells were seeded at a density of 20×10^4 cells per well (100 µL each) in 96-well plates and incubated overnight. Subsequently, the cells were exposed to a series of increasing free CAM, PEDOT, and PEDOT/CAM NPs concentrations. CAM concentrations were 0.1, 1, 10, 50, 100, 500 and 1000 µg/mL PEDOT and PEDOT/CAM NPs concentrations were 0.0655, 0.125, 0.25, 0.5 and 1 mg/mL Cells were incubated

with the treatment for 24 h. Next day, the percentage of viable cells relative to untreated control was determined on the basis of the mitochondrial conversion of 3-(4,5-dimethylthiazol-2-yl)-2,5-diphenyltetrazolium bromide to formazan. The results were expressed as the mean value $\pm$ standard deviation (SD). All the experiments were performed in triplicate. Statistical comparison of values was based on a 2-way ANOVA using Tukey's test for pair-wise comparison with $p < 0.05$.

68

3.1.2.11 Drug release

25 µL of PEDOT/CAM NPs (10 mg/mL) were deposited into dialysis buttons, covered with a 3.5 kDa MWCO (Molecular Weight Cut-Off) dialysis membrane, immersed in 1.5 mL of PBS solution (pH 7.4), and kept in a shaker at 37 ºC at 80 rpm. Each day all the immersion solution was taken out to quantify the released drug and the solution was replaced with 1.5 mL of new medium. The release process in PBS was evaluated for more than 80 days. After this, a second experiment in which the release medium was changed every week from hydrophilic to hydrophobic, was conducted for three weeks. More specifically, the release medium for the first, second and third week was PBS, PBS:EtOH 90:10, and PBS:EtOH 30:70, respectively, the latter allowing the complete drug release. All the results were normalized by the total amount of drug encapsulated within the NPs or used as a free molecule in order compare their kinetics. The amount of released drug was evaluated by UV spectroscopy using a Cary100 UV-Vis spectrophotometer controlled by the UVProbe 2.31 software. Calibration curves were obtained by plotting the absorbance measured at 280 nm against CAM concentration (**Figure 3.1.2**). Release experiments were repeated three times and the averages were plotted.

(a)

$y = 29.787 \cdot x$
$R^2 = 0.9988$

(b)

$y = 29.484 \cdot x$
$R^2 = 0.9977$

(c)

$y = 29.02 \cdot x$
$R^2 = 0.9982$
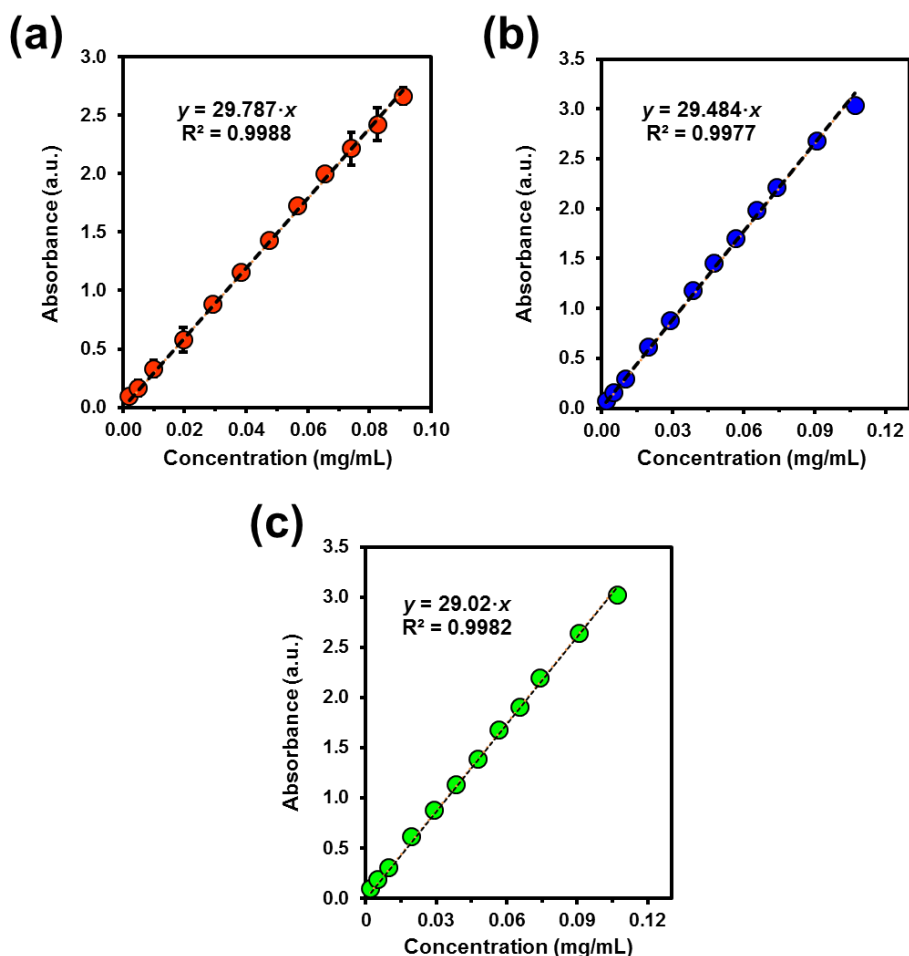
Figure 3.1.2. Calibration curves for CAM in (a) PBS, (b) PBS with 10 % ethanol (PBS:EtOH 90:10), and (c) PBS with 70 % ethanol (PBS:EtOH 30:70).

3.1.2.12 Effects of voltage and time on drug release

Washed PEDOT/CAM NPs were re-suspended in milli-Q water to a final concentration of 10 mg/mL. Then, a total of 15 μL of the resulting solution were placed on SPCEs in three rounds (5 μL each time) and dried under hood after each round. Dried NPs were covered with 5 μL of chitosan solution (20 mg/mL chitosan in 0.1 M HCl) and dried again. The chitosan layer formed after drying was used to fix the NPs, avoiding detachment. A three-electrode configuration

69

was used: the SPCE, SPCE-PEDOT/CAM or SPCE/PEDOT worked as a working electrode; a platinum wire as counter electrode; and Ag | AgCl as reference electrode. 1.5 mL of PBS 1× was used as electrolytic medium.

The appropriate voltage was applied for a fixed time. After electrical stimulation, the medium was kept to determine the drug concentration and replaced with new PBS. The absorbance was read at 280 nm. The influence of the time was evaluated by CA using a voltage of +1.0 V and by CV using a potential window from –0.50 V to +0.50 V during 5, 15 and 30 min. A control experiment was performed in the absence of the stimulus. All the measures were repeated at least three times and the average with the standard deviation plotted on the graphs.

3.1.2.13 Cyclic voltammetry (CV)

CV studies were conducted with an Autolab PGSTAT302N Galvanostat equipped with the ECD module (Ecochimie, The Netherlands). Measurements were performed on 15 μL of 10 mg/mL NPs solution, which were fixed on a SPCE with chitosan, as described previously. All electrochemical assays were performed using a three-electrode one compartment cell at room temperature. The cell was filled with 1.5 mL of PBS 1× as a supporting electrolyte. A SPCE coated with NPs (i.e. SPCE-PEDOT or SPCE-PEDOT/CAM) was used as the working electrode, platinum wire as the counter electrode, while an Ag|AgCl electrode containing KCl saturated aqueous solution was the reference electrode (offset potential versus the standard hydrogen electrode, $E° = 0.222$ V at 25 °C). Oxidation-reduction cycles were registered within the potential range of −1.5 to +1.0 V at different scan rates.

3.1.2.14 Bacterial growth detection

Bacterial growth was monitored in real time on the electrochemical cell by CV. Voltammograms of coated SPCEs in the culture medium, which was $NaHCO_3^-$ supplemented DMEM, were recorded at different incubation times (0, 2, 4, 6, 8 and 24 h) for PEDOT and PEDOT/CAM NPs in the presence and absence of *E. coli* and *S. sanguinis*. The initial and final potentials were −0.20 V, while the reversal potential and the scan rate were 0.80 V and 100 mV/s, respectively. For comparison with the results obtained by CV, the relative bacterial growth was evaluated through the variation of the absorbance at 600 nm after 24 h of culture. According to the McFarland standard, one unity of absorbance at 600 nm was associated to 10^8 CFU mL.

3.1.2.15 NADH detection

NADH was detected by CV using SPCE-PEDOT. Measures were performed using different NADH concentrations at pH 8.5 and 6 in $NaHCO_3^-$ supplemented DMEM (i.e. culture medium). The initial and final potentials were –0.20 V, while the reversal potential and the scan rate were 0.80 V and 100 mV/s, respectively.

3.1.2.16 CAM antibacterial activity test

The bactericidal activity of the loaded drug was tested with *E. coli* and *S. sanguinis*. First, 1 mL of an overnight culture (grown for 16 h) was added to 5 mL of the Lysogeny broth (LB) medium. Bacteria were seeded on LB agar plates and four paper discs impregnated with the different samples deposited on top. Three of such discs contained 25 µL of 10 mg/mL PEDOT/CAM NPs, 10 mg/mL PEDOT NPs or 2 mg/mL CAM dissolved in ethanol, respectively, while the fourth disc was impregnated with NAX, as a control. The effect of the drugs on

bacterial growth was evaluated after incubation at 37 °C for 24 h. The test was carried out in triplicate.

3.1.2.17 Bacterial growth curves

The bactericidal activity of loaded CAM was tested during *E. coli* and *S. sanguinis* growth. For this purpose, six 15 mL polystyrene tubes were filled with 5 mL of LB medium and, subsequently, 10 µL of concentrated bacteria (10^8 CFU/mL) were added, reaching 1×10^3 CFU per tube (estimated by the absorbance at 600 nm). 0 (blank), 5, 25 and 50 µL of 10 mg/mL PEDOT/CAM NPs, 50 µL of PEDOT NPs or 25 µL of 2 mg/mL CAM solution in ethanol together with 100 µL of fresh LB medium were placed in 3.5 kDa MWCO dialysis bags. Each dialysis bag was immersed in the previously described polystyrene tubes. All tubes were kept in an incubator at 37 ºC and 80 rpm. 40 µL of medium were taken from each tube after 0, 2, 4, 6, 24 and 48 h and the absorbance checked by UV at 600 nm to estimate bacterial growth. Bacterial growth in the tube with only culture medium (i.e. in the absence of NPs or drug) was considered as the maximum growth (control) and it was used to calculate the relative growth of the bacteria in the presence of the different samples. All assays were conducted in triplicate and the values averaged.

The data of the experiments were presented as mean ± standard deviation (SD). Multiple comparisons among groups (cell viability) were determined using one-way ANOVA analysis; *, $p < 0.05$; ** , $p < 0.01$; *** , $p < 0.001$ represented a significant difference.

3.1.3 Results and discussion

3.1.3.1 Chloramphenicol encapsulation

The conducting polymer used in this work is PEDOT, which is frequently employed for the fabrication of biomedical devices because of its outstanding electrochemical properties, biocompatibility and stability in continuous operation.[26–30] Furthermore, this conducting polymer was found to be very effective for the electro-stimulated release of encapsulated drugs.[31,32] A representative and common antibiotic, CAM, was loaded into the PEDOT NPs. In this work, unloaded PEDOT NPs (control) and CAM-loaded PEDOT NPs (hereafter PEDOT/CAM NPs) were prepared by *in situ* emulsion polymerization as shown in **Figure 3.1.3**. The encapsulation of the antibiotic in the NPs is promoted by the attractive interactions between the negatively charged (oxygen) and the electronegative (chlorine) atoms of CAM and the oxidized PEDOT chains. Moreover, the nitro group in CAM, a strong electron-withdrawing group, reduced the electron density of PEDOT chains, acting as electron acceptor.

73
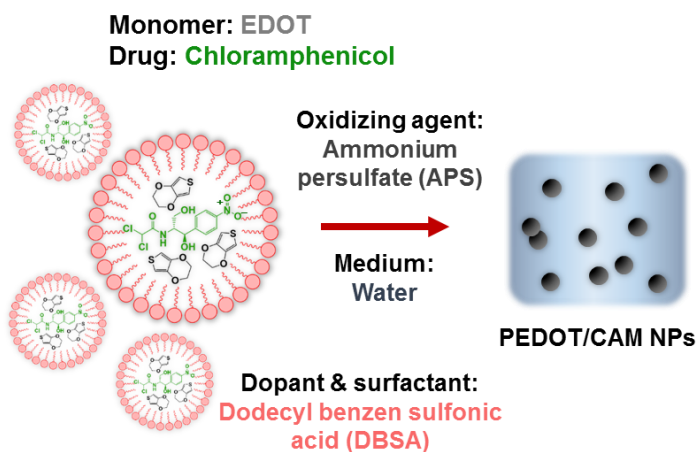
Figure 3.1.3. Synthesis of PEDOT and PEDOT/CAM NPs.

The average diameter of the resulting PEDOT and PEDOT/CAM NPs, as measured by dynamic light scattering (DLS), was 208 nm and 215 nm, respectively (**Figure 3.1.5a**). In both cases, the polydispersity (PDI) values were smaller than 0.3. As the numerical value of PDI ranges from 0.0 (for an ideal uniform sample with respect to the particle size) to 1.0 (for a highly polydisperse sample with multiple particle size distribution), the obtained values indicate a relatively narrow size distribution. The (ζ)-potential of PEDOT NPs, which was negative (**Figure 3.1.5a**), became ~7 mV less negative when CAM was loaded. This is consistent with the ζ-potential obtained for CAM solutions (**Figure 3.1.4**), which are significantly lower than for PEDOT NPs (i.e. -7.1 ± 3.2 mV and -4.7 ± 2.6 mV mV for 0.1 for 0.1 and 0.5 mg/mL CAM solutions, respectively, against, -26.0 ± 7.3 mV for PEDOT NPs). These results indicate that the presence of the drug partially neutralized the overall negative charge coming from the DBSA.
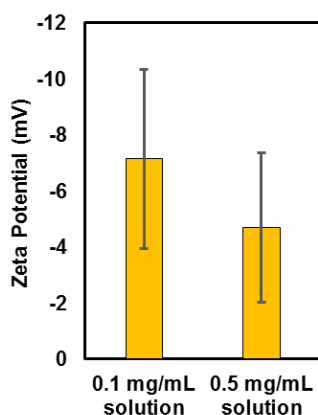
Figure 3.1.4. ζ-potential of CAM solutions.
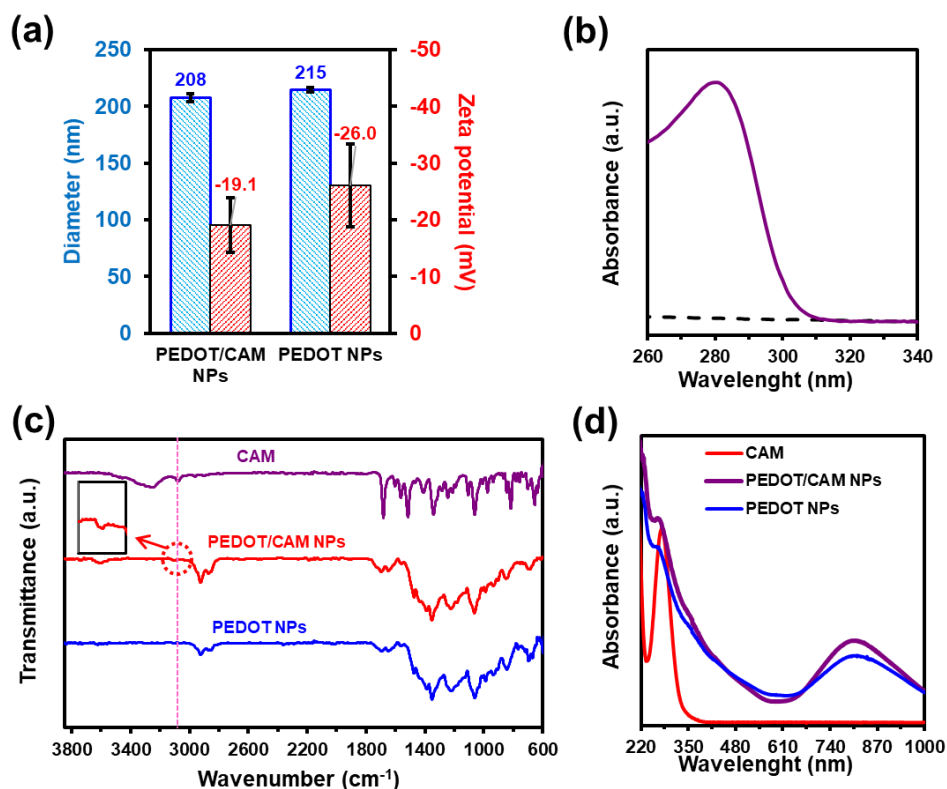
Figure 3.1.5. (a) Diameter and ζ-potential of PEDOT and PEDOT/CAM NPs ($n = 30$). (b) UV-Vis Spectra of CAM released from PEDOT/CAM in ethanol (solid line) compared to the blank (dashed line). (c) FTIR spectra of free CAM, PEDOT and PEDOT/CAM NPs.

The LC (**Equation 3.1.1**) was determined by dissolving the loaded drug in ethanol and using UV-Vis absorbance for quantification (**Figure 3.1.5b**). **Figure 3.1.1** and **Figure 3.1.2** display the calibration curve obtained in the different media used in this work. It has been previously described that PEDOT NPs can act as excellent therapeutic molecule carriers and attain successful electronic triggered release.[31,32] However, the encapsulation efficiency for small molecules is challenging, usually leading to low values. In this case, the LC was 11.9 ± 1.3 %, which was expressed as mass of loaded CAM with respect to the total mass. This value is larger than those achieved for other small drugs, such as

curcumin (CUR) and piperine (PIP) (i.e. LC= 5.9 ± 1.6 w_t % and 8.0 ± 0.4 w_t % for PEDOT/CUR and PEDOT/PIP NPs, respectively)[31] but lower than obtained for negatively charged pentapeptides, hereafter denoted generically PPEP (LC= 33.8 ± 4.3 w_t % and 43.2 ± 2.9 w_t %, depending on the PPEP sequence),[32] which acted as dopant anions.

The loading capacity (LC, in %) was calculated using the following equation:

$$LC = \frac{(W_i - W_f)}{W_{NPs}} \times 100$$

Equation 3.1.1. The loading capacity percentage, where W_i indicates CAM initial mass, W_f CAM final mass, and W_{NPs} total NPs mass.

The presence of the drug in PEDOT/CAM NPs was characterized by FTIR and Raman spectroscopy. **Figure 3.1.5c** compares the FTIR spectrum of the free CAM, PEDOT NPs and PEDOT/CAM NPs. As expected, the absorption bands found in the PEDOT NPs spectrum mainly correspond to the characteristic peaks of PEDOT chains, which appear at 1644 and 1477 cm^{-1} (C=C stretching), 1350 cm^{-1} (C−C stretching), 1215 and 1058 cm^{-1} (C−O−C vibrations) and 840 cm^{-1} (stretch of the C−S bond in the thiophene ring). Also, weak but clearly defined bands attributed to residual DBSA molecules were detected at 2922 and 2853 cm^{-1} (aliphatic −CH$_2$ and −CH$_3$ stretching), and 1644 cm^{-1} (C=C stretching from the phenyl ring). Free CAM exhibits the characteristic absorption peaks at 3333, 3264 and 3073 cm^{-1}, which have been assigned to the stretch of O−H, N−H and C−H bonds, respectively.[33] Also, absorption bands at 1680/1563 cm^{-1} due to amide I/amide II of the 2,2-dichlor-acetamide moiety, and at 1513/1340 cm^{-1} due to nitro/nitro-phenyl group are present. Finally, PEDOT/CAM NPs present mostly the bands associated with PEDOT NPs but also a very weak band associated with CAM presence at 3073 cm^{-1}, which corresponds to the C–H stretching. Unfortunately, Raman spectroscopy did not show any band from CAM

in PEDOT/CAM NPs due to the strong absorbance of PEDOT chains. The recorded spectra is shown in (**Figure 3.1.6**). On the other hand, **Figure 3.1.5d**, which compares the UV spectra of CAM, PEDOT NPs and PEDOT/CAM NPs, confirms the lack of covalent bonding between drug and the polymers chains. Furthermore, the spectra do not reveal the formation of CAM···PEDOT π-π stacking interactions, supporting the fact that the interactions between the two species are mainly electrostatic.
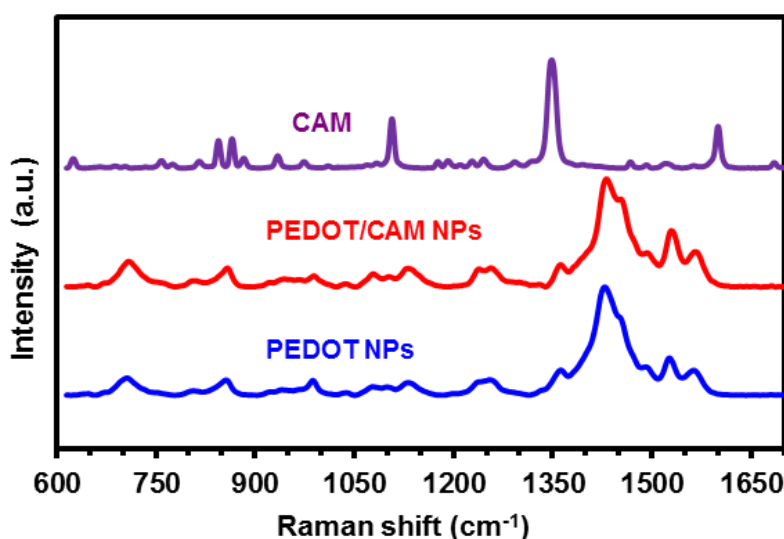
Figure 3.1.6. Raman spectra of free CAM, PEDOT and PEDOT/CAM NPs.

CAM main bands at 1107, 13351 and 1598 cm^{-1} are attributed to the C–O bending vibration, C–H bond stretching vibration and –NO$_2$ bending vibration, respectively. PEDOT NPs principal bands, which appear at 1436, 1231, 1376 and 1508 cm^{-1}, correspond to the symmetric stretching mode of the aromatic C−C bond and the antisymmetric stretching vibration of C$_\alpha$−C$_\beta$. Finally, the spectrum recorded for PEDOT/CAM NPs displays only the fingerprints of PEDOT NPs.

Quantitative data on the composition of PEDOT/CAM NPs were obtained by X-ray photoelectron spectroscopy (XPS). The EDOT:CAM ratio was determined using the atomic percentage composition, which is shown in **Table 3.1.1**. Considering that there is one sulphur atom per EDOT repeat unit and two nitrogen atoms per CAM molecule (**Figure 3.1.7**), the S 2p / N 1s ratio indicates ~4 EDOT units per CAM molecule. This value is consistent with the one derived from the S 2p / Cl 2p ratio (two chlorine atoms per CAM molecule), which is ~3 EDOT unit per CAM molecule.
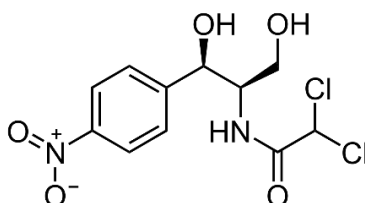
Figure 3.1.7. CAM chemical structure.

Table 3.1.1. Percentage atomic composition (C 1s, N 1s, O 1s, S 2p and Cl 2p; in %), S 2p / N 1s ratio and S 2p/Cl 2p ratio obtained by XPS for PEDOT and PEDOT/CAM NPs.

	Atomic composition (%)						
	C 1s	N 1s	O 1s	S 2p	Cl 2p	S 2p / N 1s	S 2p / Cl 2p
PEDOT	49.00	-	47.29	3.71	-	-	-
PEDOT/CAM	57.20	0.55	40.28	1.14	0.83	4.14	2.75

More detailed information regarding the chemical bonds present on the sample was extracted from the peak's deconvolution, as shown in **Figure 3.1.8** and **Figure 3.1.9**. The nitrogen peak, which is completely absent for PEDOT NPs

(**Figure 3.1.8a**), is centered at 399.8 eV for PEDOT/CAM NPs (**Figure 3.1.8b**) and has been attributed to N−H and C−N from CAM. Similarly, the Cl 2p peak only appears for PEDOT/CAM NPs (**Figure 3.1.8c** and **d**), showing a spin-split couple, Cl 2p3/2 and Cl 2p1/2, at 198.4 eV and 200 eV, respectively. This peak corresponds to the C−Cl present also in CAM.
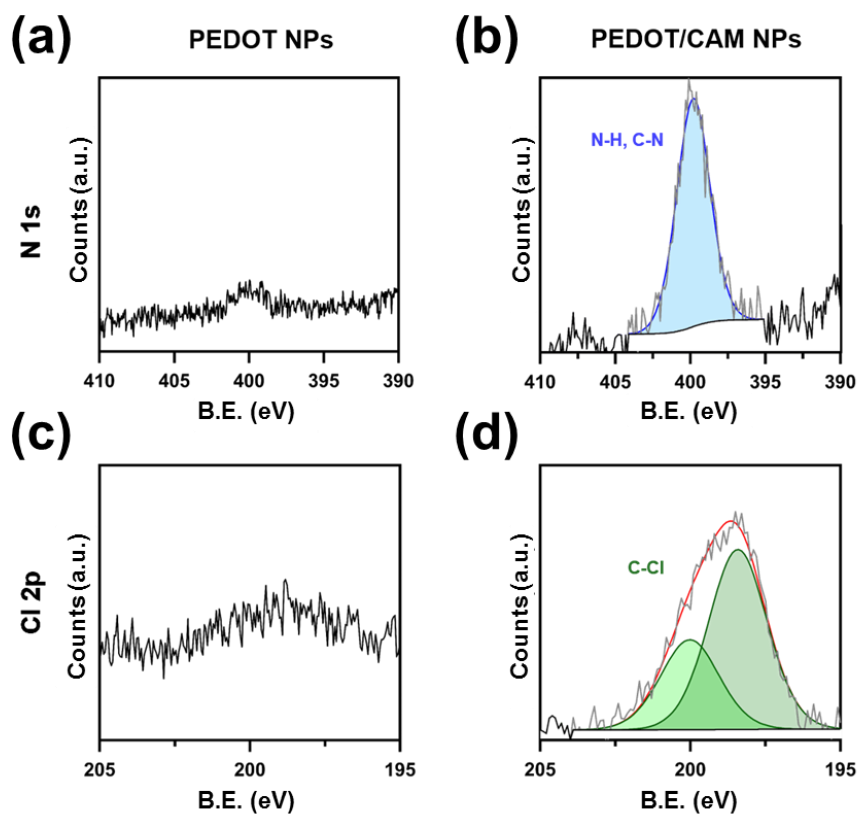
Figure 3.1.8. High-resolution XPS spectra of N 1s (a, b) and Cl 2p (c, d) regions for PEDOT (a, c) and PEDOT/CAM NPs (b, d).

Figure 3.1.9 displays the high-resolution XPS spectrum in the C 1s, S 2p and O 1s regions for PEDOT and PEDOT/CAM NPs. Deconvolution of the C 1s peak (**Figure 3.1.9a** and **b**) led to five Gaussian curves. Of these, four peaks have been attributed to bonds from PEDOT chains: C−C and C−H bonds of PEDOT chains and the surfactant molecules (284.8 eV); C−S bonds of thiophene ring (286.4 eV);

the C−O bonds of the fused dioxane ring (288.0 eV); and the $\pi\cdots\pi^*$ shake up due to the thiophene ring (289.15 eV).[34] The deconvoluted small peak centered at 283 eV has been associated to the Al−C (carbide) bond from the XPS pin substrate. On the other hand, the high resolution XPS of the S 2p region of PEDOT and PEDOT NPs (**Figure 3.1.9c** and **d**) show the spin-split sulfur coupling S2p3/2 and S2p1/2, with a separation of 1.2 eV, for the C–S–C bond of the thiophene ring (162.7 and 163.9 eV, respectively) in PEDOT chains,[35,36] and the SO_3^- of DBSA (167.6 eV and 168.8 eV, respectively).[34,37] The O 1s signal consists of three components (**Figure 3.1.9e** and **f**). The first is related to water remaining on the sample (534.0 eV),[38] while the peaks at 532.1 and 530.8 eV correspond to the C−O−C of the fused dioxane ring and the SO_3^- of DBSA dopant molecules.[39]
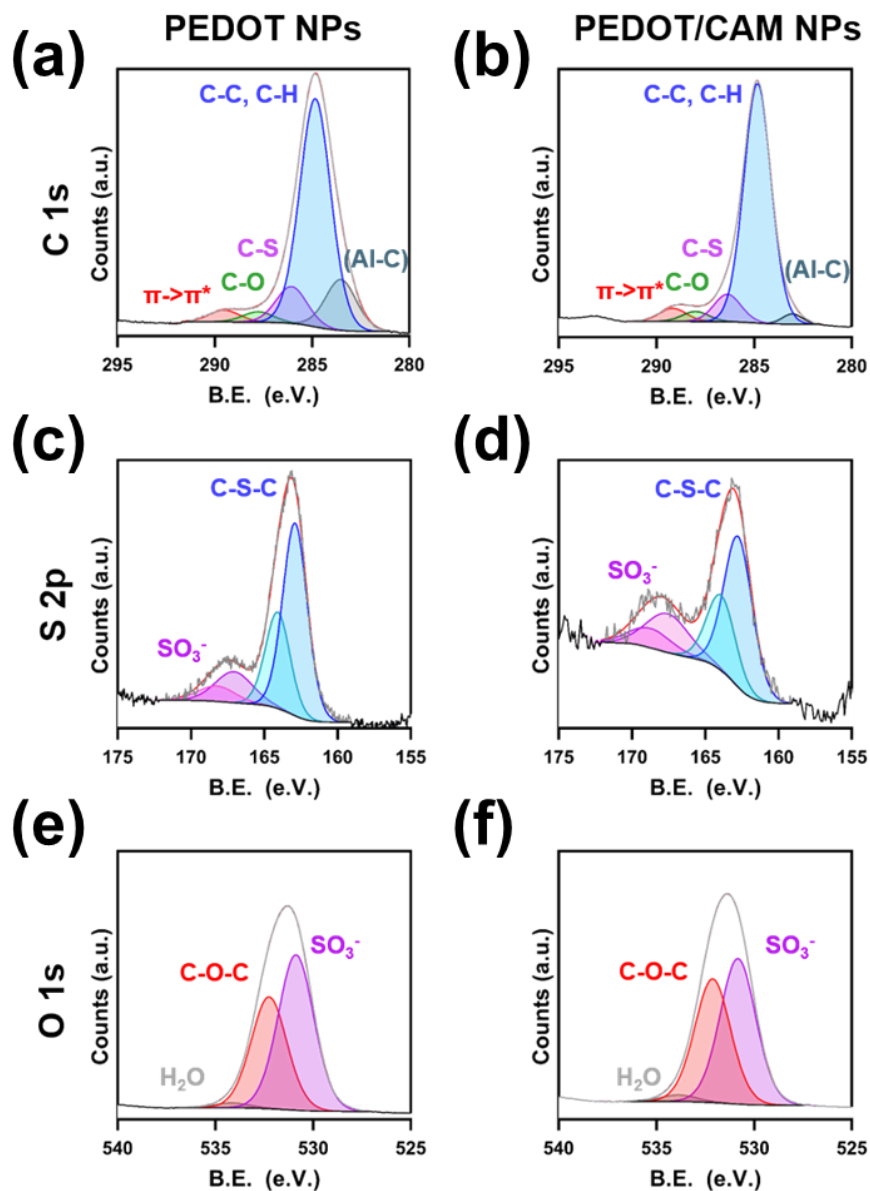
Figure 3.1.9. High-resolution XPS spectra of (a, b) C 1s, (c, d) S 2p and (e, f) O 1s regions for (a, c, e) PEDOT and (b, d, f) PEDOT/CAM NPs.

3.1.3.2 *Morphology of PEDOT and PEDOT/CAM NPs*

Scanning electron microscopy (SEM) and atomic force microscopy (AFM) were employed to visualize and characterize the morphology of the prepared NPs. SEM micrographs of PEDOT and PEDOT/CAM NPs are displayed in **Figure 3.1.10a** (top and bottom, respectively). Both types of NPs present a well defined spherical shape. The average diameter, as determined by DLS, is not altered by the encapsulated drug (i.e. 118 ± 16 and 121 ± 13 nm for PEDOT and PEDOT/CAM, respectively). The resulting histograms, which are included in **Figure 3.1.10a**, evidence that the size distribution is very narrow, in perfect correlation with the low polydispersity values obtained by DLS.

These results were confirmed by AFM, both 3D topographic and 2D phase images being displayed in **Figure 3.1.10b**. The diameter of PEDOT and PEDOT/CAM NPs, as determined from AFM images, is 139 ± 19 and 134 ± 23 nm, respectively. This noticeable similarity is in sharp contrast with the results reported for PEDOT/CUR and PEDOT/PIP NPs, which exhibited a diameter much higher than PEDOT NPs (i.e. ~150% and ~260% increment, respectively).[31] Considering that molecular sizes of CAM, CUR and PIP are similar, these observations suggest that the interactions between CAM and PEDOT chains are radically different from those formed by CUR and PIP and, therefore, the release mechanism is also expected to be different. On the other hand, after the loading of PPEPs, which are larger than CAM, PEDOT NPs resulted in an increase in diameter of only about 23%-37%.[32]
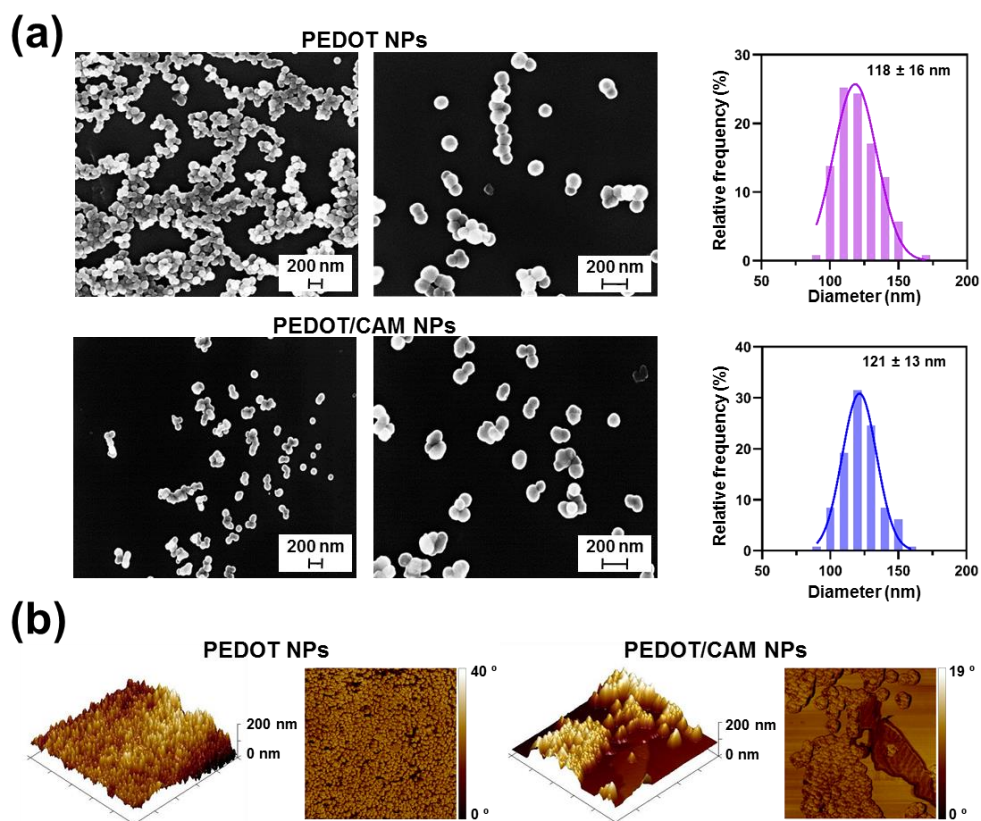
Figure 3.1.10. For PEDOT and PEDOT/CAM NPs: (a) SEM micrographs (left, 50k× magnification; right, 100k× magnification) and diameter distribution histogram ($n = 250$); and (b) 3D topographic (left) and 2D phase (right) AFM images.

3.1.3.3   CAM release

The release of CAM from the dialysis buttons containing PEDOT/CAM NPs was studied by UV-Vis in media with different hydrophilicities: phosphate buffered saline (PBS) solution alone, PBS with 10 % ethanol (PBS:EtOH 90:10), and PBS with 70 % ethanol (PBS:EtOH 30:70). In a preliminary release assay, which was performed only in PBS (not shown), we observed that cumulative release of CAM in such hydrophilic medium is very slow, reaching a value of only 19% after 82 days (not shown). Then, a second release experiment was

designed as described in the Methods section (i.e. decreasing the hydrophilicity of the medium every week by replacing PBS alone by ethanol-containing PBS solutions). The release profile, which is displayed in **Figure 3.1.11**, indicates that the release during the first two weeks was very slow. This is due to the poor affinity of the hydrophobic drug by PBS and PBS:EtOH 90:10, which does not compensate the strength of the interactions between CAM molecules and oxidized PEDOT chains. However, when the latter solution was replaced with PBS:EtOH 30:70, the release of CAM increased significantly, reaching 100 % in only six days (**Figure 3.1.12**). In summary, CAM has a great affinity towards EtOH molecules and, indeed, is very soluble in this solvent (up to 50 mg/mL), whereas the affinity towards water molecules is poor (this drug in water is only slightly soluble in water, up to 2.5 mg/mL) Accordingly, CAM···water interactions cannot compete with CAM···CAM and CAM···PEDOT interactions to favour the release of the encapsulated drug. On the other hand, it should be emphasized that, although the release of CAM in PBS is low, it is enough to inhibit the bacterial growth and, in addition, can be increased by electrical stimulation and by the alteration of the composition through the addition of nutrients (as proved in next sections).

84
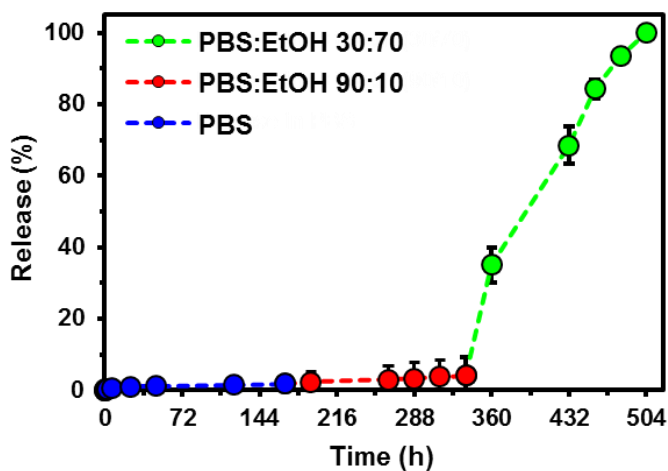
Figure 3.1.11. Drug release from PEDOT/CAM NPs in PBS (first week), PBS:EtOH 90:10 (second week) and PBS:EtOH 30:70 (third week) at 37 °C ($n = 3$).
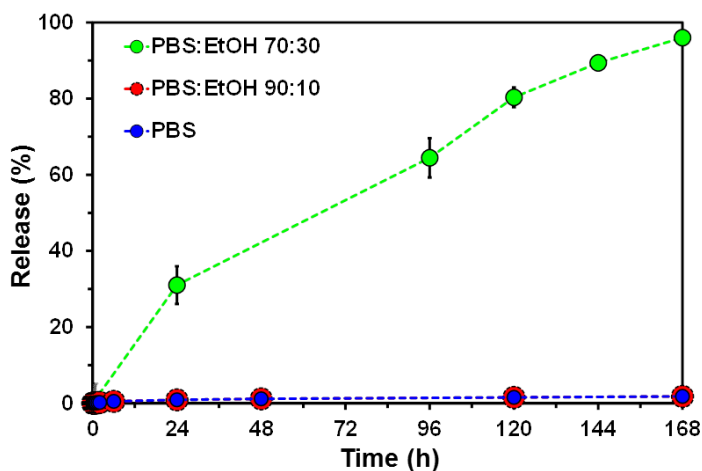
Figure 3.1.12. Drug release profiles from PEDOT/CAM NPs in PBS, PBS:EtOH 90:10 and PBS:EtOH 30:70 at 37 °C. The profiles shown in this graphic have been extracted from those displayed in Figure 3.1.11 by imposing a common starting point: release of 0% at the starting period (t= 0 h) in each environment.

In recent studies, antimicrobial CAM was encapsulated in non-electroresponsive polymeric carriers for release.[40–42] For example, CAM-loaded polycaprolactone (PCL) nanofibers and, especially, PCL-polyethylene oxide (PEO) microfibers exhibited a very fast release in PBS, reaching in 1 h more than

30% and 90%, respectively.[40] The difference between such two systems was attributed to the hydrophobic and hydrophilic nature of PCL and PCL-PEO fibers, respectively. In any case, the strength of the interaction between CAM and such polymers was significantly weaker than with PEDOT. Similarly, the release of CAM loaded in poly(vinyl alcohol)/sodium alginate hydrogels was very high, independently of the ratio between such two polymers, reaching more than 50% in less than 3 h.[41] Likewise, CAM was easily released from both loaded amorphous calcium phosphate (ACP) and hydroxyapatite nanoparticles in the simple physiological PBS medium.[42] Overall, these observations support the strength of CAM···PEDOT interactions.

3.1.3.4   Electrochemical properties

The main objective of this work is to design an implantable therapeutic device to control the progression of bacterial infections by inhibiting and, at the same time, monitoring bacterial growth. Therefore, it is necessary to evaluate the response of PEDOT and PEDOT/CAM NPs to electrical stimuli. It is worth noting that the engineered application requires stable NPs without excessive drug release when monitoring by CV (cyclic voltammetry).

A broad potential window (from –0.50 to 1.40 V) was used to record the cyclic voltammogram of SPCE-PEDOT in a solution of PBS 1× with CAM as supporting electrolyte (**Figure 3.1.13a**). CAM exhibits a well-defined cathodic peak at around –0.4 V that corresponds to the reduction of the nitro group to an amino group, following a four electron and four proton transfer mechanism.[43] The increase of the anodic current at voltages higher than 1 V has been attributed to the production of oxygen and protons due to the oxidation of water molecules.

Cyclic voltammograms recorded for the bare electrode (SPCE), SPCE coated with PEDOT/CAM NPs (SPCE-PEDOT/CAM) and SPCE coated with PEDOT

NPs (SPCE-PEDOT) in PBS are compared in **Figure 3.1.13b**. The area of the voltammogram increases considerably when the carbon SPCE is coated with PEDOT or PEDOT/CAM NPs, evidencing an enhancement of the capacitive behaviour. However, no difference was observed between PEDOT NPs and PEDOT/CAM NPs, suggesting that the amount of CAM is very low (i.e. the drug is released during the potential scan) or that the signal of the drug overlaps with the one of PEDOT NPs. In order to get a deeper understanding on this feature, the effect of the electrical voltage on the drug retention was analysed. More specifically, the release of CAM was investigated applying continuous stimulation by chronoamperometry (CA), keeping constant voltage at 1.00 V, and by CV, ramping the voltage from –0.50 to 0.50 V. In both cases, CA and CV, stimuli were applied for 5, 15 and 30 min. Control experiments (CRTL) were also performed using the same periods of time but without electrical stimulation. Results displayed in **Figure 3.1.13c** indicate that the amount of CAM released from PEDOT/CAM is only ~30% and ~20% higher for CA and CV, respectively, than for the CTRL, meaning that PEDOT/CAM NPs are very stable. Furthermore, comparison of the cyclic voltammograms recorded between –0.50 and 0.50 V after 5, 15 min and 30 min of CV stimulation (**Figure 3.1.13d**) reveals a slight decrease of the current density at the voltage where CAM is reduced. This phenomenon has been attributed to the small amount of drug released.
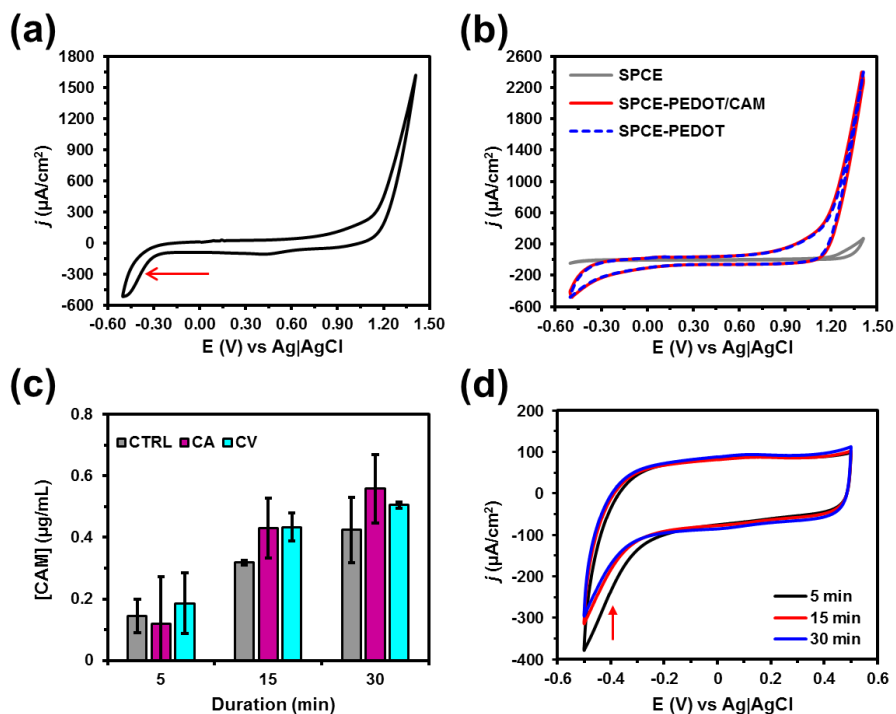
Figure 3.1.13. Cyclic voltammograms recorded from –0.50 to 1.40 V (scan rate: 100 mV/s) for (a) free CAM and (b) comparison of the bare electrode (SPCE) and the coated electrodes (SPCE-PEDOT and SPCE-PEDOT/CAM). (c) CAM release during 5, 15 and 30 min ($n = 3$) without electrical stimulation (CTRL) and with two different types of electrical stimulation CA (1.00 V) and CV (from –0.50 to 0.50 V). (d) Cyclic voltammograms recorded from –0.50 to 0.50 V (scan rate: 100 mV/s) for SPCE-PEDOT/CAM after 5, 15 and 30 min of CV stimulation.

3.1.3.5 *Evaluation of cytotoxicity*

As the proposed application for the PEDOT/CAM NPs is their therapeutic utilization as antibiotic carriers and bacterial growth monitoring, evaluation of the biocompatibility is essential. The influence of the system on in vitro cell viability was investigated using the MTT [3-(4, 5-dimethylthiazol-2-yl)-2, 5-diphenyltetrazolium bromide] assay. Different CAM concentrations were exposed for 24 h to cultures of commercial human bone osteosarcoma MG-63 cell line. **Figure 3.1.14a** shows that the half-inhibitory concentration (IC50) of free CAM for MG-63 is around 350 µg/mL, evidencing that the tolerance of the cells

to this drug is much higher than that found for other drugs, such as CUR (with a IC50 ranging from 10 to 20 µg/mL, depending on the cell line[31]). The biocompatibility of PEDOT and PEDOT/CAM NPs was also evaluated using the MG-63 cell line. **Figure 3.1.14b** shows that cells have a very high tolerance to PEDOT NPs without exhibiting any reduction in cell viability. Instead, the cell viability clearly decreases when high concentrations of PEDOT/CAM NPs are used. In any case, the IC50 of free CAM and PEDOT/CAM NPs for eukaryotic cells is much higher than the dose of antibiotic required to inhibit bacterial growth, as demonstrated below. Thus, antibiotics are much more active against bacteria than against eukaryotic cells, allowing their utilization for the treatment of bacterial infections without damaging the eukaryotic human cells.
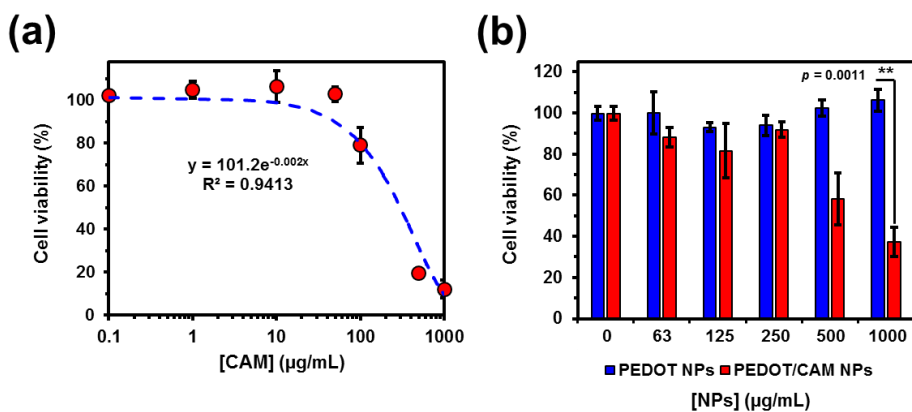
Figure 3.1.14. Dose-dependent viability of MG-63 cells treated with (a) free CAM and (b) PEDOT *vs* PEDOT/CAM NPs (*n* = 3). Statistical comparison of values was based on a 2-way ANOVA using Tukey's test for pair-wise comparison with $p < 0.05$.

3.1.3.6 Bactericidal activity

In order to confirm that the active conformation of CAM was not altered during the synthesis of PEDOT/CAM NPs, the activity of the loaded antibiotic was tested against a representative Gram-negative bacterium (*E. coli*) and a Gram-positive bacterium (*S. sanguinis*). The observed activity was compared with that of the

controls, which were free CAM, free nalidixic acid (NAX; a well-known synthetic quinolone antibiotic) and medium alone. For this purpose, we used the disk diffusion test, which provides qualitative evaluation of the susceptibility of bacteria to the molecules diffusing from the disk.

Results showed in **Figure 3.1.15a** and **b** indicate that free CAM and free NAX are the most effective for inhibiting bacterial growth, followed by PEDOT/CAM NPs. Moreover, the bactericidal activity was slightly higher for *E. coli* than for *S. sanguinis*. Instead, PEDOT NPs do not show any antibacterial behavior. On the other hand, **Figure 3.1.15c** and **d** plots the relative growth rate of *S. sanguinis* and *E. coli* when different amounts of PEDOT/CAM (*i.e.* volumes of 5, 25 and 50 µL from a 10 mg/mL suspension), free CAM, PEDOT NPs (50 µL of a 10 mg/mL suspension) are added to bacteria cultures. The growth rate in the LB medium without any kind of NPs or antibiotic was taken as the control (CTRL). Addition of free CAM to the medium causes a quick and effective inhibition of bacterial growth, whereas the relative growth obtained upon the addition of PEDOT NPs is similar to that of the CTRL. Consistently with images displayed in **Figure 3.1.15a** and **b**, the difference between the absorbance of samples incubated with PEDOT/CAM NPs and the control after 48 h is higher for the *E. coli* than for the *S. sanguinis*. Besides, the inhibition of the bacterial growth caused by the addition of PEDOT/CAM increases with the concentration of antibiotic-loaded NPs in the medium, the most effective inhibition being observed for the volume of 50 µL.
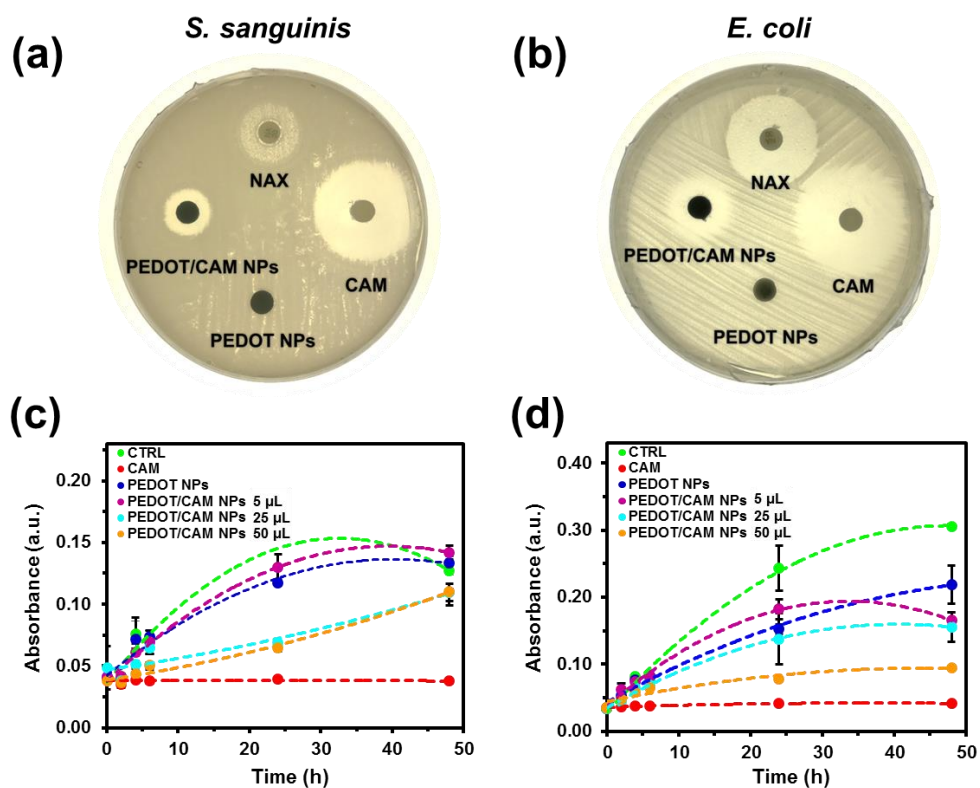
Figure 3.1.15. Bactericidal activity of free CAM, free NAX, PEDOT NPs and PEDOT/CAM NPs against (a, c) *S. sanguinis* and (b, d) *E. coli* bacteria ($n = 3$): (a, b) Inhibition halos observed using the disk diffusion method; and (c, d) growth curves obtained by treating the bacteria cultures with LB medium (CTRL), free CAM, PEDOT NPs and different volumes of PEDOT/CAM NPs (5µL, 25 µL and 50 µL). The error bar is not visible when the standard deviation is smaller than the size of the solid circle used to represent the values.

3.1.3.7   *Monitoring of bacterial growth*

The performance of PEDOT and PEDOT/CAM NPs for real-time electrochemical monitoring of bacterial growth or inhibition is discussed in this section. With the aim of orienting this sensing and release device toward clinical applications, PEDOT and PEDOT/CAM NPs were fixed on SPCEs and Dulbecco's Modified Eagle's Medium (DMEM) with the corresponding bacteria was used as electrolytic media. The electrolytic chambers were kept on an incubator at 37 ºC under mild-agitation and the growth of bacteria was followed

by examining the electrochemical response at different times, which ranged from 0 h (just when the bacteria are introduced into the cell chamber) to 24 h. **Figure 3.1.16a** displays the voltammetric response of the sensor to the culture medium without bacteria at different incubation times. As shown, the variation in the area and the position of the peaks in the voltammograms recorded at different times is negligible ($< 1\%$). Furthermore, the surface of the electrode was not damaged by the cell culture medium. This is proved in **Figure 3.1.16b** and **c**, which display a representative SEM micrograph of PEDOT NPs coated electrodes as prepared and after 24 h in $NaHCO_3^-$ supplemented DMEM without bacteria.
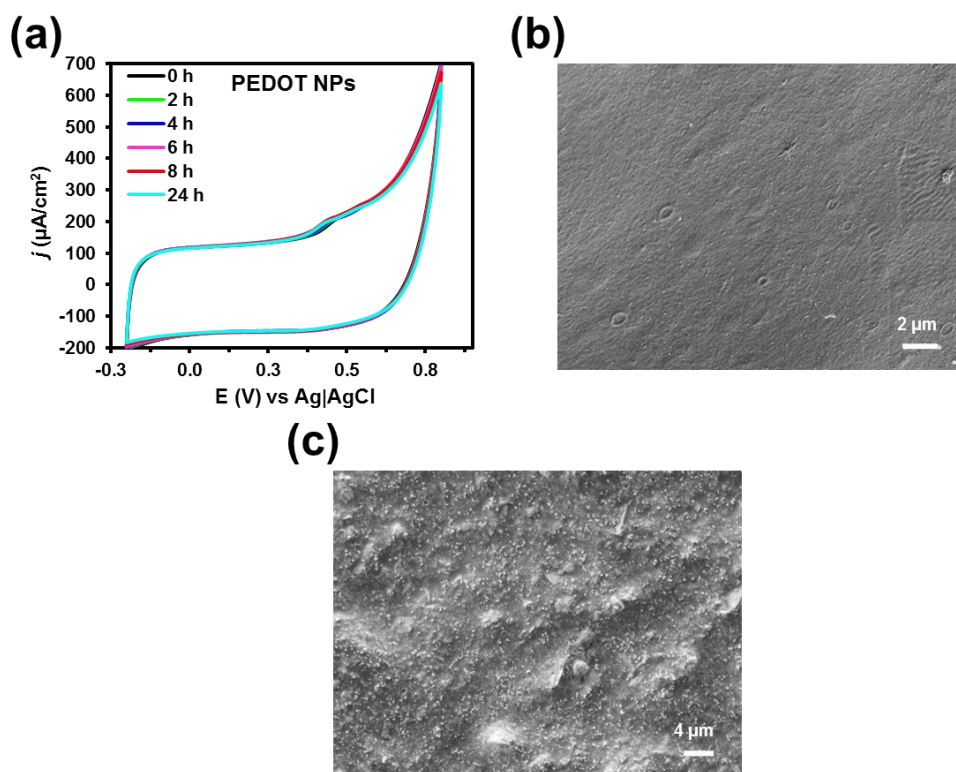
Figure 3.1.16. (a) Cyclic voltammograms of PEDOT NPs, which are coating SPCEs, in the culture medium ($NaHCO_3^-$ supplemented DMEM) recorded at different time intervals (0, 2, 4, 6, 8 and 24 h). (b) Representative SEM micrograph of the SPCE coated with PEDOT NPs after 0 h and 24 h in culture medium.

Cyclic voltammograms recorded during the *S. sanguinis* growth on PEDOT NPs-containing electrodes are displayed in **Figure 3.1.17a**. The small anodic peak at around 0.6 V detected at t= 0 h has been associated to the phenol red present in the cell culture media. Phenol red, which is one of the most common pH indicators and a weak acid, exhibits redox properties through the ionizable part of the quinone methide.[44] The current density of such oxidation peak increases with the incubation time while the potential shifts to higher values, which has been attributed to a reduction of the pH. Thus, bacterial respiration pumps out protons, causing the acidification of the medium with increasing time. Qiao *et al.*[45] reported that the anodic peak related with the oxidation of bacterial metabolites shifts to higher peak potential values with decreasing pH. On the other hand, the increment of current density at the potential peak with the incubation time evidences the presence of other molecules that are oxidizing. This has been related to the increasing concentration of NADH in the electrolytic media due to the bacteria respiration, which oxidizes at around 0.6 V.[15] Another remarkable feature is that the area of the voltammograms increases with the incubation time, which is consistent with previous studies based on the utilization of the metabolism of living microorganisms to generate renewable electrical energy flux.[46]

Comparison with the voltammetric response of PEDOT/CAM NPs against *S. sanguinis*, which is shown in **Figure 3.1.17b**, reveals important differences with respect to PEDOT NPs. More specifically, the peak at around 0.6 V does not shift and the area of the voltammograms does not increase with the incubation time. This has been attributed to the inhibition of bacterial growth by released CAM, as was corroborated by visualizing the electrode surface after the 24 h of culture. The release of CAM after such period of time (24 h) was determined to be of 14.8 ± 0.8 µg/mL, which corresponds to 2.2% ± 0.1 of the loaded drug. Comparison with the release profile obtained in PBS (**Figure 3.1.11**) indicates

that the culture medium (NaHCO$_3^-$ supplemented DMEM), which contains different nutrients (*e.g.* salts, amino acids and vitamins) that affects the chemical and physical properties of the fluid, significantly enhances the CAM release (from 0.9% in PBS to 2.2% in the culture medium). The original DMEM formula composition contains 1000 mg/L of glucose and was first reported for culturing embryonic mouse cells. SEM micrographs of PEDOT and PEDOT/CAM NPs electrode surfaces are shown in **Figure 3.1.17c** and **d**, respectively. The number of bacteria, which are artificially highlighted in orange for easy viewing, is much higher for PEDOT than for PEDOT/CAM.

In order to quantify differences in the bacteria content after 24 h, 50 µL were taken from electrolytic cells containing only culture medium, culture medium with bacteria, and bacteria cultured in the presence of PEDOT and PEDOT/CAM NPs. The observed bacterial growth, which was determined by measuring the absorbance at 600 nm, is represented in **Figure 3.1.17e**. It is worth noting that, after 24 h, the bacterial growth on PEDOT NPs coated electrodes equalled that of the control group, while it was lower than 15 % for PEDOT/CAM NPs.

Figure 3.1.17f plots the change in current density of the main peak at around 0.6 V for the different time intervals relative to the one at 0 h (Δj). It is worth remarking that Δj correlates with bacterial growth. Thus, Δj is smaller than 6 µA/cm^2 when there are no bacteria or when CAM is present in the electrode coating, whereas Δj reaches a value of up to ~16 µA/cm^2 for SPCEs coated with PEDOT NPs (which supports normal bacterial growth as CAM is not present).
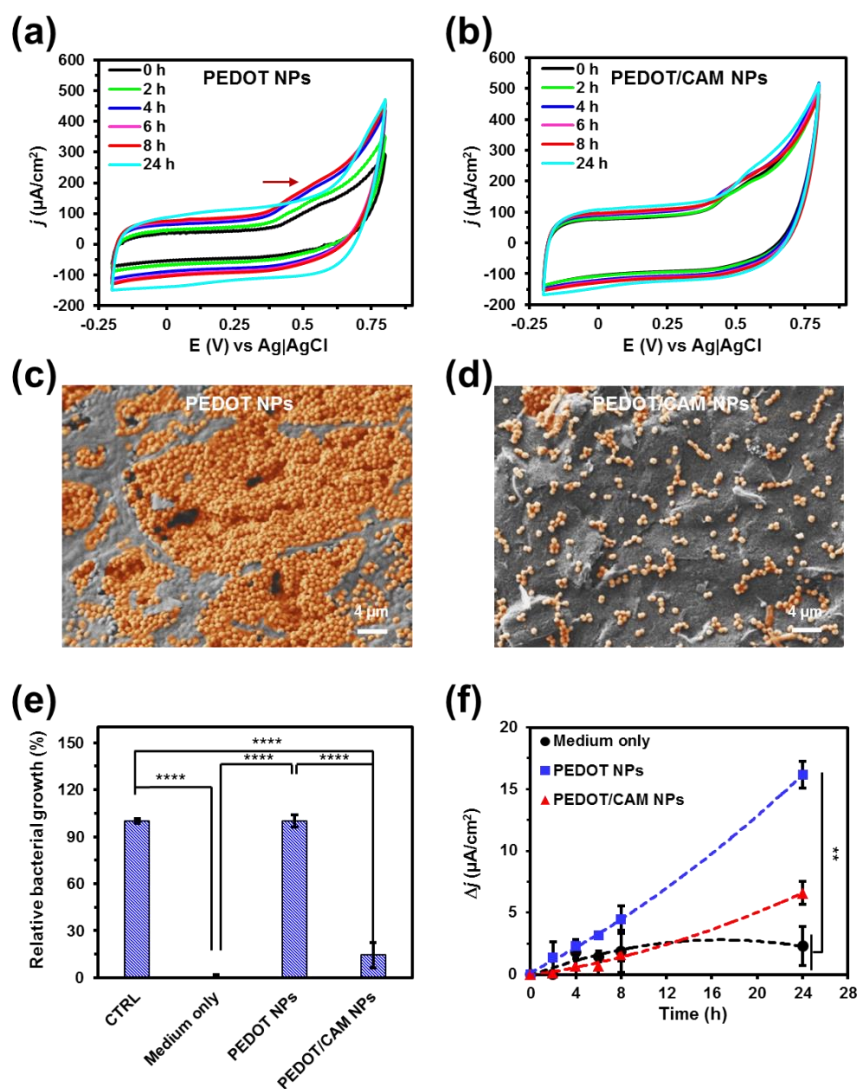
Figure 3.1.17. Cyclic voltammograms for SPCEs coated with (a) PEDOT and (b) PEDOT/CAM NPs recorded at different incubation times (0, 2, 4, 6, 8 and 24 h) in the culture medium (NaHCO$_3^-$ supplemented DMEM) with *S. sanguinis*. Initial and final potentials: −0.20 V; reversal potential: 0.80 V; and scan rate: 100 mV/s. SEM micrograph of the surface of electrodes coated with (c) PEDOT and (d) PEDOT/CAM NPs after 24 h in the presence of *S. sanguinis* (artificially colored in orange). (e) Relative bacterial growth calculated through the variation of the absorbance at 600 nm after 24 h of culture (*n* = 3). (f) Variation in peak current density with the incubation time relative to 0 h for the voltammograms displayed in (a) and (b) (*n* = 3). The statistical comparison of values in (e) and (f) was based on one-way ANOVA with multi-comparison test, with p < 0.0001 (****), p < 0.001 (***), and p < 0.01 (**).

In order to prove that the detection is independent of the type of bacteria, the same set of experiments were conducted for *E. coli* (**Figure 3.1.18**). Interestingly, we observed the same behaviour by CV. The area of the voltammograms recorded for PEDOT NPs increased with the incubation time, while this did not happen for PEDOT/CAM NPs (**Figure 3.1.18a** and **b**). These observations are consistent with SEM micrographs, which display groups of *E. coli* only on the surface of PEDOT NPs-containing electrodes (**Figure 3.1.18c** and **d**). Measurement of the absorbance at 600 nm after 24 h reflected that the relative growth of bacteria was practically zero for PEDOT/CAM NPs (**Figure 3.1.18e**), indicating that the CAM treatment is very effective for *E. coli*. Also, Δj is lower than 2 μA/cm^2 in the absence of bacteria and for bacteria cultured on PEDOT/CAM NPs, whereas a value close to 26 μA/cm^2 was reached for PEDOT NPs (**Figure 3.1.18f**).
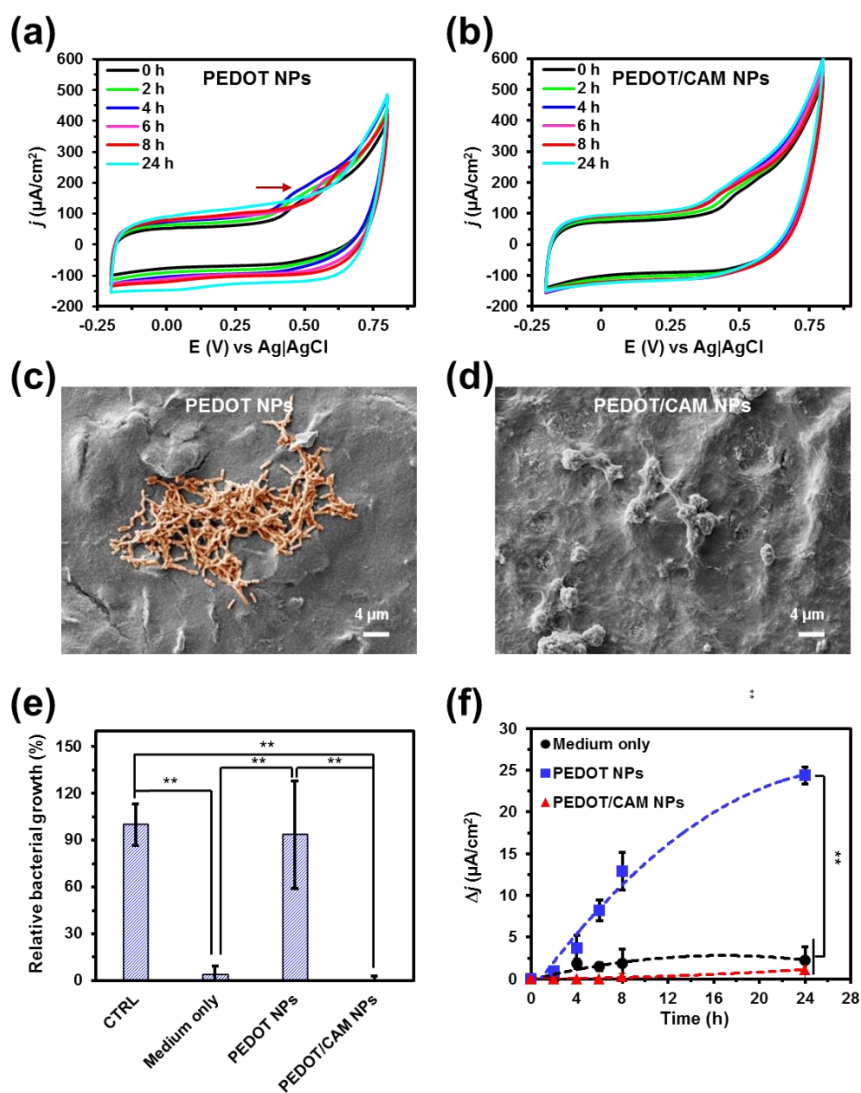
Figure 3.1.18. Cyclic voltammograms for SPCEs coated with (a) PEDOT and (b) PEDOT/CAM NPs recorded at different incubation times (0, 2, 4, 6, 8 and 24 h) in the culture medium (NaHCO$_3^-$ supplemented DMEM) with *E. coli*. Initial and final potentials: −0.20 V; reversal potential: 0.80 V; and scan rate: 100 mV/s. SEM micrograph of the surface of electrodes coated with (c) PEDOT and (d) PEDOT/CAM NPs after 24 h in the presence of *E. coli* (artificially coloured in orange). (e) Relative bacterial growth calculated through the variation of the absorbance at 600 nm after 24 h of culture. (f) Variation in peak current density with the incubation time relative to 0 h for the voltammograms displayed in (a) and (b). The statistical comparison of values in (e) and (f) was based on one-way ANOVA with multi-comparison test, with p < 0.0001 (****), p < 0.001 (***), and p < 0.01 (**).

Results related with bacteria growth and inhibition in the presence of PEDOT and PEDOT/CAM NPs, respectively, are supported by the color of the phenol red-containing medium after 24 h (**Figure 3.1.19**). Thus, the medium in contact with PEDOT NPs exhibited a yellowish color, which was attributed to the acidification induced by the bacterial growth, while the medium in contact with PEDOT/CAM was pink, reflecting a basic pH. Overall, results discussed in this section clearly demonstrate that SPCEs coated with PEDOT and PEDOT/CAM NPs can monitor the bacterial growth and the inhibition of the bacterial growth, respectively, in real time.
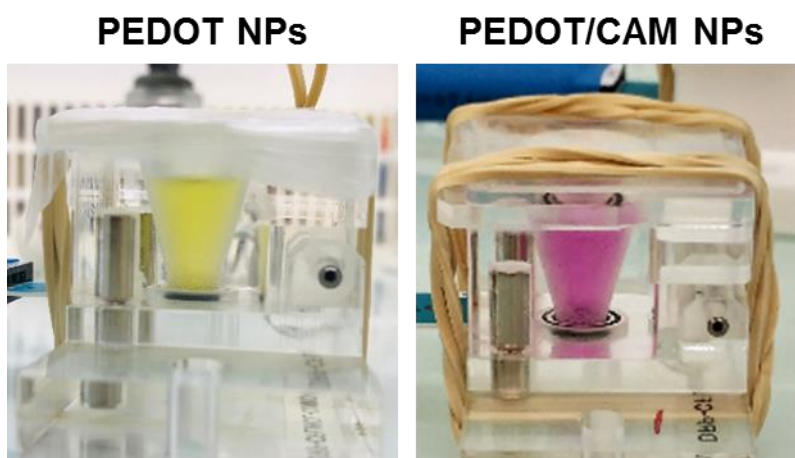
Figure 3.1.19. Color of the cell culture medium, which contains phenol red, after 24 h of bacterial incubation in the presence of PEDOT (left) or PEDOT/CAM NPs (right). The yellowish and pink colors indicate acid and basic pHs, respectively, which are consistent with bacteria growth and inhibition, respectively.

3.1.3.8 NADH detection

The increase in current density in the ~0.6 V potential region, as displayed in **Figure 3.1.17a** and **Figure 3.1.18a**, was related in previous work with the increment of NADH in the bacteria culture medium.[15] Our approach was based on the fact that aerobic respiration reactions in eukaryotic cells occur in the mitochondria, whose double membrane is impermeable to NADH and NAD^+.

Therefore, the NADH level in eukaryotic cells is restricted to the cytosolic pool. Instead, the respiration of bacteria occurs in the cytosol or on the inner surfaces of the cell membrane, which is permeable to NADH and NAD$^+$ and allows their migration to the extracellular space. This inspired us to use the oxidation of extracellular NADH to NAD$^+$ as target for the detection of bacterial growth without interference coming from the proliferation of eukaryotic cells.

In this section, we prove such relationship by measuring the influence of increasing NADH concentrations on cyclic voltammograms recorded for PEDOT NPs coated SPCEs using DMEM (pH 8.5) as electrolytic medium. **Figure 3.1.20a** compares the cyclic voltammograms obtained using a NADH concentration comprised within 0 and 2 mM. In the absence of NADH (0 mM), a small peak is detected at 0.6 V that has been attributed to the redox properties of the phenol red present in the medium, as discussed above. The addition of NADH with concentrations ranging from 250 µM to 2 mM resulted in a significant enhancement of the current density during anodic screening. The NADH oxidation peak is very broad and clearly overlaps with the small peak initially encountered at 0.6 V (*i.e.* the phenol red oxidation peak observed in the absence of NADH). Moreover, **Figure 3.1.20b** demonstrates a linear relationship between the relative increment of the current density and the concentration of NADH.

Another aspect to consider is that, during bacterial growth, the medium undergoes an acidification process. Accordingly, cyclic voltammograms were also recorded using DMEM at pH 6 as electrolytic medium. **Figure 3.1.20c** shows that the well-defined peak coming from the medium, which is centred at 0.62 V, increases with the NADH concentration. Although the potential anodic peak shifts a little bit towards higher values with increasing NADH concentration, the relative increment of the current density exhibits a linear variation (**Figure 3.1.20d**). Overall, this section supports the important role that NADH, one of the main

redox compounds produced by microbial metabolism and released to the medium, plays for *in situ* monitoring the bacterial growth using CV.
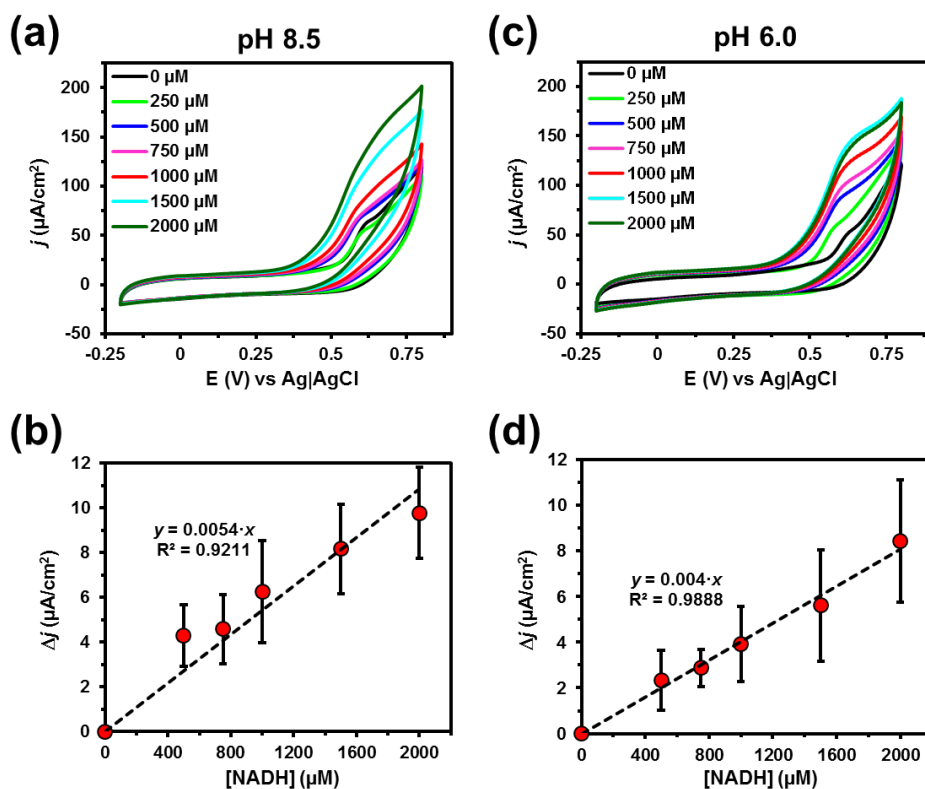
Figure 3.1.20. (a, c) Cyclic voltammograms and (b, d) calibration curves for SPCE coated with PEDOT NPs using cell culture medium at (a) pH 8.5 and (b) pH 6.0 with different NADH concentrations (*n* = 3). Voltammograms were recorded using the following operational conditions: Initial and final potentials: –0.20 V; reversal potential: +0.80 V; and scan rate: 100 mV/s. Calibration curves are expressed as the relative variation of the current density against the NADH concentrations (data taken from voltammograms displayed in (a) and (c)).

3.1.4 Conclusion

In this work, a simple and highly sensitive electrode consisting of CAM-loaded PEDOT NPs has been developed to monitor the inhibition of bacterial growth. More specifically, we have engineered a nanotheranostic system able to sense the infection progression while releasing the antibiotic, inhibiting the *E. coli* and

S. sanguinis growth. After characterization, the drug release was evaluated in hydrophilic media. Although a slow drug release was observed, independently of the presence or not of electrical stimuli (*i.e.* 14.8 ± 0.1 µg/mL of CAM after 24 h in the cell culture medium), the bacterial growth inhibition efficacy of the drug was clearly maintained after its incorporation to the polymeric NPs. Furthermore, we proved that PEDOT and PEDOT/CAM NPs can monitor the increase and inhibition of the bacterial growth, respectively, using CV by detecting the oxidation of NADH at 0.6 V, which diffuses to the extracellular medium after being produced by the bacterial metabolism. This versatility suggests that the developed nanoparticles are a promising theranostic system for the treatment and control of bacterial infections. Thus, we envisage a future with prostheses, implants and other medical devices coated with drug-loaded theranostic nanoparticles informing and reporting pathogenic growth in real time.

3.1.5　References

1.　Amiri, M., Bezaatpour, A., Jafari, H., Boukherroub, R. & Szunerits, S. Electrochemical Methodologies for the Detection of Pathogens. *ACS Sensors* **3**, 1069–1086 (2018).

2.　Monzó, J., Insua, I., Fernandez-Trillo, F. & Rodriguez, P. Fundamentals, achievements and challenges in the electrochemical sensing of pathogens. *Analyst* **140**, 7116–7128 (2015).

3.　Cagliani, R. & Sironi, M. Pathogen-Driven Selection in the Human Genome. *Int. J. Evol. Biol.* **2013**, 1–6 (2013).

4.　Aslam, B. *et al.* Antibiotic resistance: a rundown of a global crisis. *Infect. Drug Resist.* **Volume 11**, 1645–1658 (2018).

5.　Pogue, J. M., Kaye, K. S., Cohen, D. A. & Marchaim, D. Appropriate antimicrobial therapy in the era of multidrug-resistant human pathogens. *Clin. Microbiol. Infect.* **21**, 302–312 (2015).

6.　Simoska, O. & Stevenson, K. J. Electrochemical sensors for rapid diagnosis of pathogens in real time. *Analyst* **144**, 6461–6478 (2019).

7.　Lazcka, O., Campo, F. J. Del & Muñoz, F. X. Pathogen detection: A perspective of traditional methods and biosensors. *Biosens. Bioelectron.* **22**, 1205–1217 (2007).

8.　Wang, L., Lou, Z., Jiang, K. & Shen, G. Bio-Multifunctional Smart Wearable Sensors for Medical Devices. *Adv. Intell. Syst.* **1**, 1900040 (2019).

9.　Rochford, A. E., Carnicer-Lombarte, A., Curto, V. F., Malliaras, G. G. & Barone, D. G. When Bio Meets Technology: Biohybrid Neural Interfaces. *Adv. Mater.* **32**, 1903182 (2020).

10.　Park, J. H. *et al.* Self-powered flexible electronics beyond thermal limits. *Nano Energy* **56**, 531–546 (2019).

11.　Buzid, A. *et al.* Direct and Rapid Electrochemical Detection of Pseudomonas aeruginosa Quorum Signaling Molecules in Bacterial Cultures and Cystic Fibrosis Sputum Samples through Cationic Surfactant-Assisted Membrane Disruption. *ChemElectroChem* **4**, 533–541 (2017).

12.　Sismaet, H. J., Pinto, A. J. & Goluch, E. D. Electrochemical sensors for identifying pyocyanin production in clinical Pseudomonas aeruginosa isolates. *Biosens. Bioelectron.* **97**, 65–69 (2017).

13.　Sedki, M., Hassan, R. Y. A., Hefnawy, A. & El-Sherbiny, I. M. Sensing of bacterial cell viability using nanostructured bioelectrochemical system: rGO-hyperbranched chitosan nanocomposite as a novel microbial sensor platform. *Sensors Actuators B Chem.* **252**, 191–200 (2017).

14.　Butina, K., Löffler, S., Rhen, M. & Richter-Dahlfors, A. Electrochemical sensing of bacteria via secreted redox active compounds using conducting polymers. *Sensors Actuators B Chem.* **297**, 126703 (2019).

15. Molina, B. G., del Valle, L. J., Turon, P., Armelin, E. & Alemán, C. Electrochemical Sensor for Bacterial Metabolism Based on the Detection of NADH by Polythiophene Nanoparticles. *J. Phys. Chem. C* **123**, 22181–22190 (2019).

16. Okamoto, A. *et al.* Cell-secreted Flavins Bound to Membrane Cytochromes Dictate Electron Transfer Reactions to Surfaces with Diverse Charge and pH. *Sci. Rep.* **4**, 5628 (2015).

17. Okamoto, A., Hashimoto, K., Nealson, K. H. & Nakamura, R. Rate enhancement of bacterial extracellular electron transport involves bound flavin semiquinones. *Proc. Natl. Acad. Sci.* **110**, 7856–7861 (2013).

18. Li, D. *et al.* The immobilization of antibiotic-loaded polymeric coatings on osteoarticular Ti implants for the prevention of bone infections. *Biomater. Sci.* **5**, 2337–2346 (2017).

19. King, D. & McGinty, S. Assessing the potential of mathematical modelling in designing drug-releasing orthopaedic implants. *J. Control. Release* **239**, 49–61 (2016).

20. Caplin, J. D. & García, A. J. Implantable antimicrobial biomaterials for local drug delivery in bone infection models. *Acta Biomater.* **93**, 2–11 (2019).

21. Esrafilzadeh, D., Razal, J. M., Moulton, S. E., Stewart, E. M. & Wallace, G. G. Multifunctional conducting fibres with electrically controlled release of ciprofloxacin. *J. Control. Release* **169**, 313–320 (2013).

22. Anirudhan, T. S. & Mohan, A. M. Novel pH sensitive dual drug loaded-gelatin methacrylate/methacrylic acid hydrogel for the controlled release of antibiotics. *Int. J. Biol. Macromol.* **110**, 167–178 (2018).

23. Hoque, J., Bhattacharjee, B., Prakash, R. G., Paramanandham, K. & Haldar, J. Dual Function Injectable Hydrogel for Controlled Release of Antibiotic and Local Antibacterial Therapy. *Biomacromolecules* **19**, 267–278 (2018).

24. Xaplanteri, M. A. Effect of polyamines on the inhibition of peptidyltransferase by antibiotics: revisiting the mechanism of chloramphenicol action. *Nucleic Acids Res.* **31**, 5074–5083 (2003).

25. Polacek, N. *et al.* The Critical Role of the Universally Conserved A2602 of 23S Ribosomal RNA in the Release of the Nascent Peptide during Translation Termination. *Mol. Cell* **11**, 103–112 (2003).

26. Donahue, M. J. *et al.* Tailoring PEDOT properties for applications in bioelectronics. *Mater. Sci. Eng. R Reports* **140**, 100546 (2020).

27. Groenendaal, L., Zotti, G., Aubert, P.-H., Waybright, S. M. & Reynolds, J. R. Electrochemistry of Poly(3,4-alkylenedioxythiophene) Derivatives. *Adv. Mater.* **15**, 855–879 (2003).

28. Aradilla, D., Estrany, F. & Alemán, C. Symmetric Supercapacitors Based on Multilayers of

103

Conducting Polymers. *J. Phys. Chem. C* **115**, 8430–8438 (2011).

29. Kirchmeyer, S. & Reuter, K. Scientific importance, properties and growing applications of poly(3,4-ethylenedioxythiophene). *J. Mater. Chem.* **15**, 2077 (2005).

30. Fabregat, G. *et al.* Incorporation of a Clot-Binding Peptide into Polythiophene: Properties of Composites for Biomedical Applications. *ACS Appl. Mater. Interfaces* **6**, 11940–11954 (2014).

31. Puiggalí-Jou, A., Micheletti, P., Estrany, F., del Valle, L. J. & Alemán, C. Electrostimulated Release of Neutral Drugs from Polythiophene Nanoparticles: Smart Regulation of Drug-Polymer Interactions. *Adv. Healthc. Mater.* **6**, 1700453 (2017).

32. Puiggalí-Jou, A., del Valle, L. J. & Alemán, C. Encapsulation and Storage of Therapeutic Fibrin-Homing Peptides using Conducting Polymer Nanoparticles for Programmed Release by Electrical Stimulation. *ACS Biomater. Sci. Eng.* **6**, 2135–2145 (2020).

33. Rivas, M. *et al.* Loading of Antibiotic into Biocoated Hydroxyapatite Nanoparticles: Smart Antitumor Platforms with Regulated Release. *ACS Biomater. Sci. Eng.* **4**, 3234–3245 (2018).

34. Khan, M. A. *et al.* Surface characterization of poly(3,4-ethylenedioxythiophene)-coated latexes by X-ray photoelectron spectroscopy. *Langmuir* **16**, 4171–4179 (2000).

35. Zotti, G. *et al.* Electrochemical and XPS Studies toward the Role of Monomeric and Polymeric Sulfonate Counterions in the Synthesis, Composition, and Properties of Poly(3,4-ethylenedioxythiophene). *Macromolecules* **36**, 3337–3344 (2003).

36. Aradilla, D. *et al.* Poly(3,4-ethylenedioxythiophene) on self-assembled alkanethiol monolayers for corrosion protection. *Polym. Chem.* **2**, 2548 (2011).

37. Taffarel, S. R. & Rubio, J. Adsorption of sodium dodecyl benzene sulfonate from aqueous solution using a modified natural zeolite with CTAB. *Miner. Eng.* **23**, 771–779 (2010).

38. Cao, X. *et al.* Preliminary study on the electrocatalytic performance of an iron biochar catalyst prepared from iron-enriched plants. *J. Environ. Sci.* **88**, 81–89 (2020).

39. Sakmeche, N. *et al.* Improvement of the Electrosynthesis and Physicochemical Properties of Poly(3,4-ethylenedioxythiophene) Using a Sodium Dodecyl Sulfate Micellar Aqueous Medium. *Langmuir* **15**, 2566–2574 (1999).

40. Preem *et al.* Monitoring of Antimicrobial Drug Chloramphenicol Release from Electrospun Nano- and Microfiber Mats using UV Imaging and Bacterial Bioreporters. *Pharmaceutics* **11**, 487 (2019).

41. Xie, L., Wei, H., Kou, L., Ren, L. & Zhou, J. Antibiotic drug release behavior of poly (vinyl alcohol)/sodium alginate hydrogels. *Materwiss. Werksttech.* **51**, 850–855 (2020).

104

42. Rivas, M. *et al.* Incorporation of Chloramphenicol Loaded Hydroxyapatite Nanoparticles into Polylactide. *Int. J. Mol. Sci.* **20**, 5056 (2019).

43. Chuanuwatanakul, S., Chailapakul, O. & Motomizu, S. Electrochemical Analysis of Chloramphenicol Using Boron-doped Diamond Electrode Applied to a Flow-Injection System. *Anal. Sci.* **24**, 493–498 (2008).

44. Hsieh, M.-T. & Whang, T.-J. Mechanistic investigation on the electropolymerization of phenol red by cyclic voltammetry and the catalytic reactions toward acetaminophen and dopamine using poly(phenol red)-modified GCE. *J. Electroanal. Chem.* **795**, 130–140 (2017).

45. Qiao, Y., Li, C. M., Bao, S.-J., Lu, Z. & Hong, Y. Direct electrochemistry and electrocatalytic mechanism of evolved Escherichia coli cells in microbial fuel cells. *Chem. Commun.* 1290 (2008) doi:10.1039/b719955d.

46. Huang, Y.-X. *et al.* Graphene oxide nanoribbons greatly enhance extracellular electron transfer in bio-electrochemical systems. *Chem. Commun.* **47**, 5795 (2011).

105

3.2 Conducting polymer nanoparticles for voltage-controlled release of pharmacological chaperones

Pharmacological chaperones (PCs) are low molecular weight chemical molecules used for patients with some rare diseases caused primarily by protein instability. Controlled and on-demand release of PCs through nanoparticles is an alternative for cases in which long treatments are needed and prolonged oral administration could have adverse effects. In this work, pyrimethamine (PYR), which is a potent PC consisting on a pyrimidine-2,4-diamine substituted at position 5 by a *p*-chlorophenyl group and at position 6 by an ethyl group, has been successfully loaded in electroresponsive poly(3,4-ethylenedioxythiophene) nanoparticles (PEDOT NPs). The PYR-loading capacity was of 11.4 ± 1.5 %, both loaded and unloaded PEDOT NPs exhibiting similar size (215 ± 3 and 203 ± 1 nm, respectively) and net surface charge (-26 ± 7 and -29 ± 6 mV, respectively). In the absence of electrical stimulus, the release of the PC from loaded NPs is very low (1.6% in 24 h and 18% in 80 days) in aqueous environments. Instead, electrical stimuli sustained for 30 min enhanced the release of PYR, which was of ~50% when the voltage was scanned from -0.5 V to 0.5 V (cyclic voltammetry) and of ~35% when a constant voltage of 1.0 V was applied (chronoamperometry).

3.2.1 Introduction

Pharmacological chaperones (PCs) are small molecular weight drugs that are used when the primary cause of a disease is the instability of a particular protein. The hallmark of PCs is their ability to bind and stabilize their target proteins.[1–6] Although the use of PCs is considered a potential therapeutic strategy for the treatment of conformational diseases (i.e. those caused by structurally abnormal proteins that cannot fold properly and achieve their native conformation), the administration of too high doses by oral or intravenous routes can be sometimes counterproductive due to the inhibition of the target protein.[7–9] In those cases, special dosing regimens must be envisaged to maximize their stabilizing activity and minimize their inhibitory activity. Within this context, encapsulation of PCs in scaffolds for local delivery may be needed to control the effective drug distribution, the therapeutic dosing and the adverse effects of systemic drug administration.

Controlled delivery of PCs can be proposed using two very different release models. The sustained release model (i.e. without on/off control), which was firstly introduced in the sixties,[10] is based on the delivery at a programmed rate for a prolonged period of time. This model, which is controlled by the encapsulating scaffold, presents some limitations since sustained release systems are not responsive enough to the dynamic behaviour of biological systems, changes in the surrounding environment (i.e. pH, temperature, ionic strength) causing undesired effects in their performance.[11,12] The second model is based on the utilization of novel materials and modern fabrication technologies for the preparation of robust drug-loaded systems for on-demand delivery by changing the environment through external stimuli.[13] The on demand release model allows to regulate the delivery rate according to the patient needs, enabling non-uniform drug administration when it is

beneficial.[14] Accordingly, the on-demand delivery model seems very appropriated for controlling the effective PC distribution, the therapeutic dosing and the adverse effects of systemic administration.

Despite the potential clinical interest of PCs, the encapsulation and release of these small ligands in smart carriers have been scarcely investigated,[15–17] while their on-demand release using external stimuli (e.g. UV- and visible light, pH and electric voltage) remains completely unexplored. Pyrimethamine (PYR; **Figure 3.2.1**) is a synthetic derivative of ethyl-pyrimidine with potent PC properties for GM2 gangliosidosis, which is a neurodegenerative disorder caused by a deficiency of lysosomal β-hexosaminidase (β-hex).[18–20] Thus, some mutants of this enzyme show decreased folding stability and cause adult onset form of lysosomal storage diseases, while PYR stabilizes such mutants sufficiently to allow more β-hex to reach the lysosome. In addition, PYR, which is commercialized under the trade name Daraprim®, is an antiparasitic drug against infections caused by protozoan parasites (e.g. malaria and toxoplasmosis)[21–24] and is a potent pro-apoptotic inducer in cancer cells (e.g. in metastatic melanoma cells).[25–27]
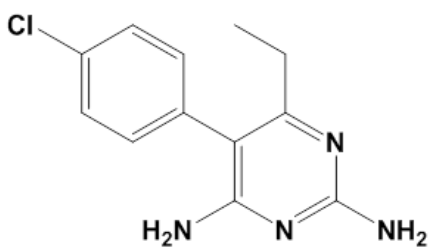
Figure 3.2.1. Chemical structure of PYR.

Despite their pharmacological interest, studies on the release of PYR from drug carriers are very scarce.[16,17,28] In an early study, Vandamme and Heller[16] prepared PYR-containing implants using bioerodible poly(ortho esters), releasing the drug by regulating the concentration of suberic acid. More

recently, Lin and coworkers[28] prepared PYR solid dispersions with different carriers to achieve release at gastric pH (~1-2). Finally, in a very recent work, Mollania and coworkers[17] prepared PYR-loaded carbon nanotubes (CNT/PYR), even though no controlled release was achieved in such study.

Conducting polymers are a special class of polymeric materials with conjugated structure, which exhibits both electronic and ionic conductivity through the mobility of electronic charge carriers (i.e. polarons and bipolarons) and ionic dopant agents, respectively.[29] Besides, the redox properties of conducting polymers are responsible for their intense electrochemical response. Due to their conducting and electrochemical properties, these materials have been used as carriers for on-demand drug release, which is controlled through externally applied voltage bias.[30] Among conducting polymers, poly(3,4-ethylenedioxythiophene) (PEDOT) has drawn the most attention due to its superior capacitive performance, high conductivity, stability in aqueous media and ambient conditions, and biocompatibility.[31–34] In recent years, PEDOT nanoparticles (NPs) have been successfully used to encapsulate different types of anticarcinogenic and antimicrobial drugs (e.g. peptides and highly hydrophobic compounds).[35–37]

Herein, we describe for the first time the encapsulation and controlled release of a representative PC of therapeutic interest, PYR, in electro-responsive polymeric nanoparticles (NPs). It should be remarked that, in general, the encapsulation of drugs of small molecular size and bearing hydrophilic groups, such as the amino groups of PYR (**Figure 3.2.1**), is challenging and problematic due to the rapid loss of drug to the external medium. For this study, PEDOT NPs have been used as carriers for the *in situ* encapsulation of PYR due to the capacity of this conducting polymer to interact with hydrophylic groups, hindering a fast release. After

characterization of the loaded PEDOT NPs, hereafter named PEDOT/PYR NPs, the release of the drug by simple diffusion (i.e. in the absence of external stimuli) and by imposing sustained electrostimulation was examined. Results showed that low release observed in the absence of stimuli can be significantly increased when the strength of PEDOT···PYR interactions is modulated by applying electrical stimuli through a potentiodynamic technique.

3.2.2   Methods

3.2.2.1   *Synthesis of unloaded poly(3,4-ethylenedioxythiophene) nanoparticles (PEDOT NPs)*

A 30 mL Corex tube was filled with 15.8 mL of milli-Q water. After this, 96 µL of dodecyl benzenesulfonic acid (DBSA) was added and the solution was stirred for 1 h using a magnetic stirrer set at 750 rpm at 40 °C and protected from light with aluminum foil. Next, 72 µL of 3,4-ethylenedioxythiophene (EDOT) monomer and 2 mL of methanol were slowly added. The mixture was allowed to stir for 1 h at 750 rpm at 40 °C. Finally, 0.73 mg of ammonium persulfate (APS) dissolved in 2 mL of milli-Q water were added drop by drop while stirring. The reaction was maintained in agitation at 40 ºC overnight. In this process, the color of the reaction mixture changed from light grey to dark blue. No sedimentation was observed after the reaction occurred, reflecting a good colloidal stability. The side products and unreacted chemicals were removed by a sequence of three centrifugations at 11000 rpm for 40 min at 4 ºC. After each centrifugation, the resulting supernatants were decanted and the pellet was dispersed in 15 mL of deionized water by using a vortex and a sonication bath (15 min at room temperature). The last pellet was left under vacuum in the same tube for two days, then

weighted and dispersed in the corresponding medium at the desired concentration.

3.2.2.2 *Synthesis of pyrimethamine (PYR)-loaded PEDOT NPs (PEDOT/PYR NPs)*

96 µL of DBSA were added to a 30 mL tube filled with 15.8 mL of milli-Q water and the solution was stirred for 1 h at 750 rpm at 40 °C. After this, 72 µL of EDOT and 2 mL of drug solution (8 mg/mL PYR in methanol) were added drop by drop while stirring and the resulting solution was stirred at 750 rpm at 40 °C during 1 h. Finally, 0.73 mg of APS dissolved in 2 mL of milli-Q water was added to the mixture. The reaction was protected from light (aluminum foil) and maintained in agitation at 40 ºC overnight. The color of the reaction mixture changed from light grey to dark blue. No sedimentation was observed after the reaction occurred, indicating good colloidal stability. The side products, extra drug and unreacted chemicals were removed by a sequence of 3 centrifugations at 11000 rpm for 40 min at 4 ºC. The resulting supernatants were decanted and the pellet was re-dispersed in deionized water by using a vortex and a sonic bath (15 min at room temperature). The last pellet was left under vacuum for two days, then weighted and re-dispersed in the corresponding medium at the desired concentration.

3.2.2.3 *Determination of the PYR loading ratio*

The drug content was determined by taking 10 µL of PEDOT/PYR NPs suspension (10 mg/mL NPs in milli-Q water) into 990 µL of methanol (PYR solvent). The suspension was sonicated and vortexed for 10 min, leading to a complete drug release in the alcoholic medium. Then, the NPs dispersion was centrifuged with a micro-centrifuge for 15 min at 2500 rpm. Finally, the

supernatant was evaluated using UV-Vis spectroscopy. The calibration curve was prepared with the drug dissolved in methanol and read at 280 nm (**Figure 3.2.2**). The same procedure was applied to determine the drug released during the dialysis or after the electrical stimuli assays.

The loading capacity (LC, in %) was calculated using the following equation:

$$LC = \frac{(W_i - W_f)}{W_{NPs}} \times 100$$

Equation 3.2.1. The loading capacity percentage, where W_i indicates PYR initial mass, W_f PYR final mass, and W_{NPs} total NPs mass.

Thus, the weight of PYR entrapped was determined by subtracting the weight of the total PYR fed (the drug introduced in the solution for the synthesis of PEDOT/PYR NPs) from the weight of the non-encapsulated drug or free drug (drug remaining in the supernatant after the synthesis of PEDOT/PYR NPs). The amount of the free PYR in the supernatant was determined by measuring the absorbance at 280 nm.
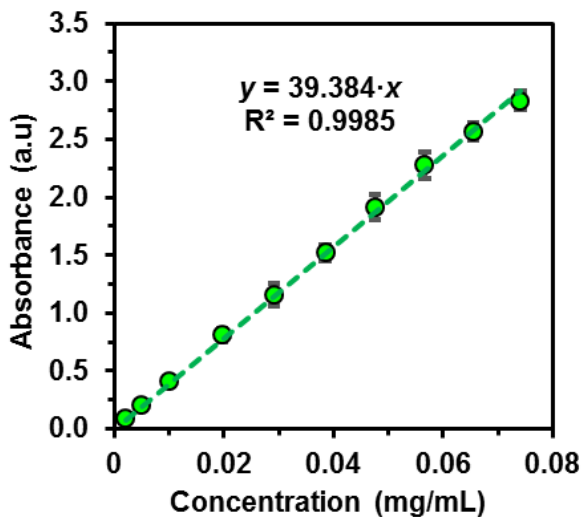
Figure 3.2.2. Calibration curve for PYR in methanol.

3.2.2.4   UV-Vis spectroscopy

UV analyses were performed using a Cary100 UV-Vis spectrophotometer controlled by the UVProbe 2.31 software.

3.2.2.5   Dynamic light scattering (DLS)

DLS studies were performed using NanoBrook Omni Zeta Potential Analyzer from Brookheaven Instruments. Measurement consisted of 3 runs of 120 s duration each one, which were averaged to obtain the effective diameter. Samples were analyzed at 25 ºC using a scattering angle of 90º. In order to know the zeta (ζ)-potential, particles were re-suspended in 1 mM KCl solution and 30 consecutive measurements were taken of each sample.

3.2.2.6 *Fourier transform infrared (FTIR) spectroscopy*

FTIR transmittance spectra were recorded on a FTIR Jasco 4100 spectrophotometer. Samples were deposited on an attenuated total reflection accessory (Top-plate) with a diamond crystal (Specac model MKII Golden Gate Heated Single Reflection Diamond ATR). For each sample, 64 scans were performed between 4000 and 600 cm^{-1} with a resolution of 4 cm^{-1}.

3.2.2.7 *RAMAN spectroscopy*

Micro-Raman spectroscopy assays were performed using a commercial Renishaw inVia Qontor confocal Raman microscope. The Raman setup consisted of a laser (785 nm with a nominal 300 mW output power) directed through a microscope (specially adapted Leica DM2700 M microscope) to the sample, after which the scattered light is collected and directed to a spectrometer with a 1200 lines·mm^{-1} grating. The exposure time was 10 s, the laser power was adjusted to 0.001-0.05% of its nominal output power, depending on the sample, and each spectrum was collected with 30 accumulations.

3.2.2.8 *X-ray photoelectron spectroscopy (XPS)*

XPS analyses were performed in a SPECS system equipped with a high intensity twin-anode X-ray source XR50 of Mg / Al (1253 eV / 1487 eV) operating at 150 W, placed perpendicular to the analyzer axis, and using a Phoibos 150 MCD-9 XP detector. The X-ray spot size was 650 µm. The pass energy was set to 25 and 0.1 eV for the survey and the narrow scans, respectively. Charge compensation was achieved with a combination of electron and argon ion flood guns. The energy and emission current of the

electrons were 4 eV and 0.35 mA, respectively. For the argon gun, the energy and the emission current were 0 eV and 0.1 mA, respectively. The spectra were recorded with pass energy of 25 eV in 0.1 eV steps at a pressure below 6×10^{-9} mbar. These standard conditions of charge compensation resulted in a negative but perfectly uniform static charge. The C 1s peak was used as an internal reference with a binding energy of 284.8 eV. The surface composition was determined using the manufacturer's sensitivity factors.

3.2.2.9 *Scanning electron microscopy (SEM)*

The morphology of the PEDOT/PYR and PEDOT NPs was studied by SEM. Micrographs were obtained using a Focused Ion Beam Zeiss Neon 40 scanning electron microscope operating at 5 kV. Samples were mounted on a double-side adhesive carbon disc and sputter-coated with a thin layer of carbon to prevent sample charging problems.

3.2.2.10 *Atomic force microscopy (AFM)*

AFM studies were conducted to obtain topographic images of the NPs surface using silicon TAP 150-G probe (Budget Sensors, Bulgaria) with a frequency of 150 kHz and a force constant of 5 N/m. Images were obtained with a Molecular Imaging PicoSPM microscope using a NanoScope IV controller under ambient conditions in tapping mode. AFM measurements were performed on various parts of the samples, which produced reproducible images similar to those displayed in this work.

3.2.2.11 Electrochemical characterization

Electrochemical characterization was performed by cyclic voltammetry (CV) using an Autolab PGSTAT302N Galvano stat equipped with the ECD module (Ecochimie, The Netherlands). Measurements were performed on 15 µL of 10 mg/mL NPs solution dried on a screen printed carbon electrode (SPCE; 4 mm diameter) coated with chitosan. For this purpose, three rounds of 5 µl of the 10 mg/ml NPs solution were placed on the SPCE and dried under the hood after each round. Then, dried NPs were covered with 5 µL of chitosan solution (20 mg/mL chitosan in 0.1 M HCl) and dried again. All electrochemical assays were performed using a three-electrode one compartment cell at room temperature. The cell was filled with 1.5 mL of phosphate buffered saline (PBS) solution 1× as a supporting electrolyte. A covered or bare SPCE was used as the working electrode, platinum as the counter electrode, while an Ag|AgCl electrode containing a KCl saturated aqueous solution was the reference electrode (offset potential versus the standard hydrogen electrode, $E° = 0.222$ V at 25 °C). Oxidation-reduction cycles were registered within the potential range of −0.5 to +1.4 V at a scan rate of 100 mV/s.

3.2.2.12 Drug release

25 µL of PEDOT/PYR NPs (10 mg/mL) were deposited into a 30 µL dialysis button, covered by a 3.5 kDa MWCO (Molecular Weight Cut-Off) dialysis membrane, immersed in 1.5 mL of PBS (pH 7.4) and kept in a shaker at 37 ℃ at 80 rpm. Each day all the immersion solution was taken out to quantify the released drug and the solution was replaced by 1.5 mL of new media. For the first experiment, the release process was evaluated for 80 days in PBS solution. For the second experiment, instead, the releasing media was

weekly changed from hydrophilic to hydrophobic during three weeks by adding ethanol (EtOH) to PBS. More specifically, for the first, second and third week the release was evaluated in PBS alone, 90:10 PBS:EtOH and 30:70 PBS:EtOH, respectively. In order to compare the kinetics of the release process, results were normalized by the total amount of PYR encapsulated within the NPs or used as a free drug. The amount of released drug was evaluated by UV spectroscopy. Calibration curves were obtained by plotting the absorbance measured at 280 nm against the PYR concentration. All drug release tests were carried out using at least three replicas and the average was plotted.

3.2.2.13 Electrical stimulation for PYR release

Washed PEDOT/PYT NPs were re-suspended in milli-Q water to have a final concentration of 10 mg/mL. Then, NPs were placed on SPCEs and covered with chitosan, as described above. A three electrode configuration was used: the SPCE coated with the corresponding NPs as a working electrode, platinum as counter electrode, and Ag│AgCl as reference electrode. 1.5 mL of PBS 1× was used as electrolytic medium. The appropriate voltage was applied for a particular period of time. After the electrical stimulation, the medium was removed to determine the concentration of released PYR and substituted by fresh medium. The absorbance was measured at 280 nm. The influence of the time was evaluated by applying a constant voltage of 1.00 V and CV from -0.5 V to 0.5 V during 5, 15 and 30 min. A control experiment was performed in the absence of the stimulus to compare the results. All the measures were repeated at least three times and the average with the corresponding standard deviation were represented in the graphs.

3.2.2.14 Cytotoxicity evaluation

In vitro cytotoxicity evaluation of free PYR, PEDOT NPs, and PEDOT/PYR NPs for MG-63 cell line was determined by the MTT assay. Free PYR was dissolved in methanol and then diluted in ethanol (the final concentration of ethanol in cell media was smaller than 10 %). All the other substances were prepared in milli-Q water. Cells were seeded at a density of 20×10^4 cells per well (100 µL each) in 96-well plates and incubated overnight. Subsequently, cells were exposed to a series of increasing free PYR, PEDOT NPs, and PEDOT/PYR NPs concentrations. Free PYR concentrations were 0.1, 1, 10, 50, 100, 500 and 1000 µg/mL, whereas PEDOT and PEDOT/PYR NPs concentrations were 0.0655, 0.125, 0.25, 0.5 and 1 mg/mL. Cells were incubated with the treatment for 24 h. Next day, the percentage of viable cells relative to untreated control was determined on the basis of the mitochondrial conversion of 3-(4,5-dimethylthiazol-2-yl)-2,5-diphenyltetrazolium bromide to formazan. The results were expressed as mean value ± standard deviation (SD). All the experiments were performed in triplicate. Statistical comparison of values was based on a 2-way ANOVA using Tukey's test for pair-wise comparison with $p < 0.05$.

3.2.3   Results and discussion

3.2.3.1   Pyrimethamine encapsulation

PEDOT/PYR NPs and unloaded PEDOT NPs (control) were prepared through emulsion polymerization in a 12.5% methanol-containing aqueous medium. Methanol was used to solubilize PYR (8 mg/mL), which is poorly soluble in water. Ammonium persulfate (APS) was employed as oxidizing agent and dodecyl benzenesulfonic acid (DBSA) as both anionic surfactant

(*i.e.* forming micelles) and dopant (*i.e.* stabilizing the formed PEDOT chains in their oxidized form). Due to the latter role, DBSA becomes a stable part of the NPs structure. The procedure used to prepare control PEDOT NPs was identical with the only exception that PYR was not incorporated into the methanol added to the aqueous monomer solution.

The FTIR spectra of free PYR, PEDOT/PYR NPs and PEDOT NPs are compared in **Figure 3.2.3a**. Free PYR exhibits broad and weak bands at 3443 and 3261 cm^{-1} (symmetrical and asymmetrical stretching of the –NH$_2$ group), a sharp and weak peak at 3073 cm^{-1} (C–H stretching from the aromatic ring), sharp and intense peaks between 1681 and 1409 (stretching vibrations of C=N and C=C from the aromatic rings), as well as at 1339 and 1243 cm^{-1} (C–H from CH$_3$ and C–N, respectively). On the other hand, PEDOT NPs show the characteristic FTIR peaks of PEDOT chains, which appear at 1648 and 1473 cm^{-1} (C=C stretching), 1351 cm^{-1} (C−C stretching), 1220 and 1061 cm^{-1} (C−O−C vibrations) and 842 cm^{-1} (stretch of the C−S bond in the thiophene ring). Also, weak but clearly defined bands attributed to DBSA dopant molecules were detected at 2923 and 2856 cm^{-1} (aliphatic −CH$_2$ and −CH$_3$ stretching), and 1693 cm^{-1} (C=C stretching from the phenyl ring). Finally, PEDOT/PYR NPs present mostly the bands associated with both PEDOT NPs and free PYR, as the–NH$_2$ group and the C=N stretching vibration.

Table 3.2.1. Atomic composition calculated from the XPS spectra for PEDOT and PEDOT/PYR NPs.

	C 1s	N 1s	O 1s	S 2p
PEDOT NPs	45.17	-	53.58	1.25
PEDOT/PYR NPs	67.89	0.56	30.34	1.21

Despite the successful identification of the loaded PC by FTIR, PEDOT/PYR NPs were complementarily studied by Raman spectroscopy and X-ray photoelectron spectroscopy (XPS). Unfortunately, the former technique was not conclusive since the spectrum of PEDOT/PYR NPs was dominated by the fingerprints of PEDOT NP (**Figure 3.2.4**), which was attributed to the strong absorbance of PEDOT chains. Although the interpretation of the obtained values is not simple due to the presence of DBSA as dopant agent, it is worth noting that N 1s is only detected for PEDOT/PYR NPs (**Table 3.2.1** and **Figure 3.2.5**), supporting the successful loading of the PC. On the other hand, **Figure 3.2.3b** and **c** display the high-resolution XPS spectrum in the N 1s region for PEDOT and PEDOT/PYR NPs. The nitrogen peak appears at 399.9 eV for PEDOT/PYR, which has been attributed to N−H and C−N from PYR.

(a)

(b)

(c)
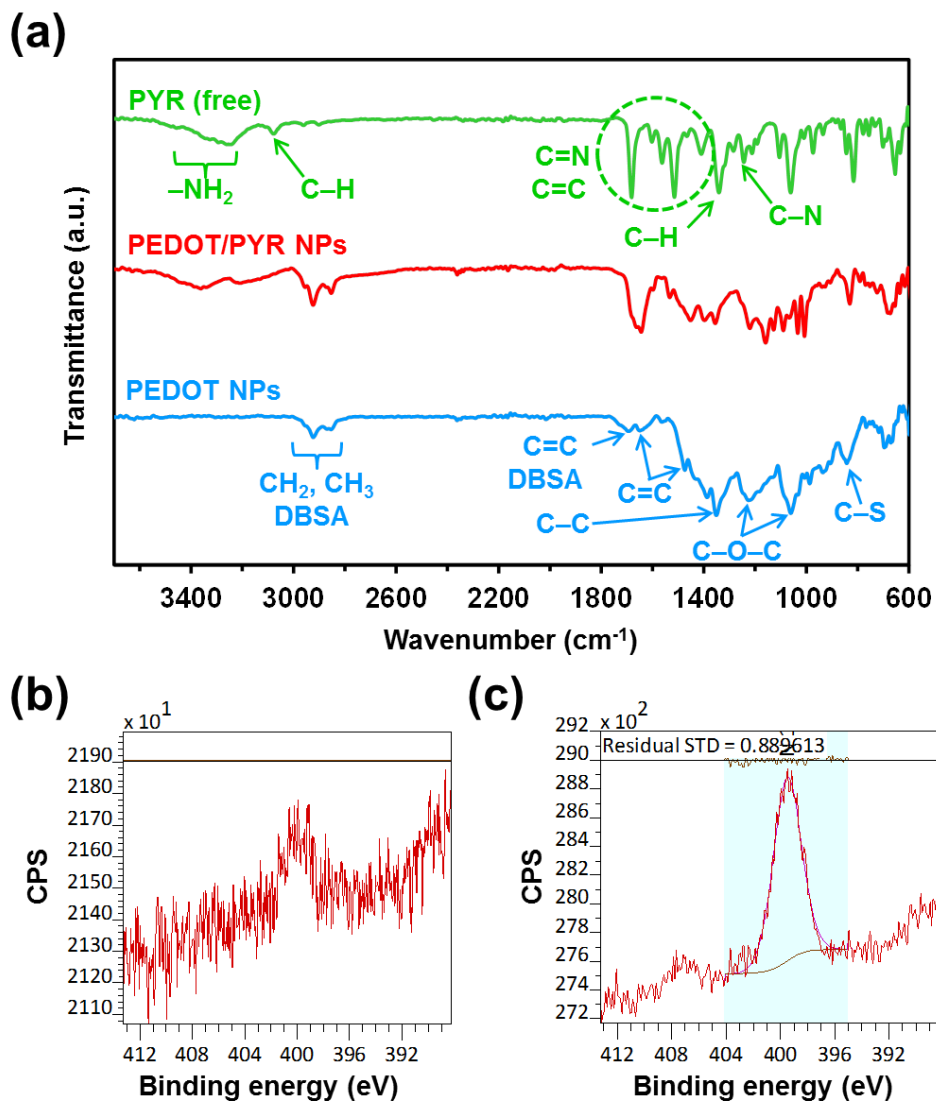
Figure 3.2.3. (a) FTIR spectra of free PYR, PEDOT/PYR NPs and PEDOT NPs. (b, c) High-resolution XPS spectra of the N 1s region for (b) PEDOT NPs and (c) PEDOT/PYR NPs.
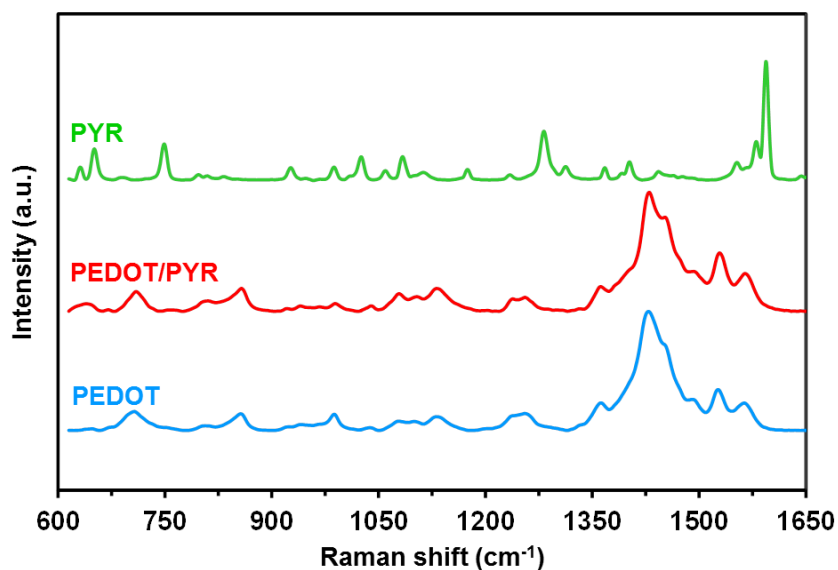
Figure 3.2.4. Raman spectra of free PYR, PEDOT NPs and PEDOT/PYR NPs.
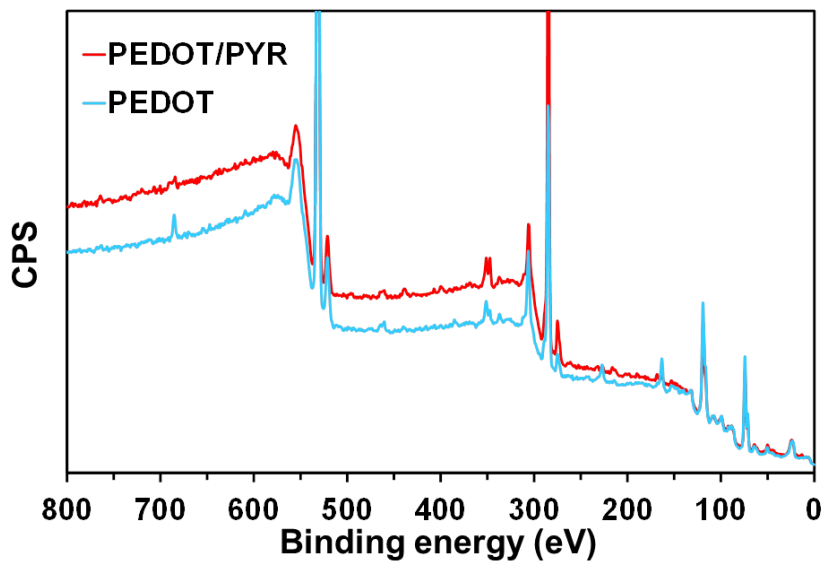
Figure 3.2.5. XPS spectra of PEDOT NPs and PEDOT/PYR NPs.

Figure 3.2.6a displays the UV spectra of independent PEDOT/PYR samples in methanol, showing a specific absorption band at 280 nm. The PYR-

loading capacity (LC, in %), which was expressed as the mass of loaded drug with respect to the total mass, was evaluated by using the absorbance at 280 nm and the calibration curve prepared by dissolving the drug in methanol (**Figure 3.2.2**). The PYR-LC was found to be 11.4 ± 1.5 %, this value being twice that reported for curcumin (CUR) encapsulated in PEDOT/CUR NPs by a similar procedure (CUR-LC = 5.9 ± 1.6 wt %).[37] Considering that CUR and PYR are both hydrophobic drugs of similar size (*i.e.* molecular mass: 368.38 and 248.71 g/mol, respectively), this difference has been attributed to the hydrogen bonding capacity of PYR, which exhibits two $-NH_2$ groups able to interact as donor groups with the oxygen atoms of the ethylenedioxy moiety of PEDOT chains. **Figure 3.2.6b** compares the UV spectra of free PYR, PEDOT NPs and PEDOT/PYR NPs, evidencing that the PC is not covalently attached to the polymers chains. Furthermore, the spectra do not reveal the formation of PYR···PEDOT π-π stacking interactions, supporting the fact that the two species mainly interact through hydrogen bonding.

The average diameter of PEDOT and PEDOT/PYR NPs, as obtained from dynamic light scattering (DLS) measurements was 215 ± 3 and 203 ± 1 nm, respectively (**Figure 3.2.6c**). The similarity in the size of the two types of NPs suggests that the PC is homogeneously dispersed in the polymeric matrix. On the other hand, the zeta (ζ)-potential of drug-loaded nanocarriers is very important, giving information on the charge at the surface of the particles and the tendency of the NPs to aggregate or to remain discrete. According to the DLVO electrostatic theory, the stability of a dispersion involving NPs with charged surfaces depends on the balance between the attractive van der Waals forces (steric stabilization) and the electrical repulsion because of the net surface charge. In general, a ζ-potential above 25 mV (positive or negative) indicates that the electrostatic repulsive forces exceed the attractive steric forces and the system is kept in a relatively stable dispersed state. The

ζ-potential measured for PEDOT and PEDOT/PYR NPs was -26 ± 7 and -29 ± 6 mV, respectively (**Figure 3.2.3c**), indicating that PYR does not reduce the stability of the polymeric NPs dispersion. Indeed, such ζ-potential values reflect that loaded PYR molecules do not shield the surface charge of PEDOT NPs.
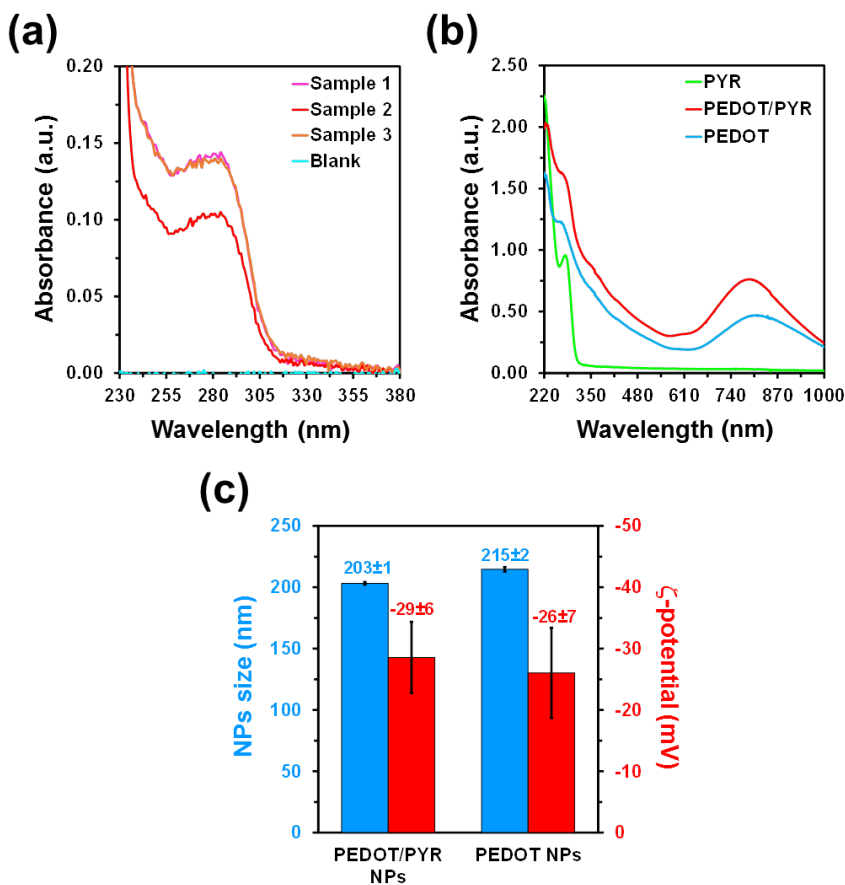
Figure 3.2.6. (a) UV-Vis spectra of PYR released from PEDOT/PYR in methanol (3 independent samples) compared to the blank. (b) UV-Vis spectra of free PYR, PEDOT/PYR NPs and PEDOT NPs. (c) Size (as determined by DLS) and ζ-potential of PEDOT/PYR and PEDOT NPs.

3.2.3.2 *Morphology of PEDOT and PEDOT/PYR NPs*

Representative high magnification (100k×) scanning electron microscopy (SEM) micrographs of PEDOT/PYR and PEDOT NPs are compared in **Figure 3.2.7**, while additional low magnification (50k×) micrographs are provided in **Figure 3.2.8**. In both cases NPs are relatively homogeneous in shape and size. PEDOT/PYR forms well defined spherical NPs with average diameter of 94 ± 12 nm, whereas unloaded PEDOT NPs exhibit an irregular shape with an average size of 109 ± 11 nm.

The sizes of the NPs visualized by SEM are approximately half of those registered by DLS. This has been attributed to two different features: 1) SEM measurements were performed in the dry state whereas DLS was measured in the solution state. Thus, the latter method provides the hydrodynamic diameter, which includes solvent molecules attached or adsorbed on the surface, while the former measures naked NPs; and 2) SEM is a number based NP size measurement that exhibits stronger emphasis on the smallest components in the size distribution whereas DLS is an intensity based measurement and emphasize on the larger NP size (*i.e.* intensity is proportional to r^6).

On the other hand, it was reported that shape and size of PEDOT NPs prepared by emulsion polymerization are affected by the surfactant type and concentration, respectively, which define the characteristics of the formed micelles.[38] Although DBSA leads to well-defined spherical micelles in water,[37,38] the addition of 12.5% methanol seems to promote micelle fusion resulting in irregular particles formed by the aggregation of smaller spherical particles. The micelle fusion with the apparent aggregation of small PEDOT NPs is probably inhibited by PYR. Despite such fusion phenomenon, the size of PEDOT NPs is only slightly larger than the diameter of spherical

PEDOT/PYR NPs, as is shown in **Figure 3.2.7** by their size distributions. 3D topographic AFM images of PEDOT/PYR and PEDOT NPs, which are included in **Figure 3.2.7**, are fully consistent with SEM micrographs, confirming that PEDOT/PYR samples are mainly made up of individual spherical NPs while the PEDOT samples exhibit irregular shapes due to fusion of nanostructures.
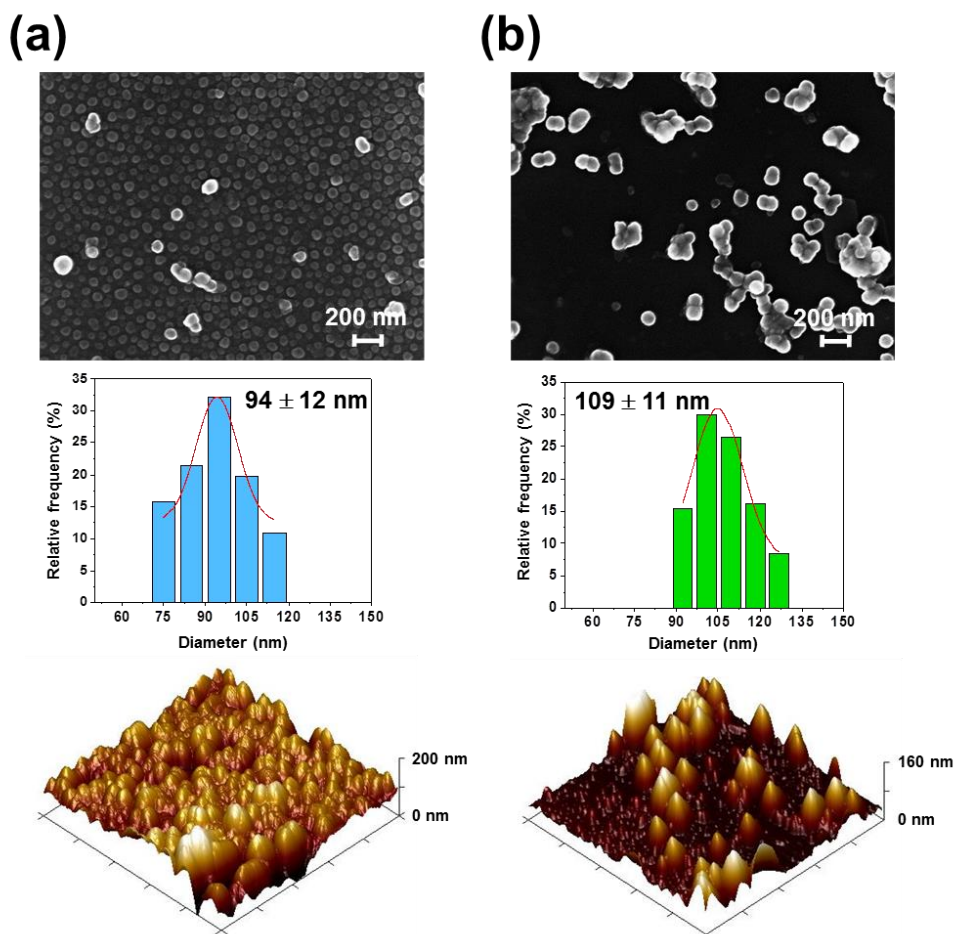
Figure 3.2.7. For (a) PEDOT/PYR NPs and (b) PEDOT NPs: SEM micrograph at 100kx magnification (top), diameter distribution histogram as determined from SEM images (middle), and 3D topographic AFM image (bottom) of 5×5 µm^2.

(a)

(b)

500 nm

500 nm
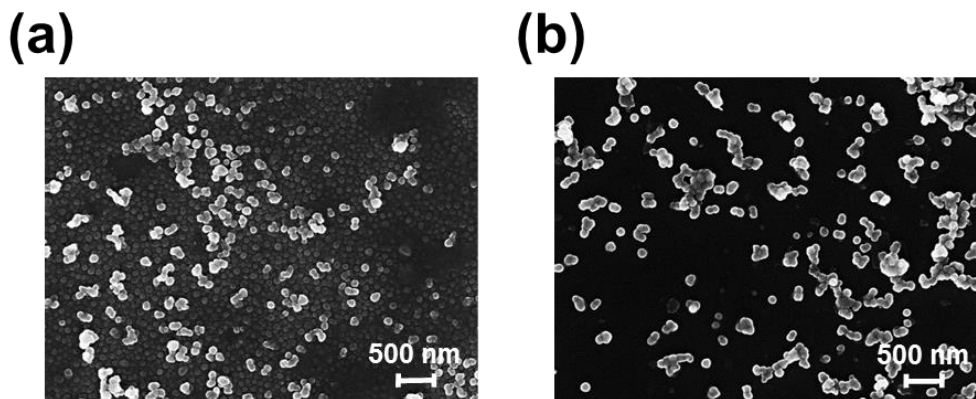
Figure 3.2.8. SEM micrographs at 50kx magnification for (a) PEDOT/PYR NPs and (b) PEDOT NPs.

3.2.3.3 PYR release

PEDOT/PYR NPs were incubated at 37 ºC in PBS (pH 7.4) and the *in vitro* release behaviour was studied over 80 days. The amount of released drug was evaluated by UV spectroscopy using the calibration curve obtained by plotting the absorbance measured at 280 nm against the PYR concentration. The cumulative release variation, which is represented in **Figure 3.2.9a**, exhibits a very slow evolution. The profile displays a biphasic regime consisting of an initial burst release for about 24 h, followed by a progressive but very slow release of PYR from PEDOT NPs. Thus, although about 1.6% of the PC was released from PEDOT/PYR NPs within the first 24 h, a very slow release was evidenced thereon, reaching only 4.1% in 5 days (*i.e.* half of that expected from a sustained mechanism: 1.6% × 5 = 8.0%). Furthermore, the release achieved after 80 days was only around 18%. The initial burst release might be related to the free PYR adhered to the surface of PEDOT/NPs. The slow release observed after that have been attributed to the fact that the poor affinity of the encapsulated hydrophobic PC towards PBS does not compensate for the strength of the interactions between PYR molecules and oxidized PEDOT chains. Indeed, the solubility of PYR in water is very low (0.01 mg/mL),[39]

evidencing that PYR⋯water interaction cannot compete with PYR⋯PYR and PYR⋯PEDOT interactions.

The solubility of PYR in ethanol (EtOH), almost 10 mg/mL, is three orders of magnitude higher than in water.[40] This property was used to obtain a complete and stable release profile as a function of the polarity of the release medium, which was achieved by replacing PBS by PBS:EtOH mixtures with increasing amount of co-solvent. More specifically, in such release assay, which took three weeks, the medium used for the first, second and third week was PBS, 90:10 PBS:EtOH, and 30:70 PBS:EtOH, respectively. The release profile is displayed in **Figure 3.2.9b**, while the profile obtained for each environment when a common starting point is imposed (*i.e.* release of 0% at the starting period of each environment) is depicted in the inset. The calibration curves obtained for such three media are plotted in **Figure 3.2.10**. Results show that, after one week, the release in PBS and 90:10 PBS:EtOH is 4.8% ± 0.5% and 3.4% ± 0.6%, respectively, indicating that the addition of a small amount of EtOH is not enough to facilitate drug diffusion from PEDOT NPs. Instead, the release is complete (100%) after 7 days of exposure when the 90:10 PBS:EtOH medium is replaced by 30:70 PBS:EtOH. These observations, which are consistent with the fact that PYR has much higher affinity towards EtOH molecules than towards water molecules, allow us to conclude that PEDOT NPs can act as effective nanocarriers, minimizing the PC's loss by simple diffusion and, therefore, reducing undesired adverse effects and increasing PC bioavailability.
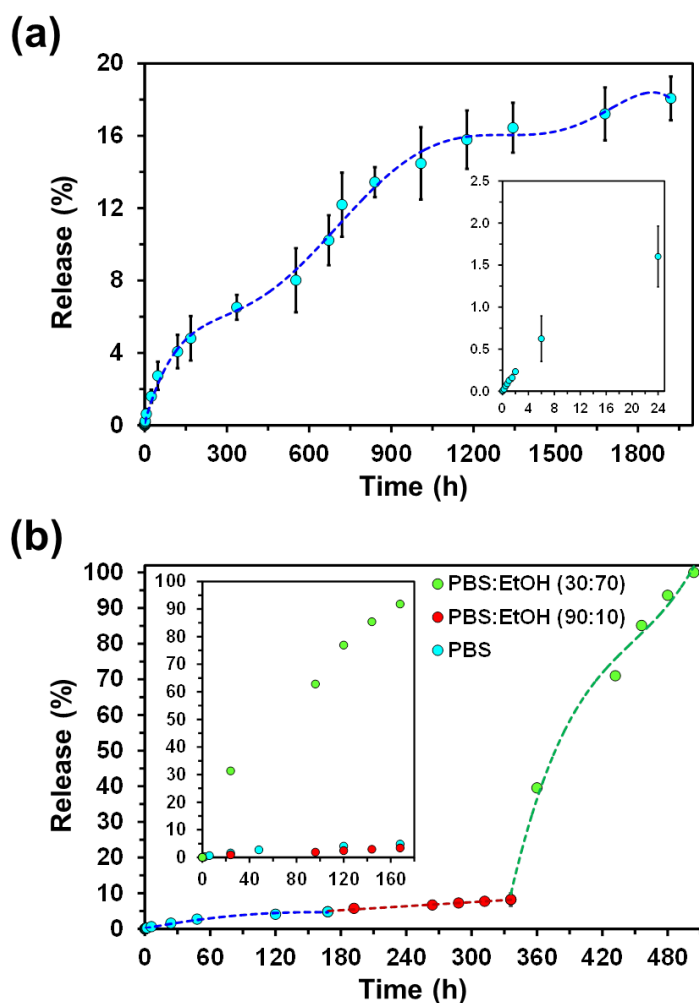
Figure 3.2.9. PC release from PEDOT/PYR NPs in: (a) PBS for 80 days at 37 ºC. Inset: magnification of the release profile for the first 24 h; and (b) PBS (first week), PBS:EtOH 90:10 (second week) and PBS:EtOH 30:70 (third week) at 37 °C. Inset: Drug release profiles from PEDOT/PYR NPs in PBS, PBS:EtOH 90:10 and PBS:EtOH 30:70 at 37 °C, which have been obtained by imposing a common starting point: release of 0% at the starting period (t= 0 h) in each environment.
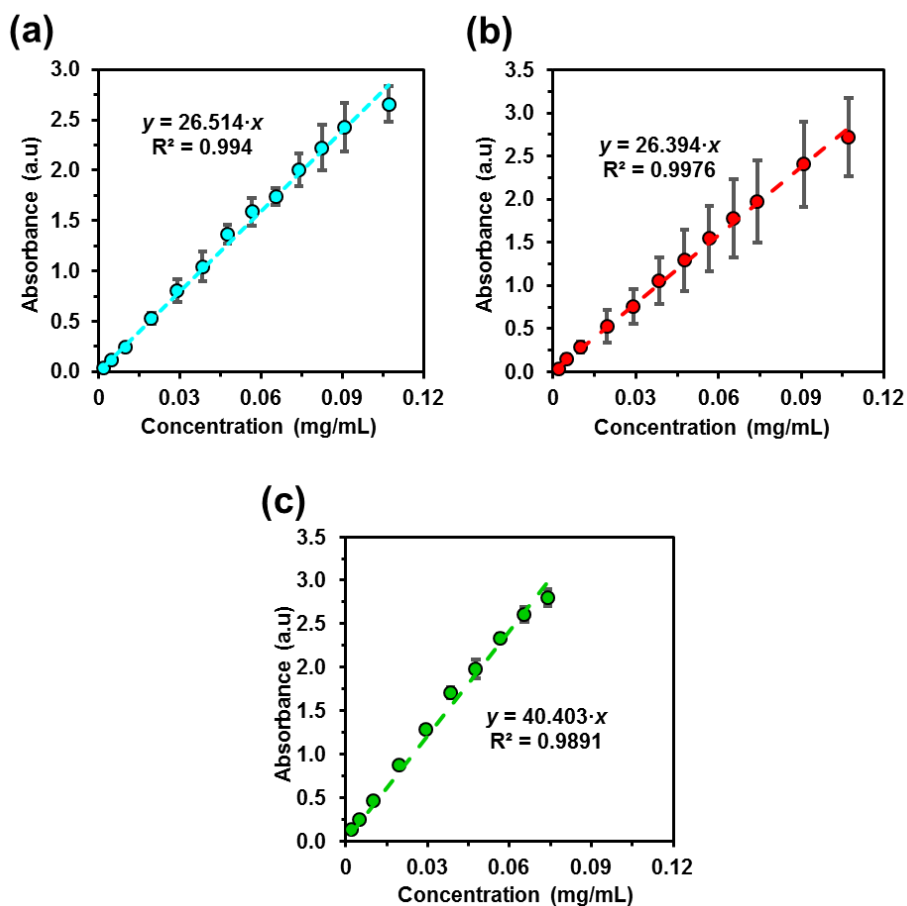
Figure 3.2.10. Calibration curve for PYR in (a) PBS, (b) 90:10 PBS:EtOH and 30:70 PBS:EtOH.

3.2.3.4 *Electrochemical properties*

In order to maximize the therapeutic efficacy of the PCs, an accurately controlled release should be achieved for prolonged and programmable treatments (*i.e.* extended treatments based on time-controlled administration of drugs). Before examining the electrochemical response of PEDOT/PYR NPs, the redox behavior of PYR on a screen-printed carbon electrode (SPCE) was investigated by cyclic voltammetry (CV) using a phosphate buffered saline (PBS) solution at pH 7.4 as supporting electrolyte. The recorded

voltammogram (**Figure 3.2.11a**) shows a well-defined anodic peak at 1.17 V in the anodic scan, even though no reduction peak appeared when the potential is reversed after oxidation. Although the characteristics of this voltammogram have been mainly associated to the irreversible electrochemical oxidation of the amino groups of PYR,[41] water electrolysis is also expected to contribute to the intensity and irreversibility of the peak.

Figure 3.2.11b compares the cyclic voltammograms obtained for bare and coated SPCEs, which were recorded in PBS at pH 7.4 and using a potential window comprised between –0.5 V (initial and final potential) and 1.4 V (reversal potential). The electrochemical activity of the bare SPCE increases noticeably upon coating with PEDOT or PEDOT/PYR NPs, as is reflected by the increment of area in the recorded voltammograms. Moreover, the enhanced electrochemical response of the coated SPCEs depends on the type of NPs, being much higher for PEDOT/PYR than for PEDOT. Considering that the amount of loaded PYR is not very high (PYR-LC = 11.4 ± 1.5 %), the large electrochemical response of PEDOT/PYR NPs in comparison to PEDOT NPs has been attributed to the synergistic effect of the two electroactive species, the PEDOT chains and the PC. Thus, the electroactivity of the PEDOT/PYR is significantly high in comparison to that of the two individual species (*i.e.* PEDOT NPs and free PYR), as shown in **Figure 3.2.12**. On the other hand, the electrochemical oxidation of PYR is still detected (as a shoulder) in the voltammogram recorded for the SPCE coated with PEDOT/PYR NPs.
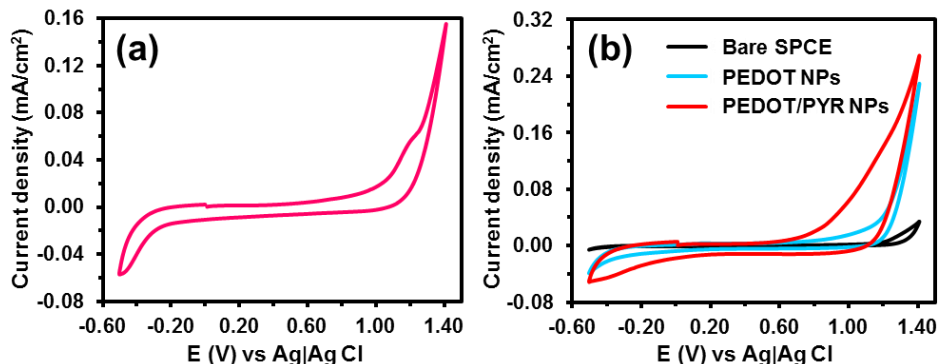
Figure 3.2.11. Cyclic voltammograms recorded from -0.5 to 1.4 V (scan rate: 100 mV/s) for (a) free PYR on SPCE and (b) bare (black) and coated (blue and red for PEDOT and PEDOT/PYR NPs) SPCEs.
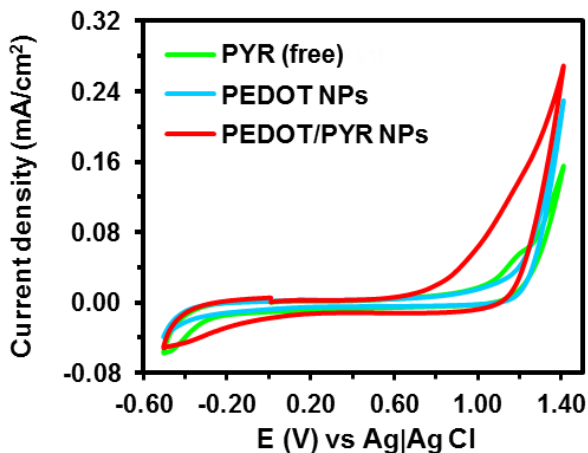
Figure 3.2.12. Cyclic voltammograms recorded from -0.5 to 1.4 V (scan rate: 100 mV/s) SPCEs coated with free PYR, PEDOT NPs or PEDOT/PYR NPs.

The effect of the electrical voltage on the PYR release was examined using two approaches: 1) CV; and 2) chronoamperometry (CA). Electrostimulation by CV was performed by scanning the voltage in a window in which the

chemical structure of the PYR could not be altered. Considering that PYR oxidizes at around 1.2 V, CV stimulation was applied by ramping the voltage linearly between –0.50 V (initial and final potential) to 0.50 V (reversal potential) at a scan rate of 100 mV/s (*i.e.* 10 s per CV cycle). CV stimulus was applied in a sustained way for 5, 15 and 30 min (*i.e.* 30, 90 and 180 consecutive CV cycles, respectively), the drug retention being evaluated after such periods of times. **Figure 3.2.13a** compares the shape of the voltammograms after 5, 10 and 15 min of sustained CV stimulation. It is worth noting that the shape and area of the voltammograms are similar, suggesting that the kinetics of the drug release is very slow. However, the reduction of the cathodic current density and the consequent enhancement of the tail close to the final potential indicate that the cathodic charge increases with time due to the release of the drug during the anodic scan. Thus, the release of PYR enhances the porosity of the NPs, favouring the exchange of ions at the interface with the electrolyte and increasing the cathodic charge, as is reflected by the enhancement of the area in the cathodic scan. **Figure 3.2.13b** represents the amount of PYR released from PEDOT/PYR NPs after 5, 15 and 30 min of stimulation by CV, which is compared with that observed from control experiments conducting using the same intervals of time but without applying external stimuli. It is worth noting that, although the PYR release is very low in both cases, the amount of released drug determined by UV is ~50% higher for CV stimulated samples than for non-stimulated ones.
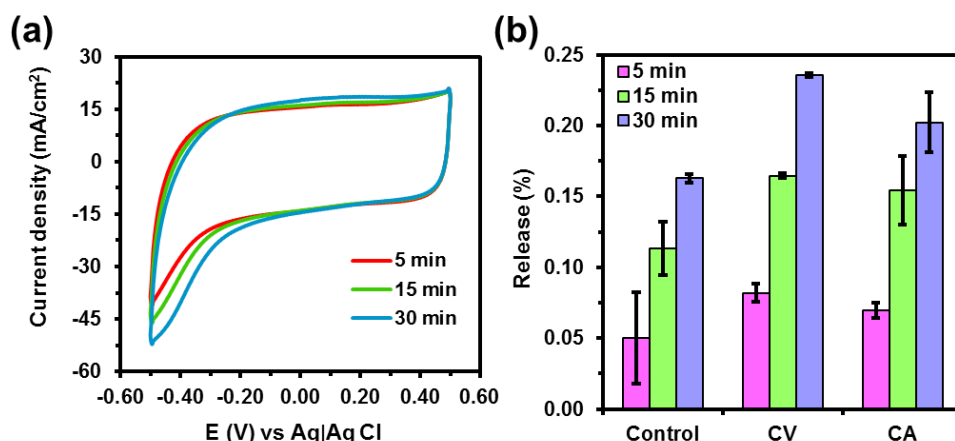
Figure 3.2.13. (a) Cyclic voltammograms recorded from –0.50 to 0.50 V (scan rate: 100 mV/s) for PEDOT/PYR NPs after 5, 15 and 30 min of CV stimulation. (b) PYR release during 5, 15 and 30 min without electrical stimulation (control) and with two different types of electrical stimulation CV (from –0.50 to 0.50 V at a scan rate of 100 mV/s) and CA (constant voltage of 1.00 V).

Electrostimulation was also examined by CA applying a constant voltage of 1.0 V during 5, 15 and 30 min. The amount of PYR released from loaded NPs at such time intervals is also plotted in **Figure 3.2.13b**. As can be seen, the drug released by CA stimulation is higher than that released in the absence of stimulus by ~35%. However, the comparison between CV and CA stimuli indicates that the former is more effective than the latter by ~15%. In both cases, the release mechanism is hypothesized to be based on the effect of the voltage in the strength of PYR···PEDOT interactions. More specifically, after the injection of electrons, the amount of positive charge distributed along the oxidized PEDOT chains decreases and, therefore, DBSA$^-$ dopant anions are expelled from the polymeric NPs. This change in the oxidation level of the conducting polymer and the consequent reduction of DBSA$^-$ anions affects the strength of the interactions with the PC, which is partially released to the medium. This treatment is more effective when the variation of the voltage is

135

performed using dynamic scans, which allows a continuous re-structuration of PYR in the polymeric NPs, than when a constant voltage is applied. On the other hand, the variation in the release was found to be larger for CA than for CV (**Figure 3.2.13b**). Thus, the application of a constant voltage of 1.0 V is expected to have more effect on the structure of PEDOT NPs (*i.e.* altering the structure of the NPs and reducing the control on the release) than the –0.50-to-0.50 V potential scan applied by CV.

136

3.2.3.5 Evaluation of cytotoxicity

Finally, the cytotoxicity of PYR was assessed on the commercial human osteosarcoma MG-63 cell line. **Figure 3.2.14a** shows cell survival for the different concentrations of such PC. The half-maximal inhibitory concentration (IC50) value of PYR was slightly lower than 100 µg/mL and, therefore, is classified as not cytotoxic. On the other hand, the cytotoxicity of PEDOT and PEDOT/PYR NPs was also examined using the MG-63 cell line. **Figure 3.2.14b** reflects that, cells are tolerant to PEDOT NPs, exhibiting moderate reductions in cell viability. Instead, the cell viability decreases significantly when the concentration of PEDOT/PYR NPs is higher than 0.5 mg/mL are used. In any case, such IC50 value is still high, reflecting that the utilization of PEDOT/PYR NPs for sustained electrical stimulation is a safe strategy for the on-demand release of PC. The cytotoxic effect of DBSA, which was used as dopant and stabilizer in the polymerization process, was studied in recent work.[35] Results showed that its cytotoxicity starts at low concentration, elimination by successive washing steps after the synthesis of the NPs being recommended.
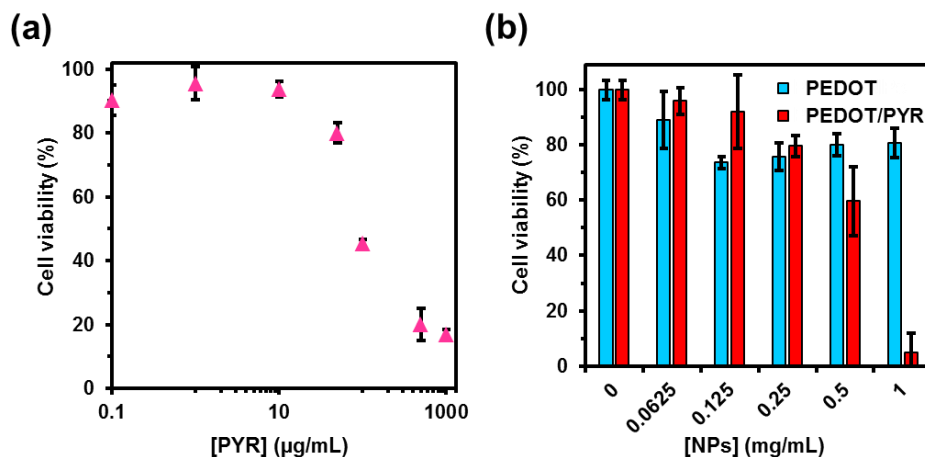
Figure 3.2.14. Dose-dependent viability of MG-63 cells treated with (a) free PYR and (b) PEDOT *vs* PEDOT/PYR NPs.

3.2.4 Conclusions

One of the major advantages provided by PEDOT NPs is that the release of PYR is very low in absence of stimulus, increasing considerably (~50%) when sustained CV stimulation is applied for 30 min by scanning the voltage in a small window. Consequently, this approach holds great promise for regulating PYR to the desired optimal dosage. Other advantages that make PEDOT NPs beneficial for the controlled release of PCs are: 1) the simplicity of the synthesis, which allows the *in situ* PC-loading; 2) the high stability and fast response against electrical signals of the PC-loaded NPs, which are even higher than for unloaded NPs; and 3) the very low toxicity of PEDOT NPs. Recent studies have demonstrated that drug-loaded conducting polymer NPs can be injected *in vivo* and the drug-release be stimulated using microelectrodes.[42] However, PEDOT NPs have the potential to be considered as promising electro-responsive nanocarriers for the on-demand wireless activated[43] delivery of other PCs.

3.2.5 References

1. Pereira, D. M., Valentão, P. & Andrade, P. B. Tuning protein folding in lysosomal storage diseases: the chemistry behind pharmacological chaperones. *Chem. Sci.* **9**, 1740–1752 (2018).

2. Mena-Barragán, T. *et al.* pH-Responsive Pharmacological Chaperones for Rescuing Mutant Glycosidases. *Angew. Chemie* **127**, 11862–11866 (2015).

3. Sánchez-Fernández, E. M., García Fernández, J. M. & Mellet, C. O. Glycomimetic-based pharmacological chaperones for lysosomal storage disorders: lessons from Gaucher, G M1 - gangliosidosis and Fabry diseases. *Chem. Commun.* **52**, 5497–5515 (2016).

4. Convertino, M., Das, J. & Dokholyan, N. V. Pharmacological Chaperones: Design and Development of New Therapeutic Strategies for the Treatment of Conformational Diseases. *ACS Chem. Biol.* **11**, 1471–1489 (2016).

5. Shin, M. H. & Lim, H.-S. Screening methods for identifying pharmacological chaperones. *Mol. Biosyst.* **13**, 638–647 (2017).

6. Hou, Z.-S., Ulloa-Aguirre, A. & Tao, Y.-X. Pharmacoperone drugs: targeting misfolded proteins causing lysosomal storage-, ion channels-, and G protein-coupled receptors-associated conformational disorders. *Expert Rev. Clin. Pharmacol.* **11**, 611–624 (2018).

7. Bhattacharya, K. *et al.* The Hsp70-Hsp90 co-chaperone Hop/Stip1 shifts the proteostatic balance from folding towards degradation. *Nat. Commun.* **11**, 5975 (2020).

8. Bernier, V., Bichet, D. G. & Bouvier, M. Pharmacological chaperone action on G-protein-coupled receptors. *Curr. Opin. Pharmacol.* **4**, 528–533 (2004).

9. Cortez, L. & Sim, V. The therapeutic potential of chemical chaperones in protein folding diseases. *Prion* **8**, 197–202 (2014).

10. Yun, Y., Lee, B. K. & Park, K. Controlled drug delivery systems: the next 30 years. *Front. Chem. Sci. Eng.* **8**, 276–279 (2014).

11. McCoy, C. P. *et al.* Triggered drug delivery from biomaterials. *Expert Opin. Drug Deliv.* **7**, 605–616 (2010).

12. Sershen, S. & West, J. Implantable, polymeric systems for modulated drug delivery. *Adv. Drug Deliv. Rev.* **54**, 1225–1235 (2002).

13. Timko, B. P., Dvir, T. & Kohane, D. S. Remotely Triggerable Drug Delivery Systems. *Adv. Mater.* **22**, 4925–4943 (2010).

14. Youan, B.-B. C. Chronopharmaceutics: gimmick or clinically relevant approach to drug delivery? *J. Control. Release* **98**, 337–353 (2004).

15. Enshaei, H. *et al.* Scaffolds for Sustained Release of Ambroxol Hydrochloride, a Pharmacological Chaperone That Increases the Activity of Misfolded β-Glucocerebrosidase. *Macromol. Biosci.* **19**, 1900130 (2019).

16. Vandamme, T. F. & Heller, J. Poly (ortho esters) as bioerodible matrices for the controlled delivery of pyrimethamine in chemoprophylaxis of malaria. *J. Control. Release* **36**, 209–213 (1995).

17. Mollania, F., Hadipour, N. L. & Mollania, N. CNT-based nanocarrier loaded with pyrimethamine for adipose mesenchymal stem cells differentiation and cancer treatment: The computational and experimental methods. *J. Biotechnol.* **308**, 40–55 (2020).

18. Maegawa, G. H. B. *et al.* Pyrimethamine as a Potential Pharmacological Chaperone for Late-onset Forms of GM2 Gangliosidosis. *J. Biol. Chem.* **282**, 9150–9161 (2007).

19. Bateman, K. S., Cherney, M. M., Mahuran, D. J., Tropak, M. & James, M. N. G. Crystal Structure of β-Hexosaminidase B in Complex with Pyrimethamine, a Potential Pharmacological Chaperone. *J. Med. Chem.* **54**, 1421–1429 (2011).

20. Clarke, J. T. R. *et al.* An open-label Phase I/II clinical trial of pyrimethamine for the treatment of patients affected with chronic GM2 gangliosidosis (Tay–Sachs or Sandhoff variants). *Mol. Genet. Metab.* **102**, 6–12 (2011).

21. Friesen, J., Borrmann, S. & Matuschewski, K. Induction of Antimalaria Immunity by Pyrimethamine Prophylaxis during Exposure to Sporozoites Is Curtailed by Parasite Resistance. *Antimicrob. Agents Chemother.* **55**, 2760–2767 (2011).

22. Okell, L. C., Griffin, J. T. & Roper, C. Mapping sulphadoxine-pyrimethamine-resistant Plasmodium falciparum malaria in infected humans and in parasite populations in Africa. *Sci. Rep.* **7**, 7389 (2017).

23. Secrieru, A., Costa, I. C. C., O'Neill, P. M. & Cristiano, M. L. S. Antimalarial Agents as Therapeutic Tools Against Toxoplasmosis—A Short Bridge between Two Distant Illnesses. *Molecules* **25**, 1574 (2020).

24. Ben-Harari, R. R., Goodwin, E. & Casoy, J. Adverse Event Profile of Pyrimethamine-Based Therapy in Toxoplasmosis: A Systematic Review. *Drugs R. D.* **17**, 523–544 (2017).

25. Chen, M., Osman, I. & Orlow, S. J. Antifolate Activity of Pyrimethamine Enhances Temozolomide-Induced Cytotoxicity in Melanoma Cells. *Mol. Cancer Res.* **7**, 703–712 (2009).

26. Giammarioli, A. M. *et al.* Pyrimethamine Induces Apoptosis of Melanoma Cells via a Caspase and Cathepsin Double-Edged Mechanism. *Cancer Res.* **68**, 5291–5300 (2008).

27. Tommasino, C. *et al.* New derivatives of the antimalarial drug Pyrimethamine in the control of melanoma tumor growth: an in vitro and in vivo study. *J. Exp. Clin. Cancer Res.* **35**, 137 (2016).

28. Khatri, P. *et al.* Preparation and characterization of pyrimethamine solid dispersions and an evaluation of the physical nature of pyrimethamine in solid dispersions. *J. Drug Deliv. Sci. Technol.* **45**, 110–123 (2018).

29. Le, T.-H., Kim, Y. & Yoon, H. Electrical and Electrochemical Properties of Conducting Polymers. *Polymers (Basel).* **9**, 150 (2017).

30. Puiggalí-Jou, A., del Valle, L. J. & Alemán, C. Drug delivery systems based on intrinsically conducting polymers. *J. Control. Release* **309**, 244–264 (2019).

31. Donahue, M. J. *et al.* Tailoring PEDOT properties for applications in bioelectronics. *Mater. Sci. Eng. R Reports* **140**, 100546 (2020).

32. Groenendaal, L., Zotti, G., Aubert, P.-H., Waybright, S. M. & Reynolds, J. R. Electrochemistry of Poly(3,4-alkylenedioxythiophene) Derivatives. *Adv. Mater.* **15**, 855–879 (2003).

33. Aradilla, D., Estrany, F. & Alemán, C. Symmetric Supercapacitors Based on Multilayers of Conducting Polymers. *J. Phys. Chem. C* **115**, 8430–8438 (2011).

34. Fabregat, G. *et al.* Incorporation of a Clot-Binding Peptide into Polythiophene: Properties of Composites for Biomedical Applications. *ACS Appl. Mater. Interfaces* **6**, 11940–11954 (2014).

35. Puiggalí-Jou, A., del Valle, L. J. & Alemán, C. Encapsulation and Storage of Therapeutic Fibrin-Homing Peptides using Conducting Polymer Nanoparticles for Programmed Release by Electrical Stimulation. *ACS Biomater. Sci. Eng.* **6**, 2135–2145 (2020).

36. Puiggalí-Jou, A., Wedepohl, S., Theune, L. E., Alemán, C. & Calderón, M. Effect of conducting/thermoresponsive polymer ratio on multitasking nanogels. *Mater. Sci. Eng. C* **119**, 111598 (2021).

37. Puiggalí-Jou, A., Micheletti, P., Estrany, F., del Valle, L. J. & Alemán, C. Electrostimulated Release of Neutral Drugs from Polythiophene Nanoparticles: Smart Regulation of Drug-Polymer Interactions. *Adv. Healthc. Mater.* **6**, 1700453 (2017).

38. Paradee, N. & Sirivat, A. Synthesis of poly(3,4-ethylenedioxythiophene) nanoparticles via chemical oxidation polymerization. *Polym. Int.* **63**, 106–113 (2014).

39. Yalkowsky, S. H., He, Y. & Jain, P. *Handbook of Aqueous Solubility Data*. (CRC Press, 2016). doi:10.1201/EBK1439802458.

40. O'Neil, M. J. and K. (Firm). *The Merck index : an encyclopedia of chemicals, drugs, and biologicals / Maryadele*. (Whitehouse Station, N.J. : Merck, 2006).

41. Radi, A.-E., Nassef, H. M. & Attallah, M. I. Investigation of antimalarial drug pyrimethamine and its interaction with dsDNA by electrochemical and spectroscopic techniques. *Anal. Methods* **7**, 4159–4167 (2015).

42. Hosseini-Nassab, N., Samanta, D., Abdolazimi, Y., Annes, J. P. & Zare, R. N. Electrically controlled release of insulin using polypyrrole nanoparticles. *Nanoscale* **9**, 143–149 (2017).

43. Joo, H. *et al.* Soft implantable drug delivery device integrated wirelessly with wearable devices to treat fatal seizures. *Sci. Adv.* **7**, eabd4639 (2021).

3.3 Polypeptide hydrogel loaded with conducting polymer nanoparticles as electroresponsive delivery system of small hydrophobic drugs

A hydrogel/nanoparticle-loaded system for the controlled delivery of small hydrophobic drugs has been prepared using poly(γ-glutamic acid) (PGGA), a naturally occurring biopolymer made of glutamic acid units connected by amide linkages between α-amino and γ-carboxylic acid groups, and poly(3,4-ethylenedioxythiophene) (PEDOT), a very stable conducting polymer with excellent electrochemical response. Specifically, curcumin (CUR)-loaded PEDOT nanoparticles (PEDOT/CUR) were incorporated to the PGGA hydrogel during the crosslinking reaction. After chemical, morphological and electrochemical characterization, the release profiles of PEDOT/CUR and PGGA/PEDOT/CUR systems have been compared in the absence and presence of electrical stimuli, which consisted on the application of a voltage of –0.5 V for 15 min every 24 h. Results show that the release is higher for electrically stimulated systems by more than twice, even though due to its hydrophobicity and poor solubility in water the release was relatively slow in both cases. This feature could be advantageous when the therapeutic treatment requires slow, controlled and sustained CUR release.

143

3.3.1 Introduction

Recent development in drug release using polymeric systems has shown the capability in delivering accurate amount of drugs using hydrogel, nanoparticles (NPs), nano- and microfibers, and membrane-based reservoir devices.[1–13] Furthermore, external stimulation signals such as temperature variation,[14,15] magnetic fields,[16,17] radiation,[18,19] pH variation,[20–22] and electric voltages,[23–27] have been used for triggering drug release rates and for controlling drug administration at specific locations. Among these polymeric devices for on-demand drug release, the ones that can be stimulated and controlled by electrical signals have shown advantages in rapid responses with remote controls for local treatments.[28–30]

Electrostatic forces between the drug and the charged polymeric matrix, usually a conducting polymer (CP), play a prominent role in the release of drugs. This is achieved by taking advantage of the oxidation-reduction properties of CPs, which are controlled through external voltages to promote the formation-disruption of drug⋯polymer interactions.[31] Moreover, the intrinsic expansion and contraction movements of CPs, which are due to their electromechanical response, can be also used to induce the mechanical release of the drug. Although such two mechanisms are frequently employed simultaneously,[32] the electromechanical properties of CPs can be used as unique mechanism for drug release.[2]

Curcumin (CUR) is a natural plant-based alkaloid derived from *Curcuma longa* with proved antimicrobial,[33] anti-inflammatory,[34] anti-diabetic,[35] and anticancer,[24,36] properties. The wide spectrum of clinical applications together with the low molecular weight, hydrophobicity, low toxicity, natural dyeing property and rapid metabolism inside the body upon systemic administration of CUR make it an ideal model compound to study the formulation design of small

144

hydrophobic molecules.[37] In fact, its extreme hydrophobicity limits the release of CUR in aqueous biological environments, unless specifically designed mechanisms based on their chemical properties are used. In recent years, different polymeric devices have been designed to regulate the release of CUR using external voltages by applying different mechanisms. The release of CUR from CP NPs attached onto a glassy carbon surface has been demonstrated using negative voltages, which induce the electrochemical de-doping (reduction) of the CP, altering CUR···polymer interactions.[38] Also, Puiggalí-Jou et al.[2] loaded CP NPs and CUR separately in electrospun poly(γ-caprolactone) (PCL) microfibers. The electromechanical response of the CP NPs to regularly applied potential pulses altered the porosity of the microfibers, promoting the release of CUR from them. In a very recent study, the release of CUR from electroresponsive hydrogels made of CP-Alginate, which were prepared by forming separated CP- and alginate-rich phases after gelling a mixture of CP and alginate, was achieved using a mechanism similar to that of the CP NPs by applying a negative voltage.[23]

Although a variety of polymeric platforms have been used for the on-demand electrostimulated release of CUR release, more investigation is still necessary, especially in the field of hydrogels. Thus, the main disadvantage of conductive CP-alginate hydrogels is their low mechanical stability in absence of Ca^{2+} ions, which are necessary to crosslink alginate chains in alginate-rich phases.[23] In this work we present a different approach for the voltage-induced release of CUR from poly-γ-glutamic acid (PGGA) hydrogels, which contain CUR-loaded CP NPs. After chemical, morphological and electrochemical characterization of such system using the technique described in the Methods section, the contribution of each element to the release of CUR has been analyzed by comparing the release profiles obtained for CUR-loaded PGGA/CP NPs with those of CUR-loaded PGGA and CUR-loaded CP NPs.

3.3.2 Methods

3.3.2.1 *Materials*

Dodecyl benzenesulfonic acid (DBSA), ammonium persulfate (APS), 3,4-ethylenedioxythiophene (EDOT), cystamine dihydrochloride, and 1-[3-(dimethylamino)propyl]-3-ethylcarbodiimide methiodide (EDC) (≥98.0%) and polyoxyethylenesorbitan monolaurate solution (Tween-20) were purchased from Sigma-Aldrich Chemical Company. Free-acid poly(γ-glutamic acid) (PGGA) from *Bacillus subtilis*, with average molecular weight M_w= 350000, was purchased from Wako Chemicals GmbH (Neuss, Germany).

3.3.2.2 *Synthesis of loaded and unloaded poly(3,4-ethylenedioxythiophene) nanoparticles (uPEDOT NPs)*

15.8 mL of milli-Q water were placed in a 30 mL tube. After this, 96 µL of DBSA were added and the solution was stirred at 40 ℃ for 1 h with a magnetic stirrer set at 750 rpm. This was followed by the addition of 72 µL of EDOT monomer and 2 mL of ethanol and, again, the mixture was stirred for 1 h at 750 rpm at 40 ℃. Finally, 0.73 g of APS dissolved in 2 mL of milli-Q water were added to the mixture. The reaction was maintained in agitation at 40 ℃ overnight protected from light with aluminium foil. In this process, the color of the reaction mixture changed from light grey to dark blue. No sedimentation was observed after the reaction occurred, indicating a good colloidal stability. The side products and unreacted chemicals were removed by a sequence of 3 centrifugations at 11000 rpm for 40 min at 4 ℃. The resulting supernatants were decanted and the pellet was dispersed in deionized water using a vortex and a sonication bath (15 min at room temperature). The last pellet was left under vacuum for two days, then weighted and re-dispersed in the corresponding media at the desired concentration.

The synthesis of curcumin-loaded PEDOT NPs (PEDOT/CUR NPs) process was identical to that described for uPEDOT NPs with the exception that 2 mL of a curcumin (CUR) solution (10 mg/mL in ethanol, EtOH) were at the same time that the EDOT monomer.

3.3.2.3   Synthesis of unloaded poly(γ-glutamic acid) (uPGGA) hydrogels

PGGA (0.071565 g) and EDC (0.14859 g) were dissolved in 1 mL of 0.5 M NaHCO$_3$ at 4 ºC under magnetic stirring (500 rpm). Then, cystamine dihydrochloride (0.0563 g), was added to the solution and mixed during 2-3 minutes. The PGGA / EDC / cystamine molar ratio was 5 / 5 / 2.5. The final solution was poured into circular molds (diameter of 10 mm and 5 mm in depth) or square 3D printed molds (7×7 mm and 3 mm in depth). The solution was let to gel at room temperature for 10 min.

3.3.2.4   Synthesis of poly(γ-glutamic acid) hydrogels loaded with uPEDOT NPs (PGGA/uPEDOT), PEDOT/CUR NPs (PGGA/PEDOT/CUR) and PGGA/CUR

The procedure described for uPGGA hydrogel was also used to prepare loaded PGGA/uPEDOT, PGGA/PEDOT/CUR and PGGA/CUR hydrogels. More specifically, the only difference with respect to the preparation of uPGGA hydrogel is that the 0.5 M NaHCO$_3$ solution used to dissolve the biopolymer already contained the uPEDOT NPs, PEDOT/CUR NPs (20% w/w of NPs with respect to the weight of PGGA) or free CUR (i.e. the exact amount of CUR that applied in the sample PGGA/PEDOT/CUR). For this purpose, uPEDOT NPs, PEDOT/CUR NPs or free CUR were dispersed in 1 mL of 0.5 M NaHCO$_3$ at 4 ºC and 1000 rpm during three days before adding the biopolymer for dissolution.

3.3.2.5 UV-Vis spectroscopy

UV-Vis spectra were obtained using a Synergy HTX multi-mode reader. All spectra were collected in reflectance mode and converted to absorbance.

3.3.2.6 Dynamic light scattering (DLS)

DLS studies were performed using NanoBrook Omni Zeta Potential Analyzer from Brookheaven Instruments. Measurement consisted of 3 runs of 120 s each, which were averaged to obtain the effective diameter. Samples were analyzed at 25 ºC using a scattering angle of 90º.

3.3.2.7 Fourier transform infrared (FTIR) spectroscopy

FTIR transmittance spectra were recorded on a FTIR Jasco 4100 spectrophotometer equipped with an attenuated total reflection accessory (Top-plate) with a diamond crystal (Specac model MKII Golden Gate Heated Single Reflection Diamond ATR). For each sample 64 scans were performed between 4000 and 600 cm^{-1} with a resolution of 4 cm^{-1}.

3.3.2.8 RAMAN spectroscopy

Micro-Raman spectroscopy assays were performed using a commercial Renishaw inVia Samples were characterized by micro-Raman spectroscopy using a commercial Renishaw inVia Qontor confocal Raman microscope. The Raman setup consisted of a laser (at 785 nm with a nominal 300 mW output power) directed through a microscope (specially adapted Leica DM2700 M microscope) to the sample after which the scattered light is collected and directed to a spectrometer with a 1200 lines·mm-1 grating. The exposure time was 10 s, the

laser power was adjusted to 1% of its nominal output power and each spectrum was collected with 3 accumulations.

3.3.2.9   Scanning electron microscopy (SEM)

Detailed inspection of the nanoparticles and hydrogel morphologies was conducted by scanning electron microscopy (SEM). A Focus Ion Beam Zeiss Neon 40 instrument (Carl Zeiss, Germany) equipped with an energy dispersive X-ray (EDX) spectroscopy system and operating at 5 kV was used. Samples were mounted on a double-sided adhesive carbon disc and sputter-coated with an ultra-thin carbon layer (6-10 nm) to prevent sample charging problems. The diameters of the nanoparticles and the hydrogel pores were measured with the SmartTiff software from Carl Zeiss SMT Ltd.

3.3.2.10 Electrochemical characterization

Electrochemical characterization was performed by cyclic voltammetry (CV) using an Autolab PGSTAT302N Galvanostat equipped with the ECD module (Ecochimie, The Netherlands). Measurements were performed on hydrogels (7×7 mm^2) fixed between two indium tin oxide coated poly(ethylene terephthalate) (ITO-PET) sheets (1×2 cm), one as the working electrode and one as the counter electrode- using a gripper. Oxidation-reduction cycles were registered within the potential range of −0.2 to +1.0 V at a scan rate of 100 mV/s. The electroactivity and electrostability were determined through direct measure of the anodic and cathodic areas in the control voltammograms, using the GPES software. The loss of electroactivity (LEA) was determined as:

$$LEA = \frac{\Delta Q}{Q_i} 100$$

Equation 3.3.1. LEA equation, where ΔQ is the difference of voltammetric charge between the second cycle and the last cycle and Q_i is the voltammetric charge corresponding to the second cycle.

Electrochemical impedance spectroscopy (EIS) diagrams were taken at open circuit (OCP) over the frequency range of 100000 kHz to 0.1 Hz with potential amplitude of 0.05 V using an AUTOLAB-302N potentiostat/galvanostat. All experiments were performed at room temperature using a PBS 0.1 M solution as electrolyte.

3.3.2.11 Release from PEDOT/CUR NPs

For the release without external stimulation, 50 µL of a 10 mg/mL PEDOT/CUR NPs dispersion in milli-Q water were introduced in an Eppendorf. After water evaporation, 1 mL of phosphate buffer saline (PBS) solution with a very small amount (0.05%) polyoxyethylenesorbitan monolaurate solution, a non-ionic emulsifying agent widely employed in biomedical and pharmaceutic applications against aggregation, was added to the Eppendorf. The system was kept in an incubator at 37 ºC with 120 rpm agitation during the release process. The medium was taken at specific time points and replaced with fresh medium.

3.3.2.12 Electrical stimulation for CUR release

For the stimulated release, 50 µL of a 10 mg/mL PEDOT NPs dispersion in milli-Q water were placed on a drop sense electrode. After drying, the electrode was put inside a three-electrode electrochemical cell with 1 mL of PBS solution with a very small amount (0.05%) polyoxyethylenesorbitan monolaurate solution. Platinum was used as the counter electrode, while an Ag|AgCl electrode

containing a KCl saturated aqueous solution was the reference electrode (offset potential versus the standard hydrogen electrode, $E° = 0.222$ V at 25 °C). The electrical stimulus consisted of applying a voltage of –0.50 V for 15 min every 24 h. The system was kept in an incubator at 37 ℃ with 120 rpm of agitation during the whole release process.

Quantification of the released CUR in the extracted medium was performed by UV-Vis spectroscopy by measuring the absorbance at $\lambda = 427$ nm.

3.3.3 Results and discussion

In this work, PEDOT was selected as CP due to its excellent electrical and electrochemical properties and great environmental stability.[39–41] Furthermore, PEDOT is a biocompatible material currently used for biomedical applications.[42–44] Indeed, PEDOT devices (*e.g.* films and NPs) exhibit very low intrinsic cytotoxicity and display no inflammatory response upon implantation, making them ideal for bioengineering applications that require electro-responsive materials.[44–47]

Unloaded (control) and CUR-loaded PEDOT NPs, hereafter denoted uPEDOT and PEDOT/CUR, respectively, were prepared by emulsion polymerization adapting a previously described procedure.[23] Dodecylbenzenesulfonic acid (DBSA) was used as surfactant to lower the interfacial tension, allowing the emulsification of 3,4-ethylenedioxythiophene (EDOT) monomers, and as dopant agent to stabilize the formed CP chains, whereas the oxidation agent was ammonium persulfate (APS). CUR was loaded by adding an ethanol drug solution to the reaction medium. The behavior of the NPs obtained using this procedure as appropriated material for biomedical applications (*i.e.* in terms of cytotoxicity, biocompatibility and inflammatory response) was previously reported.[23,47]

FTIR spectra of EDOT monomer, uPEDOT NPs, free CUR and PEDOT/CUR NPs are shown (**Figure 3.3.1a**). The FTIR spectrum of EDOT monomer shows remarkable bands centered at 1181 and 750 cm^{-1} with relative intensities of 1:1, which correspond to the C–O–C bending mode of the ethylenedioxy moiety and the C$^{\alpha}$–H out-of-plane bending mode, respectively. In uPEDOT NPs, the C–O–C bending and the C$^{\alpha}$–H out-of-plane bending modes appear at 1180 and 739 cm^{-1}, respectively, with relative intensities of 5:1. The significant reduction in the intensity of the C$^{\alpha}$–H out-of-plane bending band proves the success of the polymerization process and the formation of linear molecules through α,α-linkages. On the other hand, the characteristic CUR bands, which are identified at 3506 (OH), 1594 (C=O) and 1269 cm^{-1} (enol C–O), are detected in the spectra of the free drug and PEDOT/CUR NPs, reflecting the success of the loading process.
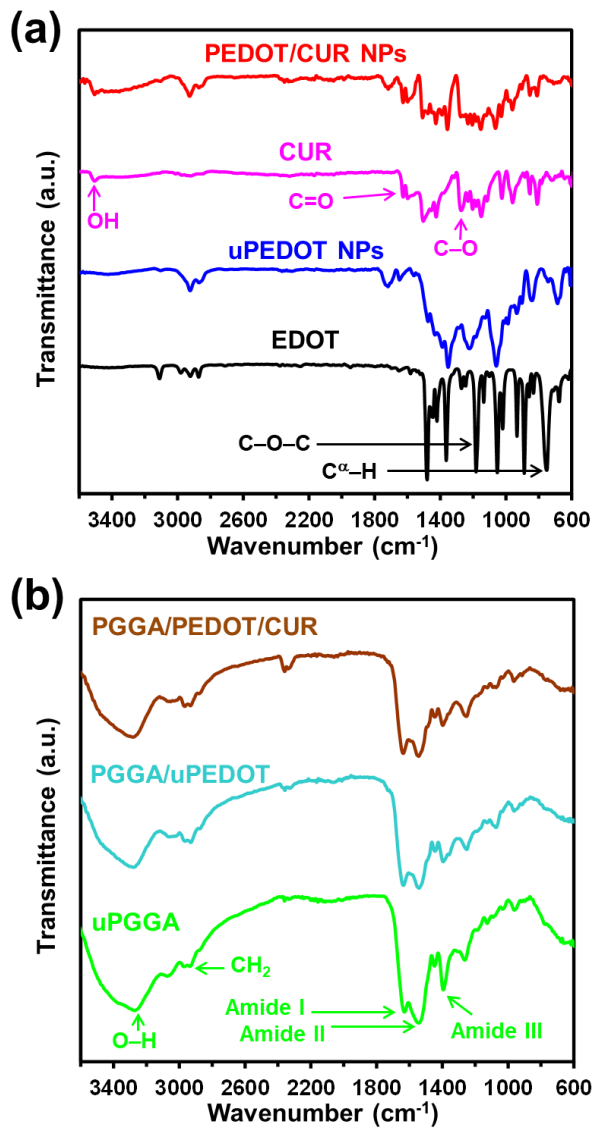
Figure 3.3.1. FTIR spectra of: (a) EDOT monomer, uPEDOT NPs, free CUR and CUR-loaded PEDOT NPs (PEDOT/CUR NPs); and (b) uPGGA, PGGA loaded with PEDOT NPs (PGGA/uPEDOT) or PEDOT/CUR NPs (PGGA/PEDOT/CUR).

After this, CP NPs were dispersed inside a biodegradable and biocompatible hydrogel. Poly(γ-glutamic acid) (PGGA), which is a naturally occurring biopolymer made of glutamic acid units connected by amide linkages between

α-amino and γ-carboxylic acid groups, was selected since it fulfils the requirements for controlled drug delivery, as recently reviewed.[48,49] PEDOT/CUR and uPEDOT NPs were dispersed *in situ* during the PGGA crosslinking, which was performed using a previously reported procedure.[50] More specifically, PGGA was dissolved in a 0.5 M NaHCO₃ solution containing the corresponding NPs, while 1-[3-(dimethylamino)propyl]-3-ethylcarbodiimide methiodide (EDC) and cystamine dihydrochloride were used to activate and crosslink the biopolymer chains, respectively. Hereafter, the hydrogels loaded with PEDOT/CUR and uPEDOT NPs are denoted PGGA/PEDOT/CUR and PGGA/uPEDOT (control), respectively. In addition, unloaded PGGA (uPGGA) and PGGA loaded *in situ* with free CUR (PGGA/CUR) were prepared for comparison. The complete synthetic procedures used for all hydrogels, which gelled in circular molds (diameter of 10 mm and 5 mm in depth) or square 3D printed molds (7×7 mm and 3 mm in depth), are described in the Methods section.

Figure 3.3.2a compares the consistency and color of uPGGA, PGGA/PEDOT/CUR and PGGA/uPEDOT hydrogels. Although all samples were robust, the color exhibited by loaded hydrogels reflected the success of the encapsulation process. Thus, PGGA/uPEDOT and PGGA/PEDOT/CUR showed a dark blue coloration, which was attributed to the CP NPs, whereas PGGA/CUR was orange, confirming the encapsulation of CUR. **Figure 3.3.1b** compares the FTIR spectra of uPGGA, PGGA/uPEDOT and PGGA/PEDOT/CUR. uPGGA exhibits the typical amide I (C=O stretching) and amide II (C–N stretching, N–H bending, and C–C stretching) bands at 1628 and 1537 cm^{-1}, respectively. The absence of the C=O stretch of the free carboxylic acid and the asymmetric COO^- stretch, which are detected at 1728 and 1589 cm^{-1} before the crosslinking reaction PGGA (**Figure 3.3.3**), respectively, together with the significant enhancement of the amide I and II bands, evidence the formation of cystamine-mediated –CONH– crosslinks between the biopolymer chains.
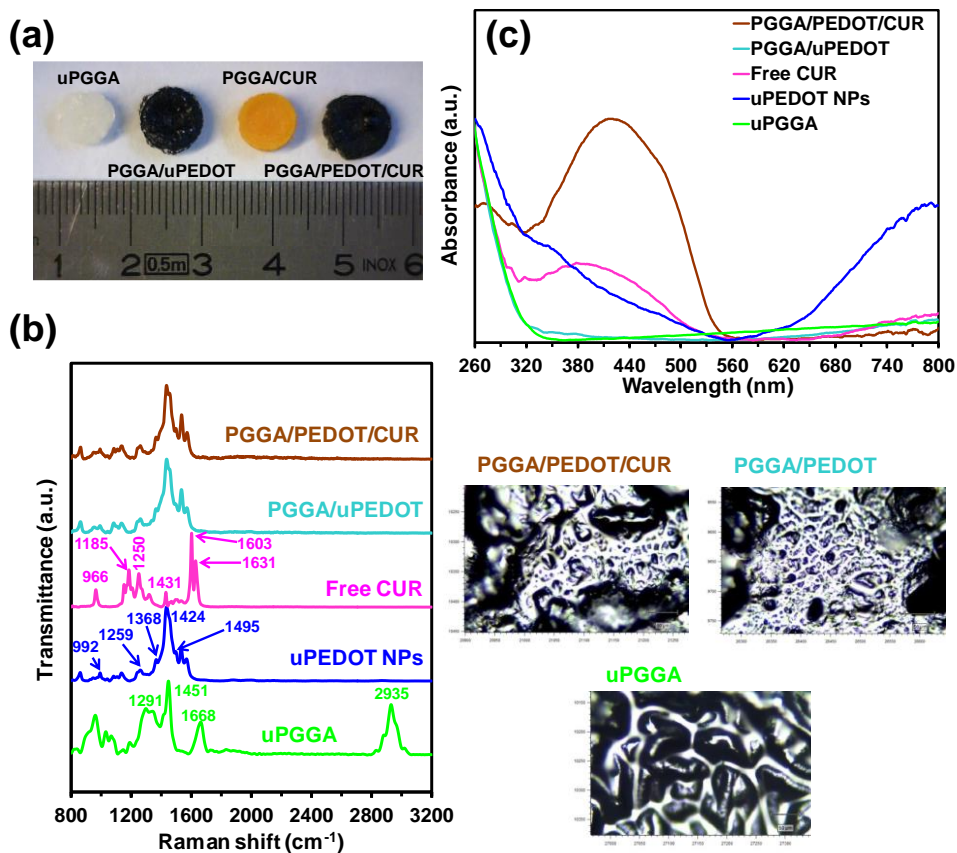
Figure 3.3.2. (a) Photographs of the prepared hydrogels: uPGGA, PGGA/uPEDOT, PGGA/CUR and PGGA/PEDOT/CUR; (b) Left: Raman spectra of uPGGA, uPEDOT NPs, free CUR, PGGA/uPEDOT and PGGA/PEDOT/CUR. Excitation wavelength: 785 nm. Right: images obtained using a confocal Raman microscope for uPGGA, PGGA/uPEDOT and PGGA/PEDOT/CUR hydrogels. (c) UV-Vis spectra of uPGGA, uPEDOT NPs, free CUR, PGGA/uPEDOT and PGGA/PEDOT/CUR.

Other important bands for uPGGA appear at 3270, 2930, 1392 and 1260 cm^{-1}, which correspond to the O–H stretching, CH$_2$ asymmetrical stretching, amide III (νC–N + δNH) and the free OH in plane bending. Although the shoulder at 1060 cm^{-1} has been attributed to the C–O–C stretching vibration of PEDOT chains, the loading of uPEDOT and PEDOT/CUR NPs in PGGA/uPEDOT and PGGA/PEDOT/CUR hydrogels cannot be clearly disclosed from the

corresponding FTIR spectra, as they are clearly dominated by the PGGA fingerprints.

In order to confirm the loading of PEDOT/CUR and uPEDOT NPs in the hydrogels, micro-Raman spectroscopic analyses were performed. Raman fingerprints of uPGGA hydrogel, uPEDOT NPs and free CUR are shown in **Figure 3.3.2b**. The PGGA hydrogel shows the characteristic peak at 1291, 1451 and 1668 and 2935 cm^{-1}, which correspond to the amide III, CH_2 deformation (i.e. the amide II band is generally very weak or not observed in Raman spectra), amide I and CH_2 stretching, respectively. The Raman fingerprints of uPEDOT NPs appear at 992, 1259, 1368, 1424 and 1495 cm^{-1}, which have been related to the oxyethylene ring, C_α–$C_{\alpha'}$ inter-ring stretching, C_β=C_β stretching, symmetric C_α=C_β stretching and asymmetric C_α=C_β stretching vibrations, respectively.[51] For free CUR powder, the most intense bands appearing at 1603 and 1631 cm^{-1} were assigned to the benzene ring, while the bands at 966 and 1185 cm^{-1} were associated to the C–O–H and C–O–C vibrations. The C–O stretching vibrations of enol and phenol were identified with the peaks detected at 1250 and 1431 cm^{-1}, respectively.
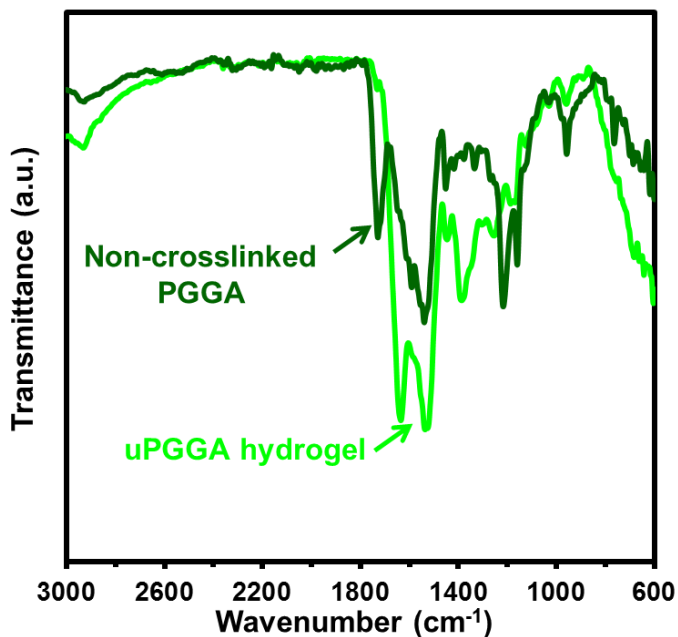
Figure 3.3.3. FTIR spectra for non-crosslinked PGGA powder (dark green) and the lyophilized uPGGA hydrogel (light green).

In the Raman spectrum of the loaded PGGA/CUR hydrogel (**Figure 3.3.4**), characteristic peaks of the free drug (1185, 1252, 1433, 1602 and 1630 cm^{-1}) and the unloaded hydrogel (1452, 1666 and 2935 cm^{-1}) are clearly distinguished, evidencing that the drug can be directly loaded in the hydrogel. Inspection of the optical microscopy images taken from the regions analyzed by micro-Raman spectroscopy does not reveal significant morphological differences between the unloaded and CUR-loaded hydrogels (**Figure 3.3.4**). Conversely, **Figure 3.3.2b** shows that the Raman spectra of PGGA/uPEDOT and PGGA/PEDOT/CUR are clearly dominated by the CP fingerprints. This observation is clearly illustrated in **Figure 3.3.5a** and **b**, which display the spectra of PGGA/PEDOT and PGGA/PEDOT/CUR, respectively, superposed to those of their individual components. This fact occurs due to the resonance Raman effect, which increases the intensity of the bands of the material when the incident radiation coincides

with the frequency of an electronic transition of the sample.[52,53] In PGGA/uPEDOT and PGGA/PEDOT/CUR, the excitation wavelength (785 nm) corresponds to an electronic transition occurring in CP NPs, the intensity of their bands being enhanced compared to those of uPGGA and CUR. On the other hand, optical microscopy images reveal significant morphological differences between uPGGA and both PGGA/uPEDOT and PGGA/PEDOT/CUR (**Figure 3.3.2b**), which have been attributed to the unloaded or loaded CP NPs.
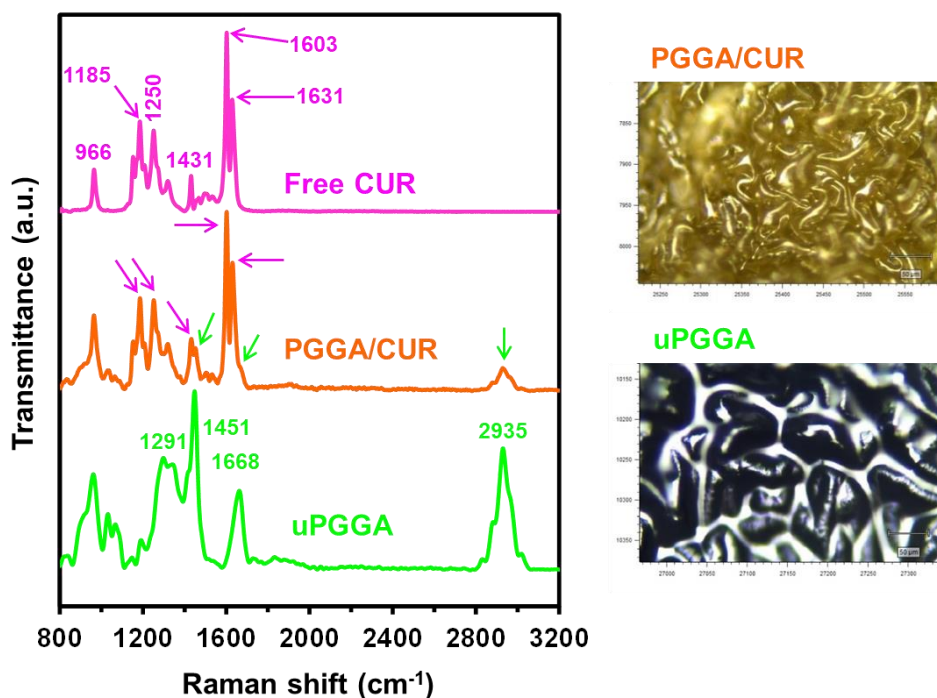
Figure 3.3.4. Left: Raman spectra of uPGGA hydrogel, free CUR and PGGA/CUR hydrogel. Right: Images obtained using a confocal Raman microscope for uPGGA and PGGA/CUR hydrogels. The shift is labelled for the most characteristic peaks of uPGGA and free CUR spectra. Arrows in the PGGA/CUR spectrum indicate the peaks coming from uPGGA (green) and free CUR (pink).
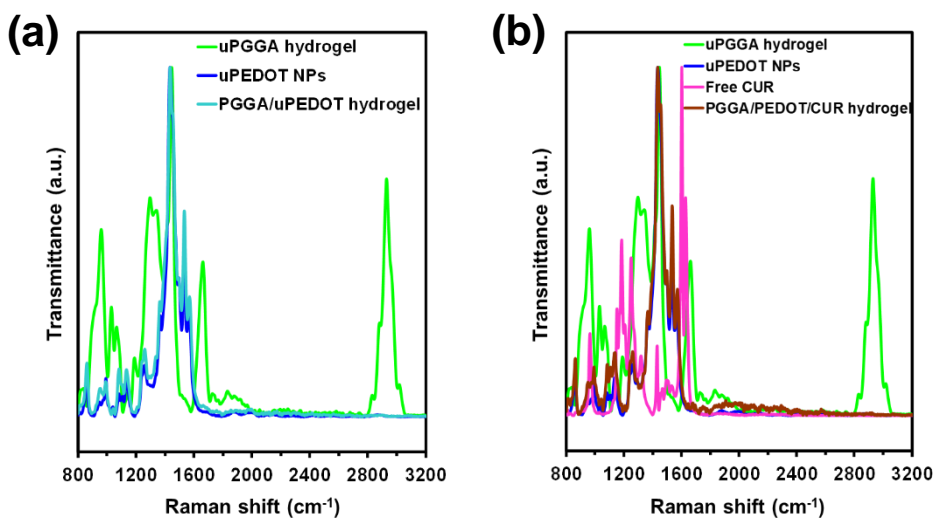
Figure 3.3.5. (a) Superposition of the Raman spectra recorded for uPGGA hydrogel, uPEDOT NPs and PGGA/uPEDOT hydrogel. (b) Superposition of the Raman spectra recorded for uPGGA hydrogel, uPEDOT NPs, free CUR and PGGA/PEDOT/CUR hydrogel.

Despite the presence of drug in PGGA/PEDOT/CUR was not detected by micro-Raman spectroscopy, the fact that the drug remains charged once the hydrogel has formed was unambiguously demonstrated by UV-Vis spectroscopy. **Figure 3.3.2c** compares the absorption spectra recorded for uPGGA, uPEDOT NPs, free CUR, PGGA/uPEDOT and PGGA/PEDOT/CUR. uPEDOT NPs show an absorption band centered at 791 nm that is related with bipolaronic states of the CP.[54] CUR exhibits an absorption band with a maximum at 380 nm, which has been attributed to its neutral form,[55] that does not overlap the CP NPs absorption peak at 791 nm. The UV-Vis spectrum of PGGA/PEDOT/CUR maintains the peak of CUR, even though the maximum shifts to 420 nm due to the effect of CP NPs. As shown in the figure, this peak is completely absent for PGGA/uPEDOT.

The average diameter of uPEDOT and PEDOT/CUR NPs, as determined by dynamic light scattering (DLS) is shown in **Figure 3.3.6a**. The encapsulation of

the drug increased the size by around 25%. Conversely, micrographs recorded by scanning electron microscopy (SEM) reflected that the average diameter is similar for the drug-loaded and unloaded NPs (**Figure 3.3.6b**). The expected difference between DLS- and SEM-measured diameters should be attributed to the following two reasons: 1) DLS measures the intensity of the scattered light, which is proportional to the sixth power of the particle diameter and, therefore, overrates the larger particles due to their much stronger scattered light intensity. Instead, SEM averages depend on the number of measures, gives the same weight to all them; and 2) SEM sizes represent the core of the particles because the solvated polymeric shell collapses during drying and in the high vacuum chamber of the microscopy, whereas DLS represents the hydrodynamic size of the nanoparticles dispersed in liquids, including the surrounding solvent layer and leading to a larger nanoparticle size, in general. On the other hand, **Figure 3.3.6c** and **d** present representative SEM micrographs of PEDOT/CUR and uPEDOT NPs, which illustrate their coral-like morphology.

The average size and the unimodal size distribution histogram (**Figure 3.3.7**) are optimal for the utilization of PEDOT/CUR in biomedical applications, as for example the delivery of CUR as anticancer drug, since it would enable intravenous administration and passive tumor targeting via the enhanced permeability and retention effect.[56] The encapsulation efficiency (EE, in %), which was expressed as percentage of CUR successfully encapsulated with respect to the CUR introduced in the reaction medium for preparing PEDOT/CUR NPs, and the loading capacity (LC, in %), which corresponds to the percentage of CUR encapsulated with respect to the total weight of the NPs, were determined by dissolving the loaded drug in ethanol and using UV-Vis absorbance for quantification. The EE and LC values obtained using the calibration curve in ethanol (**Figure 3.3.8a**) were 3.8±0.4% and 19.0±7.2%, respectively. These values decrease when the PGGA hydrogel is used to encapsulate both the

PEDOT/CUR NPs and free CUR, which was attributed to the hydrophobicity of the drug. Thus, for PGGA/PEDOT/NPs the EE and LC values were 0.53±0.04% and 0.93±0.03%, respectively, and for PGGA/CUR were 0.49±0.04% and 1.92±0.18%, respectively.
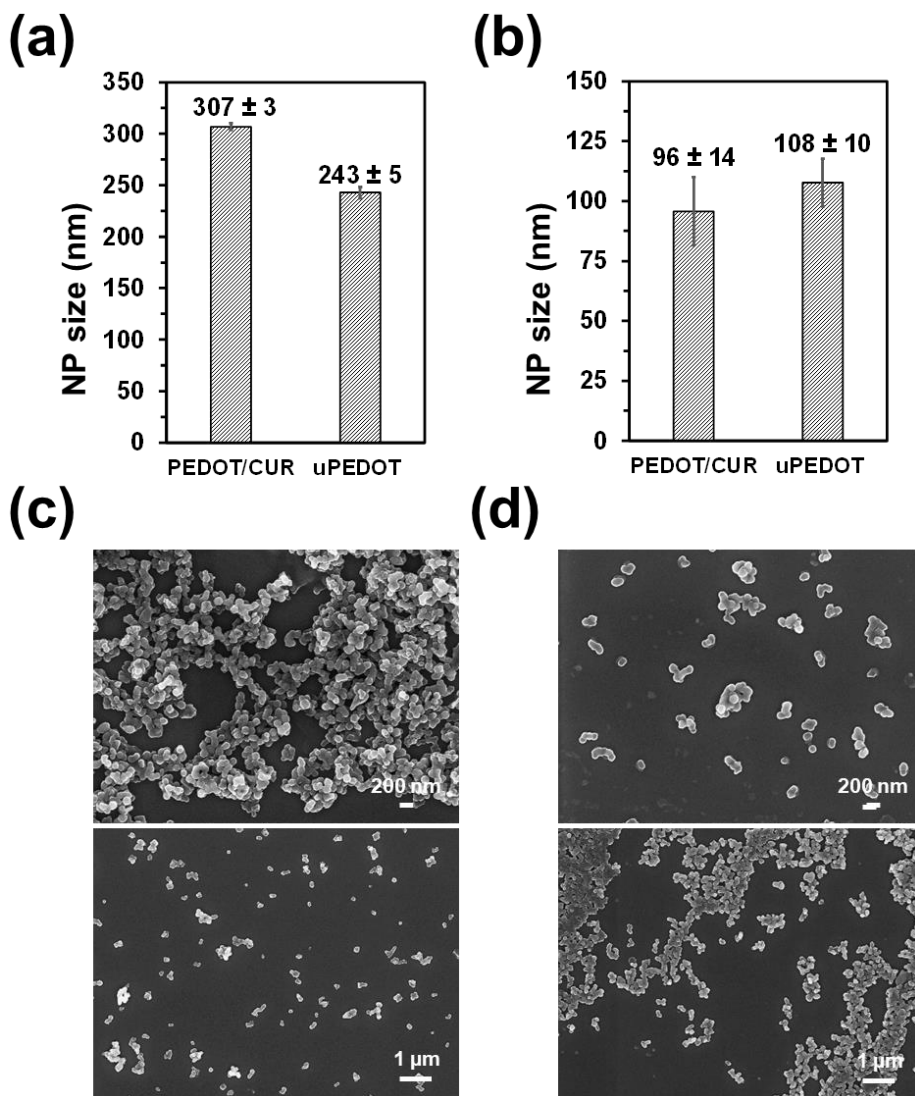
Figure 3.3.6. (a,b) Comparison of PEDOT/CUR and uPEDOT NPs size as determined by (a) DLS and (b) SEM measurements. Average values and the corresponding standard deviations are indicated in nm. (c,d) SEM micrographs with 20 k magnification (top) and 10 k magnification (bottom) of (c) PEDOT/CUR and (d) uPEDOT NPs.
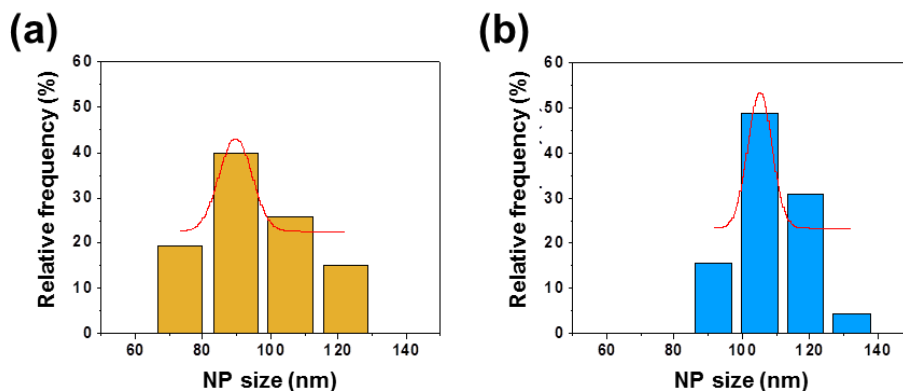
Figure 3.3.7. Size distribution histograms for (a) PEDOT/CUR and (b) uPEDOT NPs as obtained from SEM-measurements.
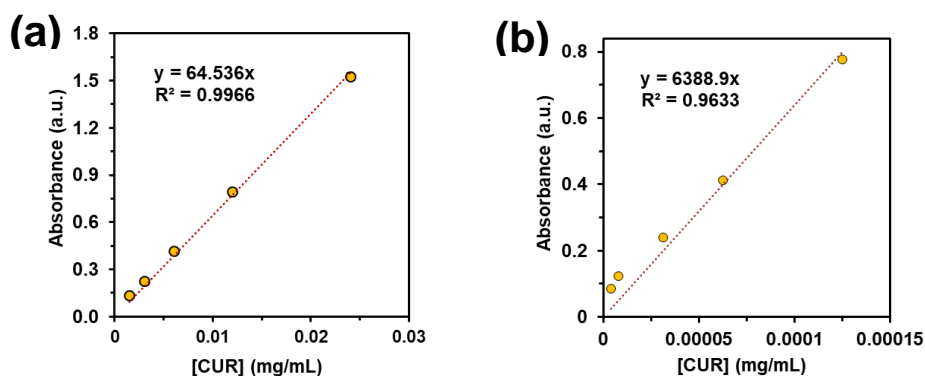
Figure 3.3.8. (a) Calibration profile for CUR in ethanol (absorbance measured at λ = 427 nm). (b) Calibration profile for CUR in PBS with a very small amount (0.05%) polyoxyethylenesorbitan monolaurate solution (absorbance measured at λ = 427 nm).

The porous structure of the prepared hydrogels was also characterized by SEM. **Figure 3.3.9** compares cross-sectional low- and high-magnification SEM micrographs of uPGGA, PGGA/CUR, PGGA/uPEDOT and PGGA/PEDOT/CUR hydrogels. The uPGGA hydrogel exhibits a highly porous *honeycomb*-like appearance (**Figure 3.3.9a**). The long axis of the pores, which showed irregular shape, was found to be 12.8 ± 4.4 µm, whereas the thickness of

the pore wall was less than 1 µm. The structure of the hydrogel changes in PGGA/CUR (**Figure 3.3.9b**). Thus, the drug, which organizes forming NPs of diameter less than 0.1 µm, is adsorbed on the surface of the pore walls. Indeed, the thickness of the pore wall and the average pore size increase heterogeneously upon several tens of micrometers and 18.3 ± 5.9 µm, respectively. Similarly, the pore size distribution becomes wider in comparison to uPGGA. The distinctive structure of PGGA/CUR has been attributed to a phase separation process between the *in situ* loaded hydrophobic CUR and hydrophilic biopolymer chains during the crosslink process. On the other hand, the pore size decreases upon loading of uPEDOT NPs (**Figure 3.3.9c**). Thus, although PGGA/uPEDOT hydrogel exhibits a honeycomb-like structure with thin pore walls, the size of the pore is around 40% smaller than for uPGGA. Moreover, uPEDOT NP aggregates attached to the pore walls are clearly distinguished.

PGGA/PEDOT/CUR hydrogels present a structure that is intermediate between those of PGGA/CUR and PGGA/uPEDOT. Thus, PGGA/PEDOT/CUR presents thick pore walls, similar to those found for PGGA/CUR. Instead, the average pore size (9.0±1.4 µm) is close to that of PGGA/uPEDOT, even though exhibiting a wider distribution. Furthermore, adhered PEDOT/CUR NPs are not forming aggregates, as uPEDOT NPs, but are dispersed on the pore walls, as drug NPs in PGGA/CUR.
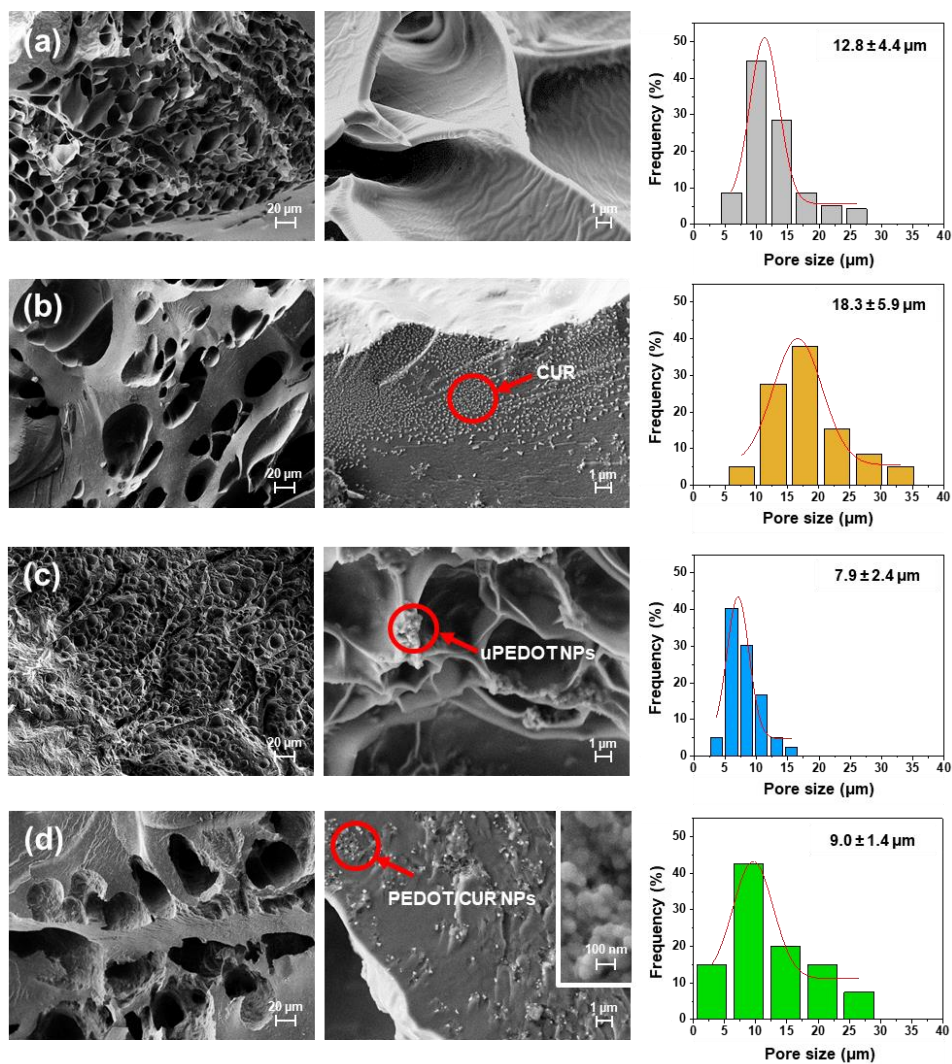
Figure 3.3.9. Low- and high-magnification cross-sectional SEM images (left and center, respectively) and distribution of the pore size (right) of (a) uPGGA, (b) PGGA/CUR, PGGA/uPEDOT and PGGA/PEDOT/CUR hydrogels. Representative NPs are marked by red circles. The average pore size (long axis) is provided for each hydrogel.

The electrochemical properties of uPGGA, PGGA/CUR, PGGA/uPEDOT PGGA/PEDOT/CUR, which were evaluated using cyclic voltammetry (CV) and electrochemical impedance spectroscopy (EIS), are displayed in **Figure 3.3.10**. Comparison between uPGGA and PGGA/CUR cyclic voltammograms recorded

in PBS 0.1 M (pH 7.3) reveals that the latter exhibits an oxidation peak with an oxidation potential higher than the reversal potential (1.0 V), which has been attributed to the irreversible electro-oxidation of CUR (**Figure 3.3.10a**).[57] The loading of uPEDOT or PEDOT/CUR NPs resulted in a significant increment of the electrochemical activity, as reveals the increment in the voltammetric area of PGGA/uPEDOT and PGGA/PEDOT/CUR with respect to uPGGA.

Detailed inspection of the cyclic voltammogram recorded for PGGA/uPEDOT reveals two oxidation peaks (O_1 and O_2 in **Figure 3.3.10a**): the first at around 0.2 V and the second at a potential higher than the reversal potential. In addition, two reduction peaks at around 0.15 and 0.75 V (R_1 and R_2 in **Figure 3.3.10a**) were detected in the cathodic scanning, indicating the presence of redox pairs in the recorded potential windows (from –0.2 V to 1.0 V). This has been interpreted as the formation of polarons in the CP chains. Although similar features are observed for PGGA/PEDOT/CUR, these are less pronounced, which has been attributed to the interfering effects of the electroactive drug. These features are quantitatively reflected in **Figure 3.3.10b**, which represents the voltametric charge (Q) of the four studied hydrogels. As shown, the highest Q was reached for PGGA/uPEDOT, whereas the loading of PEDOT/CUR NPs resulted in a reduction of 12% due to interfering effects.
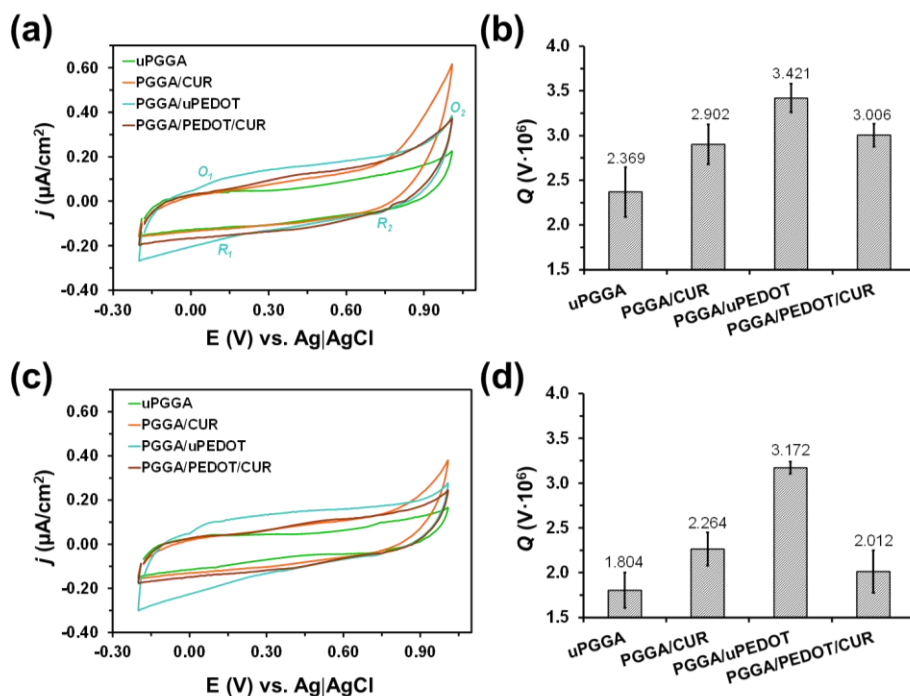
Figure 3.3.10. (a, c) Cyclic voltammograms and (b, d) voltammetric charges determined for uPGGA, PGGA/CUR, PGGA/uPEDOT and PGGA/PEDOT/CUR hydrogels in PBS 0.1 M (pH 7.4). Graphics correspond to the (a, b) first and the (c, d) 50th consecutive redox cycle. Initial and final potentials: –0.2 V; reversal potential: 1.0 V; scan rate: 100 mV/s. Oxidation and reduction peaks found for PGGA/uPEDOT are labelled in (a) as O1, O2, R1 and R2.

Cyclic voltammograms obtained after 50 consecutive redox cycles in a potential between –0.2 V (initial and final potential) and 1.0 V (reversal potential), are shown in **Figure 3.3.10c**. Comparison with the control voltammograms (**Figure 3.3.10a**) reveals that, in all cases, the area of the voltammograms decreased with the increasing number of cycles, as is also reflected by the values of Q displayed in **Figure 3.3.10d**. As it was expected, the loss of electrochemical activity (LEA; **Equation 3.3.1**) was found to depend on the composition of the hydrogel. More specifically, the LEA of uPGGA and PGGA/CUR was very similar (22% ± 3% and 25% ± 5%, respectively), which is consistent with the fact that electrooxidation of CUR is an irreversible process. Conversely, the LEA of

PGGA/uPEDOT is very small (13% ± 4%), indicating that uPEDOT NPs impart electrochemical activity to the PGGA hydrogel. Thus, the electrostability of PEDOT has been proved to be outstanding among CPs.[38,58,59] However, a higher LEA was reached by PGGA/PEDOT/CUR (20% ± 4%), indicating that the interference between CUR and PEDOT also affects negatively to the electrochemical stability of the loaded hydrogel.

The conductivity of uPGGA, PGGA/uPEDOT and PGGA/PEDOT/CUR hydrogels was determined by electrochemical impedance spectroscopy (EIS). Before recording the spectra, hydrogels were anchored on indium tin oxide coated poly(ethylene terephthalate) (ITO-PET) and incubated in PBS 0.1 M (pH 7.3) for 24 h to ensure swelling to equilibrium. Results, which were plotted in the form of Nyquist and Bode plots, are shown in **Figure 3.3.11**. Inspection of the Nyquist plots (**Figure 3.3.11a**), in which the real part of the impedance (Z') is plotted versus the negative part of the impedance (–Z''), reveals a similar profile for all hydrogels, which contains only spike. The bulk resistance (R_b) value of the hydrogels was obtained from the intersection between the spike and the real axis. The fact that the R_b of hydrogels is very similar to that of bare ITO-PET electrodes indicates that the studied hydrogels present good interfacial contacts with the ITO-PET electrode. R_b is largely influenced by the resistance of the electrolytic solution inside the pore, which depends on the ionic concentration, type of ions, temperature and the geometry of the area in which the current is carried (*i.e.* hydrogel pore area). Considering that in this work all hydrogels were soaked in a PBS 0.1 M electrolytic solution and that the temperature was very similar in all experiments, the small variation expected among the different analyzed systems should be attributed to the different concentration of ions inside the hydrogels (*i.e.* the doping capacity of the hydrogels) and the morphology of the hydrogel (*i.e.* pore area). Thus, the lower the concentration and the mobility of ions (*i.e.* more restricted by the morphology) in the hydrogel, the higher the R_b value will be.

The Bode diagram, which represents the frequency response of impedance (**Figure 3.3.11b**), reflect that all hydrogels exhibited high impedance values at high frequencies (> 1 kHz) due to capacitive currents, even though at physiologically-relevant low frequencies the impedance is lower for hydrogels than for ITO. Despite this expected result, it should be remarked that PGGA/PEDOT/CUR is the hydrogel with highest impedance at low frequencies.
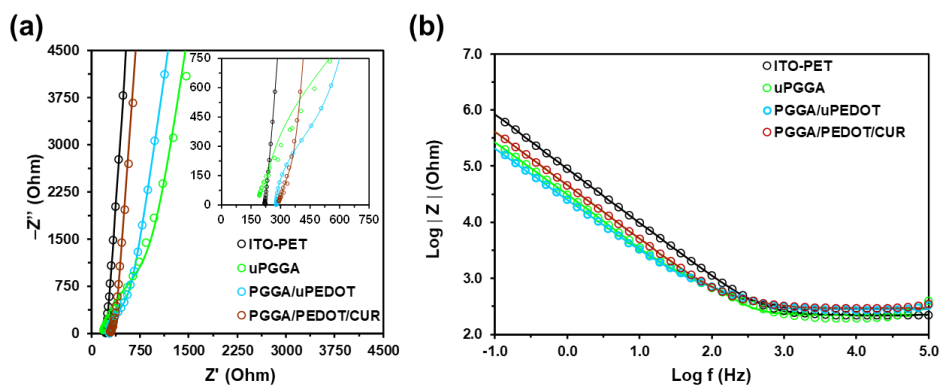
Figure 3.3.11. (a) Nyquist and (b) Bode plots of uPGGA, PGGA/PEDOT and PGGA/PEDOT/CUR hydrogels.

The CUR release profiles without and with electrical stimulation (ST) obtained for PEDOT/CUR NPs in phosphate buffer saline (PBS) solution with a very small amount (0.05%) polyoxyethylenesorbitan monolaurate solution, a non-ionic emulsifying agent widely employed in biomedical and pharmaceutic applications against aggregation, are compared in **Figure 3.3.12a**. The stimulation consisted in the application of an electric voltage of –0.50 V for 15 min every 24 h. Although a sustained release was observed in both cases, it should be remarked that it was two and a half higher with ST than without stimulus, which is consistent with previous observations in which the capacity of PEDOT NPs as electro-responsive drug carriers was proved.[2]
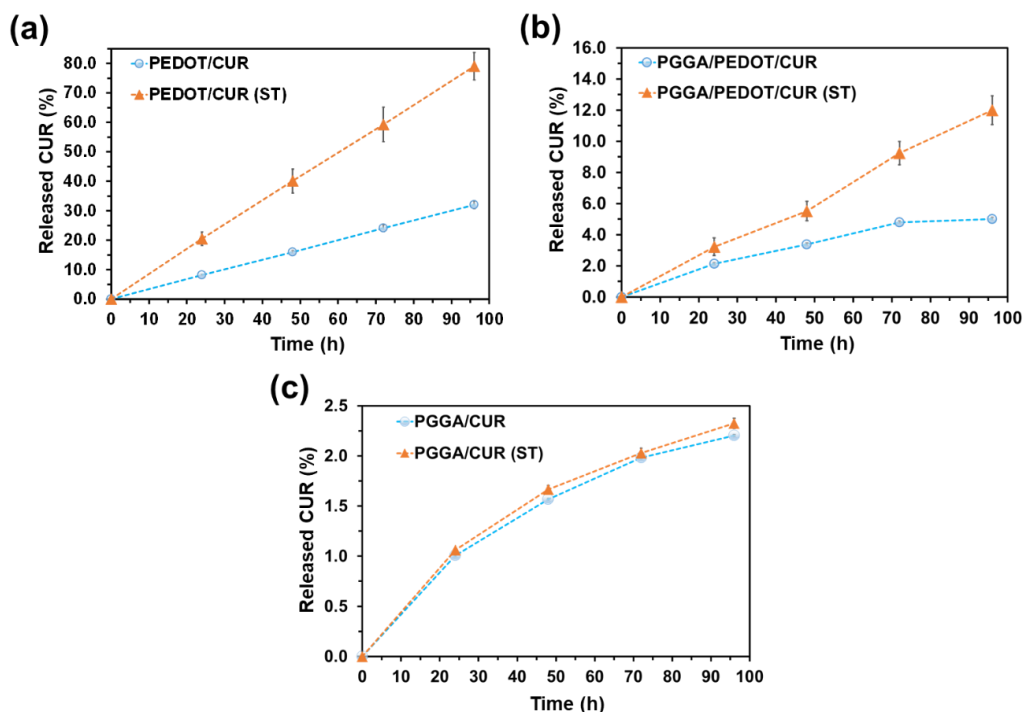
Figure 3.3.12. Release profiles without (blue circles) and with (orange triangles) electrical stimulation (ST)obtained for (a) PEDOT/CUR NPs, (b) PGGA/PEDOT/CUR and (c) PGGA/CUR hydrogels in PBS with a very small amount (0.05%) of polyoxyethylenesorbitan monolaurate solution.

Figure 3.3.12b displays the release profiles of PGGA/PEDOT/CUR hydrogels without and with ST, which present significant differences with respect to those obtained for PEDOT/CUR. Thus, the release of CUR is much slower from hydrogels than from CP NPs, independently of the ST. This feature suggests that, as this drug is hydrophobic and exhibits very poor solubility in water, it remains encapsulated inside the hydrogel, interacting with PGGA chains, once it is released from the NP. In spite of this, the amount of CUR released with ST is more than twice that without ST (*i.e.* ~12% vs. ~5% after 96 h). This hypothesis is fully consistent with the release profiles obtained for PGGA/CUR (**Figure 3.3.12c**), which reflect very slow release of drug. Moreover, as it was

169

expected from the absence of electrochemically responsive CP NPs, the profiles with and without ST are very similar.

3.3.4 Conclusions

We have introduced a new system, which combines the advantages of biohydrogels and the electrochemical activity of CP NPs to regulate the release of CUR. The release of this drug, which is a potent anti-inflammatory molecule that halts cancer initiation and progression, represents a challenge due to its poor solubility in water and rapid metabolism. PEDOT NPs, which are much smaller than hydrogel micropores (i.e. nanometric versus micrometric length scales), were chosen as suitable nanocarriers of CUR due to their excellent electrochemical response, high stability and previously proved biocompatibility. On the other hand, hydrogels prepared using PGGA, which is a water-soluble, anionic, biodegradable, and edible biopolymer, are biocompatible and environmentally friendly materials that can be used for biomedical applications. The innovative combination of PEDOT NPs and PGGA hydrogel, two entirely different types of biomaterials, has generated a novel hybrid material with increased structural diversity and enhanced drug delivery properties for the controlled release of CUR. This hybrid biomaterial has shown that the slow but sustained CUR release observed in the absence of external stimulus can be enhanced by applying an electrical voltage, allowing to modulate the release kinetics.

In summary, progress in materials development by combining hydrogels and conducting NPs has led to design a smart stimuli-responsive system, PGGA/PEDOT/CUR, which is able to deliver the small hydrophobic drug in temporal and dosage-controlled fashions. The assembly of biocompatible

170

materials susceptible to specific exogenous stimulus allows great flexibility in the design of specific drug-carriers with potential biomedical applications.

3.3.5 References

1.   Wang, X.-X. *et al.* Conductive polymer ultrafine fibers via electrospinning: Preparation, physical properties and applications. *Progress in Materials Science* **115**, 100704 (2021).

2.   Puiggalí-Jou, A., del Valle, L. J. & Alemán, C. Drug delivery systems based on intrinsically conducting polymers. *Journal of Controlled Release* **309**, 244–264 (2019).

3.   Preman, N. K., Barki, R. R., Vijayan, A., Sanjeeva, S. G. & Johnson, R. P. Recent developments in stimuli-responsive polymer nanogels for drug delivery and diagnostics: A review. *European Journal of Pharmaceutics and Biopharmaceutics* **157**, 121–153 (2020).

4.   Nguyen, D. D. & Lai, J.-Y. Advancing the stimuli response of polymer-based drug delivery systems for ocular disease treatment. *Polymer Chemistry* **11**, 6988–7008 (2020).

5.   Santos, A. M. *et al.* Recent advances in hydrogels as strategy for drug delivery intended to vaginal infections. *International Journal of Pharmaceutics* **590**, 119867 (2020).

6.   Shahriari, M. *et al.* "Smart" self-assembled structures: toward intelligent dual responsive drug delivery systems. *Biomaterials Science* **8**, 5787–5803 (2020).

7.   Behl, A., Parmar, V. S., Malhotra, S. & Chhillar, A. K. Biodegradable diblock copolymeric PEG-PCL nanoparticles: Synthesis, characterization and applications as anticancer drug delivery agents. *Polymer* **207**, 122901 (2020).

8.   dos Santos, D. M., Correa, D. S., Medeiros, E. S., Oliveira, J. E. & Mattoso, L. H. C. Advances in Functional Polymer Nanofibers: From Spinning Fabrication Techniques to Recent Biomedical Applications. *ACS Applied Materials & Interfaces* **12**, 45673–45701 (2020).

9.   Peers, S., Montembault, A. & Ladavière, C. Chitosan hydrogels for sustained drug delivery. *Journal of Controlled Release* **326**, 150–163 (2020).

10.   Idrees, H. *et al.* A Review of Biodegradable Natural Polymer-Based Nanoparticles for Drug Delivery Applications. *Nanomaterials* **10**, 1970 (2020).

11.   Ayoubi-Joshaghani, M. H. *et al.* Potential Applications of Advanced Nano/Hydrogels in Biomedicine: Static, Dynamic, Multi-Stage, and Bioinspired. *Advanced Functional Materials* **30**, 2004098 (2020).

12. Scicluna, M. C. & Vella-Zarb, L. Evolution of Nanocarrier Drug-Delivery Systems and Recent Advancements in Covalent Organic Framework–Drug Systems. *ACS Applied Nano Materials* **3**, 3097–3115 (2020).

13. Wang, Y., Zhang, H., Wang, Z. & Feng, L. Photothermal Conjugated Polymers and Their Biological Applications in Imaging and Therapy. *ACS Applied Polymer Materials* **2**, 4222–4240 (2020).

14. Wang, H. *et al.* Chiral, thermal-responsive hydrogels containing helical hydrophilic polyacetylene: preparation and enantio-differentiating release ability. *Polymer Chemistry* **10**, 1780–1786 (2019).

15. Le, P. N., Huynh, C. K. & Tran, N. Q. Advances in thermosensitive polymer-grafted platforms for biomedical applications. *Materials Science and Engineering: C* **92**, 1016–1030 (2018).

16. Kubo, T. *et al.* Magnetic Field Stimuli-Sensitive Drug Release Using a Magnetic Thermal Seed Coated with Thermal-Responsive Molecularly Imprinted Polymer. *ACS Biomaterials Science & Engineering* **5**, 759–767 (2019).

17. Wang, C.-Y. *et al.* Electrostatic droplets assisted in situ synthesis of superparamagnetic chitosan microparticles for magnetic-responsive controlled drug release and copper ion removal. *Journal of Materials Chemistry B* **1**, 2205 (2013).

18. Yap, J. E., Zhang, L., Lovegrove, J. T., Beves, J. E. & Stenzel, M. H. Visible Light—Responsive Drug Delivery Nanoparticle via Donor–Acceptor Stenhouse Adducts (DASA). *Macromolecular Rapid Communications* **41**, 2000236 (2020).

19. Misra, R. *et al.* Radioluminescent nanoparticles for radiation-controlled release of drugs. *Journal of Controlled Release* **303**, 237–252 (2019).

20. Ma, B.-A. & Sun, C.-Y. Tumor pH-triggered "charge conversion" nanocarriers with on-demand drug release for precise cancer therapy. *Journal of Materials Chemistry B* **8**, 9351–9361 (2020).

21. Ye, M. *et al.* pH-Responsive Polymer–Drug Conjugate: An Effective Strategy to Combat the Antimicrobial Resistance. *Advanced Functional Materials* **30**, 2002655 (2020).

22. Neumann, S. E., Chamberlayne, C. F. & Zare, R. N. Electrically controlled drug release using pH-sensitive polymer films. *Nanoscale* **10**, 10087–10093 (2018).

23. Puiggalí-Jou, A., Micheletti, P., Estrany, F., del Valle, L. J. & Alemán, C. Electrostimulated Release of Neutral Drugs from Polythiophene Nanoparticles: Smart Regulation of Drug-Polymer Interactions. *Advanced Healthcare Materials* **6**, 1700453 (2017).

24. Puiggalí-Jou, A., del Valle, L. J. & Alemán, C. Encapsulation and Storage of Therapeutic Fibrin-Homing Peptides using Conducting Polymer Nanoparticles for Programmed Release by Electrical Stimulation. *ACS Biomaterials Science & Engineering* **6**, 2135–2145 (2020).

25.   Samanta, D., Hosseini-Nassab, N. & Zare, R. N. Electroresponsive nanoparticles for drug delivery on demand. *Nanoscale* **8**, 9310–9317 (2016).

26.   Samanta, D., Hosseini-Nassab, N., McCarty, A. D. & Zare, R. N. Ultra-low voltage triggered release of an anti-cancer drug from polypyrrole nanoparticles. *Nanoscale* **10**, 9773–9779 (2018).

27.   Thorat, N. D. *et al.* Progress in Remotely Triggered Hybrid Nanostructures for Next-Generation Brain Cancer Theranostics. *ACS Biomaterials Science & Engineering* **5**, 2669–2687 (2019).

28.   Du, Z. J., Bi, G. & Cui, X. T. Electrically Controlled Neurochemical Release from Dual-Layer Conducting Polymer Films for Precise Modulation of Neural Network Activity in Rat Barrel Cortex. *Advanced Functional Materials* **28**, 1703988 (2018).

29.   Park, Y., Jung, J. & Chang, M. Research Progress on Conducting Polymer-Based Biomedical Applications. *Applied Sciences* **9**, 1070 (2019).

30.   Puiggalí-Jou, A., Cejudo, A., del Valle, L. J. & Alemán, C. Smart Drug Delivery from Electrospun Fibers through Electroresponsive Polymeric Nanoparticles. *ACS Applied Bio Materials* **1**, 1594–1605 (2018).

31.   Krausz, A. E. *et al.* Curcumin-encapsulated nanoparticles as innovative antimicrobial and wound healing agent. *Nanomedicine: Nanotechnology, Biology and Medicine* **11**, 195–206 (2015).

32.   Cavaleri, F. Presenting a New Standard Drug Model for Turmeric and Its Prized Extract, Curcumin. *International Journal of Inflammation* **2018**, 1–18 (2018).

33.   Daugherty, D. J., Marquez, A., Calcutt, N. A. & Schubert, D. A novel curcumin derivative for the treatment of diabetic neuropathy. *Neuropharmacology* **129**, 26–35 (2018).

34.   Lerdchai, K., Kitsongsermthon, J., Ratanavaraporn, J., Kanokpanont, S. & Damrongsakkul, S. Thai Silk Fibroin/Gelatin Sponges for the Dual Controlled Release of Curcumin and Docosahexaenoic Acid for Anticancer Treatment. *Journal of Pharmaceutical Sciences* **105**, 221–230 (2016).

35.   Ye, M.-X., Li, Y., Yin, H. & Zhang, J. Curcumin: Updated Molecular Mechanisms and Intervention Targets in Human Lung Cancer. *International Journal of Molecular Sciences* **13**, 3959–3978 (2012).

36.   Mehanny, M., Hathout, R. M., Geneidi, A. S. & Mansour, S. Exploring the use of nanocarrier systems to deliver the magical molecule; Curcumin and its derivatives. *Journal of Controlled Release* **225**, 1–30 (2016).

37.   Puiggalí-Jou, A. *et al.* Electroresponsive Alginate-Based Hydrogels for Controlled Release of Hydrophobic Drugs. *ACS Biomaterials Science & Engineering* **6**, 6228–6240 (2020).

38.   Bubnova, O. *et al.* Semi-metallic polymers. *Nature Materials* **13**, 190–194 (2014).

173

39. Kayser, L. v. & Lipomi, D. J. Stretchable Conductive Polymers and Composites Based on PEDOT and PEDOT:PSS. *Advanced Materials* **31**, 1806133 (2019).

40. Sappia, L. D. *et al.* Integration of Biorecognition Elements on PEDOT Platforms through Supramolecular Interactions. *Advanced Materials Interfaces* **4**, 1700502 (2017).

41. Luo, S.-C. *et al.* Poly(3,4-ethylenedioxythiophene) (PEDOT) Nanobiointerfaces: Thin, Ultrasmooth, and Functionalized PEDOT Films with in Vitro and in Vivo Biocompatibility. *Langmuir* **24**, 8071–8077 (2008).

42. Peramo, A. *et al. In Situ* Polymerization of a Conductive Polymer in Acellular Muscle Tissue Constructs. *Tissue Engineering Part A* **14**, 423–432 (2008).

43. Fabregat, G. *et al.* Incorporation of a Clot-Binding Peptide into Polythiophene: Properties of Composites for Biomedical Applications. *ACS Applied Materials & Interfaces* **6**, 11940–11954 (2014).

44. Khodagholy, D. *et al.* Highly Conformable Conducting Polymer Electrodes for In Vivo Recordings. *Advanced Materials* **23**, H268–H272 (2011).

45. Hempel, F. *et al.* PEDOT:PSS organic electrochemical transistor arrays for extracellular electrophysiological sensing of cardiac cells. *Biosensors and Bioelectronics* **93**, 132–138 (2017).

46. Yang, B. *et al.* A conductive PEDOT/alginate porous scaffold as a platform to modulate the biological behaviors of brown adipose-derived stem cells. *Biomaterials Science* **8**, 3173–3185 (2020).

47. Puiggalí-Jou, A., del Valle, L. J. & Alemán, C. Cell Responses to Electrical Pulse Stimulation for Anticancer Drug Release. *Materials* **12**, 2633 (2019).

48. Khalil, I. *et al.* Bacterial-Derived Polymer Poly-y-Glutamic Acid (y-PGA)-Based Micro/Nanoparticles as a Delivery System for Antimicrobials and Other Biomedical Applications. *International Journal of Molecular Sciences* **18**, 313 (2017).

49. Luo, Z. *et al.* Microbial synthesis of poly-γ-glutamic acid: current progress, challenges, and future perspectives. *Biotechnology for Biofuels* **9**, 134 (2016).

50. Pérez-Madrigal, M. M., Edo, M. G., Díaz, A., Puiggalí, J. & Alemán, C. Poly-γ-glutamic Acid Hydrogels as Electrolyte for Poly(3,4-ethylenedioxythiophene)-Based Supercapacitors. *The Journal of Physical Chemistry C* **121**, 3182–3193 (2017).

51. Saborío, M. G. *et al.* Isomeric cationic ionenes as n-dopant agents of poly(3,4-ethylenedioxythiophene) for *in situ* gelation. *Soft Matter* **14**, 6374–6385 (2018).

174

52. Stavytska-Barba, M. & Kelley, A. M. Surface-Enhanced Raman Study of the Interaction of PEDOT:PSS with Plasmonically Active Nanoparticles. *The Journal of Physical Chemistry C* **114**, 6822–6830 (2010).

53. Ivanko, I., Pánek, J., Svoboda, J., Zhigunov, A. & Tomšík, E. Tuning the photoluminescence and anisotropic structure of PEDOT. *Journal of Materials Chemistry C* **7**, 7013–7019 (2019).

54. Fabregat, G., Alemán, C., Casas, M. T. & Armelin, E. Controlling the Morphology of Poly(*N* - cyanoethylpyrrole). *The Journal of Physical Chemistry B* **116**, 5064–5070 (2012).

55. Erez, Y., Simkovitch, R., Shomer, S., Gepshtein, R. & Huppert, D. Effect of Acid on the Ultraviolet– Visible Absorption and Emission Properties of Curcumin. *The Journal of Physical Chemistry A* **118**, 872–884 (2014).

56. Danhier, F., Feron, O. & Préat, V. To exploit the tumor microenvironment: Passive and active tumor targeting of nanocarriers for anti-cancer drug delivery. *Journal of Controlled Release* **148**, 135–146 (2010).

57. Masek, A., Chrzescijanska, E. & Zaborski, M. Characteristics of curcumin using cyclic voltammetry, UV–vis, fluorescence and thermogravimetric analysis. *Electrochimica Acta* **107**, 441– 447 (2013).

58. Aradilla, D., Estrany, F., Armelin, E. & Alemán, C. Ultraporous poly(3,4-ethylenedioxythiophene) for nanometric electrochemical supercapacitor. *Thin Solid Films* **520**, 4402–4409 (2012).

59. Aradilla, D., Estrany, F., Casellas, F., Iribarren, J. I. & Alemán, C. All-polythiophene rechargeable batteries. *Organic Electronics* **15**, 40–46 (2014).

3.4 Scaffolds for sustained release of ambroxol hydrochloride, a pharmacological chaperone that increases the activity of misfolded β-Glucocerebrosidase

Ambroxol is a pharmacological chaperone (PC) for Gaucher disease that increases lysosomal activity of misfolded β-glucocerebrosidase (GCase) while displaying a safe toxicological profile. In this work, we have developed different poly(ε-caprolactone) (PCL)-based systems to regulate the sustained release of small polar drugs in physiological environments. For this purpose, ambroxol has been selected as test case since the encapsulation and release of PCs using polymeric scaffolds have not been explored yet. More specifically, ambroxol has been successfully loaded in electrospun PCL microfibers, which have been subsequently coated with additional PCL layers using dip-coating or spin-coating. The time needed to achieve 80% release of loaded ambroxol increases from ~15 min for uncoated fibrous scaffolds to 3 days and 1 week for dip-coated and spin-coated systems, respectively. Furthermore, we have proved that the released drug maintains its bioactivity, protecting GCase against induced thermal denaturation.

177

3.4.1   Introduction

Existing polymer-based drug delivery systems can be divided into two groups based on their mode of administration. The first relies on systemic delivery and consists of nano-materials such as polymer nanoparticles, liposomes, and dendrimers. These delivery vehicles, which are predominantly intended for oral or intravenous administration, find their target by passive diffusion or by triggering the release of payload from an environment-responsive nano-carrier using a local stimulus (*i.e.* pH, temperature, etc). However, systemic delivery may result in suboptimal drug therapeutic concentration, leading to erroneous conclusions regarding agent efficacy. The second group of polymer delivery vehicles (and focus of this research) includes controlled release drug delivery depot systems for implantation inside or adjacent to the target tissue. The majority of these local polymer device systems are biodegradable so as to circumvent a second surgery for device removal and to avoid a chronic foreign-body immune response. The polymers used in these systems are often hydrophobic in nature, and are ideally suited for long-term delivery and internal stabilization of sensitive water-insoluble hydrophobic drugs. Nevertheless, long-term delivery of polar drugs remains a challenge since they are rapidly extracted from the vehicle by the aqueous environment of the target, making difficult the achievement of sustained concentrations in detriment of the localized therapy.

On the other hand, pharmacological chaperone (PC) therapy is an emerging therapeutic approach for the treatment of protein misfolding diseases, which consists of a diverse group of disorders associated with the incorrect folding of specific proteins.[1–4] Some misfolding diseases are due to missense protein mutations that cause abnormal conformations and the consequent loss of the function. PC therapy is based on the use of small molecule ligands (*i.e.* the PCs) that selectively bind and stabilize mutated proteins, thus, favoring their correct conformation.[5–11] Therefore, the activity of the mutated proteins is partially

178

rescued, which has a favorable impact on the patient status and the rate of disease progression.

This work aims to design a long-term delivery polymer vehicle for polar hydrophilic drugs, which does not affect the bioactivity. For this purpose, we have chosen ambroxol hydrochloride (AH; **Figure 3.4.1**), a mucolytic agent that potentiates the activity of sodium channels, which has been shown to act also as a PC for the lysosomal enzyme β-glucocerebrosidase (GCase). Mutations in the GCase gene cause Gaucher's disease, which is the most prevalent lysosomal storage disease. AH has been shown to promote and stabilize the proper folding of GCase in the endoplasmic reticulum.[12] The PC role played by AH in the enhancement of the activity of misfolded GCase has been demonstrated using *in vitro*[12–15] and *in vivo* models.[16,17] Furthermore, recent clinical trials in patients with Gaucher disease showed that AH led to substantial clinical improvement.[18]
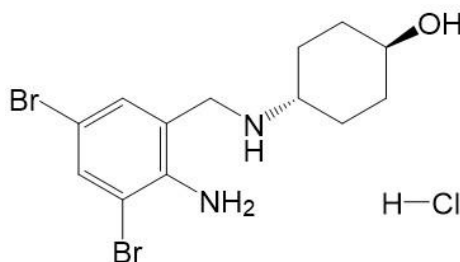
Figure 3.4.1. Chemical structure of AH

Although AH can be administered orally or through intravenous injection, the tissue distribution is unfortunately rather heterogeneous (*e.g.* AH is much easily distributed in lung tissue than in brain tissue)[12] and, therefore, its encapsulation into carriers to regulate its release might be highly desirable from a therapeutic point of view. In general, on demand local delivery of drug molecules provides a means for effective drug distribution and dosing, fulfilling requirements for a variety of therapeutic applications while reducing the adverse effects of systemic drug administration.[19–21] Indeed, recent advances have facilitated the use of

various cues, such as UV- and visible-wavelength light, NIR radiation, magnetic field, ultrasound or electrical stimulation to trigger the release of different types of drugs from smart materials.[21–26] Besides, as the utilization of PCs is a therapeutic paradigm recently launched, the encapsulation and release of these small ligands using polymeric scaffolds have not been explored yet. Studies oriented towards this aim might be useful in a near future.

In this work we have engineered poly(ε-caprolactone) (PCL) layered systems consisting of electrospun microfibers (MFs), which successfully encapsulate the PC, protected with a coating that regulates the release. This protection has been achieved by sandwiching the loaded MFs between two outer spin-coated nanomembranes (NMs) or by dip-coating the loaded MFs into a polymer solution. Electrospinning is a well-known electrostatic technique that uses a high voltage field to charge the surface of a polymer solution droplet at the end of a capillary tube and induce the ejection of a liquid jet towards a grounded target (collector).[27–30] Morphology of fibers obtained in the collector depends on the solution properties (*e.g.* viscosity, dielectric constant, volatility and concentration) and operational parameters (*e.g.* strength of the applied electric field, deposition distance and flow rate), which should be conveniently addressed.[31,32] In recent years, electrospinning experienced a fast developing to simultaneous treatment of multiple fluids for creating complex nanostructures, such as core-shell, tri-layer from the coaxial and tri-axial electrospinning processes.[33,34] Although these core-shell nanostructures can provide tunable drug sustained release profiles,[35,36] the after-treatment of nanofibers from a single-fluid blending process represents another way for achieving an improved sustained release. We have focused on this second approach which, due to its macro-scale nature, has the advantage of being more easily scaled-up.

On the other hand, PCL has attracted an increasing interest in recent decades due to its biodegradability, easy processability and suitability for tissue

engineering applications.[37–39] The use of this aliphatic polyester for biomedical applications was approved by the USA Food and Drug Administration (FDA) in the seventies and PCL can be found in many common sutures and suture components. Although small hydrophobic drugs were successfully loaded and smartly released from PCL electrospun fibers,[26,40] the polarity of the studied PC has motivated the design of the PCL-based layered systems to obtain slow and sustained release of active AH in physiological media. Thus, the polar hydrogen bonding acceptor and donor groups identified in the chemical structure of AH (**Figure 3.4.1**) are expected to favor a very fast release rate in hydrophilic physiological environments, making difficult its dosage when continued administration is required. In order to avoid such limitation, which is can be extrapolated to other polar and hydrophilic drugs, in this work we propose different coating strategies to regulate the release depending on the necessities.

3.4.2 Methods

3.4.2.1 *Materials*

PCL (Aldrich, UK, Mn: 80,000), AH (Sigma, Italy), chloroform (Scharlau, Spain; stabilized with amylene, 99.8% pure), acetone (Sigma, South Korea, 99.9% pure) formic acid (FA; Panreac, E.U., 98% pure), and 2,2,2-trifluoroethanol (TFE; Sigma, USA, 99% pure) were used as received.

3.4.2.2 *Electrospinning*

PCL is frequently electrospun from chloroform or chloroform:acetone solutions[38,40] but AH is insoluble in such organic solvents. However, AH can be solubilized in chloroform:acetone if either TFE or FA is present. Accordingly, electrospun MFs were prepared by dissolving PCL in a 2:1 *v/v*

chloroform:acetone mixture while AH was dissolved in either TFE or FA. Electrospun AH-loaded PCL MFs coming from TFE and FA solutions have been denoted PCL/AH(TFE) and PCL/AH(FA), respectively, while unloaded PCL MFs (controls) are labelled as PCL(TFE) and PCL(FA). Although PCL and AH concentrations, as well as the electrospinning operational conditions, were optimized to avoid the formation of undesirable beads and droplets in PCL/AH(TFE) and PCL/AH(FA) MFs, only the optimized parameters are described below.

Specifically, PCL/AH(TFE) MFs were prepared by dissolving 1.3 g of PCL in 7.5 mL of a 2:1 *v/v* chloroform:acetone mixture using an incubator (37 ℃ and 120 rpm) for 12 h, while 0.0375 g of AH were added to 2.88 mL of TFE and vortexed extensively until completely dissolved. Then both solutions were thoroughly mixed together by additional strong vortexing. On the other hand, electrospun PCL/AH(FA) MFs were obtained by dissolving 1.3 g of PCL in 9.85 mL of the same 2:1 *v/v* chloroform:acetone solution. In this case, the PC was prepared by adding 0.0375 g of AH to 50 μL of 2:1 v/v chloroform:acetone. Then, 0.1 mL of FA was immediately added and the mixture was intensively vortexed until the drug was completely dissolved. Again, both solutions were mixed together with vigorous and extensive shaking. PCL(TFE) and PCL(FA) controls were prepared using identical procedures and solvents but without including the AH. The concentration of drug in PCL/AH(TFE) and PCL/AH(FA) MFs was below the cytotoxic threshold.[12]

Electrospinning was carried out in a non-conductor chamber. Solutions were loaded in a 10 mL BD Discardit (Becton Dickson Co., Franklin Lakes, NJ, USA) plastic syringe for delivery through a blunt-tipped (*i.e.* without bevel) 18 G needle (inner diameter 0.84 mm). The flow rate and the needle tip-collector distance were 5 mL/h and 15 cm, respectively, for PCL/AH(TFE) and PCL(TFE), whereas these parameters changed to 4 mL/h and 25 cm, respectively, for PCL/AH(FA) and

PCL(FA). The voltage, which was applied through a high-voltage Gamma High Voltage Research (ES30-5W) power supply, was 20 kV in all cases. All electrospinning experiments were carried out at room temperature.

3.4.2.3 Spin-coating and dip-coating

Poly(ε-caprolactone) nanomembranes (PCL NMs) were spin-coated for the preparation of multilayered AH-loaded systems. Spin-coating was performed with a spin-coater (WS-400BZ-6NPP/A1/AR1 Laurell Technologies Corporation). In all cases, the first PCL NM was spin-coated using a Teflon® square plate as substrate (area: 2×2 cm^2), which was previously cleaned by sonication in three different solvents (5 min each): milli-Q water, acetone and ethanol. For the fabrication of the PCL NMs, 1 mL of a 60 mg/mL polymer solution in acetone was first spin-coated onto the Teflon® substrate at 750 rpm for 1 min (first layer). After placing a 1×1 cm^2 piece of an AH-loaded fibrous mat on top of this layer, a second PCL NM was created by spin-coating under the same conditions (top layer). Alternatively, coating was also performed by dipping the fibrous mat for 3 seconds in a 60 mg/mL PCL solution in acetone (dip-coating). In all cases, multilayered systems with non-drug-containing fibrous mats were also prepared as controls.

3.4.2.4 Scanning electron microscopy (SEM)

The morphology and texture of electrospun MFs was examined by SEM using a Focus Ion Beam Zeiss Neon 40 instrument (Carl Zeiss, Germany). Fibrous mats, which were cut in 1×1 cm^2 samples, were mounted on a double-sided adhesive carbon disc and sputter-coated with a thin layer of carbon to prevent sample charging problems. All samples were observed at an accelerating voltage of 5 kV.

Diameters of electrospun MFs were measured with the SmartTiff software from Carl Zeiss SMT Ltd.

3.4.2.5 *Atomic force microscopy (AFM)*

AFM studies were conducted to obtain topographic and phase images of the surface of MFs using TAP 150-G silicon tapping probes. Images were obtained with an AFM Dimension microscope using the NanoScope IV controller under ambient conditions in tapping mode. The root mean square roughness (R_q), which is the average height deviation taken from the mean data plane, was determined using the statistical application of the NanoScope Analysis software (1.20, Veeco).

3.4.2.6 *Fourier transform infrared (FTIR) Spectroscopy*

FTIR spectra were recorded with a Fourier Transform FTIR 4100 Jasco spectrometer (Jasco Analytical Instruments, Easton, USA) in the 4000–600 cm^{-1} range. An attenuated total reflection (ATR) system with a heated Diamond ATR Top-Plate (model MKII Golden Gate™, Specac Ltd., Orpington, UK) was used.

3.4.2.7 *RAMAN spectroscopy*

Raman spectra were obtained using a Renishaw inVia Qontor confocal Raman microscope. The Raman setup consisted of a laser (at 532 nm with a nominal 250 mW output power) directed through a microscope (specially adapted Leica DM2700 M microscope) to the sample, after which scattered light is collected and directed to a spectrometer with a 2400 lines·mm^{-1} grating. The exposure time was 10 s, the laser power was adjusted to 0.1% of its nominal output power depending on the sample, and each spectrum was collected with five accumulations.

184

3.4.2.8 UV-Vis spectroscopy

UV-Vis absorption spectra were recorded to confirm the presence of AH in electrospun MFs. For this purpose, fibrous mats were cut into 1×1 cm^2 samples, weighted and dissolved in 200 μL of chloroform. Then, 1 mL of milli-Q water was added and vortexed for 5 min to extract the PC. The two phases were separated by centrifuging at 12900 rpm for 3 min. Spectra of the aqueous phase were obtained using a UV-Vis-NIR Shimadzu 3600 spectrophotometer equipped with a tungsten halogen visible source, a deuterium arc UV source, a photomultiplier tube UV-Vis detector, and a InGaAs photodiode and cooled PbS photocell NIR detectors. Spectra were recorded in the absorbance mode at room temperature, the wavelength range and bandwidth being 190-400 nm and 2 nm, respectively.

3.4.2.9 X-ray photoelectron spectroscopy (XPS)

XPS analyses were performed in a SPECS system equipped with a high-intensity twin-anode X-ray source XR50 of Mg/Al (1253 eV / 1487 eV) operating at 150 W, placed perpendicular to the analyzer axis, and using a Phoibos 150 MCD-9 XP detector. The X-ray spot size was 650 μm. The pass energy was set to 25 and 0.1 eV for the survey and the narrow scans, respectively. Charge compensation was achieved with a combination of electron and argon ion flood guns. The energy and emission current of the electrons were 4 eV and 0.35 mA, respectively. For the argon gun, the energy and the emission current were 0 eV and 0.1 mA, respectively. The spectra were recorded with a pass energy of 25 eV in 0.1 eV steps at a pressure below 6×10^{-9} mbar. These standard conditions of charge compensation resulted in a negative but perfectly uniform static charge. The C 1s peak was used as an internal reference with a binding energy of

284.8 eV. The surface composition was determined using the manufacturer's sensitivity factors.

3.4.2.10 Contact angle (CA)

CA measurements were conducted using the sessile drop method. 0.5 µL of milliQ water drops were deposited onto the surface of the electrospun mats, which were cut into rectangular pieces and fixed on a holder, and recorded after stabilization with the equipment OCA 15EC (DataPhysics Instruments GmbH, Filderstadt). The SCA20 software was used to measure the CA, which is shown here as the average of at least 40 measures for each condition.

3.4.2.11 AH-release experiments

AH-loaded and unloaded (controls) fibrous mats were cut into small squares (1×1 cm^2), which were weighed and placed into Eppendorf tubes. Phosphate buffered saline (PBS) solution of pH 7.4 was considered as the release medium. Assays, which were performed in triplicate, were carried out by immersing sample mats in 1 mL of the release medium and using a rotating agitator. The medium was removed at predetermined time intervals and replaced by fresh one. The removed medium was used to quantify the released AH by measuring its absorbance in a UV-Vis-NIR Shimadzu 3600 spectrophotometer as described above. Finally, the mats were dissolved in chloroform and the residual PC was extracted for quantification. The calibration curve ($y= 6.838 \cdot x$, $R^2= 0.999$) was obtained by plotting the absorbance against AH concentration from triplicate samples (**Figure 3.4.2**). On the other hand, PCL controls evidenced that the polymer degradation products do not interfere with the AH concentration measurements in long term assays.
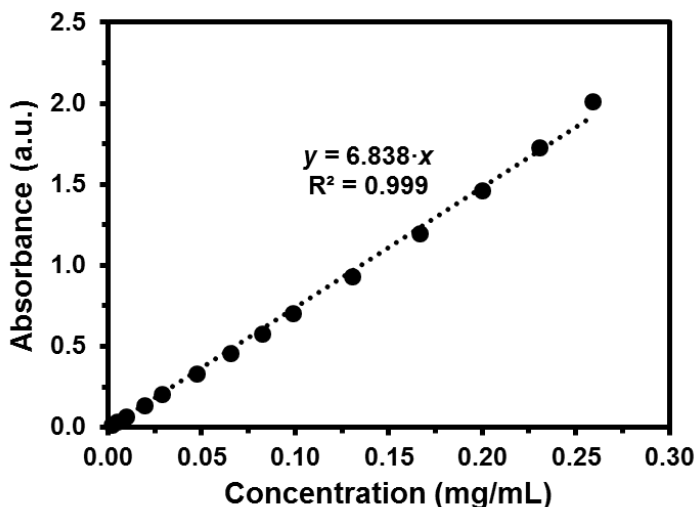
Figure 3.4.2. AH calibration curve in PBS using the absorbance at 307 nm.

3.4.2.12 Evaluation of the activity of released AH

Cell lysates, containing the lysosomal enzyme GCase, were obtained from IMR90 fibroblasts (human lung fibroblasts, ATCC-CCL-186). For this purpose, fibroblasts were grown to confluence in 100 mm dishes using DMEM high glucose medium (Invitrogen) supplemented with antibiotics (100 U/mL penicillin/streptomycin, Gibco) and 10% fetal bovine serum (FBS, Gibco) at 37 ºC in a 5% CO_2 humidified atmosphere. Cells from each plate were detached with 1 mL of trypsin (0.05% trypsin/EDTA, Invitrogen) for 10 min at 37 ºC and 4 mL of fresh medium were added to re-suspend the cells. The concentration of cells was determined by counting in a Neubauer camera using trypan blue as a vital stain. For the biological assays, cells from three plates were transferred to a 50 mL conical tube and centrifuged (10 min, 300×g), washed with PBS and centrifuged again. Cells were then re-suspended with 1 mL of PBS, counted, aliquoted and transferred to an Eppendorf tube and centrifuged (5 min, 600×g). The final cell pellet was frozen in liquid nitrogen and stored at –80 ºC until use.

Cell lysates were obtained from the harvested IMR90 fibroblasts. Aliquots of 10.7×10^6 cell pellets (each coming from three 100-mm dishes) were homogenized with 450 µL of lysis buffer (100 mM NaCl, 1 mM $MgCl_2$, 0.2% Triton X-100 (v/v), 10 mM HEPES, pH 7.4) containing 1 µg/mL aprotinin, 1 µg/mL leupeptin and 0.1 mM PMSF as protease inhibitors. Cells were broken by 20 strokes using an Eppendorf pestle and left on ice for 15 min. Cell debris was removed by centrifugation (600×g, 5 min, 4 °C) and the supernatant was aliquoted, frozen in liquid nitrogen and stored at –80 ºC.

To check the activity of the AH released from the electrospun MFs and multilayered devices, a modification of the thermal denaturation and enzyme activity assays described by Diettrich et al.[41] and Maegawa et al.[12] was used. Briefly, cell lysates (23 µL) were incubated for 60 min at 50 °C with one volume of PBS either with or without AH (fresh or released from PCL-based systems). Samples were then kept on ice for 5 min and left to equilibrate at room temperature for 5 more minutes. The same procedure using samples not submitted to thermal denaturation (kept on ice) was also carried out as a control. All the samples were prepared by duplicate.

GCase activity of the samples was tested using the fluorogenic substrate 4-methylumbelliferyl-β-D-glucopyranoside, MUbGlc (Sigma). To do this, one volume (46 µL) of substrate solution (12 mM MUbGlc, 50 mM sodium taurocholate, 0.2% Triton X-100 v/v, 0.2% human serum albumin w/v, 40 mM $CaCl_2$ in McIlvaine's citrate-phosphate buffer, pH 5.40) was added to each sample. After incubation for 1 h at 37 ºC, the reaction was stopped by adding 2.5 volumes of stop solution (0.25 M Glycine/NaOH buffer, pH 10.5). Samples were placed in a 96-well black plate (300 µL/well) and the fluorescence from the 4-methylumbelliferone (MU) reporter group released after hydrolysis of the substrate was measured in a microplate spectrofluorometer (Synergy HTX

multimode reader, BioTek) with the excitation wavelength set at 360 nm and the emission wavelength at 460 nm. The relative remaining activity of GCase after thermal denaturation was calculated by comparison with the activity measured for the corresponding control samples kept on ice (*i.e.* not submitted to thermal denaturation).

3.4.3 Results and discussion

3.4.3.1 Preparation and characterization of AH-loaded fibers

Mixtures of PCL dissolved in chloroform:acetone and AH dissolved in TFE or FA were electrospun to obtain PCL/AH(TFE) or PCL/AH(FA) MFs, respectively. The wt % of AH used in the feeding solution, which was identical in both cases, was completely incorporated into the PCL matrix during the electrospinning process. **Figure 3.4.3** compares SEM micrographs and diameter distributions of PCL/AH(TFE) and PCL/AH(FA) MFs obtained after optimization of the electrospinning conditions with those of unloaded PCL(TFE) and PCL(FA) control samples.

The utilization of TFE and FA resulted in the formation of well-defined MFs, in which droplets and beads were not detected. However, the morphology was seriously affected by both the incorporation of the drug into the polyester matrix and the effect of the solvent used to dissolve the PC in the viscosity of the feeding solution. More specifically, PCL/AH(FA) MFs present a cylindrical morphology with an average diameter (*D*) of 717±32 nm, while PCL/AH(TFE) MFs are much flatter, exhibiting a ribbon-like morphology and similar diameter (*D*= 694±13 nm). Both unloaded PCL(TFE) and PCL(FA) fibers exhibited cylindrical morphology, evidencing that, in spite of its low concentration, the influence of the PC in the viscosity of the feeding solution is much higher when it is dissolved in TFE than in FA. Clearly, this is due to the amount of TFE in the feeding

solutions used to prepare PCL/AH(TFE) and PCL(TFE), which is almost 30 times greater than the amount FA in the solutions employed to electrospun PCL/AH(FA) and PCL(FA). The remarkable influence of the TFE solvent on the viscosity of the feed solution is confirmed by the diameter of PCL(TFE) MFs (D= 1488±88 nm), which is more than twice that of PCL(FA) MFs (D= 633±33 nm).

Interestingly, PCL/AH(TFE) and PCL/AH(FA) show well-adhered particles homogeneously distributed along surface of the MFs (**Figure 3.4.3**). These round-like particles, which exhibit a diameter of several hundred of nanometers and ~100 nm for PCL/AH(TFE) and PCL/AH(FA), respectively, have been assigned to crystallized AH. These results have been attributed to the influence of AH···solvent interactions during the electrospinning process. Thus, the drug, which bears polar groups, forms crystalline domains that remain at the surface of hydrophobic PCL MFs when the electrospinning process causes the elimination of favorable AH···solvent interactions.[42] Moreover, the flat ribbon-like geometry of PCL/AH(TFE) fibers is probably due to the influence of unfavorable PCL···AH interactions in the chain entanglement of the solution mixture.[42] Thus, both the incorporation of a low molecular weight drug and the formation of such PCL···AH interactions decrease the degree of chain entanglement in the feeding solution, which is a parameter that significantly influence the fiber morphology.
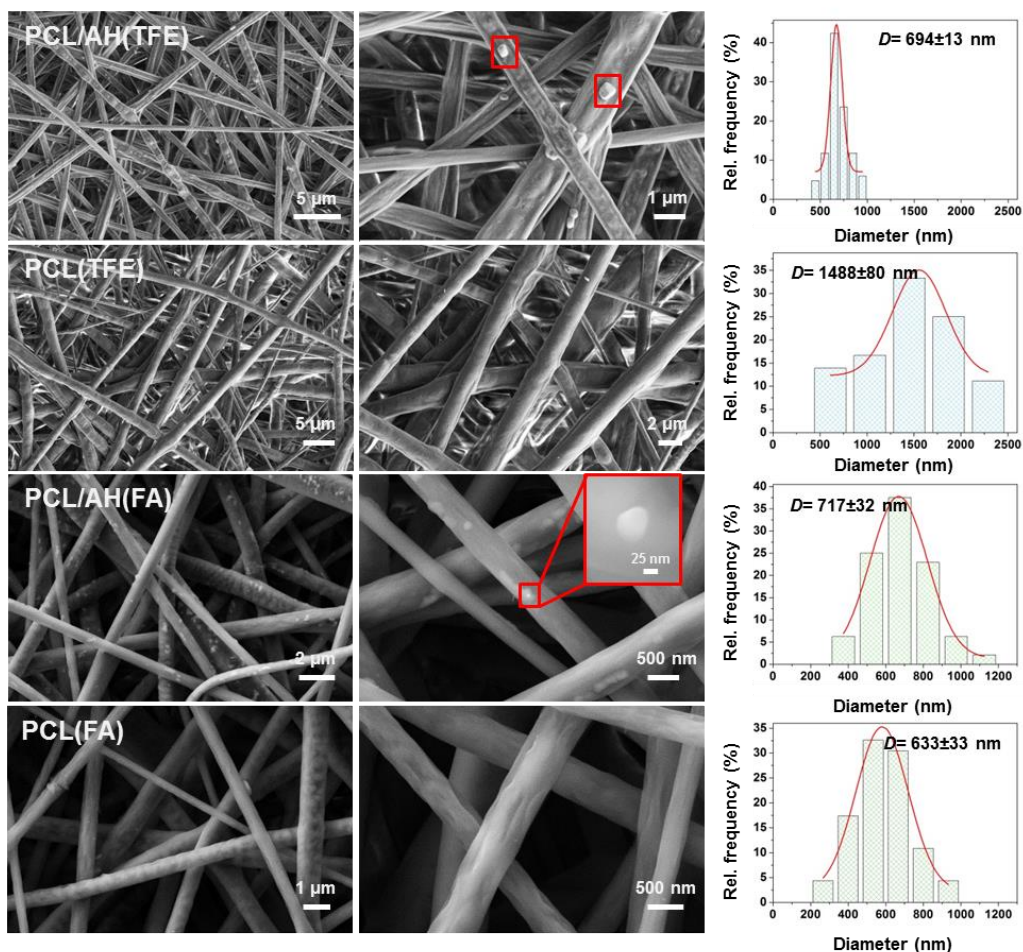
Figure 3.4.3. SEM micrographs taken at low (left) and high (center) magnification for electrospun fibers of PCL/AH(TFE), PCL(TFE), PCL/AH(FA) and PCL(FA). The diameter distribution of the electrospun microfibers and the corresponding average value ± standard deviation are displayed at the right. Particles adhered to the surface of the PCL matrix, which have been associated to the crystallized drug, are marked by red boxes for PCL/AH(TFE) and PCL/AH(FA).

AFM height and phase-contrast images are displayed in **Figure 3.4.4** for all electrospun MFs, 3D topographic images being additionally included for PCL/AH(TFE) and PCL/AH(FA). AFM images are fully consistent with previously discussed SEM observations. Both AH-loaded and unloaded MFs present a very smooth surface, the roughness ranging from $R_q= 6\pm2$ nm for

PCL/AH(TFE) to 16±3 nm for PCL(FA). Furthermore, AFM phase-contrast images obtained for PCL/AH(TFE) and PCL/AH(FA) allow to distinguish two materials with different elastic properties, which have been associated to the AH aggregates and the PCL matrix. This observation, which is much clearer for PCL/AH(TFE) than for PCL/AH(FA) due to the different sizes of AH aggregates, supports that the polar drug organizes in microphases separated from the non-polar polyester matrix.
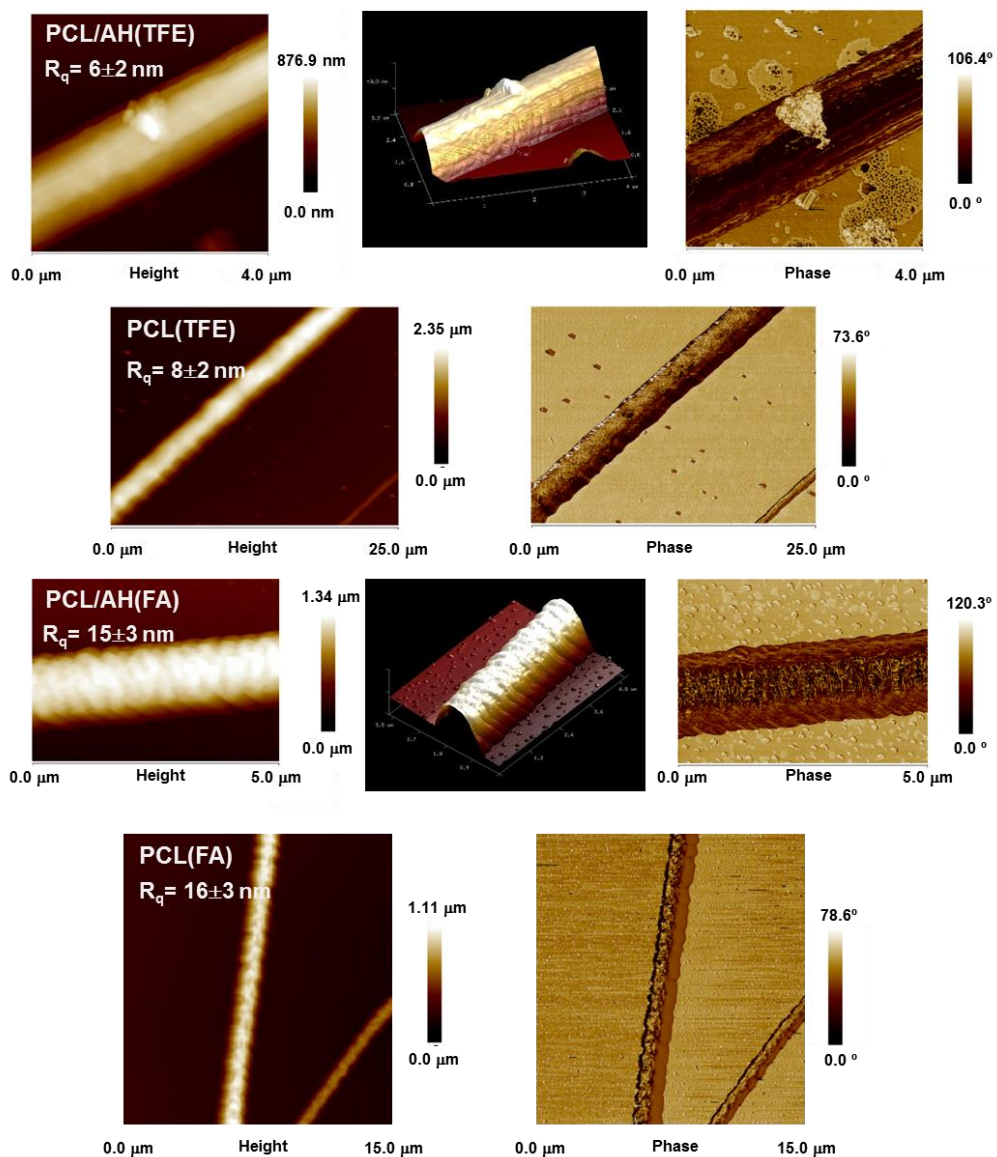
Figure 3.4.4. AFM images of PCL/AH(TFE), PCL(TFE), PCL/AH(FA) and PCL(FA): 2D height (left), 3D topographic (center; only for AH-loaded MFs) and phase-contrast (right) images. The root mean square roughness (R_q) is displayed for each system.

In order to corroborate that AH was successfully loaded in the PCL MFs, FTIR, Raman and UV-Vis spectroscopic studies were conducted. Unfortunately, the FTIR spectra recorded for AH-loaded MFs were practically identical to the spectrum of unprocessed PCL powder and, therefore, the characteristic bands

associated to the drug were undistinguishable (**Figure 3.4.5**). On the other hand, **Figure 3.4.6a** and b display the Raman spectra of electrospun MFs obtained using TFE and FA solvents, respectively. The spectrum of AH is included in both graphics for comparison. In addition to the bands observed for unloaded PCL, the spectra of AH-loaded MFs present some bands that have been associated to the PC. The weak bands at 1590 and 1555 cm^{-1}, which are detected in the spectra of both PCL/AH(TFE) and PCL/AH(FA), have been attributed to the primary and secondary amines of AH (**Figure 3.4.1**), respectively.[43] Besides, the weak signals observed at around 800 cm^{-1} in the PCL/AH(TFE) spectrum have been related with the Ar-Br Raman active modes,[43] even though these are practically undetectable for PCL/AH(FA).
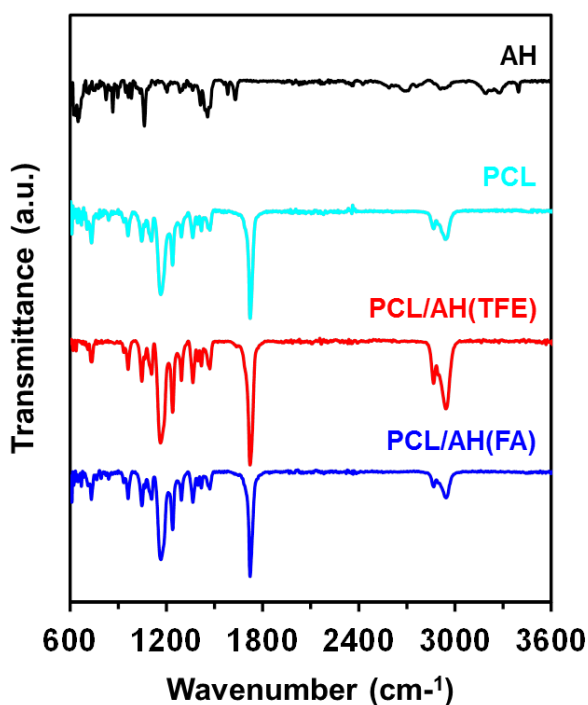
Figure 3.4.5. FTIR spectra recorded for PCL/AH(TFE) and PCL/AH(FA) MFs, PCL powder and AH.
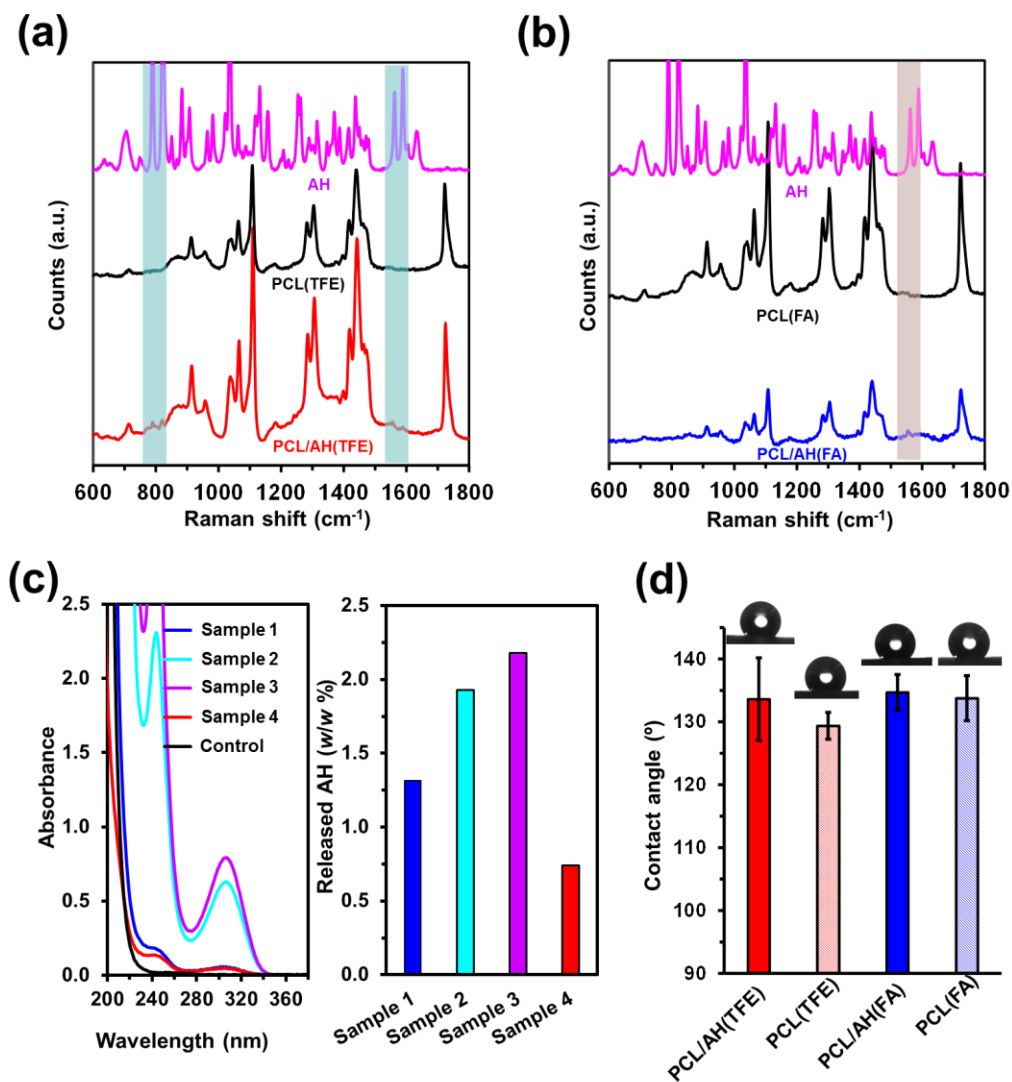
Figure 3.4.6. Comparison between the Raman spectra recorded for: (a) PCL/AH(TFE), PCL(TFE) and AH; and (b) PCL/AH(FA), PCL(FA) and AH. The weak peaks associated to AH in the spectra of PCL/AH(TFE) and PCL/AH(FA) are marked by the colored bars. (c) UV-Vis spectra of the AH-containing water solutions extracted from four samples of PCL/AH(TFE) MFs dissolved in chloroform (left) and quantification of the AH contained in the extraction medium (right). The spectra corresponding to the PCL/AH(FA) mats are displayed in **Figure 3.4.7**. (d) Contact angle for water of PCL/AH(TFE), PCL(TFE), PCL/AH(FA) and PCL(FA) fibrous mats.

The presence of AH in loaded MFs was also investigated by UV-Vis spectroscopy. For this purpose, 1×1 cm^2 samples were cut from AH-loaded fibrous mats and dissolved in chloroform. Then, the PC was extracted using water, as described in the Methods section. UV-Vis spectra of four different AH-containing aqueous solutions derived from PCL/AH(TFE) fibrous mats are displayed in **Figure 3.4.6c** together with the quantification of the PC. All spectra showed an absorption band at 307 nm, even though its intensity differs from sample to sample. Although the presence of the band confirms the successful loading of AH, the dispersion in the quantified value, with an average value of 1.54 ± 0.64 *w*/*w*%, reflects that the drug is heterogeneously distributed in the PCL matrix. Similar results were observed in the spectra recorded from PCL/AH(FA) mats (**Figure 3.4.7**), the average content being in this case 1.55 ± 0.81 *w*/*w*%. AH loading is further supported by the XPS atomic compositions obtained for the different studied MFs, which are compared in **Table 3.4.1**. Both N and Br are detected in PCL/AH(TFE) and PCL/AH(FA), while these atoms are absent in PCL(TFE) and PCL(FA).

Scaffolds for Sustained Release of Ambroxol Hydrochloride, a Pharmacological Chaperone that Increases the Activity of Misfolded β-Glucocerebrosidase.
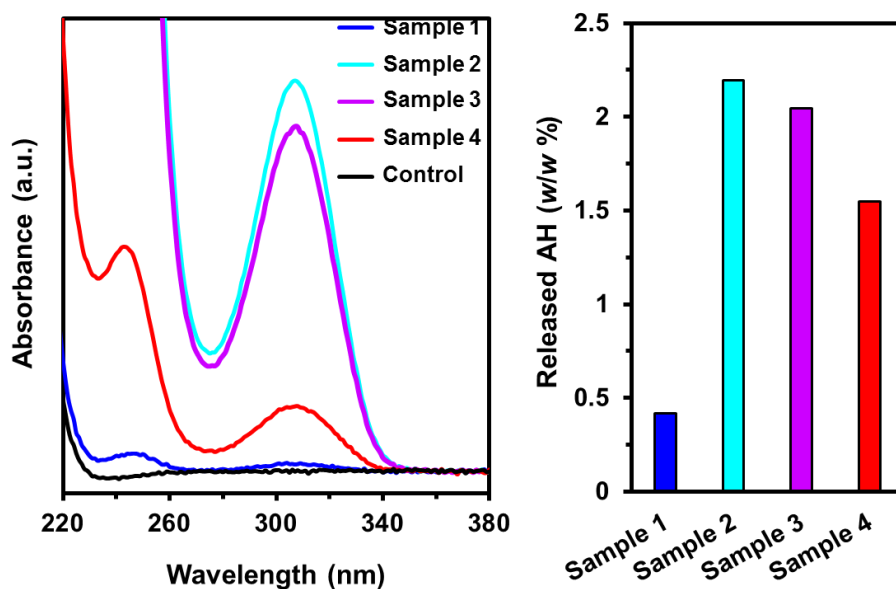
Figure 3.4.7. UV-Vis spectra of the AH-containing water solutions extracted from four samples of PCL/AH(FA) MFs dissolved in chloroform (left) and quantification of the AH contained in the extraction medium.

Table 3.4.1. Atomic percent composition obtained by XPS for AH-loaded and unloaded PCL fibers.

	C	N	O	Br
PCL/AH(TFE)	81.81	0.19	17.95	0.05
PCL(TFE)	80.04	-	19.96	-
PCL/AH(FA)	81.77	0.12	18.08	0.03
PCL(FA)	82.32	-	17.68	-

The water contact angle (θ) of fibrous mats was determined for AH-loaded and unloaded PCL matrixes (**Figure 3.4.6d**). The contact angles indicate that all materials are hydrophobic (*i.e.* $\theta > 90°$) and, interestingly, the wettability does not change upon the incorporation of the polar PC. This behavior can be explained by the combination of three factors: *i*) the PCL matrix is hydrophobic; *ii*) the concentration of AH in the loaded fibers is very small; and *iii*) the micro-nanopatterned structure on the surface of the mat. Regarding to the latter, the micrometric diameter of the electrospun fibers (*i.e.* 0.6-1.5 μm in **Figure 3.4.3**) combined with the nanometric roughness (*i.e.* 8-16 nm in **Figure 3.4.4**) and holes among neighboring fibers favor the entrapment of air, which may give place to a Cassie Baxter stable state.[44,45]

3.4.3.2   *Release from loaded fibers*

AH release from loaded electrospun MFs is expected to depend on the relative strength of the interactions between the drug and the PCL matrix or the molecules from the release medium (*i.e.* water and ions). AH-loaded and unloaded (negative control) fibrous mats were immersed in PBS using Eppendorf tubes, as described in the Methods section. At regular time intervals (*i.e.* 5, 15, 30, 45, 60, 90, 120, 360, 1440 min), release medium (1 mL) was withdrawn from the tube, replaced by 1 mL of fresh medium, and analyzed by UV-Vis spectroscopy. The amount of AH released to the medium was quantified using the band centered at 307 nm, which corresponds to the PC.

Figure 3.4.8a compares the UV-Vis spectra of the released media extracted after 5, 15, 30 and 60 min from samples consisting of PCL/AH(TFE) mats immersed in PBS. The content of AH in the release medium was high at the beginning and decreased very rapidly with time (*i.e.* from 1.59 *w/w* % after 5 min to 0.06 *w/w* % after 60 min), evidencing a very fast release. Accordingly, the

release curve (**Figure 3.4.8b**) indicates that 80% of the PC was released to the PBS medium during the first 15 min, whereas the amount of AH that remained in the MFs after 6 h was lower than < 1%. The behavior of samples from PCL/AH(FA) mats immersed in PBS was practically identical, as reflected in the UV-Vis spectra and the release curve displayed in **Figure 3.4.9a** and **b**. The very fast release in PBS has been associated to the weakness of AH···PCL interactions, which are expected to be rapidly compensated by the strong interactions between the polar groups of AH and the components of PBS medium. In order to enhance the efficiency of therapies based on the controlled release of polar drugs, the fast mechanism observed for loaded PCL MFs requires modification into an extended release mechanism. For this purpose, in the following sub-sections we first demonstrate the activity of the released AH and, then, we show how different coating strategies allow to delay and regulate the drug release dosage.

Figure 3.4.8. (a) UV-Vis spectra of the PBS release media withdrawn at selected time intervals from Eppendorf tubes containing samples of PCL/AH(TFE). (b) AH release profile in PBS from PCL/AH(TFE) MFs. Complete description of the procedure employed for the release assays is provided in the Methods section. Results obtained for PCL/AH(FA) MFs are displayed in **Figure 3.4.9**. (c) Remaining GCase activity (%) (*i.e.* ratio between the enzymatic activity after thermal denaturation compared with the activity of the enzyme kept at 0 ºC) in the presence of AH released from PCL/AH(TFE) and PCL/AH(FA) fibrous mats after 5 min immersed in PBS, fresh AH in PBS and without AH (PBS alone).
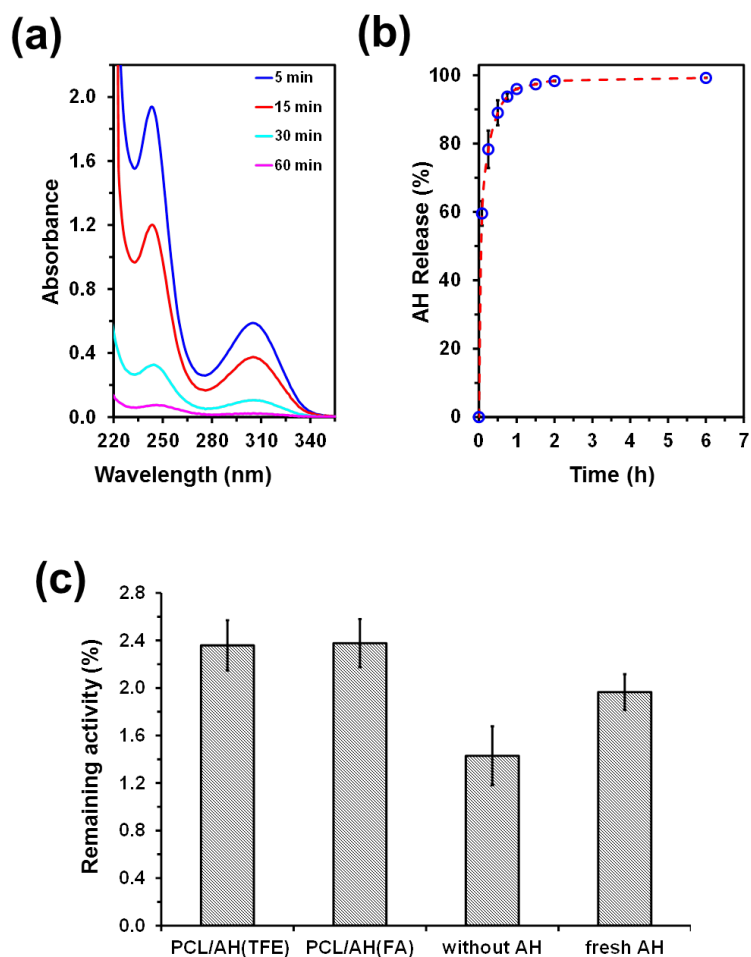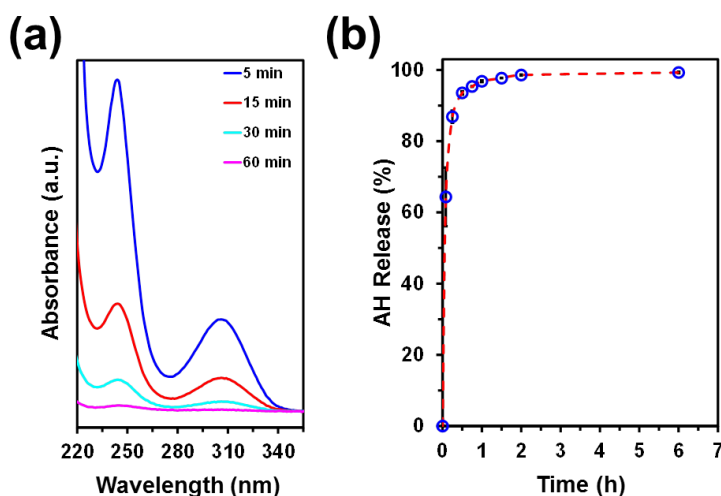
Figure 3.4.9. (a) UV-Vis spectra of the PBS release media withdrawn at selected time intervals from Eppendorf tubes containing samples of PCL/AH(FA). (b) AH release profile in PBS from PCL/AH(FA) MFs. Complete description of the procedure employed for the release assays is provided in the Methods section. Results obtained for PCL/AH(TFE) MFs are displayed in **Figure 3.4.8**.

3.4.3.3 Activity of released AH

Many lysosomal storage disorders (LSDs) originate from mutations that affect the proper folding of the enzyme in the endoplasmic reticulum (ER). PCs allow mutant enzymes to be correctly folded, thus avoiding ER retention and granting their transportation to the lysosomes, where the enzyme–PC complex dissociates due to the low pH and high substrate concentration.[46] Specifically, AH has been reported to be an excellent PC candidate for Gaucher disease, which is the most common autosomal recessive LSD.[12,47] Gaucher disease is caused by mutations in the gene encoding lysosomal GCase and ultimately resulting in the accumulation of glucosylceramide in macrophages and the development of hepatosplenomegaly, anaemia, skeletal lesions and central nervous system dysfunctions.[48]

Previous studies pointed to the efficacy of AH in increasing GCase activity[12,18] and thermal stability.[12,47] In this section, we examine if AH maintains this

stabilizing activity once released from loaded electrospun PCL MFs. For this purpose, a thermal denaturation assay utilizing GCase from lysed fibroblasts was conducted in the absence or in the presence of both fresh and released AH (see Methods section). Residual GCase activity after thermal denaturation was standardized by comparison with the GCase activity obtained from the sample that was kept at 0 ℃ (non-denaturation control). Enzyme activity was evaluated by measuring the fluorescence resulting from the release of the fluorescent reporter 4-MU group from the substrate. Thus, the remaining activity in the presence of either fresh or released AH was obtained dividing the fluorescence measured for the thermally denatured samples by the fluorescence of the corresponding sample kept at 0 ℃.

Figure 3.4.8c compares the remaining activity of GCase after thermal denaturation in the presence of the AH released from PCL/AH(TFE) and PCL/AH(FA) MFs after 5 min in PBS, fresh AH in PBS, and PBS alone (without AH). Results show the protecting effect on GCase activity of AH, which is in agreement with the reported literature.[12] Thus, all the samples of GCase that have been submitted to heating in the presence of AH (either fresh or released from the fibers) show more activity than the enzyme sample heated without AH being present. Moreover, the GCase activity is slightly higher in the presence of AH released from MFs than with fresh AH, showing that the functionality of the PC is not damaged by the aggressive conditions of the electrospinning process. These results indicate that PCL is a suitable vehicle to encapsulate biactive polar drugs such as AH and, thus, improvement of the release mechanism to obtain a gradual dosage deserves consideration.

3.4.3.4   Regulating the AH release by applying coating strategies

In order to delay the delivery of the PC, two different coating approaches were examined. In the first one, PCL/AH(TFE) and PCL/AH(FA) fibrous mats were sandwiched between two spin-coated PCL NMs. The process used to prepare these 3-layered NM/MFs/NM systems, hereafter denoted PCL//PCL/AH(TFE)//PCL and PCL//PCL/AH(FA)//PCL, respectively, is summarized in **Scheme 3.4.1a**. Free-standing sandwiched systems were prepared by spin-coating a PCL NM onto a Teflon® substrate using an acetone polymer solution (see Methods). Then, a 1 cm^2 PCL/AH(TFE) or PCL/AH(FA) square piece, which was cut from the corresponding fibrous mat, was put onto the first PCL NM and the second PCL NM was spin-coated onto it. Finally, the sandwiched system was easily detached from the Teflon® substrate. It is worth noting that the solubility of PCL in acetone is very slow, especially with respect to chloroform or chloroform:acetone mixtures, which allowed to minimize the attack of the solvent to the PCL MFs during the spin-coating process. Sandwiched systems using unloaded PCL(TFE) and PCL(FA) fibrous mats were also prepared as controls for release assays. Sandwiched systems supported onto the Teflon® substrate were employed for SEM characterization.

In the second coating strategy, AH-loaded fibrous mats were modified through a dip-coating method, as schematically described in Scheme 3.4.1b. More specifically, 1×1 cm^2 PCL/AH(TFE) and PCL/AH(FA) square pieces were immersed in a solution of PCL in acetone for 3 s. The resulting samples, hereafter denoted PCL[PCL/AH(TFE)] and PCL[PCL/AH(FA)], were dried and used for release assays. Control samples were prepared using unloaded fibrous mats.
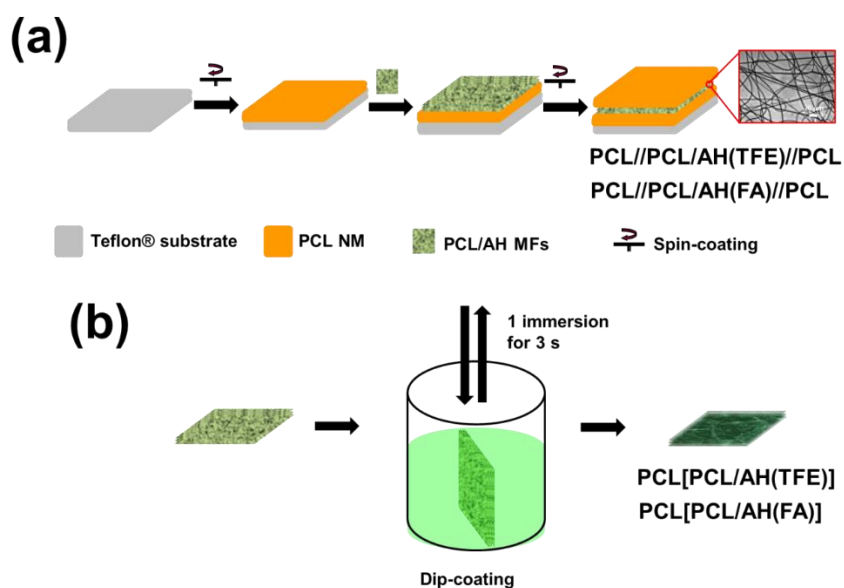
Scheme 3.4.1. Procedure used to prepare: (a) free-standing PCL//PCL/AH(TFE)//PCL and PCL//PCL/AH(FA)//PCL by sandwiching the fibrous mat between two spin-coated PCL NMs; (b) Preparation of PCL[PCL/AH(TFE)] and PCL[PCL/AH(FA)] by dip-coating fibrous mats.

SEM micrographs of the bottom PCL NM and the two sandwiched systems are displayed in **Figure 3.4.10a**. The bottom PCL NM presents a very flat, homogeneous and smooth surface, the thickness being of only 747±85 nm. In contrast, the shape of the top PCL layer adapts to the ribbon-like and the cylindrical morphology of PCL/AH(TFE) and PCL/AH(FA) MFs, respectively, acting as a coating. It is worth noting that, in the latter case, the top PCL NM wraps perfectly the MFs and the only fingerprint of its presence corresponds to the pseudo-periodic folds that systematically appears in the direction perpendicular to the fiber axis. These folds can be associated to the effect of the acetone used to dissolve PCL. In contrast, the PCL NM spin-coated onto PCL/AH(TFE) MFs exhibits a heterogeneous aspect. In these samples, regions involving wrapped MFs with the previously described folds coexist with small

areas in which the structure of the MFs is no longer distinguishable, which is probably due to the flat morphology of the ribbon-like PCL/AH(TFE) MFs.

SEM micrographs of PCL[PCL/AH(TFE)] and PCL[PCL/AH(FA)] are displayed in **Figure 3.4.10b**. Although the morphologies of the latter systems are apparently similar to those obtained for PCL//PCL/AH(TFE)//PCL and PCL//PCL/AH(FA)//PCL, detailed inspection evidences important differences. For example, PCL[PCL/AH(FA)] shows a heterogeneous structure in which neighboring MFs are partially joined by irregular portions of films formed after solvent evaporation, while these elements are imperceptible in PCL[PCL/AH(TFE)]. In contrast, the density of folds is much lower at the surface of PCL[PCL/AH(TFE)] than at the surface of all the other coated systems. Overall, these differences indicate that the dip-coating technique is much more influenced by the morphology of the MFs than the spin-coating.
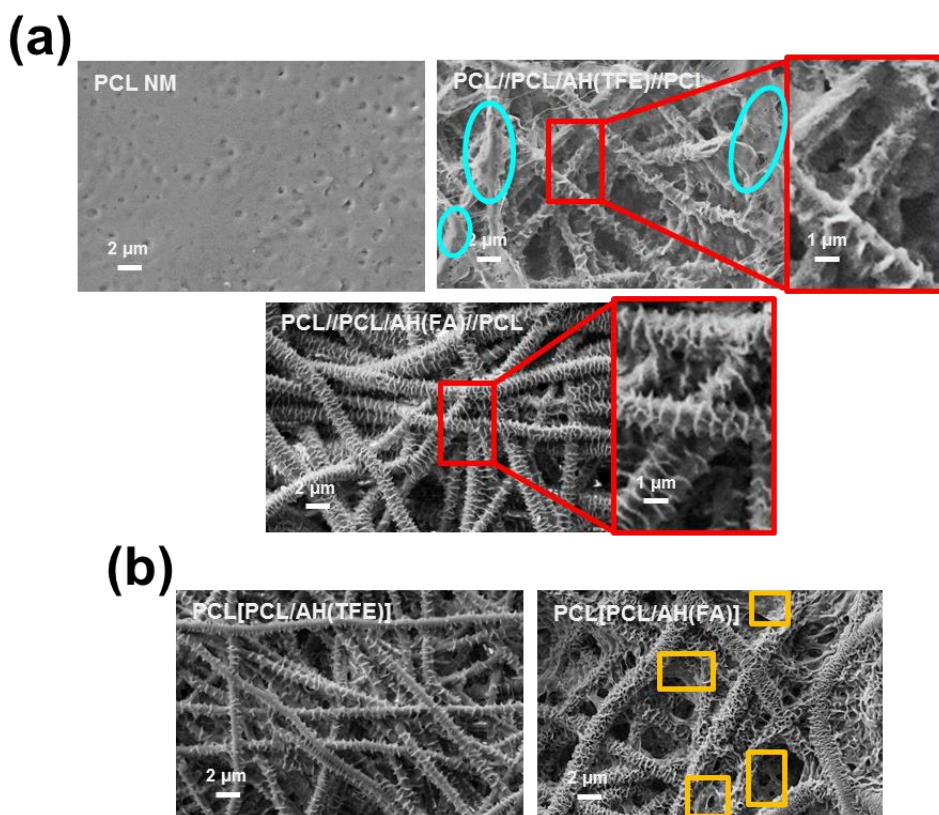
Figure 3.4.10. SEM micrographs of: (a) the PCL NM and the PCL//PCL/AH(TFE)//PCL and PCL//PCL/AH(FA)//PCL sandwiched systems obtained by spin-coating (**Scheme 3.4.1a**). Representative regions in which the morphology of PCL/AH(TFE) MFs is lost are indicated by blue ellipsoids; (b) PCL[PCL/AH(TFE)] and PCL[PCL/AH(FA)] obtained by dip-coating (**Scheme 3.4.1b**). Irregular portions of films joining neighboring MFs are indicated by yellow squares.

The water contact angle of fibrous mats coated with PCL by spin-coating and dip-coating are displayed in **Figure 3.4.11a** and **b**. The measured contact angles ranged from 85° to 99°, evidencing a significant reduction with respect to uncoated fibrous mats (**Figure 3.4.6d**). This reduction has been attributed to the fact that the external coating eliminates the micro-nanopatterned structure found on the surface of the fibrous mats. Thus, the PCL coating dominates the wettability of the new scaffolds, which exhibit in all cases contact angles close to the lowest threshold of hydrophocity (*i.e.* $\theta > 90°$).
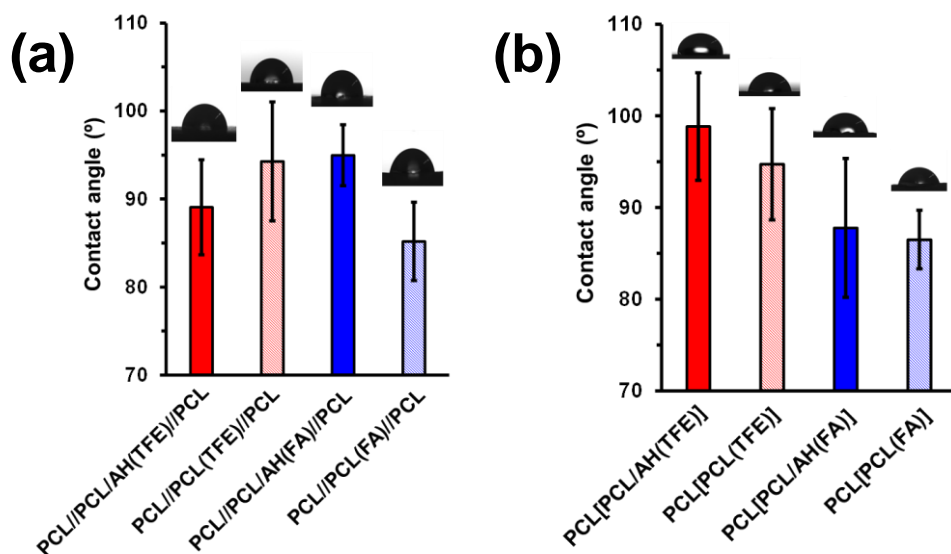
Figure 3.4.11. (a) Contact angle for water of PCL//PCL/AH(TFE)//PCL, PCL//PCL(TFE)//PCL, PCL//PCL/AH(FA)//PCL and PCL//PCL(FA)//PCL sandwiched systems obtained by spin-coating. **(b)** Contact angle for water of PCL[PCL/AH(TFE)], PCL[PCL(TFE)], PCL[PCL/AH(FA)] and PCL[PCL(FA)] sandwiched systems obtained by dip-coating.

Figure 3.4.12 compares the release profiles of AH-loaded systems prepared by spin-coating and dip-coating. The release was very slow in all cases, even though with some differences. For example, a release percentage of 95% was reached after ~2 and ~1 months of exposure to the medium for sandwiched and dip-coated systems, respectively, while the time required by uncoated MFs was only ~1 h. Accordingly, the coating has a very significant impact in the kinetics of the release. Moreover, the extent of the delay in the release of the PC largely depends on the technique used to protect the MFs. The delay is much longer when fibrous mats are sandwiched between two spin-coated NMs than when coated through simple immersion in a PCL solution. Indeed, the effect of the coating technique is observed even in the first steps of the release, as evidenced in the insets displayed in **Figure 3.4.12**. Thus, the release profiles obtained for PCL//PCL/AH(TFE)//PCL and PCL//PCL/AH(FA)//PCL are very similar for

both short and large times of exposure, which indicate that the protection imparted by homogeneous spin-coated NMs does not depend on the morphology of the fibrous mats. In contrast, the profiles obtained for PCL[PCL/AH(TFE)] and PCL[PCL/AH(FA)] present important differences, especially for short times (*e.g.* after 6 h of exposure the release percentage was 64% and 42% for the former and the latter, respectively). These differences are attributed to the heterogeneous structure of the systems prepared by dip-coating (**Figure 3.4.10b**), which is apparently affected by the morphology of the MFs.
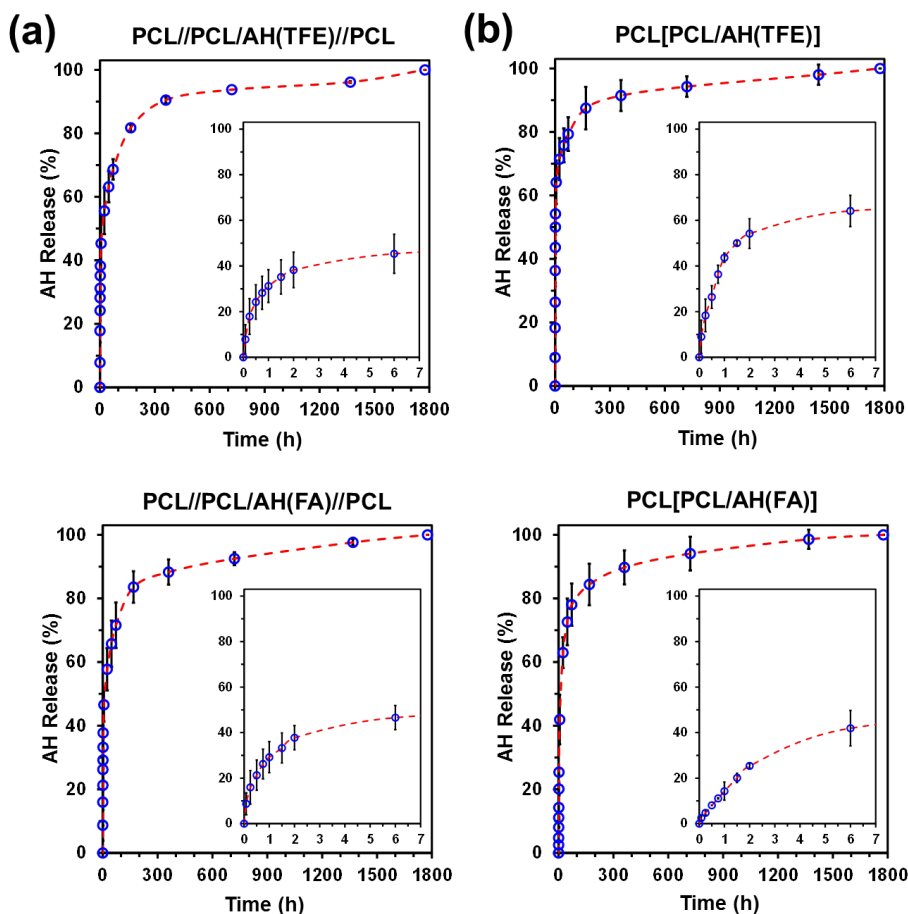
Figure 3.4.12. AH release profile in PBS from (a) sandwiched and (b) dip-coated systems.

Figure 3.4.13 compares the time required to release 50% and 80% of loaded AH from all the studied systems. A it was expected, the delivery of coated systems was clearly delayed with respect to that observed from the MFs alone since AH had to diffuse through the PCL coats. However, the most remarkable result displayed in **Figure 3.4.13** is that it demonstrates that the AH release can be regulated through the morphology of the scaffold without changing the composition of the PCL matrix. Thus, the time required for release can extend from a few minutes for uncoated MFs to few days or almost a week for dip-coated or sandwiched systems, respectively.
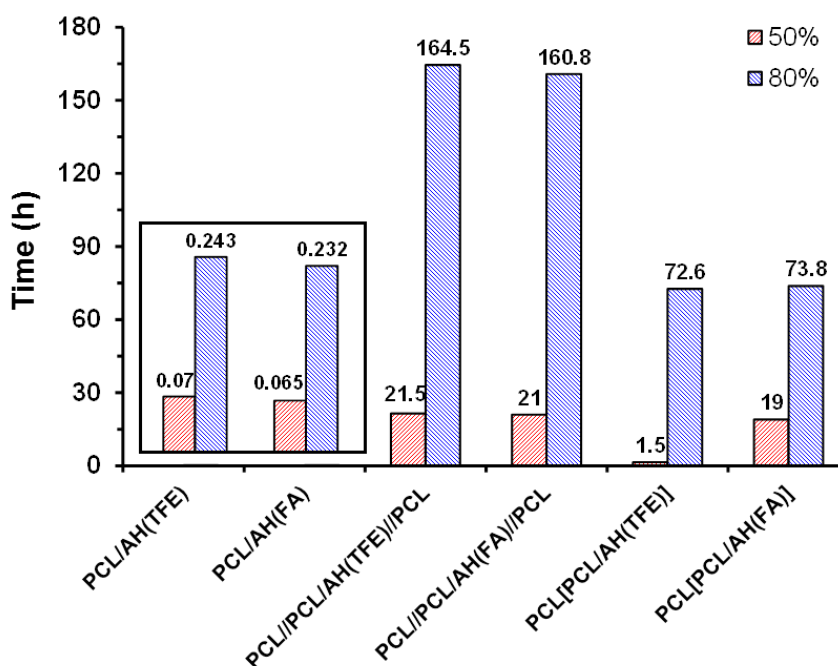
Figure 3.4.13. Comparison of the time required to release 50% and 80% of the loaded AH from all the studied systems.

3.4.4 Conclusions

The present study reveals that AH, a small and polar PC that increases the activity of misfolded GCase, can be loaded in fibrous PCL scaffolds by electrospinning. The fast release rate of this drug from such fibrous scaffolds, which occurs in less than an hour, has been controlled by applying external coatings to the MFs. These coatings, which have been achieved by dip-coating and by spin-coating, have been obtained using PCL dissolved in acetone to avoid the rapid dissolution of the AH-loaded MFs. The AH release extends to weeks and months when coated fibrous scaffolds are prepared by dip-coating and spin-coating, respectively. The released AH retains the protecting effect on the activity of GCase, demonstrating that the electrospinning process does not affect the functionality of the drug. Moreover, PCL coated-fibrous scaffolds can be used to regulate strategically the dosage of polar drugs depending on the therapeutic needs.

3.4.5 References

1. Gregersen, N., Bross, P., Vang, S. & Christensen, J. H. Protein Misfolding and Human Disease. *Annu. Rev. Genomics Hum. Genet.* **7**, 103–124 (2006).

2. Hartl, F. U. Protein Misfolding Diseases. *Annu. Rev. Biochem.* **86**, 21–26 (2017).

3. Herczenik, E. & Gebbink, M. F. B. G. Molecular and cellular aspects of protein misfolding and disease. *FASEB J.* **22**, 2115–2133 (2008).

4. Leandro, P. & Gomes, C. Protein Misfolding in Conformational Disorders: Rescue of Folding Defects and Chemical Chaperoning. *Mini-Reviews Med. Chem.* **8**, 901–911 (2008).

5. Parenti, G., Andria, G. & Valenzano, K. J. Pharmacological Chaperone Therapy: Preclinical Development, Clinical Translation, and Prospects for the Treatment of Lysosomal Storage Disorders. *Mol. Ther.* **23**, 1138–1148 (2015).

6. PARENTI, G., PIGNATA, C., VAJRO, P. & SALERNO, M. New strategies for the treatment of lysosomal storage diseases (Review). *Int. J. Mol. Med.* **31**, 11–20 (2013).

7. Valenzano, K. J. *et al.* Identification and Characterization of Pharmacological Chaperones to Correct Enzyme Deficiencies in Lysosomal Storage Disorders. *Assay Drug Dev. Technol.* **9**, 213–235 (2011).

8. Parenti, G. Treating lysosomal storage diseases with pharmacological chaperones: from concept to clinics. *EMBO Mol. Med.* **1**, 268–279 (2009).

9. Banning, A., Gülec, C., Rouvinen, J., Gray, S. J. & Tikkanen, R. Identification of Small Molecule Compounds for Pharmacological Chaperone Therapy of Aspartylglucosaminuria. *Sci. Rep.* **6**, 37583 (2016).

10. Parenti, G., Andria, G. & Ballabio, A. Lysosomal Storage Diseases: From Pathophysiology to Therapy. *Annu. Rev. Med.* **66**, 471–486 (2015).

11. Boyd, R. E. *et al.* Pharmacological Chaperones as Therapeutics for Lysosomal Storage Diseases. *J. Med. Chem.* **56**, 2705–2725 (2013).

12. Maegawa, G. H. B. *et al.* Identification and Characterization of Ambroxol as an Enzyme Enhancement Agent for Gaucher Disease. *J. Biol. Chem.* **284**, 23502–23516 (2009).

13. McNeill, A. *et al.* Ambroxol improves lysosomal biochemistry in glucocerebrosidase mutation-linked Parkinson disease cells. *Brain* **137**, 1481–1495 (2014).

14. Babajani, G., Tropak, M. B., Mahuran, D. J. & Kermode, A. R. Pharmacological chaperones facilitate the post-ER transport of recombinant N370S mutant β-glucocerebrosidase in plant cells: Evidence that N370S is a folding mutant. *Mol. Genet. Metab.* **106**, 323–329 (2012).

211

15. Ivanova, M. M., Changsila, E. & Goker-Alpan, O. Individualized screening for chaperone activity in Gaucher disease using multiple patient derived primary cell lines. *Mol. Genet. Metab.* **123**, S69 (2018).

16. Luan, Z. *et al.* The chaperone activity and toxicity of ambroxol on Gaucher cells and normal mice. *Brain Dev.* **35**, 317–322 (2013).

17. Suzuki, T. *et al.* Expression of Human Gaucher Disease Gene GBA Generates Neurodevelopmental Defects and ER Stress in Drosophila Eye. *PLoS One* **8**, e69147 (2013).

18. Narita, A. *et al.* Ambroxol chaperone therapy for neuronopathic Gaucher disease: A pilot study. *Ann. Clin. Transl. Neurol.* **3**, 200–215 (2016).

19. Staples, M. Microchips and controlled-release drug reservoirs. *Wiley Interdiscip. Rev. Nanomedicine Nanobiotechnology* **2**, 400–417 (2010).

20. Timko, B. P. & Kohane, D. S. Materials to Clinical Devices: Technologies for Remotely Triggered Drug Delivery. *Clin. Ther.* **34**, S25–S35 (2012).

21. Mura, S., Nicolas, J. & Couvreur, P. Stimuli-responsive nanocarriers for drug delivery. *Nat. Mater.* **12**, 991–1003 (2013).

22. Timko, B. P., Dvir, T. & Kohane, D. S. Remotely Triggerable Drug Delivery Systems. *Adv. Mater.* **22**, 4925–4943 (2010).

23. Puiggalí-Jou, A., Micheletti, P., Estrany, F., del Valle, L. J. & Alemán, C. Electrostimulated Release of Neutral Drugs from Polythiophene Nanoparticles: Smart Regulation of Drug-Polymer Interactions. *Adv. Healthc. Mater.* **6**, 1700453 (2017).

24. Merino, S., Martín, C., Kostarelos, K., Prato, M. & Vázquez, E. Nanocomposite Hydrogels: 3D Polymer–Nanoparticle Synergies for On-Demand Drug Delivery. *ACS Nano* **9**, 4686–4697 (2015).

25. Satarkar, N. S., Biswal, D. & Hilt, J. Z. Hydrogel nanocomposites: a review of applications as remote controlled biomaterials. *Soft Matter* **6**, 2364 (2010).

26. Puiggalí-Jou, A., Cejudo, A., del Valle, L. J. & Alemán, C. Smart Drug Delivery from Electrospun Fibers through Electroresponsive Polymeric Nanoparticles. *ACS Appl. Bio Mater.* **1**, 1594–1605 (2018).

27. Reneker, D. H. & Chun, I. Nanometre diameter fibres of polymer, produced by electrospinning. *Nanotechnology* **7**, 216–223 (1996).

28. Frenot, A. & Chronakis, I. S. Polymer nanofibers assembled by electrospinning. *Curr. Opin. Colloid Interface Sci.* **8**, 64–75 (2003).

212

29.   Dzenis, Y. Material science: Spinning Continuous Fibers for Nanotechnology. *Science.* **304**, 1917–1919 (2004)

30.   Jayaraman, K., Kotaki, M., Zhang, Y. & Mo, X. Recent Advances in Polymer Nanofibers. *J. Nanosci. Nanotechnol.* **4**, 52–65 (2003).

31.   Dhakate, S. R. Effect Of Processing Parameters On Morphology And Thermal Properties Of Electrospun Polycarbonate Nanofibers. *Adv. Mater. Lett.* **1**, 200–204 (2010).

32.   Sharma, S. Ferrolectric Nanofibers: Principle, Processing And Applications. *Adv. Mater. Lett.* **4**, 522–533 (2013).

33.   Liu, X. *et al.* Tunable zero-order drug delivery systems created by modified triaxial electrospinning. *Chem. Eng. J.* **356**, 886–894 (2019).

34.   Yu, D.-G., Li, J.-J., Williams, G. R. & Zhao, M. Electrospun amorphous solid dispersions of poorly water-soluble drugs: A review. *J. Control. Release* **292**, 91–110 (2018).

35.   Hai, T. *et al.* Electrospun lipid-coated medicated nanocomposites for an improved drug sustained-release profile. *Mater. Des.* **162**, 70–79 (2019).

36.   Yang, Y. *et al.* Tunable drug release from nanofibers coated with blank cellulose acetate layers fabricated using tri-axial electrospinning. *Carbohydr. Polym.* **203**, 228–237 (2019).

37.   Woodruff, M. A. & Hutmacher, D. W. The return of a forgotten polymer—Polycaprolactone in the 21st century. *Prog. Polym. Sci.* **35**, 1217–1256 (2010).

38.   Dong, R.-H. *et al.* In situ deposition of a personalized nanofibrous dressing via a handy electrospinning device for skin wound care. *Nanoscale* **8**, 3482–3488 (2016).

39.   del Valle, L. J. *et al.* Electrospinning of polylactide and polycaprolactone mixtures for preparation of materials with tunable drug release properties. *J. Polym. Res.* **18**, 1903–1917 (2011).

40.   Bosworth, L. A. & Downes, S. Acetone, a Sustainable Solvent for Electrospinning Poly(ε-Caprolactone) Fibres: Effect of Varying Parameters and Solution Concentrations on Fibre Diameter. *J. Polym. Environ.* **20**, 879–886 (2012).

41.   Diettrich, O., Mills, K., Johnson, A. W., Hasilik, A. & Winchester, B. G. Application of magnetic chromatography to the isolation of lysosomes from fibroblasts of patients with lysosomal storage disorders. *FEBS Lett.* **441**, 369–372 (1998).

42.   Maione, S. *et al.* Biodegradable nanofibrous scaffolds as smart delivery vehicles for amino acids. *J. Appl. Polym. Sci.* **134**, (2017).

43.   Socrates, G. *Infrared and Raman characteristic group frequencies. Tables and charts*. *Journal of Raman Spectroscopy* (2001).

213

44. Moradi, S., Kamal, S., Englezos, P. & Hatzikiriakos, S. G. Femtosecond laser irradiation of metallic surfaces: effects of laser parameters on superhydrophobicity. *Nanotechnology* **24**, 415302 (2013).

45. Armelin, E., Moradi, S., Hatzikiriakos, S. G. & Alemán, C. Designing Stainless Steel Surfaces with Anti-Pitting Properties Applying Laser Ablation and Organofluorine Coatings. *Adv. Eng. Mater.* **20**, 1700814 (2018).

46. Pereira, D. M., Valentão, P. & Andrade, P. B. Tuning protein folding in lysosomal storage diseases: the chemistry behind pharmacological chaperones. *Chem. Sci.* **9**, 1740–1752 (2018).

47. Aymami, J., Barril, X., Rodríguez-Pascau, L. & Martinell, M. Pharmacological chaperones for enzyme enhancement therapy in genetic diseases. *Pharm. Pat. Anal.* **2**, 109–124 (2013).

48. Thomas, A. S., Mehta, A. & Hughes, D. A. Gaucher disease: haematological presentations and complications. *Br. J. Haematol.* **165**, 427–440 (2014).

3.5 Semi-interpenetrated hydrogels-microfibers electroactive assemblies for release and real-time monitoring of drugs

Simultaneous drug release and monitoring using a single polymeric platform represents a significant advance in the utilization of biomaterials for therapeutic use. Tracking drug release by real-time electrochemical detection using the same platform is a simple way to guide the dosage of the drug, improve the desired therapeutic effect, and reduce the adverse side effects. The platform developed in this work takes advantage of the flexibility and loading capacity of hydrogels, the mechanical strength of microfibers, and the capacity of conducting polymers to detect the redox properties of drugs. The engineered platform is prepared by assembling two spin-coated layers of poly-γ-glutamic acid hydrogel, loaded with poly(3,4-ethylenedioxythiophene) (PEDOT) microparticles, and separated by a electrospun layer of poly-ε-caprolactone microfibers. Loaded PEDOT microparticles are used as reaction nuclei for the polymerization of poly(hydroxymethyl-3,4-ethylenedioxythiophene) (PHMeDOT), that semi-interpenetrate the whole three layered system while forming a dense network of electrical conduction paths. After demonstrating its properties, the platform has been loaded with levofloxacin and its release monitored externally by UV-Vis spectroscopy and *in situ* by using the PHMeDOT network. *In situ* real-time electrochemical monitoring of the drug release from the engineered platform holds great promise for the development of multi-functional devices for advanced biomedical applications.

215

3.5.1 Introduction

Drug delivery systems, as engineered technologies for the targeted delivery and/or the controlled release of therapeutic agents, have long been used to improve health. Biomedical engineers have contributed substantially to our understanding of the physiological barriers to efficient drug delivery, while biomaterial engineers have developed platforms able to act as vehicles and/or cargos for therapeutic drug delivery, helping cope with drawbacks of classical pharmaceuticals (e.g. increasing the solubility of the drugs, reducing side effects, and improving biodistribution). Although many materials have been employed as therapeutic platforms for drug delivery, polymers have received special attention because of their properties and versatility.[1–7]

Over the last years, drug delivery using polymeric platforms based on (nano)particles,[8–13] (nano)fibers,[14–20] (nano)films,[20–24] and hydrogels[25–30] have been extensively investigated. Among polyesters, poly-γ-caprolactone (PCL) has attracted great interest for drug release due to its biodegradable and biocompatible nature,[31] as well as by the approval of PCL-based devices by the U.S. Food and Drug Administration (FDA) for many medical applications, including drug delivery devices, in the human body. The release mechanism from PCL formulations depends on the degradation of the polymer and on the polarity of the drug. Lipophilic drugs are usually encapsulated inside the PCL formulations (e.g. microsphere, nanoparticles, scaffolds, films and fibers, micelles) and the release occurs slowly upon surface erosion by enzymatic degradation.[31,32] Instead, hydrophilic drugs tend to accumulate at the surface of polymeric platform and a fast burst release occurs by desorption at the initial period or dosage intake.[31,33] Besides, the utilization of polypeptides in drug release applications is receiving increasing attention not only because of their versatility in macromolecular design and synthesis, but also due to the incorporation of functionalities present in natural proteins, which facilitates their interaction with tissues and cells.[34–37] Compared

to conventional synthetic polymers, polypeptides exhibit some advantages, as for example, non-immunogenicity, enhanced biodegradability, remarkable biocompatibility properties, and multiple functional groups to enhance the loading efficiency.[38–43]

On the other hand, dual-functional platforms for real-time drug release monitoring have become of major significance in the last few years. Two main approaches have been developed for this purpose. The simplest one is based on the construction of assembled devices in which drug release systems are chemically or physically coupled to modified electrodes for detecting the drug remaining in the platform.[44–47] The second approach, which is more recent, is based on connecting elements that release the desired drug with elements that visualize such drug via imaging, like specific fluorescent or luminescent reporters.[48–55] Although the latter approach represents an improvement with respect to the former in terms of integration, aspects related with the chemical design and experimentation are much more tedious and complex.

Because of the simplicity and fast response of the electrochemical sensors used in the assembled systems, as well as the associative advantages offered by the connected elements in the integrative systems, the design of hybrid platforms by combining the benefits of each approach is very attractive. In this work, we report a new strategy for the fabrication of dual-functional platforms by merging the best of each of the two approaches. More specifically, we propose the preparation of assemblies involving two spin-coated layers of polypeptide hydrogel separated by a mat of electrospun PCL microfibers (MFs). Then, the elements of such three-layered assembly are connected through a semi-interpenetrated (sINP) three-dimensional network. Polypeptide hydrogels, which exhibit poor mechanical properties, act as drug loading systems, while PCL MFs provide strength to the assembly,[56,57] which is robust and manageable. The semi-interpenetration of the

assembly is performed using an intrinsically conducting polymer (ICP), poly(3,4-ethylenedioxythiophene) (PEDOT), which is incorporated by in situ anodic polymerization. This ICP is recognized as the most stable and electroactive heterocyclic ICP and, in addition, is biocompatible.[58–61] After complete characterization, the engineered platform, hereafter named sINP/PCL/sINP, was loaded with levofloxacin (LVX), which is one of the outstanding representatives of the third generation of quinolone antibiotics that have been a useful class of broad-spectrum antimicrobials.[62] The release of LVX has been monitored in real time by detecting the oxidation of the antibiotic that remains inside the matrix. Finally, the electrochemical detection through the dual-functional platform has been correlated with spectroscopic measurements to evaluate the sensitivity of the former.

3.5.2 Methods

3.5.2.1 *Materials*

Free-acid poly-γ-glutamic acid (γPGA, from *Bacillus subtilis*), with average molecular weight $M_w = 350000$, was purchased from Wako Chemicals GmbH (Neuss, Germany). Cystamine dihydrochloride (Cys;≥98.0%), 1-[3-(dimethylamino)propyl]-3-ethylcarbodiimide methiodide (CDI), 3,4-ethylenedioxythiophene (EDOT;95%) and hydroxymethyl-3,4-ethylenedioxythiophene (HMeDOT; 95%) were purchased from Sigma-Aldrich. Acetonitrile (Reagent European Pharmacopoeia for analysis, ACS) and $NaHCO_3$ were obtained from Panreac. Anhydrous lithium perchlorate ($LiClO_4$), analytical reagent grade from Aldrich, was stored in an oven at 70 ºC before use in electrochemical experiments. Milli-Q water grade (0.055 S/cm) was used in all synthetic processes. Poly-ε-caprolactone (PCL; Aldrich, UK; M_n:80,000), chloroform (Scharlau, Spain; stabilized with amylene, 99.8% pure) and acetone

(Sigma, South Korea; 99.9% pure) were used as received. Levofloxacin (LVX, ≥98%) and nalidixic acid (NAX, ≥98%) were purchased from Sigma-Aldrich.

3.5.2.2   Synthesis of γPGA hydrogel

The polypeptide hydrogel was prepared by dissolving γPGA and CDI in 0.75 mL of 0.5 M NaHCO₃ at 4 °C under magnetic stirring. Then, Cys, previously dissolved in 0.25 mL of 0.5 M NaHCO₃, was added to the solution and mixed during 2−3 min. The γPGA:CDI:Cys molar ratio was 5:5:4. The solution was let to gel at room temperature for 1 h. To remove any compound in excess, the resulting hydrogel was washed with distilled water three times.

3.5.2.3   Synthesis and sonication of poly(3,4-ethylenedioxythiophene) (PEDOT) films

PEDOT films were prepared by applying a constant potential of 1.40 V during 600 s to the reaction medium, which consisted on an acetonitrile solution with 10 mM EDOT and 0.1 M LiClO₄ (supporting electrolyte). This process was performed in a potentiostat-galvanostat Autolab PGSTAT101 equipped with the ECD module (Ecochimie, The Netherlands) using a three electrode compartment cell under nitrogen atmosphere (99.995% pure) at room temperature. Steel AISI 316 sheets of 6 cm² in area were used as working and counter electrodes. The reference electrode was an Ag|AgCl electrode containing a KCl saturated aqueous solution (offset potential versus the standard hydrogen electrode, $E^0 = 0.222$ V at 25 °C).

PEDOT films were processed into microparticles (MPs) by sonication (Ultrasons H-D sonicator) in different solvents during 15 min and, subsequent, centrifugation (Sorvall RC5B Plus centrifuge) during 45 min at 11000 rpm. This

process was repeated successively in acetonitrile, acetone and milli-Q water. The diameter of the resulting PEDOT particles was determined at room temperature by dynamic light scattering (DLS) in milli-Q water dispersions (0.3% v/v) using a NanoBrook Omni zeta potential analyser from Brookheaven Instruments Corporation.

3.5.2.4 Synthesis of PEDOT-γPGA hydrogel

PEDOT-γPGA hydrogel samples supported on steel tweezers, which were kept in to the reaction medium overnight, were used as working electrodes for the anodic polymerization of poly(hydroxymethyl-3,4-ethylenedioxythiophene) (PHMeDOT) by chronoamperometry. The reaction medium was a 10 mM HMeDOT aqueous solution with 0.1 M LiClO$_4$ as supporting electrolyte. The anodic polymerization was conducted under a constant potential of 1.10 V using a polymerization time of 7 hours. The experimental setup used for the *in situ* modification of the PEDOT-γPGA hydrogel was identical to that described above for the synthesis of PEDOT films.

3.5.2.5 Spin coating

γPGA:CDI:Cys and PEDOT-γPGA:CDI:Cys solutions, prepared as described for the synthesis of γPGA and PEDOT/γPGA hydrogels (*i.e.* 5:5:4 molar ratio and 20% w/w of PEDOT MPs), were spin-coated using a WS-400BZ6NPP/A1/AR1 spin-coater (Laurell Technologies Corporation). In all cases, glass square plates (area: 2×2 cm^2), previously cleaned by sonication in milliQ water, acetone and ethanol (5 min each), were used as substrates. This process was conducted at 500 rpm for 1 min.

3.5.2.6   Electrospinning of PCL

Electrospun mats of PCL microfibers (MFs) were obtained at room temperature. The feeding solution was obtained by dissolving 1.3 g of PCL in 3 mL of a 2:1 v/v chloroform:acetone mixture using an stirrer for 12 h. Electrospinning was carried out in a non-conductor chamber. The feeding solution was loaded in a 5 mL BD Discardit (Becton Dickson Co., Franklin Lakes, NJ, USA) plastic syringe for delivery through a blunt-tipped (*i.e.* without bevel) 18 G needle (inner diameter 0.84 mm). The flow rate and the needle tip-collector distance were 5 mL/h and 20 cm, respectively. A voltage of 20 kV h was applied through a highvoltage Gamma High Voltage Research (ES30-5W) power supply.

3.5.2.7   Scanning electron microscopy (SEM)

Scanning electron microscopy (SEM) studies were performed using a Focus Ion Beam Zeiss Neon 40 instrument (Carl Zeiss, Germany). Samples of area 1×1 cm^2 were mounted on a double-sided adhesive carbon disc and sputter coated with a thin layer of carbon to prevent sample charging problems. All micrographs were recorded at an accelerating voltage of 5 kV. The size of the pores in the hydrogel and diameter of the PEDOT MPs and PCL MFs were measured with ImageJ software.

3.5.2.8   Fourier Transform Infrared Spectroscopy

FTIR spectra were recorded with a Fourier Transform FTIR 4100 Jasco spectrometer (Jasco Analytical Instruments, Easton, USA) in the 4000–500 cm^{-1} range. An attenuated total reflection (ATR) system with a heated Diamond ATR Top-Plate (model MKII Golden Gate, Specac, Ltd., Orpington, UK) was used.

3.5.2.9 RAMAN spectroscopy

Hydrogel samples were characterized by micro-Raman spectroscopy using a commercial Renishaw inVia Qontor confocal Raman microscope. The Raman setup consisted of a laser (at 785 nm with a nominal 300 mW output power) directed through a microscope (specially adapted Leica DM2700 M microscope) to the sample after which the scattered light is collected and directed to a spectrometer with a 1200 lines·mm^{-1} grating. The exposure time was 10 s, the laser power was adjusted to 1% of its nominal output power and each spectrum was collected with 3 accumulations.

3.5.2.10 Electrochemical experiments

All electrochemical experiments were run in triplicate using water with 0.1 M LiClO$_4$ as supporting electrolyte. Cyclic voltammetry (CV) was carried out to evaluate the electroactivity, the areal specific capacitance (*SC*), and the electrochemical stability of the different systems. The initial and final potentials were −0.50 V in all cases, while the reversal potential was 1.10 V and 1.50 V for unloaded and LVX-loaded samples, respectively. A scan rate of 100 mV/s was used in all cases. For electrochemical measurements using unloaded and LVX-loaded samples, the counter electrode was steel tweezers of 1 cm^2 and platinum (Pt) sheets of 0.5 cm^2, respectively. Ag|AgCl 3 M KCl was used as reference electrode in all cases.

The *SC* (in mF/cm^2) was determined using the following expression:

$$SC = \frac{Q}{\Delta V \cdot A}$$

Equation 3.5.1. The areal specific capacitance (*SC*) equation, where Q is voltammetric charge determined by integrating the oxidative or the reductive regions of the cyclic voltammograms, ΔV is the potential window (in V), and A is the area of the electrode (in cm^2).

The electrochemical stability was examined by evaluating the loss of electroactivity (LEA, in %) against the number of oxidation−reduction cycles:

$$LEA = \frac{\Delta Q}{Q_2} = \frac{Q_i - Q_2}{Q_2}$$

Equation 3.5.2. The loss of electroactivity (LEA) equation, where ΔQ is the difference between the oxidation charge (in C) in the second (Q_2) and the evaluated oxidation−reduction cycle (Q_i).

3.5.2.11 Thermal gravimetric analysis (TGA)

The thermal stability of the prepared system was studied by TGA at a heating rate of 20 ºC/min (sample weight *ca.* 5 mg) with a Q50 thermogravimetric analyser of TA Instruments and under a flow of dry nitrogen. Test temperatures ranged from 30 to 590 ºC.

3.5.2.12 Swelling Evaluation

The swelling ratio (SR, in %) of the studied systems was determined according to:

$$SR(\%) = \frac{w_W - w_D}{w_D} \times 100$$

Equation 3.5.3. The swelling ratio (SR), where w_W is the weight after 30 min plunged in distilled water and w_D is the weight of the system after freeze-drying (dried system). All swelling experiments were conducted at room temperature.

3.5.2.13 Mechanical properties

Mechanical properties and peel tests were evaluated with a Zwick Z2.5/TN1S testing machine with integrated testing software (testXpert, Zwick). The deformation rate for stress-strain assays was 1 mm/min. Samples with a surface area of 1×3 cm^2 and a thickness of 1.1 ± 0.2 mm were cut for experiments. Peel

tests were conducted on a bi-layered γPGA/PCL system to examine the adhesion between the hydrogel and the fibrous mat. After preparation, platforms were allowed to dry at room temperature for 24 h before conducting the assays, which were performed in triplicate.

3.5.2.14 Release and electrochemical detection of levofloxacin (LVX)

Unloaded and LVX-loaded platforms supported on steel tweezers were put inside an electrochemical cell filled with a 0.1 M LiClO$_4$ aqueous solution, which was used as the release medium. For the electrochemical detection of the LVX remaining at the platform, CV assays were done at well-defined time intervals (*i.e.* 5 min, 15 min, 30 min, 60 min and 24 h) using the methodology described above. After doing each CV, the release medium was replaced by a fresh one, the removed medium being used to quantify the released LVX by UV-Vis spectroscopy. UV–Vis spectra were recorded using a UV-Vis Cary 100 Bio spectrophotometer (Agilent, Santa Clara, CA, USA). Additional release assays were performed in 0.1 M PBS solution.

3.5.2.15 Antimicrobial test: Inhibition of bacterial growth

Escherichia coli (*E. coli*) and *Staphylococcus sanguinis* (*S. sanguinis*) were selected to evaluate the activity of loaded LVX against bacteria. The bacteria were previously grown aerobically by exponential phase in Luria-Bertani (LB) broth (at 37 ºC and agitated at 80 rpm). In addition to the LVX-loaded platform, the unloaded platform (negative control), NAX discs (positive control) and free LVX (positive control) were also considered for antimicrobial assays.

The agar diffusion test was performed in Petri dishes of 90 mm. A standardized 0.5 McFarland of the test strain culture was inoculated homogeneously on the

surface of LB agar using a sterile nylon swab. Then, samples were pasted onto the agar plate. Bacteria were incubated at 37 ºC for 24 h and the inhibition zone for each sample on the plate was observed.

3.5.3 Results and discussion

3.5.3.1 *Preparation of sINP hydrogel and the sINP/PCL/sINP platform*

The hydrogel used in this work for the dual-functional device was based on poly-γ-glutamic acid (γPGA), which is a water soluble, anionic, biodegradable and edible biopolymer.[63] In this polypeptide, which is produced by *Bacillus subtilis*,[64] the peptide bonds are formed between the amino group of glutamic acid (Glu) and the carboxyl group at the end of the Glu side chain. γPGA hydrogels, which are produced by the chemical crosslink of the polypeptide in its free form, have been tested in multifarious potential applications in healthcare,[65] water treatment[66] and energy storage.[67,68] In this work, the γPGA hydrogel was prepared using a condensation reaction with 1-[3-(dimethylamino)propyl]-3-ethylcarbodiimide methiodide (CDI) and cystamine (Cys) as condensation agent and cross-linker, respectively.[67] The γPGA:CDI:Cys molar ratio was 5:5:4.

sINP γPGA hydrogels have been prepared using a recently reported strategy.[68] For this purpose, poly(3,4-ethylenedioxythiophene) (PEDOT) microparticles (MPs) were obtained by sonicating films previously synthesized by anodic polymerization. The resulting MPs were loaded in situ during the formation of γPGA hydrogels. Thus, PEDOT-γPGA hydrogels were prepared using the condensation reaction of γPGA with CDI and Cys but incorporating 20% w/w of PEDOT MPs to the initial γPGA solution. This solution was stirred for 12 hours at 1000 rpm prior to the condensation reaction.

PEDOT MPs embedded inside the γPGA were used as reaction nuclei for the in situ polymerization of hydroxymethyl-3,4-ethylenedioxythiophene (HMeDOT) and, thus, produce the sINP [PEDOT-γPGA]PHMeDOT hydrogel, where PHMeDOT refers to poly(hydroxymethyl-3,4-ethylenedioxythiophene). For this purpose, PEDOT-γPGA hydrogel samples supported onto steel tweezers were kept immersed in an aqueous solution containing 10 mM HMeEDOT and 0.1 M LiClO4 for 12 hours under stirring. This step previous to the polymerization guaranteed the penetration into the PEDOT-γPGA matrix of the HMeDOT monomers, which are more soluble in water than EDOT due to the exocyclic hydroxymethyl group. After that, the anodic polymerization was performed applying a constant potential of 1.10 V for 7 h. This process, allowed the formation of conductive PHMeDOT networks extending inside the hydrogel matrix (**Figure 3.5.1a**).[68]

The procedure used to prepare the three-layered dual-functional platform, sINP/PCL/sINP, is depicted in **Figure 3.5.1b**. Firstly, 600 μL of a 20% w/w PEDOT MPs-containing γPGA solution with CDI and Cys, formulated as described for the preparation of the PEDOT-γPGA hydrogels (5:5:4 molar ratio), was spin-coated onto a square glass substrate (area: 2×2 cm^2) at 500 rpm for 1 min. Then, a mat of PCL MFs was electrospun on the top of the PEDOT-γPGA:CDI:Cys layers. After this, the top layer of PEDOT-γPGA:CDI:Cys was spin coated onto the PCL mat using the same experimental conditions that for the first layer. The final three-layered system was let to gel at room temperature for 1 h. To remove any compound in excess the resulting system was washed with distilled water three times.

After gelation, the whole three-layered system, which was separated from the glass substrate using steel tweezers of 0.5 cm width, was used as working electrode for the anodic polymerization of HMeDOT using the experimental conditions described above for the preparation of sINP [PEDOT-

γPGA]PHMeDOT hydrogels. After the anodic polymerization step, the assembled elements of the resulting three-layered system, sINP/PCL/sINP, were expected to be completely crossed and, therefore, interconnected by PHMeDOT conductive networks. sINP/PCL/sINP behaved as free-standing platforms once detached from the steel tweezers. **Figure 3.5.1b** includes photographs of sINP/PCL/sINP before and after being detached from the steel tweezers.

On the other hand, bi-layered γPGA/γPGA, PEDOT-γPGA/PEDOT-γPGA and sINP/sINP platforms, which were prepared using the same process but omitting the incorporation of PEDOT MPs, the anodic polymerization step or the intermediate PCL layer, respectively, were used as control systems for a better understanding of the role played by the different elements in the platform.

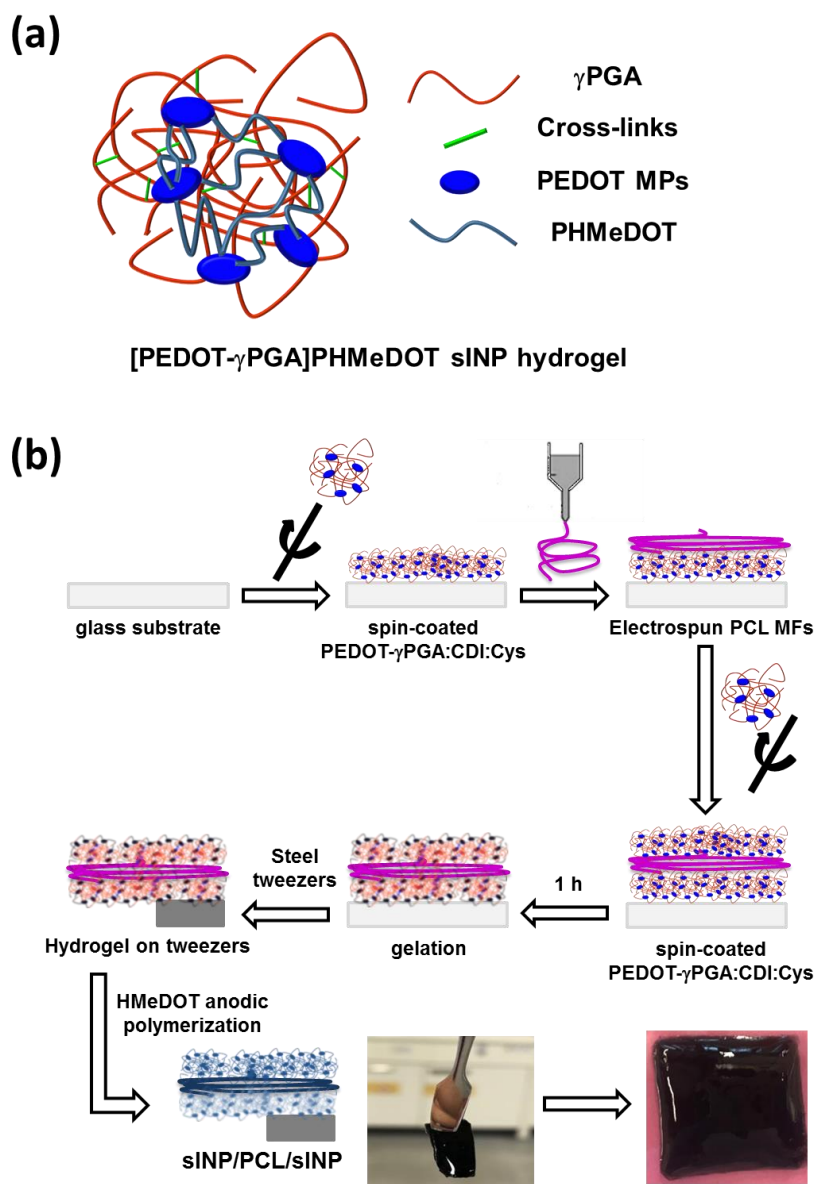**Figure 3.5.1.** (a) Sketch of the sINP [PEDOT-γPGA]PHMeDOT hydrogel. (b) Scheme of the procedure used to prepare three-layered sINP/PCL/sINP platforms. Photographs of platforms supported onto steel tweezers and free-standing are included.

3.5.3.2 Morphology

As described in the previous section, the resulting platforms are composed of several elements. Hence, special attention was placed to characterize their

morphological features in an effort to understand the effect of each one of the constitutive elements on the overall performance of the device. The surface structure of lyophilized γPGA hydrogels consists in a cellular architecture with macropores, which are relatively uniform in both size and shape (**Figure 3.5.2 2a**). Thus, although the pores are irregularly shaped, differences among them are small enough to allow their organization in to a pseudo-honeycomb pattern. Besides, the effective pore size was measured to be 7 ± 2 μm.

The process employed to transform PEDOT films into PEDOT MPs is of vital importance to control the final size of the MPs (**Figure 3.5.2b**). More specifically, sonication of PEDOT films in acetonitrile and subsequent centrifugation resulted in dense agglomerates of PEDOT MPs, which exhibited an effective diameter of 1.7 ± 0.3 μm (**Figure 3.5.2b**, left). In order to reduce the size and increase the dispersibility of the MPs, the sonication and centrifugation processes were successively repeated in acetonitrile, acetone and milli-Q water. After this treatment, well-dispersed PEDOT NPs with an effective diameter of 0.9 ± 0.5 μm were obtained (**Figure 3.5.2b**, right).

The morphological characterization of the PEDOT-γPGA hydrogel was carried out before and after the semi-interpenetration with PHMeDOT (**Figure 3.5.2c** and **d**, respectively). The incorporation of PEDOT MPs to the γPGA hydrogel does not affect the morphology of the latter (**Figure 3.5.2c**). Furthermore, the dispersion of these MPs, which are not in contact, indicates that their electrochemical response could be improved creating conduction paths to connect them. Instead, the sINP [PEDOT-γPGA]PHMeDOT hydrogel exhibits a drastic morphological change (**Figure 3.5.2d**). More specifically, PHMeDOT completely coats the surface of the hydrogel, the largest pores being the only ones that remain uncovered by the ICP after the anodic polymerization process.
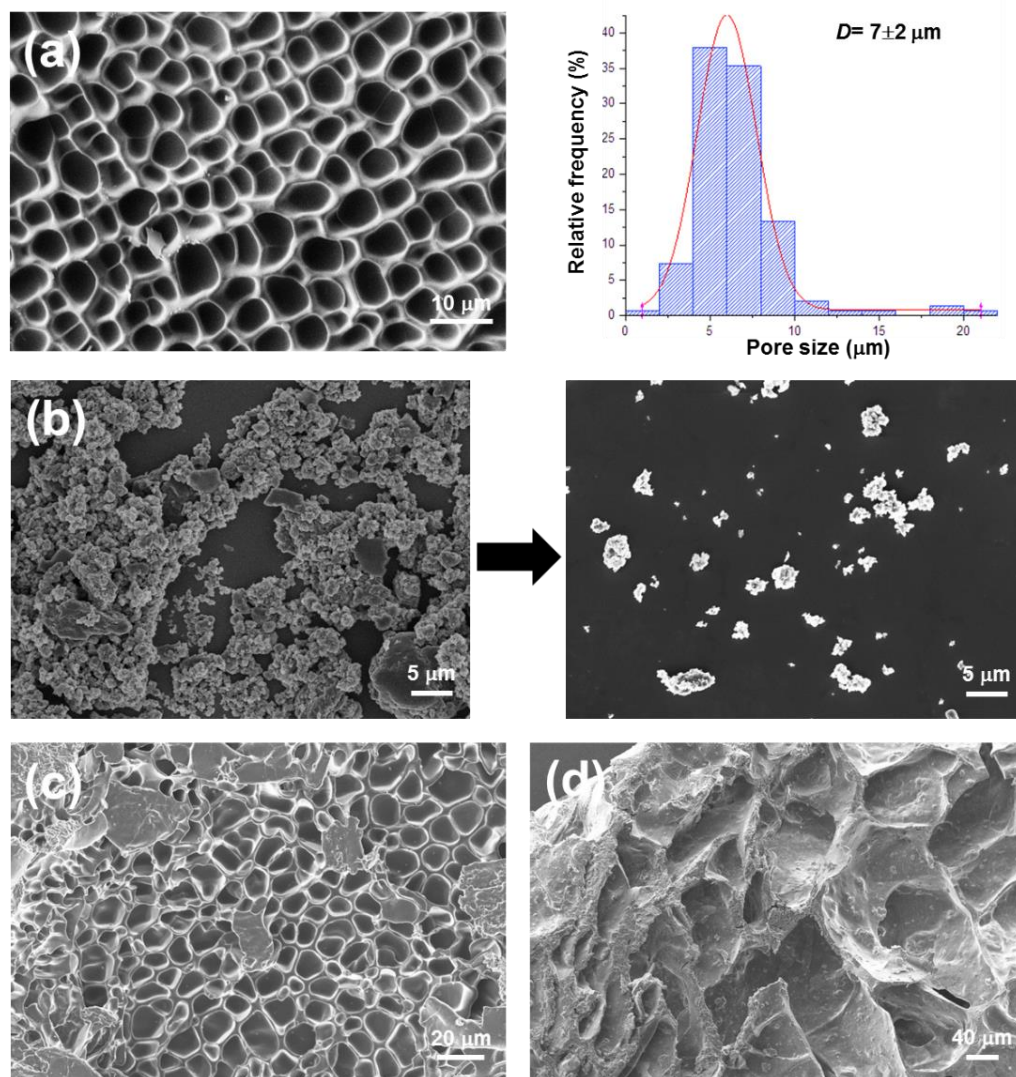
Figure 3.5.2. Representative SEM micrographs of (a) γPGA hydrogel, (b) PEDOT MPs, (c) PEDOT-γPGA hydrogel and (d) sINP [PEDOT-γPGA]PHMeDOT hydrogel. The diameter distribution of the hydrogel pores and the corresponding average value ± standard deviation are displayed in (a). The influence of the sonication and centrifugation process in the dispersibility and size of the MPs is displayed in (b): left side micrograph corresponds to MPs sonicated in acetonitrile and, subsequently, centrifuged, while the right side one refers to MPs sonicated and centrifuged repeatedly in acetonitrile, acetone and milli-Q water.

The shape and the diameter distribution of electrospun PCL MFs were also determined (**Figure 3.5.3a**). MFs present a cylindrical morphology with an average diameter (D) of 742 ± 44 nm. An important observation is that

electrospun MFs are collected forming a very porous mat, which is consequence of their random alignment. Because of this porosity, the mat of PCL MFs is expected to be penetrated by the PHMeDOT chains in three-layered sINP/PCL/sINP platforms, facilitating the formation of conduction paths connecting the two external hydrogel layers. Finally, the two hydrogel layers and the intermediate PCL fibrous mat are well-assembled in the sINP/PCL/sINP platform (**Figure 3.5.3b**), which is also demonstrated below by the peel test. Furthermore, micrographs reveal that the electropolymerized PHMeDOT network is not restricted to the two hydrogel layers but successfully extends over the PCL fibrous mat, thus favoring the electrochemical response of the platform as a whole (see below).
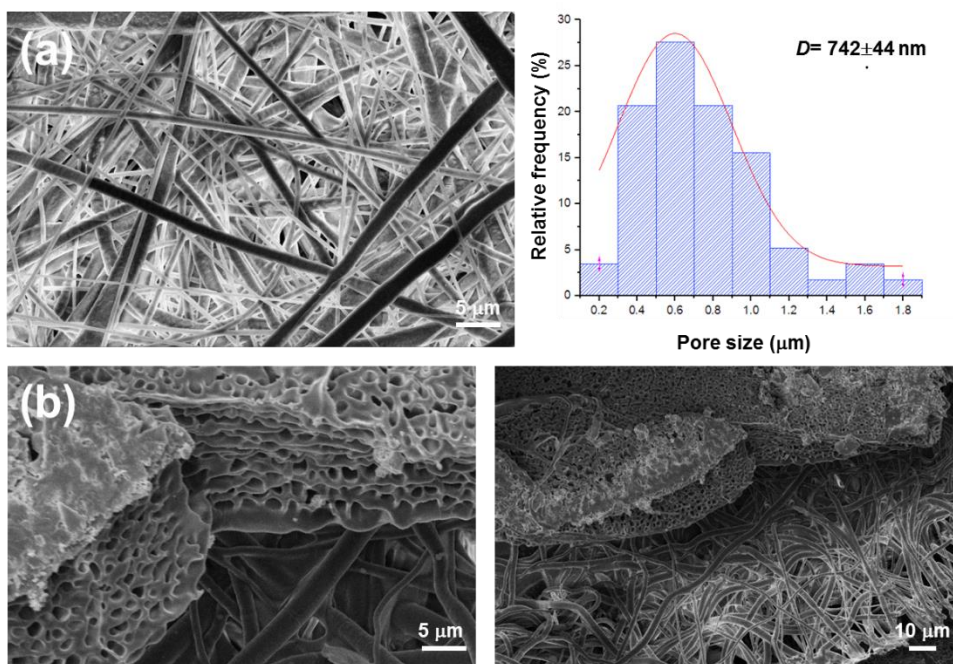
Figure 3.5.3. Representative SEM micrographs of: (a) the PCL fibrous mat; and (b) the sINP/PCL/sINP platform (two different magnifications). The diameter distribution of PCL MFs and the corresponding average value ± standard deviation is displayed in (a).

3.5.3.3 *Chemical and electrochemical characterization of sINP/PCL/sINP platforms*

The FTIR spectra recorded for γPGA hydrogel, PEDOT film, sINP hydrogel and PCL electrospun mat are shown in **Figure 3.5.4a**. Detailed discussion of each is provided below:

γPGA hydrogel. The spectrum of γPGA shows sharp and intense absorption peaks at 1636, 1542 and 1257 cm^{-1}, which correspond to stretching vibration of the amide carbonyl group (amide I), the –CONH– bond vibration (amide II) and the C–N vibration, respectively, and a broad peak at 3291 cm^{-1} attributable to the N–H stretching. Such four peaks confirm the presence of amide groups in γPGA, including cross-link bonds, whereas the absence of peaks at approximately 1728 (free carboxylic acid), 1580 (asymmetric COO$^-$) and 1400 cm^{-1} (symmetric COO$^-$) reflects the success of the condensation reaction used to form the hydrogel.[67]

PEDOT film. The spectrum displays characteristic absorption bands at 1513 (asymmetric C=C stretching) and 1291 cm^{-1} (inter-ring C–C stretching). Besides, the bands appearing at 1166, 1120, 1064 and 1031 cm^{-1} are attributed to the C–O–C vibrations in the ethylenedioxy group, while the C–S–C vibrations in the thiophene ring occur at 954, 902 and 869 cm^{-1}.

sINP hydrogel. The spectrum of the [PEDOT-γPGA]PHMeDOT hydrogel includes: the amide I, amide II and the C–N vibrations of γPGA hydrogel (1628, 1536 and 1255 cm^{-1}, respectively); the C=C and C–C stretching modes, which overlaps the amide I and amide II, as well as the C–O–C (1169, 1120, 1065 and 1033 cm^{-1}) and the C–S (954 cm^{-1}) vibrations of PEDOT; and a very intense and broad peak centered at 3248 cm^{-1} associated to the vibrations of the hydroxyl groups of PHMeDOT. The small peak at 1729 cm^{-1} was associated with enhanced oxidation processes due to the large polymerization time (7 h).[68]

PCL electrospun mat. The spectrum of PCL is well-known[69] It shows a strong band associated to the carbonyl stretching mode at 1721 cm^{-1}. Other important bands that can be easily identified in fibrous PCL mats are the asymmetric and symmetric CH$_2$ stretching (2939 and 2866 cm^{-1}, respectively), the C–O and C–C stretching in the crystalline phase (1293 cm^{-1}), asymmetric and symmetric COC stretching (1239 and 1176 cm^{-1}, respectively), and the C–O and C–C stretching in the amorphous phase (1160 cm^{-1}).[69]

In summary, the γPGA hydrogel spectrum shows the typical bands ascribed to the amide bond (*i.e.* amide I, amide II, C–N stretch and N–H stretch), whereas the absence of the free carboxylic acid, asymmetric COO$^-$ and symmetric COO$^-$ reflects the success of the condensation reaction used to form the hydrogel.[21] On the other hand, PEDOT film displays the characteristic absorption bands of the thiophene and ethylenedioxy groups. The spectrum of the sINP [PEDOT-γPGA]PHMeDOT hydrogel includes the amide peaks of γPGA hydrogel, the characteristic vibrations of the thiophene and ethylenedioxy groups, and a very intense and broad band associated to the vibrations of the hydroxyl groups of PHMeDOT.[68] The FTIR spectrum of PCL is fully consistent with those reported in the literature.[69]

Regarding the sINP/PCL/sINP spectrum, although clear identification of the absorption bands is not possible for all individual components, the most characteristic trends of sINP hydrogels and PLC mats are observed (marked by semi-transparent boxes in **Figure 3.5.4a**).

The success of the *in situ* PHMeDOT electropolymerization was also demonstrated by Raman spectrometry comparing the spectra obtained for PEDOT-γPGA and sINP [PEDOT-γPGA]PHMeDOT hydrogels (**Figure 3.5.5**). Indeed, after the incorporation of PHMeDOT, the peaks at 1430 and 1485 cm^{-1}, which correspond to the C=C symmetrical and asymmetrical stretching,

respectively, shift to 1433 and 1496 cm^{-1}, respectively, and become more intense. Moreover, the peaks at 2878 and 2960 cm^{-1}, which have been associated with the exocyclic hydroxyl group, are only detected for the sINP hydrogel.

Cyclic voltammograms recorded for γPGA/γPGA, PEDOT-γPGA/PEDOT-γPGA and sINP/sINP bi-layered systems in water with 0.1 M LiClO$_4$ are compared in **Figure 3.5.4b**. As it is reflected by the very small cathodic and anodic areas, the electrochemical activity of γPGA/γPGA is practically inexistent. However, these areas increase considerably when conducting PEDOT MPs are incorporated into the biopolymer matrix. Thus, PEDOT-γPGA/ PEDOT-γPGA shows an oxidation peak at 0.82 V and a reduction shoulder between -0.1 and 0.1 V, which have been associated with the reversible formation of polarons and bipolarons in PEDOT chains, supporting the successful loading of PEDOT MPs and showing their essential contribution to the redox charge storage capacity. As expected, the electrochemical response is more pronounced for sINP/sINP than for PEDOT-γPGA/PEDOT-γPGA on account of the formation of PHMeDOT networks semi-interpenetrating the hydrogel matrix. The effect of PHMeDOT conduction paths is also evidenced by the enhancement of the current density at both the initial/final and reversal potentials.

Figure 3.5.4b, which includes the voltammogram recorded for the sINP/PCL/sINP platform in the same electrolytic medium, shows that the electrochemical activity increases when the two sINP hydrogels are separated by the fibrous PCL layer. This feature has been attributed to the fact that PHMeDOT conduction networks grow not only inside the sINP hydrogel layers but especially inside the fibrous PCL layer. Thus, the diffusion of HMeDOT monomers across the porous PCL mat is favored, facilitating the anodic polymerization of PHMeDOT and, therefore, promoting the connection between the two sINP hydrogel layers.

234

The areal specific capacitance (SC, in mF/cm^2) values, which were determined by applying **Equation 3.5.1**, are fully consistent with the discussion of the electrochemical activity. SC increases as follows: γPGA/γPGA < PEDOT-γPGA/PEDOT-γPGA < sINP/sINP < sINP/PCL/sINP (**Figure 3.5.4c**). On the other hand, the loss of electrochemical activity (LEA, in %), which refers to the stability of the platform against consecutive oxidation-reduction cycles, was calculated through the variation of voltammetric charge (**Equation 3.5.2**). Thus, the electrochemical stability decreases with increasing LEA values. The LEA parameter, which indicates the electrochemical stability of the system, increases as follows: PEDOT-γPGA/PEDOT-γPGA < sINP/sINP < sINP/PCL/sINP (**Figure 3.5.4d**). Hence, not only do the conduction paths provide higher ability to store charge (as it is reflected by the SC value) by semi-interpenetrating the hydrogel layers and connecting them across the PCL layer, but also enhanced longevity against redox processes.
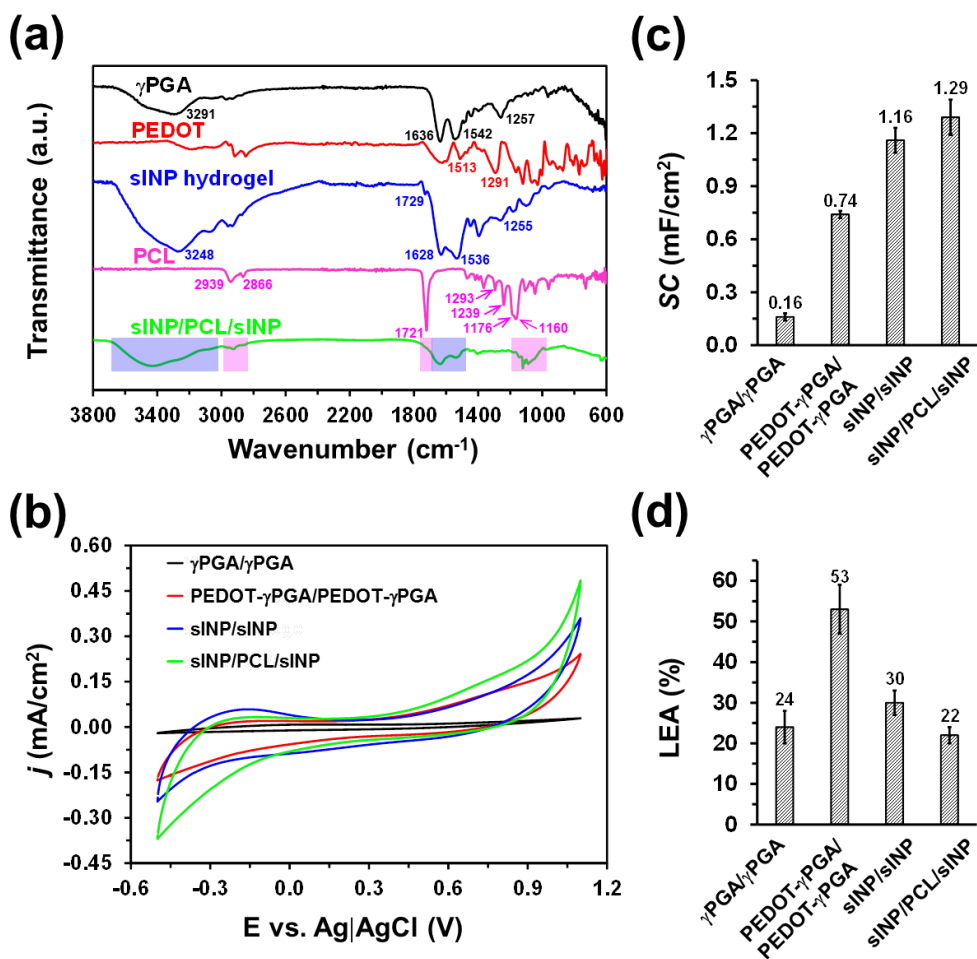
Figure 3.5.4. (a) FTIR spectra, (b) cyclic voltammograms (scan rate: 100 mV/s), (c) areal specific capacitances (*SC*) and (d) loss of electrochemical activity (LEA) of different bi- and three-layered platforms prepared in this work.
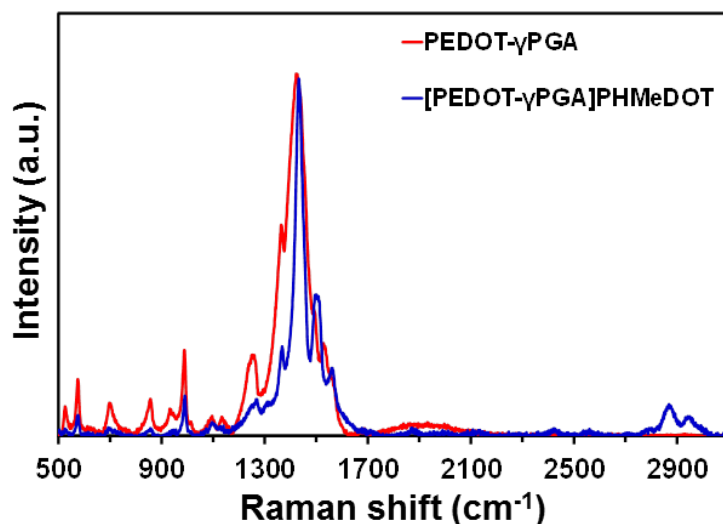
Figure 3.5.5. Raman spectra of PEDOT-γPGA and sINP [PEDOT-γPGA]PHMeDOT hydrogels.

3.5.3.4 *Thermal stability, swellability and mechanical characterization of sINP/PCL/sINP platforms*

Thermal gravimetric analysis (TGA) was conducted for γPGA/γPGA, PEDOT-γPGA/PEDOT-γPGA, sINP/sINP, γPGA/PCL/γPGA and sINP/PCL/sINP to examine their degradation profiles. In all cases, a small weight loss (*i.e.* ~10 %) is detected at around 100 °C, which has been attributed to the evaporation of absorbed water (**Figure 3.5.6a**). The thermal degradation of γPGA/γPGA, PEDOT-γPGA/PEDOT-γPGA and sINP/sINP starts at a similar temperature, the predominant decomposition step occurring at ~275 ºC for such three bi-layered systems. Moreover, the chemical heterogeneity of γPGA hydrogels, which is related to the influence of the long and short molecular tracts (*i.e.* the polypeptide backbone and the crosslinks, respectively) in the diffusion of the degraded molecules, explains the different degradation steps observed for γPGA/γPGA in the DGTA profile. The incorporation of PEDOT MPs enhances the problems associated with the diffusion of the degradation products, adding

complexity to the degradation process. In contrast, the anodic polymerization of PHMeDOT provides homogeneity to the polymeric matrix, facilitating the diffusion of the degraded molecules (*i.e.* a single predominant peak is observed in the DGTA profile).

It is well-known that the thermal degradation of PCL fibrous mats starts at 350 ºC.[70,71] This value, which is higher than that found for γPGA hydrogel, explains the enhanced thermal stability of γPGA/PCL/γPGA and sINP/PCL/sINP with respect to γPGA/γPGA and sINP/sINP, respectively. The most prominent peak in the DGTA curve of γPGA/PCL/γPGA and sINP/PCL/sINP appears at 305 and 280 ºC, respectively. The difference between such two systems is again caused by the chemical heterogeneity of γPGA in γPGA/PCL/γPGA (*i.e.* the predominant peak is surrounded by local peaks at 281 and 342 ºC, evidencing restrictions related to degraded products diffusion, as in γPGA/γPGA) and the homogeneity caused by the anodic polymerization in the sINP/PCL/sINP platform (*i.e.* the predominant peak is much clearly defined, as for sINP/sINP).

The incorporation of PCL MFs between the two hydrogel layers affects not only the thermal stability, but also the swellability of the platform (**Figure 3.5.6b**). The swelling ratio (SR, **Equation 3.5.3**) of γPGA/γPGA and sINP/sINP decreases upon the incorporation of the intermediate PCL layer by 65% and 49%, respectively. This observation is attributed to the poor wettability of PCL fibrous mats, which behave as hydrophobic systems with water contact angles of ∼120º.[72] On the other hand, the incorporation of PEDOT MPs into γPGA/γPGA enhanced the SR by 65%, this effect being slightly more pronounced (*i.e.* 8%) after the anodic polymerization of PHMeDOT. The increment of the SR for PEDOT-γPGA/PEDOT-γPGA and sINP/sINP with respect to γPGA/γPGA has been attributed to the incorporation of doped PEDOT and PHMeDOT chains, which

enhance the hydrophilicity of the γPGA matrix due to the charges (*i.e.* each ICP chain stores n positive charges balanced with n perchlorate anions).

As the mechanical integrity of anodically polymerized ICPs is null,[73–76] the influence of the PCL intermediate layer on the strength of the platform was evaluated by conducting stress-strain assays in γPGA/γPGA and γPGA/PCL/γPGA samples. An important factor in mechanical tests is good sample grip, which is particularly difficult when the specimens are formed by sticky and soft hydrogels. The strategy used to overcome this challenge includes the utilization of elastic materials to help grip the samples (*i.e.* to reduce the pressure of grip), as shown in **Figure 3.5.7a**. The measured stress-strain curves which are compared in **Figure 3.5.6c**, reflect the notable influence of the PCL layer. Thus, γPGA/γPGA displays an elastic behavior with a very low Young modulus of 0.2 ± 0.1 kPa. Unfortunately, tensile strength measurements at strain values higher than ~50% were not possible because of the loss of grip. Interestingly, the incorporation of the fibrous layer not only improved the gripping, allowing measures at higher strains, but also reinforced the mechanical resistance of the platform. Thus, the Young modulus estimated for γPGA/PCL/γPGA was 1.1 ± 0.5 kPa, which represents an increase of more than five times with respect to γPGA/γPGA.

A peel test was conducted using a tensile testing equipment to determine the strength of the adhesive bond between the γPGA hydrogel and the PCL fibrous mat (**Figure 3.5.7b**). For this purpose, a bi-layered γPGA/PCL system was prepared by applying spin coating and electrospinning successively. After drying at room temperature for 24 h, the resulting stress-strain curve, which is shown in **Figure 3.5.6d**, indicate that the peel strength required to detach the two layers is of around 1.5 MPa. This adhesive strength is very high considering that the interface between hydrophilic γPGA hydrogel and the hydrophobic PCL MFs

does not involve covalent bonds. Thus, the adhesive strength of hydrogels is usually around 1 MPa or even lower.[77,78] For example, hydrophilic adhesive formulations made by blending poly(N-vinylpyrrolidone) and hydroxyl terminated poly(ethylene glycol) exhibited debonding stresses comprised between 0.6 and 1.1 MPa.[78]
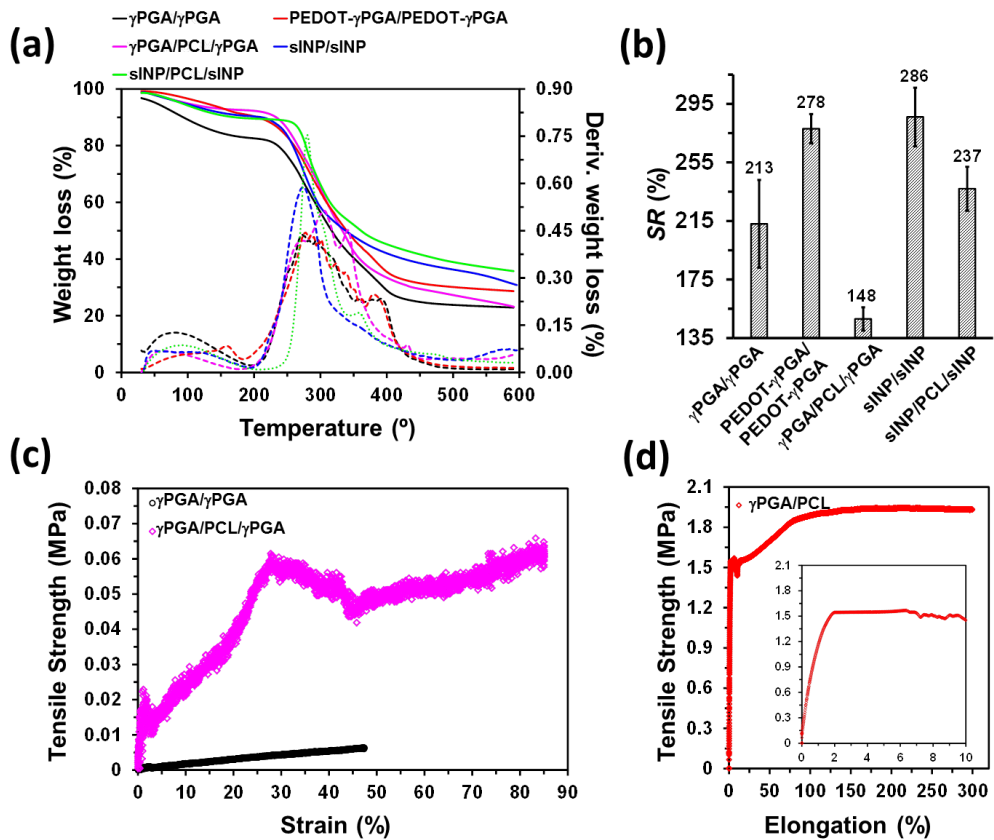
Figure 3.5.6. (a) Thermogravimetric (solid lines) and derivative thermogravimetric curves (dashed lines), (b) swelling ratio (*SR*), (c) strain-stress curves and (d) peel test of different bi- and three-layered bioplatforms prepared in this work.
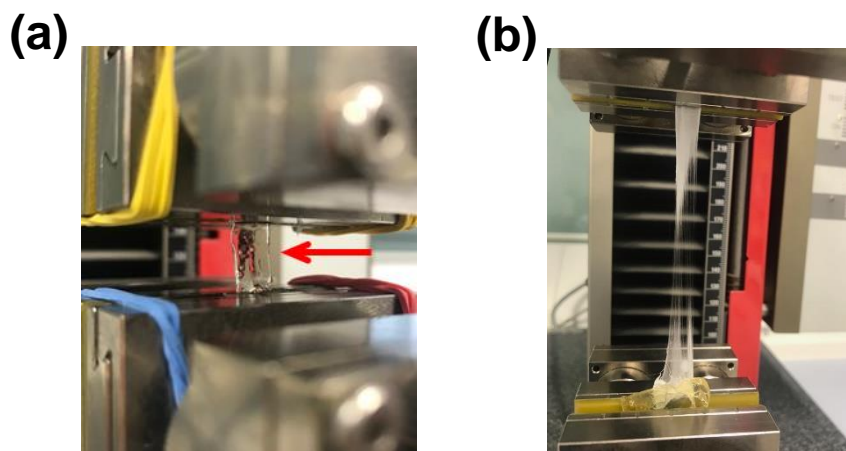
Figure 3.5.7. (a) γPGA/γPGA sample preparation for strain-stress tests. The position of the sample is indicated by the red arrow. (b) Peel test for the bi-layered γPGA/PCL sample.

3.5.3.5 Loading of levofloxacin

sINP/PCL/sINP platforms loaded with levofloxacin (LVX), hereafter named [sINP/PCL/sINP]LVX, were prepared by adapting the last step of the procedure sketched in **Figure 3.5.1b**. More specifically, the antibiotic (2 mM) was added to the aqueous solution with HMeEDOT (10 mM) and LiClO$_4$ (0.1 M) used in the anodic polymerization step. As mentioned above, the PEDOT-γPGA/PCL/ PEDOT-γPGA was kept immersed in this reaction medium for 12 h under stirring before to initiate the polymerization of PHMeDOT, which favoured not only the penetration of the HMeDOT monomer but also of the antibiotic LVX inside the platform.

The successful incorporation of LVX into the bioplatform was evidenced by UV-Vis spectrometry (**Figure 3.5.8a**). Indeed, the absorption peak centered at 286 nm and the shoulder at ~320 nm indicate the presence of LVX in the [sINP/PCL/sINP]LVX platform. According to the calibration curve obtained with the peak at 286 nm in a 0.1 M LiClO$_4$ aqueous solution (**Figure 3.5.8b**), the

amount of antibiotic loaded in the [sINP/PCL/sINP]LVX platform was of 219.5 ± 40.1 µM.
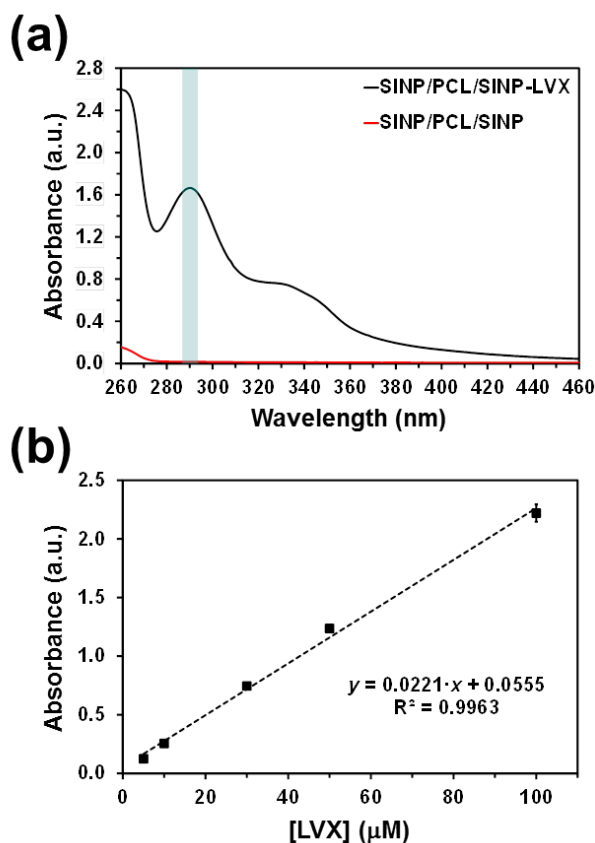
Figure 3.5.8. (a) Comparison between the UV-Vis spectra of sINP/PCL/sINP and [sINP/PCL/sINP]LVX bioplatforms. (b) LVX calibration curve in 0.1 M LiClO₄ aqueous solution using the absorbance at 286 nm.

3.5.3.6 *Release and detection of levofloxacin*

The release of the antibiotic from [sINP/PCL/sINP]LVX was expected to depend on the relative strength of the interactions between the drug and the different polymeric components of the platform or the molecules from the 0.1 M LiClO₄ aqueous solution used as release medium (*i.e.* water and ions). [sINP/PCL/sINP]LVX square pieces of 0.5×0.5 cm² were immersed in the release medium using Eppendorf tubes. At regular time intervals (*i.e.* 5 min, 15 min, 30

min, 1 h and 24 h), the release medium (1 mL) was withdrawn from the tube and analyzed by UV-Vis spectroscopy. The amount of released LVX was quantified by UV-Vis spectroscopy, using the band centered at 286 nm and the calibration curve displayed in **Figure 3.5.8b**.

The antibiotic was rapidly released to the medium (**Figure 3.5.9a**). More specifically, ~80% of LVX was released to the medium during the first 30 min, whereas only 7% of the antibiotic content remained inside the platform after 1 h. This fast release has been attributed to the weakness of the interactions between LVX and the polymeric components of the platform, which are rapidly compensated by the strong interactions between the carboxylate of LVX and the ions of the medium. Despite this inconvenience, it should be noted that this work focuses on the conceptualization of a dual platform for real-time detection of the released drug. Hence, investigations on the dependence between the chemical structure of potential drugs and the kinetics of their release are beyond the scope of this study.

On the other hand, **Figure 3.5.10** shows the LVX release profile from [sINP/PCL/sINP]LVX in 0.1 M phosphate buffer saline (PBS) solution. As expected, the behavior is very similar to that observed in 0.1 M LiClO$_4$ aqueous solution. Small differences have been attributed to side effects occurring in PBS, as for example the competition of the different anions (perchlorate – used in the synthesis of the ICP -, phosphate and chloride) to act as dopant agent or the competition from the different cations (Li$^+$, Na$^+$ and K$^+$) to interact with LVX, which may affect the release response.

Figure 3.5.9b shows the cyclic voltammograms for [sINP/PCL/sINP]LVX samples as prepared and after being immersed in the release medium for 5 min, 15 min, 30 min and 1 h. For comparison, the voltammogram recorded for unloaded sINP/PCL/sINP (control) is included in the graphic. The curve for as

prepared [sINP/PCL/sINP]LVX shows shoulders at ~0.3 V (cathodic scan) and 1.10 V (anodic scan), which are associated with the oxidation and reduction of the loaded LVX, respectively, and are not observed for as prepared sINP/PCL/sINP. The peak intensity of the loaded LVX oxidation decreases with increasing immersion time, which evidences that the release of antibiotic to the medium is successfully detected by the integrated bioplatform. Consistently, the voltammograms of sINP/PCL/sINP (control) did not show such oxidation and reduction shoulders after 60 min of immersion in the release medium (**Figure 3.5.11**).

The detection of loaded LVX is clearly observed in **Figure 3.5.9c**, which represents the current density at a potential of 1.10 V. The current density decreases linearly with the immersion time of the [sINP/PCL/sINP]LVX platform into the release medium, evidencing that the integrated platform is sensible enough to detect very low concentrations of LVX. Apparently, this sensitivity is independent of area of the voltammogram, which decreases with the number of redox cycles.

The sensitivity of the detection process is demonstrated by the graphics displayed in **Figure 3.5.9d** and **e**. The former graphic represents the current density at a potential of 1.10 V measured by cyclic voltammetry for [sINP/PCL/sINP]LVX samples as prepared and after being immersed in the release medium for 5 min, 15 min, 30 min and 1 h (**Figure 3.5.9b**) *vs* the LVX concentration remaining at the platform at such time intervals, as determined by UV-Vis spectroscopy (**Figure 3.5.9a**). The linear relation, $R^2 = 0.9802$, reflects that the ICP internally distributed across the hydrogels and MFs layer can be successfully applied to detect the antibiotic loaded into the semi-interpenetrated platform.

The calibration curve for the detection of LVX (**Figure 3.5.9e**) was obtained using flat PHMeDOT films prepared by anodic polymerization on steel tweezers by applying a constant potential of 1.10 V for 600 s. As expected, a linear correlation with $R^2 = 0.9371$ was achieved, confirming that this ICP-based method is able to detect LVX. Most importantly, application of the linear equation obtained in **Figure 3.5.9d** to the LVX concentrations used for the latter calibration curve provides very similar current densities (empty symbols in **Figure 3.5.9e**). The small differences between the experimental and theoretical calibration curves should be attributed to the fact that (i) the accessibility of ICP is much easier in the film than in the semi-interpenetrated platform; and (ii) the amount of ICP, which is different in the compared systems.
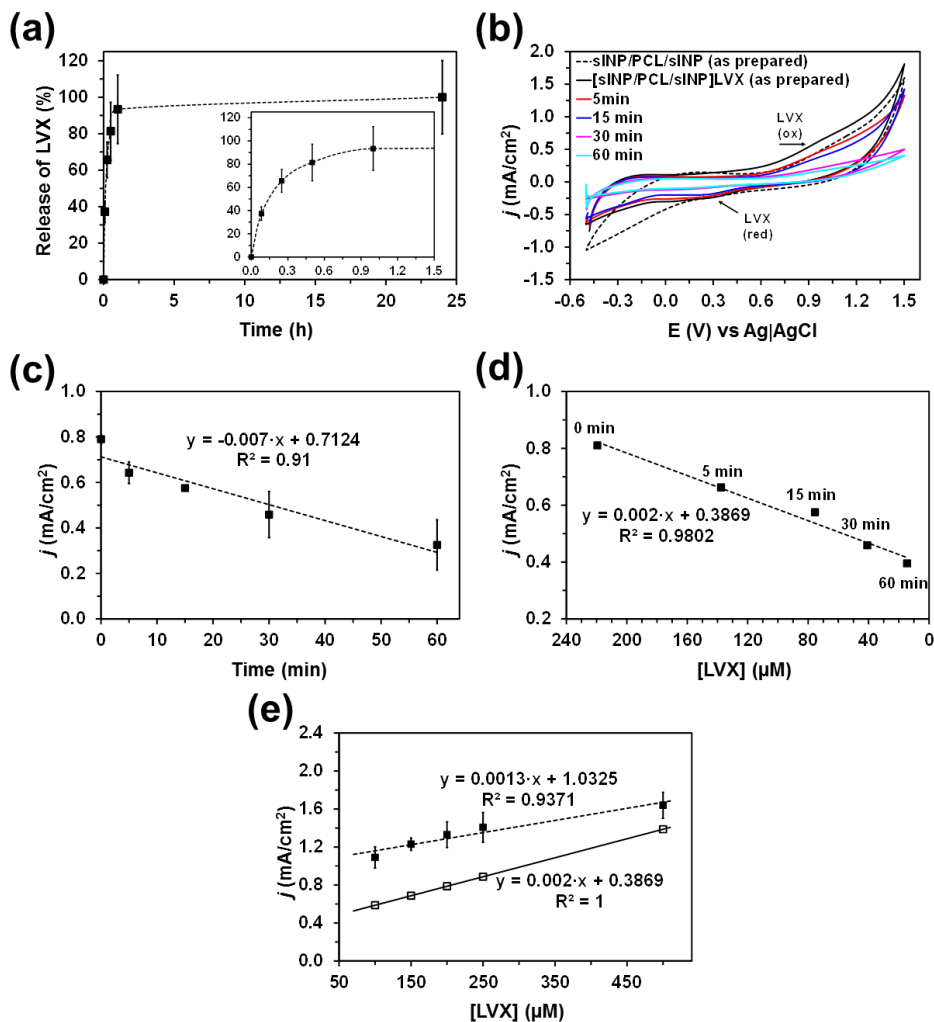
Figure 3.5.9. (a) LVX release profile in 0.1 M LiClO₄ aqueous solution from [sINP/PCL/sINP]LVX bioplatform. (b) Cyclic voltammogrands (scan rate: 100 mV/s) obtained using unloaded sINP/PCL/sINP and [sINP/PCL/sINP]LVX. Voltammograms for the latter were recorded for samples as prepared and after 5, 15, 30 and 60 min of immersion into the release medium. (c) Variation of the current density at a potential of 1.10 V for LVX at the integrated [sINP/PCL/sINP]LVX bioplatform against the time immersed into the release medium. (d) Graphic representing the current density at a potential of 1.10 V measured by cyclic voltammetry for [sINP/PCL/sINP]LVX as prepared and after 5 min, 15 min, 30 min and 1 h immersed in the release medium *vs* the LVX concentration remaining at the platform at such time intervals, as determined by UV-Vis spectroscopy. (e) Calibration curve for the detection of LVX using flat PHMeDOT films (filled symbols) and representation of the current density obtained by applying the linear equation obtained in (d) to the same LVX concentrations (empty symbols).
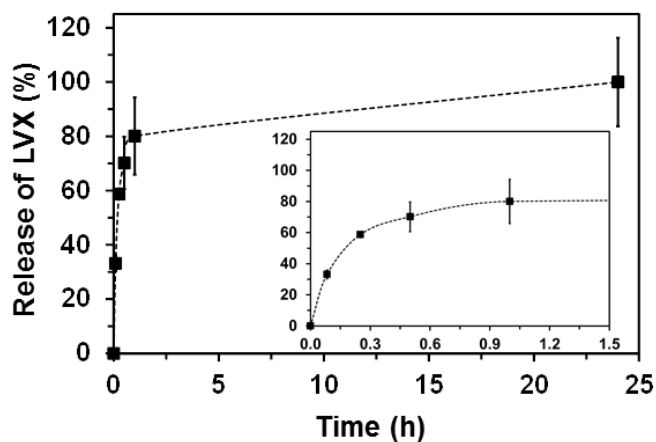
Figure 3.5.10. LVX release profile in 0.1 M PBS solution from [sINP/PCL/sINP]LVX bioplatform.
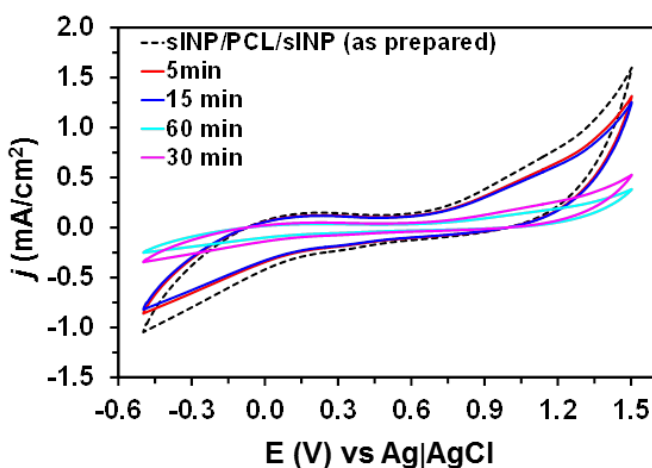
Figure 3.5.11. Cyclic voltammogrands (scan rate: 100 mV/s) obtained using unloaded sINP/PCL/sINP Voltammograms were recorded for samples as prepared and after 5, 15, 30 and 60 min of immersion into the release medium.

3.5.3.7 *Activity of released levofloxacin*

Investigation of the antibacterial mechanism of released LVX is out of the scope of this work, even though the possible mechanisms of action of antibacterial

agents released from hydrogels have been exhaustively reviewed.[79] In this section we demonstrate that the antibiotic, which was loaded by diffusion before the anodic polymerization of HMeDOT monomers, was not damaged by the applied potential, preserving its activity. For this purpose, the antibacterial activity of the platform loaded with LVX was tested against *E. coli* and *S. sanguinis* as representative of Gram-negative and Gram-positive bacteria, respectively, using the agar diffusion test. Thus, [sINP/PCL/sINP]LVX and control samples were emplaced in an agar plate where bacteria were grown to test the extent to which bacteria are affected by released LVX. Both free LVX and discs of nalidixic acid (NAX), which is a well-known Gram-negative antibacterial agent, were used as positive controls, while unloaded sINP/PCL/sINP was considered as the negative control.

After incubating for 24 h, inhibition zones around [sINP/PCL/sINP]LVX, free LVX and NAX samples were clearly identified for the two tested bacteria indicating that compounds with bactericidal activity diffuse outward from the samples (**Figure 3.5.12**). Thus, such clear zones are halos of inhibited bacterial growth, which indicate the inability of the tested organisms to survive in presence of free LVX and antibiotic released from the platform. Moreover, the size of the halos obtained for [sINP/PCL/sINP]LVX and free LVX are very similar, indicating that the susceptibility of the tested bacteria towards the released antibiotic is similar to that towards the free one. This observation is fully consistent with the fast release of the antibiotic from the [sINP/PCL/sINP]LVX platform. Besides, the antimicrobial action is more pronounced for *E. coli* than for *S. sanguinis*, as it is revealed by the size of the halos, since both LVX and NAX are more effective against Gram-negative bacteria. On the other hand, no inhibition zone *S. sanguinis* or a small halo *E. coli* was detected for sINP/PLC/sINP samples, thus confirming that the polymeric matrix is harmless to bacteria. The small halo found for sINP/PLC/sINP controls in *E. coli* cultures

has been attributed to the bacteriostatic effect of residual solvent or reagent, which resulted innocuous in *S. sanguinis* cultures. However, as both [sINP/PCL/sINP]LVX and sINP/PLC/sINP were prepared using identical procedures and materials, such small bacteriostatic effect does not affect the qualitative conclusions extracted from the experiments.
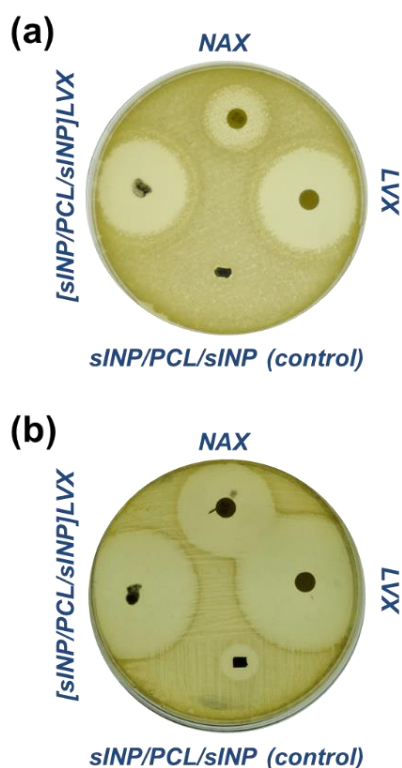
Figure 3.5.12. (a) *S. sanguinis* and (b) *E. coli* bacterial cultures showing the inhibition zones around [sINP/PCL/sINP]LVX, free LVX (positive control) and NAX discs (positive control). Unloaded sINP/PCL/sINP was also tested as negative control.

3.5.4 Conclusion

Four different biocompatible polymers (*i.e.* γPGA, PEDOT, PCL and PHMeDOT) have been used to manufacture the sINP/PCL/sINP and sINP/PCL/sINP]LVX platforms. These systems consist on electrospun PCL MFs in the middle of two PEDOT-γPGA hydrogel layers, the whole three-layered system being semi-interpenetrated by PHMeDOT conducting networks. In addition of good mechanical and electrochemical properties, sINP/PCL/sINP exhibits drug-loading capacity, which has been used to prepare sINP/PCL/sINP]LVX. Although LVX, which has been loaded during the semi-interpenetration step, was released very rapidly, the antibiotic was electrochemically monitored in real-time while remaining inside the platform. Moreover, the antibiotic has been demonstrated to preserve its antimicrobial activity. The design of dual-functional polymeric devices with drug-loading capacity and electrochemical response is a very promising approach for the development of advanced biomedical applications. However, much work is still required to use this multi-functionality as a practical loading-monitoring tool. Future studies will focus on the effect of the multi-component nature of the sINP/PCL/sINP platform in the drug loading capacity, establishing relationships with the chemical structure of the loaded drug, as well as in its (bio)degradability rate.

3.5.5 References

1. Xiao, H. *et al.* Recent progress in polymer-based platinum drug delivery systems. *Prog. Polym. Sci.* **87**, 70–106 (2018).

2. Liechty, W. B., Kryscio, D. R., Slaughter, B. V. & Peppas, N. A. Polymers for Drug Delivery Systems. *Annu. Rev. Chem. Biomol. Eng.* **1**, 149–173 (2010).

3. Xu, Y., Kim, C.-S., Saylor, D. M. & Koo, D. Polymer degradation and drug delivery in PLGA-based drug-polymer applications: A review of experiments and theories. *J. Biomed. Mater. Res. Part B Appl. Biomater.* **105**, 1692–1716 (2017).

4. Luliński, P. Molecularly imprinted polymers based drug delivery devices: A way to application in modern pharmacotherapy. A review. *Materials Science and Engineering C* vol. 76 1344–1353 (2017).

5. Ulbrich, K. *et al.* Targeted Drug Delivery with Polymers and Magnetic Nanoparticles: Covalent and Noncovalent Approaches, Release Control, and Clinical Studies. *Chem. Rev.* **116**, 5338–5431 (2016).

6. Alvarez-Lorenzo, C. & Concheiro, A. Smart drug delivery systems: from fundamentals to the clinic. *Chem. Commun.* **50**, 7743–7765 (2014).

7. Siegel, R. A. Stimuli sensitive polymers and self regulated drug delivery systems: A very partial review. *J. Control. Release* **190**, 337–351 (2014).

8. Fortuni, B. *et al.* Polymeric Engineering of Nanoparticles for Highly Efficient Multifunctional Drug Delivery Systems. *Sci. Rep.* **9**, 2666 (2019).

9. Dunn, S. S., Luft, J. C. & Parrott, M. C. Zapped assembly of polymeric (ZAP) nanoparticles for anti-cancer drug delivery. *Nanoscale* **11**, 1847–1855 (2019).

10. Wang, J.-L. *et al.* The effect of surface poly(ethylene glycol) length on in vivo drug delivery behaviors of polymeric nanoparticles. *Biomaterials* **182**, 104–113 (2018).

11. Karthik, S. *et al.* Coumarin polycaprolactone polymeric nanoparticles: light and tumor microenvironment activated cocktail drug delivery. *J. Mater. Chem. B* **5**, 1734–1741 (2017).

12. Puiggalí-Jou, A., Micheletti, P., Estrany, F., del Valle, L. J. & Alemán, C. Electrostimulated Release of Neutral Drugs from Polythiophene Nanoparticles: Smart Regulation of Drug-Polymer Interactions. *Adv. Healthc. Mater.* **6**, 1700453 (2017).

13. Goyal, R., Macri, L. K., Kaplan, H. M. & Kohn, J. Nanoparticles and nanofibers for topical drug delivery. *J. Control. Release* **240**, 77–92 (2016).

251

14. Cleeton, C., Keirouz, A., Chen, X. & Radacsi, N. Electrospun Nanofibers for Drug Delivery and Biosensing. *ACS Biomater. Sci. Eng.* **5**, 4183–4205 (2019).

15. Puiggalí-Jou, A., Cejudo, A., del Valle, L. J. & Alemán, C. Smart Drug Delivery from Electrospun Fibers through Electroresponsive Polymeric Nanoparticles. *ACS Appl. Bio Mater.* **1**, 1594–1605 (2018).

16. Eslamian, M., Khorrami, M., Yi, N., Majd, S. & Abidian, M. R. Electrospinning of highly aligned fibers for drug delivery applications. *J. Mater. Chem. B* **7**, 224–232 (2019).

17. Singh, A., Rath, G., Singh, R. & Goyal, A. K. Nanofibers: An Effective Tool for Controlled and Sustained Drug Delivery. *Curr. Drug Deliv.* **15**, 155–166 (2018).

18. Liberato, M. S. *et al.* Polycaprolactone fibers with self-assembled peptide micro/nanotubes: a practical route towards enhanced mechanical strength and drug delivery applications. *J. Mater. Chem. B* **4**, 1405–1413 (2016).

19. Hu, X. *et al.* Electrospinning of polymeric nanofibers for drug delivery applications. *J. Control. Release* **185**, 12–21 (2014).

20. Enshaei, H. *et al.* Scaffolds for Sustained Release of Ambroxol Hydrochloride, a Pharmacological Chaperone That Increases the Activity of Misfolded β-Glucocerebrosidase. *Macromol. Biosci.* **19**, 1900130 (2019).

21. Sun, S. *et al.* Episcleral drug film for better-targeted ocular drug delivery and controlled release using multilayered poly-ε-caprolactone (PCL). *Acta Biomater.* **37**, 143–154 (2016).

22. Anandhakumar, S., Gokul, P. & Raichur, A. M. Stimuli-responsive weak polyelectrolyte multilayer films: A thin film platform for self triggered multi-drug delivery. *Mater. Sci. Eng. C* **58**, 622–628 (2016).

23. Garvie-Cook, H., Frederiksen, K., Petersson, K., Guy, R. H. & Gordeev, S. N. Biophysical elucidation of the mechanism of enhanced drug release and topical delivery from polymeric film-forming systems. *J. Control. Release* **212**, 103–112 (2015).

24. Pérez-Madrigal, M. M., Armelin, E., Puiggalí, J. & Alemán, C. Insulating and semiconducting polymeric free-standing nanomembranes with biomedical applications. *J. Mater. Chem. B* **3**, 5904–5932 (2015).

25. Tao, G. *et al.* Design and performance of sericin/poly(vinyl alcohol) hydrogel as a drug delivery carrier for potential wound dressing application. *Mater. Sci. Eng. C* **101**, 341–351 (2019).

26. Wang, S., Attah, R., Li, J., Chen, Y. & Chen, R. A pH-Responsive Amphiphilic Hydrogel Based on Pseudopeptides and Poly(ethylene glycol) for Oral Delivery of Hydrophobic Drugs. *ACS Biomater. Sci. Eng.* **4**, 4236–4243 (2018).

252

27. Mahanta, A. K., Senapati, S. & Maiti, P. A polyurethane–chitosan brush as an injectable hydrogel for controlled drug delivery and tissue engineering. *Polym. Chem.* **8**, 6233–6249 (2017).

28. Liu, M., Song, X., Wen, Y., Zhu, J.-L. & Li, J. Injectable Thermoresponsive Hydrogel Formed by Alginate- g -Poly(N -isopropylacrylamide) That Releases Doxorubicin-Encapsulated Micelles as a Smart Drug Delivery System. *ACS Appl. Mater. Interfaces* **9**, 35673–35682 (2017).

29. Yang, J. *et al.* Polypeptide-Engineered Hydrogel Coated Gold Nanorods for Targeted Drug Delivery and Chemo-photothermal Therapy. *ACS Biomater. Sci. Eng.* **3**, 2391–2398 (2017).

30. Wang, X. *et al.* A Polydopamine Nanoparticle-Knotted Poly(ethylene glycol) Hydrogel for On-Demand Drug Delivery and Chemo-photothermal Therapy. *Chem. Mater.* **29**, 1370–1376 (2017).

31. Dash, T. K. & Konkimalla, V. B. Poly-ϵ-caprolactone based formulations for drug delivery and tissue engineering: A review. *J. Control. Release* **158**, 15–33 (2012).

32. Wang, X. *et al.* Drug distribution within poly(ε-caprolactone) microspheres and in vitro release. *J. Mater. Process. Technol.* **209**, 348–354 (2009).

33. Gorna, K. & Gogolewski, S. In vitro degradation of novel medical biodegradable aliphatic polyurethanes based on ϵ-caprolactone and Pluronics® with various hydrophilicities. *Polym. Degrad. Stab.* **75**, 113–122 (2002).

34. Banskota, S., Yousefpour, P., Kirmani, N., Li, X. & Chilkoti, A. Long circulating genetically encoded intrinsically disordered zwitterionic polypeptides for drug delivery. *Biomaterials* **192**, 475–485 (2019).

35. Rodríguez-Cabello, J. C., Arias, F. J., Rodrigo, M. A. & Girotti, A. Elastin-like polypeptides in drug delivery. *Adv. Drug Deliv. Rev.* **97**, 85–100 (2016).

36. Qu, J. *et al.* Stepwise pH-sensitive and biodegradable polypeptide hybrid micelles for enhanced cellular internalization and efficient nuclear drug delivery. *Colloids Surfaces B Biointerfaces* **181**, 315–324 (2019).

37. Cohen-Erez, I. & Rapaport, H. Coassemblies of the Anionic Polypeptide γ-PGA and Cationic β-Sheet Peptides for Drug Delivery to Mitochondria. *Biomacromolecules* **16**, 3827–3835 (2015).

38. Lin, W. *et al.* Development of Zwitterionic Polypeptide Nanoformulation with High Doxorubicin Loading Content for Targeted Drug Delivery. *Langmuir* **35**, 1273–1283 (2019).

39. Feng, N. *et al.* Reduction-Responsive Polypeptide Nanogel for Intracellular Drug Delivery in Relieving Collagen-Induced Arthritis. *ACS Biomater. Sci. Eng.* **4**, 4154–4162 (2018).

40. Lu, C. *et al.* A hydrazone crosslinked zwitterionic polypeptide nanogel as a platform for controlled drug delivery. *RSC Adv.* **4**, 50301–50311 (2014).

253

41. Chilkoti, A., Dreher, M. R. & Meyer, D. E. Design of thermally responsive, recombinant polypeptide carriers for targeted drug delivery. *Adv. Drug Deliv. Rev.* **54**, 1093–1111 (2002).

42. Dong, Y. *et al.* Site-Specific Drug-Releasing Polypeptide Nanocarriers Based on Dual-pH Response for Enhanced Therapeutic Efficacy against Drug-Resistant Tumors. *Theranostics* **5**, 890–904 (2015).

43. Gao, Y. & Dong, C.-M. Reduction- and thermo-sensitive core-cross-linked polypeptide hybrid micelles for triggered and intracellular drug release. *Polym. Chem.* **8**, 1223–1232 (2017).

44. Mora, L. *et al.* Real-time electrochemical monitoring of drug release from therapeutic nanoparticles. *J. Control. Release* **140**, 69–73 (2009).

45. Yang, G. *et al.* 4-Phosphatephenyl Covalently Modified Glassy Carbon Electrode for Real-Time Electrochemical Monitoring of Paracetamol Release from Electrospun Nanofibers. *Electroanalysis* **24**, 1937–1944 (2012).

46. Zhou, T. *et al.* 4-Phosphatephenyl-modified glassy carbon electrode for real-time and simultaneous electrochemical monitoring of paracetamol and diclofenac release from electrospun nanofibers. *Anal. Methods* **7**, 9289–9294 (2015).

47. Fabregat, G., Giménez, A., Díaz, A., Puiggalí, J. & Alemán, C. Dual-Functionalization Device for Therapy through Dopamine Release and Monitoring. *Macromol. Biosci.* **18**, 1800014 (2018).

48. Wang, T.-T. *et al.* AIE/FRET-based versatile PEG-Pep-TPE/DOX nanoparticles for cancer therapy and real-time drug release monitoring. *Biomater. Sci.* **8**, 118–124 (2020).

49. Zhu, J. *et al.* Real-time monitoring of etoposide prodrug activated by hydrogen peroxide with improved safety. *J. Mater. Chem. B* **7**, 7548–7557 (2019).

50. Wei, R. *et al.* Versatile Octapod-Shaped Hollow Porous Manganese(II) Oxide Nanoplatform for Real-Time Visualization of Cargo Delivery. *Nano Lett.* **19**, 5394–5402 (2019).

51. Hu, F. *et al.* Real-time monitoring of pH-responsive drug release using a metal-phenolic network-functionalized upconversion nanoconstruct. *Nanoscale* **11**, 9201–9206 (2019).

52. Li, X. *et al.* Core–Satellite Nanomedicines for in Vivo Real-Time Monitoring of Enzyme-Activatable Drug Release by Fluorescence and Photoacoustic Dual-Modal Imaging. *ACS Nano* **13**, 176–186 (2019).

53. Gnaim, S. *et al.* Direct Real-Time Monitoring of Prodrug Activation by Chemiluminescence. *Angew. Chemie* **130**, 9171–9175 (2018).

54. Cao, F. *et al.* Encapsulation of aggregated gold nanoclusters in a metal–organic framework for real-time monitoring of drug release. *Nanoscale* **9**, 4128–4134 (2017).

55. Fan, Z., Sun, L., Huang, Y., Wang, Y. & Zhang, M. Bioinspired fluorescent dipeptide nanoparticles for targeted cancer cell imaging and real-time monitoring of drug release. *Nat. Nanotechnol.* **11**, 388–394 (2016).

56. Ding, J. *et al.* Electrospun polymer biomaterials. *Prog. Polym. Sci.* **90**, 1–34 (2019).

57. Feng, X. *et al.* Electrospun polymer micro/nanofibers as pharmaceutical repositories for healthcare. *J. Control. Release* **302**, 19–41 (2019).

58. Bubnova, O. *et al.* Semi-metallic polymers. *Nat. Mater.* **13**, 190–194 (2014).

59. Aradilla, D. *et al.* Hybrid polythiophene–clay exfoliated nanocomposites for ultracapacitor devices. *J. Mater. Chem.* **22**, 13110 (2012).

60. Kayser, L. V. & Lipomi, D. J. Stretchable Conductive Polymers and Composites Based on PEDOT and PEDOT:PSS. *Adv. Mater.* **31**, 1806133 (2019).

61. del Valle, L. J., Estrany, F., Armelin, E., Oliver, R. & Alemán, C. Cellular Adhesion, Proliferation and Viability on Conducting Polymer Substrates. *Macromol. Biosci.* **8**, 1144–1151 (2008).

62. Izadi, E. *et al.* Levofloxacin: Insights Into Antibiotic Resistance and Product Quality. *Front. Pharmacol.* **10**, (2019).

63. Ogunleye, A. *et al.* Poly-γ-glutamic acid: production, properties and applications. *Microbiology* **161**, 1–17 (2015).

64. Ashiuchi, M. *et al.* Isolation of Bacillus subtilis (chungkookjang), a poly-?-glutamate producer with high genetic competence. *Appl. Microbiol. Biotechnol.* **57**, 764–769 (2001).

65. Matsusaki, M., Serizawa, T., Kishida, A. & Akashi, M. Novel functional biodegradable polymer. III. The construction of poly(γ-glutamic acid)-sulfonate hydrogel with fibroblast growth factor-2 activity. *J. Biomed. Mater. Res. Part A* **73A**, 485–491 (2005).

66. Taniguchi, M. *et al.* Physicochemical properties of cross-linked poly-γ-glutamic acid and its flocculating activity against kaolin suspension. *J. Biosci. Bioeng.* **99**, 130–135 (2005).

67. Pérez-Madrigal, M. M., Edo, M. G., Díaz, A., Puiggalí, J. & Alemán, C. Poly-γ-glutamic Acid Hydrogels as Electrolyte for Poly(3,4-ethylenedioxythiophene)-Based Supercapacitors. *J. Phys. Chem. C* **121**, 3182–3193 (2017).

68. Saborío, M. C. G. *et al.* Flexible Electrodes for Supercapacitors Based on the Supramolecular Assembly of Biohydrogel and Conducting Polymer. *J. Phys. Chem. C* **122**, 1078–1090 (2018).

69. Coleman, M. M. & Zarian, J. Fourier-transform infrared studies of polymer blends. II. Poly(ε-caprolactone)–poly(vinyl chloride) system. *J. Polym. Sci. Polym. Phys. Ed.* **17**, 837–850 (1979).

70. Lee, J. M. *et al.* Three dimensional poly(ε-caprolactone) and silk fibroin nanocomposite fibrous matrix for artificial dermis. *Mater. Sci. Eng. C* **68**, 758–767 (2016).

71. Ren, K., Wang, Y., Sun, T., Yue, W. & Zhang, H. Electrospun PCL/gelatin composite nanofiber structures for effective guided bone regeneration membranes. *Mater. Sci. Eng. C* **78**, 324–332 (2017).

72. Planz, V. *et al.* Three-dimensional hierarchical cultivation of human skin cells on bio-adaptive hybrid fibers. *Integr. Biol.* **8**, 775–784 (2016).

73. Seki, Y., Takahashi, M. & Takashiri, M. Effects of different electrolytes and film thicknesses on structural and thermoelectric properties of electropolymerized poly(3,4-ethylenedioxythiophene) films. *RSC Adv.* **9**, 15957–15965 (2019).

74. Abdelhamid, M. E., Snook, G. A. & O'Mullane, A. P. Electropolymerisation of Catalytically Active PEDOT from an Ionic Liquid on a Flexible Carbon Cloth Using a Sandwich Cell Configuration. *Chempluschem* **80**, 74–82 (2015).

75. Bhagwat, N., Kiick, K. L. & Martin, D. C. Electrochemical deposition and characterization of carboxylic acid functionalized PEDOT copolymers. *J. Mater. Res.* **29**, 2835–2844 (2014).

76. Michalska, A., Galuszkiewicz, A., Ogonowska, M., Ocypa, M. & Maksymiuk, K. PEDOT films: multifunctional membranes for electrochemical ion sensing. *J. Solid State Electrochem.* **8**, 381–389 (2004).

77. Heinzmann, C., Weder, C. & de Espinosa, L. M. Supramolecular polymer adhesives: advanced materials inspired by nature. *Chem. Soc. Rev.* **45**, 342–358 (2016).

78. Hofman, A. H., van Hees, I. A., Yang, J. & Kamperman, M. Bioinspired Underwater Adhesives by Using the Supramolecular Toolbox. *Adv. Mater.* **30**, 1704640 (2018).

79. Li, S. *et al.* Antibacterial Hydrogels. *Adv. Sci.* **5**, 1700527 (2018).
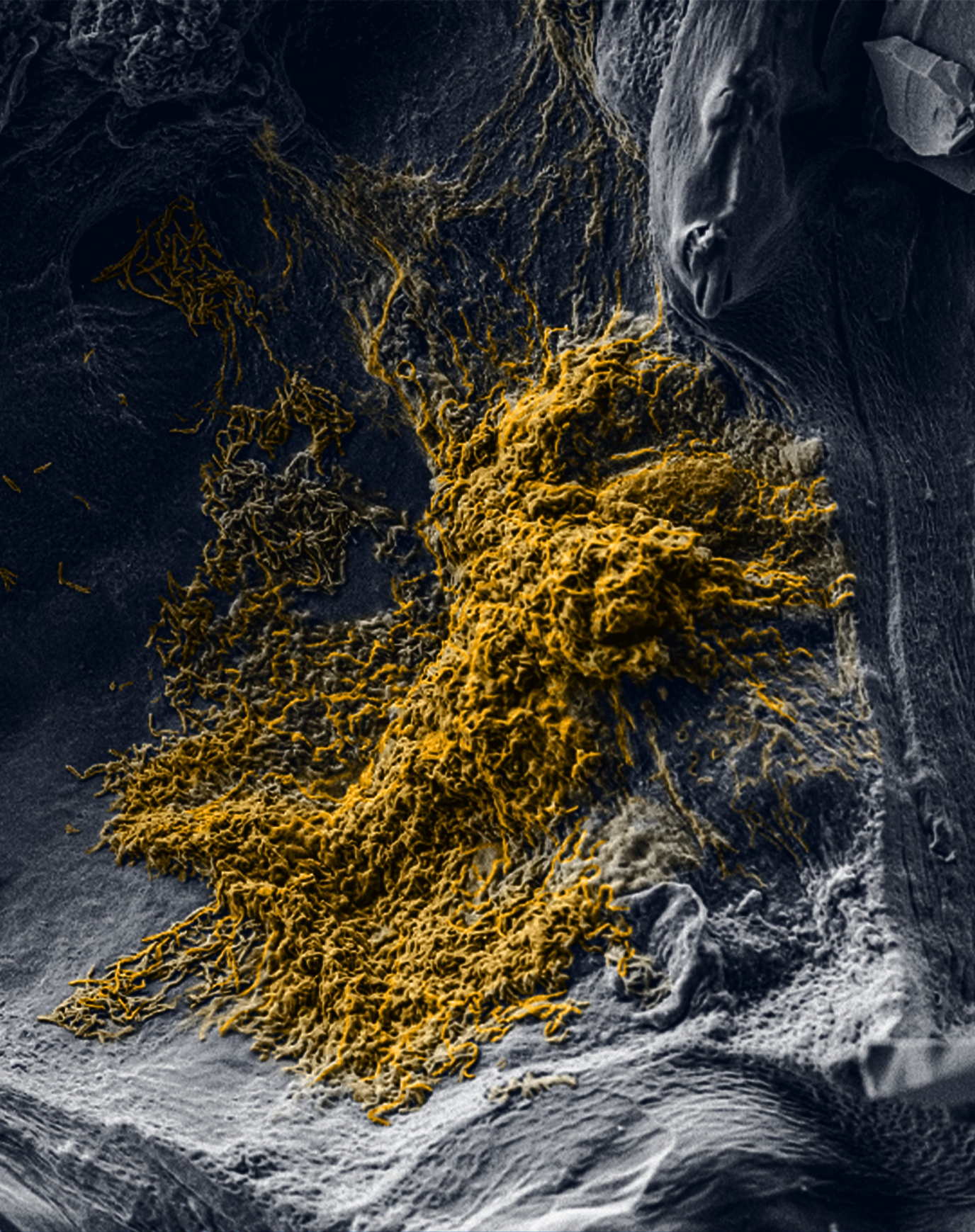
256

Chapter 4

Conclusions

Conclusions

1. A simple and highly sensitive electrode consisting of CAM-loaded PEDOT NPs has been developed to monitor the inhibition of bacterial growth in real-time using CV.

2. Both CAM and PYR have been successfully loaded in PEDOT NPs. The loading capacity was similar for CAM and PYR (i.e. 11.9 ± 1.3 % w/w and 11.4 ± 1.5 %), which has been attributed to their chemical and physical similarity.

3. PEDOT/CAM and PEDOT/PYR NPs are promising electro-responsive platforms for regulating CAM and PYR, respectively, to the desired optimal dosage. Important advantages are: a) the simplicity of the synthesis, which allows the *in situ* drug-loading; b) the high stability and fast response against electrical signals of the drug-loaded NPs, which are even higher than for unloaded NPs; and c) the very low toxicity of PEDOT NPs.

4. Although the release of CAM from PEDOT/CAM NPs was very slow, even applying external electrical stimuli, the bacterial growth inhibition has been demonstrated.

5. The release of PYR from loaded PEDOT NPs is very low in absence of stimulus, while it increases considerably (~50%) when sustained CV stimulation is applied for 30 min.

6. The dual functions of PEDOT/CAM NPs, which allow to follow the infection progression while releasing the antibiotic, reflect not only their versatility but also their potential utility for the treatment and control of bacterial infections.

7. A new system, which combines the advantages of PGGA biohydrogel and the electrochemical activity of PEDOT NPs, have been prepared to regulate the release of CUR, a hydrophobic drug with poor solubility in water.

8. The innovative combination of PEDOT NPs and PGGA hydrogel allows to tune the CUR release kinetics by applying an electrical voltage.

9. PGGA/PEDOT should be considered a smart stimuli-responsive drug-carrier able to deliver the small hydrophobic drug in a temporal and dosage-controlled fashion.

10. AH, a small and polar PC that increases the activity of misfolded GCase, can be loaded in fibrous PCL scaffolds by electrospinning.

11. The fast release rate of AH from PCL MFs, which occurs in less than one hour, has been regulated by coating the fibrous scaffold with films, which were prepared by dip-coating and by spin-coating.

12. The AH release extends to weeks and months when coatings were achieved by dip-coating and spin-coating, respectively. Accordingly, PCL coated-fibrous scaffolds can be used to regulate strategically the dosage of polar drugs depending on the therapeutic needs.

13. The released AH retains the protecting effect on the activity of GCase, demonstrating that the electrospinning process used to produce PCL MFs does not affect the functionality of the drug.

14. A multifunctional biomedical platform, sINP/PCL/sINP, has been manufactured by combining four different biocompatible polymers (*i.e.* γPGA, PEDOT, PCL and PHMeDOT).

15. The sINP/PCL/sINP platform has been developed using not only different polymeric materials but also different formats: electrospun PCL MFs,

γPGA hydrogel loaded with PEDOT MPs, and PHMeDOT coating for the semi-interpenetrations of the previous elements.

16. LVX has been successfully loaded in the sINP/PCL/sINP platform during the semi-interpenetration step.

17. Although the release of LVX from [sINP/PCL/sINP]LVX occurred very rapidly, the antibiotic was electrochemically monitored in real-time while remaining inside the platform.

18. The antibiotic released from [sINP/PCL/sINP]LVX has been demonstrated to preserve its antimicrobial activity.

19. The design of dual-functional polymeric devices with drug-loading capacity and electrochemical response is a very promising approach for the development of advanced biomedical applications.